Development and characterisation of the double Penning trap PIPERADE and mass measurements of neutron-rich isotopes near N=40

Mathieu Flayol

THÈSE PRÉSENTÉE

POUR OBTENIR LE GRADE DE

DOCTEUR
DE L'UNIVERSITÉ DE BORDEAUX

ECOLE DOCTORALE SCIENCES PHYSIQUES ET DE L'INGENIEUR

ASTROPHYSIQUE, PLASMAS, NUCLEAIRE

Par **Mathieu FLAYOL**

Développement et caractérisation du double piège de Penning PIPERADE et mesures de masses d'isotopes riches en neutrons proches de $N = 40$

Sous la direction de : **Stéphane GREVY**
Co-encadrante : **Pauline ASCHER**

Soutenue le 29 novembre 2024

Membres du jury :

Mme. Pauline ASCHER	Chargée de recherche	CNRS	membre invitée
M. Maxime BRODEUR	Professeur associé, eq. HDR	University of Notre Dame	Rapporteur
M. Mathias GERBAUX	Maitre de conférences	Université de Bordeaux	membre invité
M. Stéphane GREVY	Directeur de recherche	CNRS	Directeur
M. Vladimir MANEA	Chargé de recherche	CNRS	Examinateur
Mme. Sarah NAIMI	Directrice de recherche	CNRS	Rapporteure
Mme. Nadezda SMIRNOVA	Professeur	Université de Bordeaux	Présidente

Acknowledgements

Bon... ça y est... le moment est venu de remercier tous les gens qui ont partagé mon aventure bordelaise.

Tout d'abord, je tiens à remercier le jury pour le temps, l'attention et l'intérêt portés à mon travail. Je tiens aussi à vous remercier, car, malgré des emplois du temps très chargés, j'en suis sûr, vous avez su trouver le temps de venir faire la fête avec moi, ma famille et mes amis. Cela m'a vraiment touché, et j'ai hâte de pouvoir vous retrouver autour d'une bière dans une future conférence, un colloque ou un workshop !

Je tiens maintenant à remercier Pauline... Il n'y a pas de mots assez forts pour exprimer à quel point ça a été un plaisir de travailler avec toi. Depuis le stage où on passait des après-midi devant le PC à réfléchir pour setup la BGC jusqu'aux derniers moments de l'écriture, tu as été là (moins quelques mois en début de thèse, mais t'inquiète, personne n'est irremplaçable). Toujours à l'écoute, positive, souriante, brillante, empathique, patiente, et tout ça avec ou sans l'alcool (au labo et en dehors). Donc, même si tu n'es jamais venue aux nombreux repas que j'ai organisés dans mon bel appart de Gradignan, MERCI !

Je vais maintenant passer au deuxième des trois mousquetaires, Mathias. Même si tu t'es fait virer de mes encadrants par l'ED, tu as toujours été là pour répondre à mes questions, des plus basiques aux plus complexes. Tu as toujours essayé de me remettre dans le droit chemin quand mes envies de pirates ou de camembert faisaient surface. Et pour finir, je dirais que ta culture, ta rigueur scientifique, tes efforts de vulgarisation, ton empathie et ta serviabilité seraient les choses qui te caractérisent le mieux si tu ne serrais pas aussi fort les boulons et que tu n'étais pas aussi nul au ping. Tu es la personne qui m'a le plus appris en trois ans, alors pour ça et le reste, MERCI ! (Je vais bientôt passer récupérer mes bouteilles de vin, promis !)

Et voilà le dernier mousquetaire, Stéphane, ou El Director ! Même si tu as été un peu moins présent, tu as toi aussi toujours été là quand j'en avais besoin, et je t'en remercie. J'ai aussi énormément apprécié ton engagement, ta passion, ton pragmatisme, ton courage, ta franchise et ton tiramisu. La poudre de cacao que nous avons utilisée pour booster Chantal est toujours dans le hall si tu la cherches... Je crois que je ne t'y ai

pas revu depuis cette fois-là, alors c'est cohérent (j'étais obligé de faire ça, désolé, mais j'y ai pris du plaisir, sache-le). Pour tous les tails, les débats politiques et les séances de cassage de crâne sur la théorie, MERCI !

Je tiens aussi à remercier Laurent, Dinko et Audric, qui m'ont tous les trois transmis leur savoir-faire, leur passion et leur rigueur au travail. Vous avez tous les trois eu une place cruciale dans mon apprentissage et, grâce à vous, je suis toujours allé au travail en sachant que je verrais un ami, que ce soit le matin très tôt ou le soir très tard !

Merci aussi à Antoine, qui a bien voulu de moi en stage et qui m'a expliqué le fonctionnement des pièges de Penning et leurs techniques. Merci à toi de m'avoir guidé dans toutes les étapes qui ont mené au succès de l'expérience en Finlande. Tu as aussi eu un grand rôle dans mon intégration dans la vie au labo et dans le milieu scientifique en général, donc encore une fois, merci.

J'aimerais aussi remercier toute l'équipe de Jyvaskyla et, plus particulièrement, Marjut, avec qui ça a été un régal de batailler sur PIPERADE. Et comment pourrais-je parler de la Finlande sans mentionner Arthur, qui a été une de mes plus belles rencontres lors de cette thèse, autant sur le plan professionnel que personnel. J'espère seulement avoir la chance de retravailler avec toi à l'avenir.

Merci aussi à Frédéric et Duc pour nous avoir accueillis et guidés avec Quentin, Stéphane et Pauline dans cette aventure strasbourgeoise.

J'aimerais aussi remercier la nouvelle génération de trappiste, Corentin, Emmanuel et Gauthier grace à qui j'ai pu avoir une grande partie des plots de cette thèse. J'espère vraiment que vous allez vous régalez autant que j'ai pu m'amuser sur PIPERADE (surtout toi Gauthier). Merci aussi pour tout le travail et l'énergie que vous mettez dans l'amélioration des programmes d'acquisition ! C'est vraiment rassurant et réconfortant de voir que ces programmes ne seront pas abandonnés.

Merci aussi à tous les doctorants et post-doctorants du labo, anciens et nouveaux ! Que ce soit à travers des randonnées, des jeux de rôle, des jeux de plateau, des crosiflettes, des concerts, des raclettes, du ciné, du karaoké, du surf ou des journées à Aqualand, vous avez grandement participé à l'écriture de cette thèse. Pour tous ces moments, encore MERCI !

Je ne vais pas remercier le groupe NEX (puisque tout le monde sait que je suis dans le groupe PIPERADE) mais plutôt tous les permanents avec qui j'ai partagé des repas et des soirées discussions. Je pense notamment à Jérôme, Jérôme, Bertram, Béatrice, Francis, Maud, Fred, Marianne, Christine, Philippe, Thierry, Benoit, Mehdi, Marie-Hélène, Nadine et Pascale ! Merci à vous tous !

Je me dois aussi de remercier Julien et Laure, avec qui j'ai eu les meilleures soirées et discussions au BB, au Sherlock ou à la coloc. Grâce à vous et à Riflondor, je vais pouvoir laisser une trace dans l'histoire bordelaise des concours de Blind Test.

Je remercie aussi évidemment Quentin ! Tu as, durant ces trois années, été un vrai

pilier de ce labo. Toujours souriant, rayonnant (même dans les moments les plus difficiles) et surtout serviable (parfois même à tes dépens) ! Toujours chaud pour n'importe quel type de soirée, n'importe où et n'importe quand. Pour tous nos moments de déconnade et de détresse partagée, MERCI !

Il faut aussi absolument que je remercie Chaan, sans qui je ne serais même pas venu à Bordeaux. Tu as toujours été là pour moi, toi aussi, et je sais que je pourrai toujours compter sur toi.

Je tiens à remercier chaleureusement ChatGPT, qui m'a accompagné tout au long de la rédaction de cette thèse. Toujours disponible, précis et efficace, il m'a apporté une aide précieuse pour clarifier mes idées, reformuler des passages complexes et même résoudre des problèmes techniques en LaTeX. Son assistance a grandement facilité ce travail et m'a permis de me concentrer sur l'essentiel : partager ma passion pour la physique.

Je tiens aussi à remercier l'université de bordeaux et le laboratoire de physique des 2 infinis de Bordeaux pour m'avoir donné la chance de faire ma thèse et de m'avoir supporté tout au long de cette dernière.

Avant de conclure, il me reste le plus important : ma famille, mes parents, ma sœur, Gabin et surtout Pauline. Je n'aurai pas de trop d'une vie pour vous remercier assez pour le soutien que vous m'avez apporté tout au long de ce parcours. Merci infiniment !

Pour finir, j'aimerais remercier tous les inclassables et tous les gens que j'ai pu oublier : Loïc, Thomas, Quentin, Lena, Agathe, Thomas, Patrick et Françoise.

Contents

Introduction

Nuclear mass measurements play a central role in understanding the fundamental properties of atomic nuclei. Precise knowledge of nuclear masses allows for the determination of nuclear binding energies, which are essential for studying the structure of both stable and exotic nuclei and, in particular, their stability. These measurements have far-reaching implications, not only for nuclear structure physics but also for astrophysical processes such as nucleosynthesis, where the properties of neutron-rich nuclei are crucial for modeling the creation of elements in stellar environments.

In this thesis, we focus on mass spectrometry with Penning traps, a widely used and highly accurate device for measuring nuclear masses. The Penning-trap mass spectrometer combines electromagnetic fields to confine charged particles and allows the measurement of their cyclotron frequencies, which can be directly related to the particle's mass. The development and optimization of trapping techniques are fundamental for expanding our knowledge of exotic nuclei, especially those far from the valley of stability.

The experimental work of this thesis revolves around two Penning trap systems: PIPERADE, developed at LP2i Bordeaux and to be installed at the future DESIR facility at GANIL, Caen, France, and JYFLTRAP, located at the IGISOL facility in Jyväskylä, Finland. This second Penning trap system is at the forefront of precision mass spectrometry, contributing to our understanding of key regions in the nuclear chart, such as $N = 40$. The work conducted with this trap aims to constrain nuclear models and improve our knowledge of nuclear structure in regions where important changes in behavior, such as the appearance of new shell closures, may occur. The same will be true in the near future for PIPERADE at DESIR with the advantage of being able to reach other regions such as the fascinating $N = Z = 50$ region.

This thesis is structured as follows: the first chapter provides the scientific motivations behind this work. In the second chapter, the working principles of Penning traps will be explained, along with the associated mass measurement and purification techniques. Chapter three offers a technical description of the setup at LP2iB in Bordeaux with a particular focus on the new micro-channel plate with three-layer delay-lines. Chapter four focuses on the characterization of PIPERADE, covering the process from ion trapping, through the

Buffer Gas Cooling (BGC) technique, and the Time-of-Flight Ion-Cyclotron-Resonance (ToF-ICR) method, concluding with the Phase-Imaging Ion-Cyclotron-Resonance (PI-ICR) technique. Finally, the fifth chapter presents the results of the mass measurement experiment conducted using the double Penning trap JYFLTRAP in Jyväskylä and comparisons with modern shell-model calculations.

Chapter 1

Mass spectrometry

Contents

This chapter presents the physical concepts needed to understand the thesis's experimental results. First, the binding energy and the liquid drop model are introduced. Then, nuclear models are addressed, starting with the basic harmonic oscillator, progressing to the inclusion of the spin-orbit coupling, and finishing with the modern shell model introduction. This is followed by the presentation of the so-called mass filters, exploring key nuclear observables like neutron separation energy (S_n), two-neutron separation energy (S_{2n}), and related quantities. Finally, the chapter presents the thesis's motivations, highlighting the need for precise mass measurements to constrain nuclear models and outlining the scientific goals of the PIPERADE experiment at DESIR and the mass measurement campaign at Jyväskylä.

1.1 Definition

1.1.1 Binding energy

In nuclear physics, the binding energy is the energy needed to separate a nucleus into its protons and neutrons. It reflects how tightly these nucleons are bound together within the nucleus by the strong nuclear force. The greater the binding energy per nucleon, the more stable the nucleus is. The binding energy $B_N(Z,N)$ of a nucleus with Z protons and N neutrons, is defined as:

$$\frac{-B_N(Z,N)}{c^2} = M(Z,N) - Zm_p - Nm_n \tag{1.1}$$

where c is the speed of light in vacuum while m_p, m_n, and $M(Z,N)$ are the masses of the proton, the neutron, and the nucleus. The binding energy arises from multiple interactions, making it difficult to break down into individual components when measuring the mass. However, it is possible to explore these different contributions by comparing experimental data to models and looking at their evolution along isotopic or isotonic chains. In experimental mass measurements, however, the data is not typically provided in terms of binding energy but rather in an "ad-hoc" quantity known as the atomic mass excess. This approach allows for presenting only the relevant portion of the mass information with fewer digits. The mass excess, $\Delta(Z,N)$, is defined as:

$$\Delta(Z,N) = M_{at}(Z,N) - (Z+N)u \tag{1.2}$$

where u is the unified atomic mass unit, defined as $1/12^{th}$ of the atomic mass of ^{12}C, and $M_{at}(Z,N)$ is the atomic mass defined by:

$$M_{at}(Z,N) = M(Z,N) + Zm_e - B_e \tag{1.3}$$

with B_e the total binding energy of the Z electrons in the atom and m_e the mass of the electron.

1.1.2 The liquid drop model

In order to describe the nuclear binding energy, the empirical Bethe-Weizsäcker formula [Weizsacker 35], based on the so-called liquid drop model [Gamow 30][Bethe 36], is defined as:

$$B_N(Z,N) = a_v A - a_s A^{2/3} - a_c \frac{Z(Z-1)}{A^{1/3}} - a_A \frac{(N-Z)^2}{A} + \delta(Z,N) \tag{1.4}$$

where, a_v, a_s, a_c, and a_A are empirically determined coefficients. A represents the total number of nucleons, i.e. the sum of neutron number (N) and proton number (Z). The term $\delta(Z,N)$ takes a value of either zero or $\pm\delta_0(Z,N)$, depending on whether Z and

N are even or odd. In this case, $\delta_0(Z,N) = a_p A^{-1/2}$, where a_p is another empirically determined coefficient.

- The volume term, $a_v A$, scales proportionally to the number of nucleons, representing the effect of the strong nuclear force that binds them together. Note that it also indicates that the strong nuclear force has a range limited to a few nucleons. Otherwise, it would be proportional to $A(A-1)$, which is the number of pairs in a system of A constituents.

- The surface term, $a_s A^{2/3}$, accounts for nucleons at the surface, which experience fewer interactions than those in the interior, reducing the overall binding energy.

- The Coulomb term, $a_c \frac{Z(Z-1)}{A^{1/3}}$, reflects the effect of the repulsive electrostatic force between protons, which weakens binding energy as the number of protons increases.

- The asymmetry term, $a_A \frac{(N-Z)^2}{A}$, penalizes deviations from equal numbers of protons and neutrons, as balanced numbers are energetically more favorable due to the Pauli principle [Pauli 25].

- The pairing term, $\delta(Z,N)$, reflects the additional stability that comes from paired identical nucleons. For odd-odd nuclei, this term is negative; for odd-even nuclei, it is zero; for even-even nuclei, it is positive [Lilley 01].

The liquid drop model provides a valuable macroscopic description of the binding energy of a nucleus, explaining, for example, the phenomenon of spontaneous fission when the number of protons increases but falls short in capturing microscopic effects inherent to nuclear structure. One significant limitation is its inability to accurately reproduce the binding energies of nuclei at the experimentally observed magic numbers. These magic numbers, which are 2, 8, 20, 28, 50, 82, and 126, represent specific nucleon configurations that lead to the enhancement of the stability, and, therefore, higher binding energy, of certain nuclei from ^{4}He ($2p$ and $2n$) up to ^{208}Pb ($82p$ and $126n$). These magic numbers highlight the macroscopic model's inadequacies in explaining the nuances of nuclear behavior. Consequently, while the liquid drop model is a foundational framework, it requires refinement to address these discrepancies and better characterize individual nuclei.

1.2 Theoretical approach

While the liquid drop model provides a macroscopic perspective on nuclear binding energy, a more detailed understanding of nuclear structure requires microscopic models that account for the interaction of an individual nucleon with the mean-field produced by the other nucleons composing the nucleus. This can be done using a quantum mechanics

approach in which the quantum state of the nucleons is represented by a wave function, denoted as Ψ. In a system with A nucleons, the first simple analytical model is the independent particle model. A nucleon in the system evolves within a mean-field generated by the other $A-1$ nucleons. The behavior of the nucleon can be determined by solving the Schrödinger equation:

$$H|\psi\rangle = E|\psi\rangle. \tag{1.5}$$

The Hamiltonian H of a nucleon in a central potential is expressed as:

$$H = T + V, \tag{1.6}$$

with T a kinetic term and V the potential created by the $A-1$ nucleons.

1.2.1 The quest for the lost magic numbers

The potential V can be constructed to reproduce the different trends in the binding energy. In the independent particle model, nucleons are considered to move within a central potential, which is often modeled as an isotropic harmonic oscillator or a modified square well potential. Such a potential, as any other confining one, automatically generated states with quantified energies and, therefore, a "shell" structure. It is defined as follows:

$$V_{HO}(r) = \frac{m\omega^2 r^2}{2} \tag{1.7}$$

where ω is the angular frequency of the oscillator. This potential provides a remarkably good approximate solution and is particularly easy to handle mathematically, thus yielding many results analytically. The eigenvalues E_{nl} are:

$$E_{nl} = (2n + l - 1/2)\hbar\omega \tag{1.8}$$

with n the radial quantum number and l the orbital angular momentum. It is conventional in nuclear physics to give names to different l values following the convention:

$$l = 0, 1, 2, 3, 4, 5... \qquad s, p, d, f, g, h... \tag{1.9}$$

The quantum number n specifies the number of nodes (zeros) of the wave function with the usual, but not universal, convention that one counts the node at infinity but not that at $r = 0$, that is, $n = 1, 2, ...$

The energy levels of the harmonic oscillator potential are shown in figure 1.1. This arrangement of energy levels forms what are known as shells, leading to energy gaps at specific nucleon numbers. According to the Pauli principle, a finite number of particles can be contained on each level. Therefore, if we fill such a potential well with either

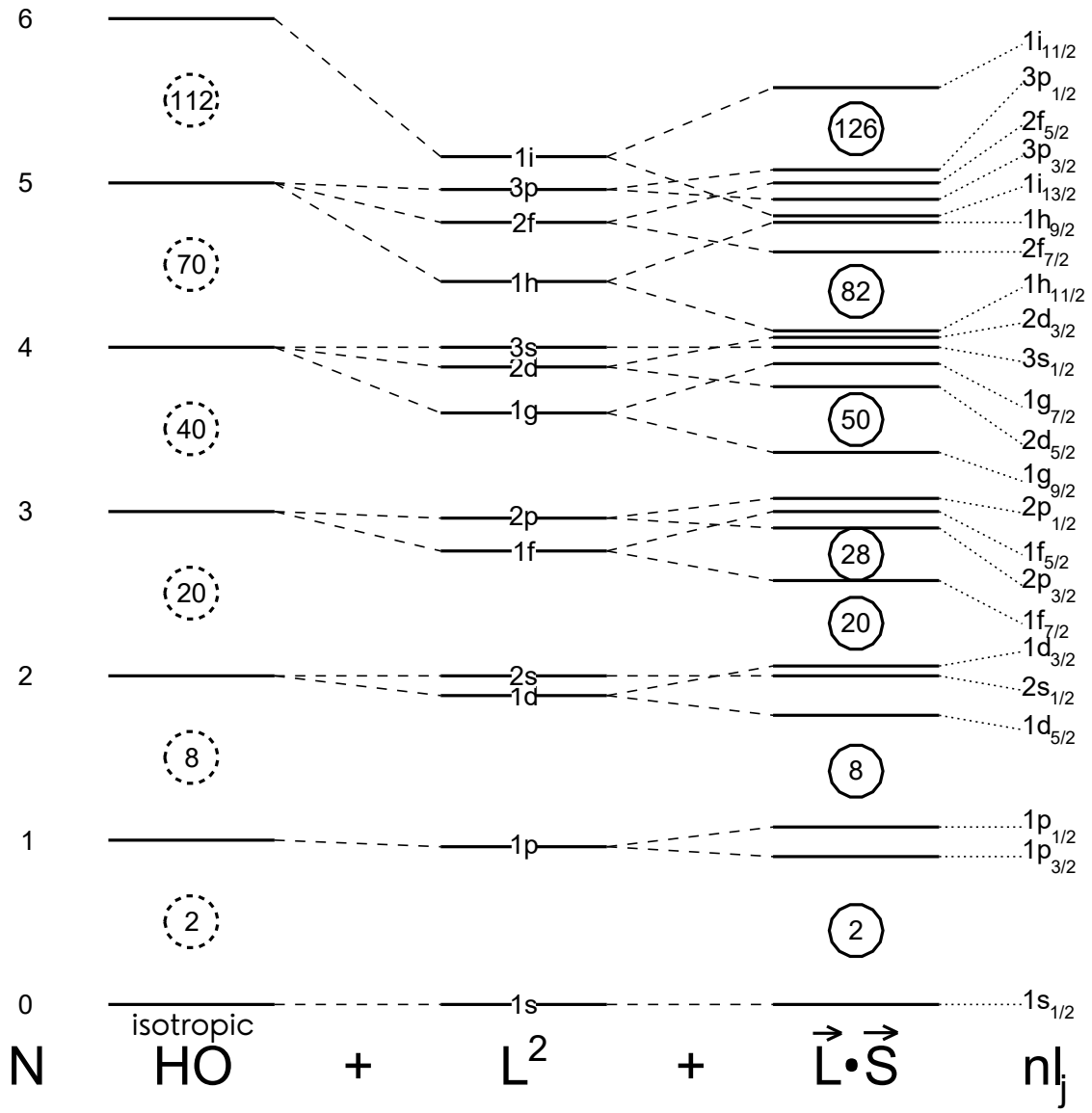

Figure 1.1: Evolution of the nuclear orbitals with the additions of the different potentials for quantum numbers N going from 0 to 6. Isotropic HO stands for the isotropic harmonic oscillator term, then L^2 for the centrifugal term, and $\vec{L}.\vec{S}$ for the spin-orbit term. On the right-most column is nl_j associated with the corresponding orbital. Figure credit: Q. Delignac.

protons or neutrons, each orbital can contain, at most, a specific number of particles. Unfortunately, the gaps created by these shells do not correspond to the empirical magic numbers of nuclear physics, except for the lowest few $(2, 8,$ and $20)$. Therefore, while the harmonic oscillator potential is a first-order approximation of the effective nuclear potential, it must be modified to reproduce the full sequence of magic numbers.

Maria Goeppert-Mayer [Mayer 49] and, independently Haxel, Jensen, and Suess [Haxel 49], introduced, in addition to the harmonic oscillator, a centrifugal term dependent on L^2 and a spin-orbit term dependent on $\vec{L}.\vec{S}$, such that:

$$V(r) = V_{OH}(r) + V_{l^2}(r)L^2 + V_{ls}(r)\vec{L}.\vec{S} \tag{1.10}$$

By adding the centrifugal term, the degeneracy in orbital angular momentum is lifted. This term separates the levels that share the same harmonic oscillator quantum number N (defined as $N = 2(n-1)+l$) but have different orbital angular momentum l. Adding the spin-orbit term lifts a further degeneracy, separating levels with the same l but different spin s. The experimentally observed magic number sequence is thus finally reproduced (see on the right of Figure 1.1). However, it has been shown in the last decades that, studying the structure of nuclei away from stable ones, these magic numbers can be weakened or even disappear. New magic numbers may emerge in these exotic regions, revealing nuclear behavior that differs from what is observed near stable isotopes. Returning to the nuclear potential, this observation tells us that the derived nuclear potential for the stable nuclei was only a "good" approximation but that a more refined nucleon-nucleon interaction is needed to capture the richness of the nuclear structure. In other words, components of the nuclear interaction that were either not directly taken into account or just averaged over the nucleus are important to be able to describe the behavior of the nuclear structure all over the nuclear chart.

1.2.2 Introduction to the modern shell model

The mean field vision approximates the nucleon-nucleon interaction as if all nucleons act similarly with each other. Even though magic numbers are well reproduced close to stability with such an approach, this ordering of levels may not hold for nuclei between shell closures or far from stability. To address these inconsistencies, individual nucleon-nucleon interactions must be taken into account in addition to the mean-field interaction. However, fully accounting for these interactions among all nucleons would demand immense computational power to solve the Schrödinger equation accurately.

To simplify this complex problem, the shell model (described in section 5.5) proposes to consider that the nucleus has an inert core that produces a mean field in which the remaining nucleons can interact all together through an "effective" nucleon-nucleon interaction. In such a frame, the Schrödinger equation will be computed for the nucleons that are in the valence space, which is the space where the nucleons are allowed to interact and, therefore, able to move among the different orbitals. Finally, an external space containing all the orbitals too high in energy for the nucleons to be accessible is defined (a representation of these three spaces is given in figure 5.12). In doing so, the computations are only constrained by the number of valence nucleons and the number of orbitals, drastically reducing the difficulty in finding solutions to the Schrödinger equation. This model allows us to account for 2-body interactions (or even 3-body forces), which will be discussed in Chapter 5.

In the following sections, we will explore how the so-called "mass filters" derived from nuclear masses can reveal information about nuclear structure and interactions and how these filters are a powerful tool in advancing nuclear theory.

1.3 Observables from mass spectrometry

Mass measurements are essential for understanding nuclear structure and testing theoretical models. Differences in binding energies derived from these measurements, commonly called mass filters, provide critical insights into the properties of nuclei. Examining the trends exhibited by these filters as a function of the neutron or proton number allows for exploring the underlying interactions within the nucleus.

Figure 1.2 illustrates the trends observed when applying various mass filters to the binding energies of the Nickel isotopic chain. The choice of the Nickel chain is not random as it not only has a magic number of protons but also, this isotope crosses a line of enhanced stability on three occasions: at $N = 20$, $N = 28$, and $N = 50$ even if ^{48}Ni is very exotic, and therefore, experimental data are scarce. As seen from the top part of Figure 1.2, the change of slope usually associated with the crossing of such a magic number of neutrons is barely visible from the trend of the binding energy itself as a function of the neutron number. The only visible effect is the dominant augmentation of binding energy as a function of A due to the strong nuclear force. Therefore, looking at the variation in binding energy, which is the neutron separation energy, S_n, representing the energy required to remove a single neutron from a nucleus is more straightforward. It is defined as follows:

$$S_n(Z, N) = B_N(Z, N) - B_N(Z, N-1) \tag{1.11}$$

Figure 1.2 plots the S_n below the binding energy, revealing three key features. First, it shows the odd-even staggering S_n, primarily driven by pairing effects, which is the dominant feature in the plot. Second, it reveals that the S_n generally decreases with the increase of neutrons, which gives the result that, aside from the pairing interaction, the residual interaction between like nucleons (here neutrons) is repulsive (shown by [Talmi 62]). Third, a noticeable drop in S_n at the magic neutron numbers $N = 28$ and $N = 50$ corresponds to the filling of new neutron orbitals. This drop is linked to the energy of the last occupied neutron single-particle level. As long as neutrons fill the same shell, the binding energy changes only slightly. However, once the shell is filled, additional neutrons begin to populate a higher-energy level, leading to a sudden reduction in S_n with the addition of just one neutron (due to the gap generated by the magic numbers and the fact that the next orbital is less bound), causing the observed drop in S_n.

The contribution of the odd-even staggering can be washed out by taking differences of binding energies of nuclei differing by two neutrons, which gives the two-neutron sepa-

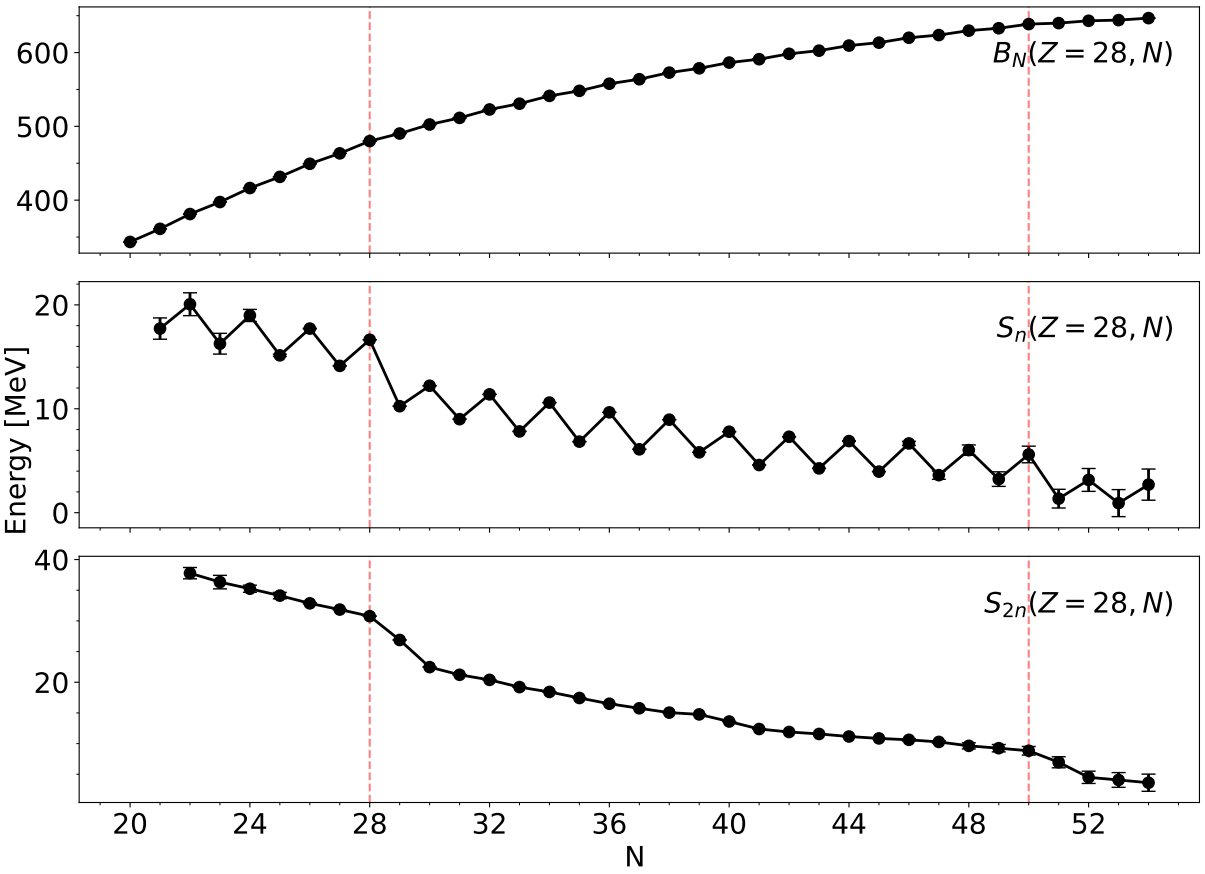

Figure 1.2: Experimental binding energies and different mass filters for the Nickel isotopes as a function of the neutron number N. Red vertical dotted lines are placed at the magic numbers $N = 28$ and $N = 50$. Mass values are taken from [Huang 21].

ration energy (S_{2n}):

$$S_{2n}(Z,N) = B_N(Z,N) - B_N(Z,N-2) \tag{1.12}$$

It is now clearly visible at the bottom of figure 1.2 that the odd-even staggering contribution is now largely suppressed. What defines the trend of S_{2n} is the characteristic two-step drop following the crossing of the neutron magic numbers $N = 28$ and $N = 50$. As discussed with S_n, while neutrons are being added to the same shell, there is only a slight variation of the S_{2n} with N, and therefore, no significant shift is observed in the trend of two-neutron separation energies. However, when a neutron shell is filled, and the first neutron occupies a higher-energy single-particle level (e.g., at $N = 29$), $B_N(Z,N)/A$ experiences a sudden decrease. At the same time, $B_N(Z,N-2)/(A-2)$ remains relatively unchanged. This creates the first step of the S_{2n} drop. Adding another neutron to the higher-energy level (e.g., at $N = 30$) causes $B_N(Z,N)/A$ to rise again due to pairing effects, while $B_N(Z,N-2)/(A-2)$ remains unchanged, resulting in the second step of the S_{2n} decrease. In this plot, another (small) kink appears at $N = 39$. This effect is not understood yet. This kink is close to the $N = 40$ subshell closure, a region that will be

at the center of the present work.

These mass filters are particularly helpful for studying shell effects, as they are sensitive to energy gaps between levels. The two-neutron separation energy can also be used to investigate the emergence of nuclear collectivity, as any deviation from the smooth variation between magic numbers may highlight changes due to collectivity. They are also a powerful tool for comparing models and adjusting them accordingly. However, all this discussion is valid if we consider that the different isotopes are considered in their ground state. The accuracy of the S_{2n} can be compromised by the presence of unresolved isomeric states, leading to a wrong binding energy measurement.

In mass-measurement techniques based on the use of Penning traps, the use of the Phase-Imaging Ion-Cyclotron-Resonance (PI-ICR) technique overcomes this issue by allowing the precise separation of most isomers, ensuring more reliable measurements of S_{2n} and related observables. Additionally, this technique allows for measuring excitation energies for long-lived isomers. In cases where these isomers beta decay, their excitation energies cannot be determined through gamma spectroscopy, making mass spectrometry the only viable method for this measurement.

1.4 Scientific motivations

This thesis has two distinct parts: the characterization of the PIPERADE Penning trap for future experimental campaigns at DESIR and a mass measurement experiment at Jyväskylä to bring new physical input that may constrain nuclear models in the region of $N = 40$.

1.4.1 PIPERADE at DESIR

The PIPERADE double Penning trap, which will be located at the GANIL laboratory's DESIR facility, is being developed to perform precision mass measurements of exotic nuclei and secondary beam purification for other experiments of the DESIR hall.

The DESIR facility at GANIL will receive neutron-deficient ion beams produced by fusion-evaporation at S3 (Super Separator Spectrometer) and exotic light nuclei from fragmentation produced by the SPIRAL1 device. Among the regions of particular interest accessible at DESIR is the $N = Z$ one. In this region, neutrons and protons occupy similar orbitals, resulting in a high degree of symmetry. This makes it an ideal environment for studying fundamental aspects of nuclear structure, such as isospin symmetry-breaking effects [Xayavong 24]. Mass measurements in this region can also provide insights into the roles of Coulomb and strong interactions, both of which may contribute to the Nolen-Schiffer anomaly [Okamoto 64], [Nolen 69], allowing us to determine which interaction is primarily responsible for the systematic reduction of estimated differences between the binding energies of mirror nuclei.

Another motivation for precise mass measurements in the $N = Z$ region is understanding the "Wigner energy"; an extra binding energy observed in $N = Z$ nuclei, hypothesized to result from enhanced proton-neutron (np) pairing with isospin $T = 0$, rather than the more common $T = 1$ pairing between like nucleons [Van Isacker 95]. Additionally, this region offers potential insights into $SU(4)$ spin-isospin symmetry, which could provide a more unified understanding of nuclear interactions. Strong shell effects are predicted near the doubly magic nucleus $N = Z = 50$, leading to significant deformation phenomena that can be confirmed through precise mass measurements.

In astrophysical contexts, mass measurements of nuclei near the proton drip line in this region are crucial for understanding the rapid proton capture process (rp-process), which occurs in explosive stellar environments. The half-lives and Q-values (the energy absorbed or released during a reaction, which can be determined from nuclear masses) in these nuclei strongly influence the rp-process, making precise mass determinations critical for modeling these astrophysical events [Hao 23], [Clement 03].

Further, the unitarity of the Cabibbo-Kobayashi-Maskawa (CKM) matrix is rigorously tested through precise measurements of V_{ud} from nuclear β-decays. Super-allowed $0^+ \rightarrow 0^+$ Fermi transitions in $T_z = 0$, -1, and -2 nuclei provide crucial tests of CKM unitarity and the Conserved Vector Current (CVC) hypothesis. Achieving the precision needed for these tests requires both high-purity beams to avoid contamination and accurate mass measurements to minimize uncertainties [Hardy 20]. The measurement of the mass difference between parent and daughter nuclei (Q value) is directly involved in the calculation of the ft value, making mass measurements also directly relevant. Mirror transitions in $T_z = -1/2$ nuclei offer complementary insights, as they involve both Fermi and Gamow-Teller transitions, reinforcing the need for high-purity beams and precise mass measurements in this region [Severijns 23].

Another region of interest at DESIR is the neutron-rich $N = 28$ region, which offers a unique opportunity to study the evolution of shell structure far from stability. In particular, mass measurements in isotopes with proton numbers $Z < 19$ are essential for probing the weakening of the $N = 28$ shell gap in neutron-rich environments. This weakening arises due to changes in the proton-neutron (pn) interaction, where central, tensor, and spin-orbit forces play distinct roles in shaping the effective shell gaps [Gade 19]. The central and tensor forces, in particular, are responsible for modifying the relative energies of the orbitals as more neutrons are added, while the spin-orbit interaction contributes to splitting the energy levels of different angular momenta. Precise mass measurements in this region can help quantify the changes in these interaction components and how they drive the quenching of the $N = 28$ shell gap.

Another motivation is refining the Isobaric Mass Multiplet Equation (IMME). This equation describes the masses of the $2T + 1$ members of an isobaric multiplet, accounting for charge-dependent effects through first-order perturbation theory. This equation is a

powerful tool for predicting unknown nuclear masses (for instance, for rp-process). However, deviations from the IMME have been observed, and there is currently no consensus on their origin [Kamil 21]. To resolve this, it is crucial to gather more experimental data, which will guide further theoretical developments. Such data could lead to the formulation of a revised "new IMME," better suited for predicting exotic masses. Additionally, this expanded experimental basis will help to test nuclear models that include isospin-symmetry breaking (ISB) components, providing a more comprehensive understanding of nuclear interactions [Lam 13].

Finally, DESIR will also explore superheavy nuclei (SHN), which lie at the upper end of the chart of nuclides. In this region, mass measurements are motivated by exploring shell closures and searching for a potential "island of stability" at extreme proton and neutron numbers [Ramirez 12]. These measurements will refine theoretical mass models, which become less reliable for such heavy nuclei. Additionally, mass measurements may reveal new isomeric states and shape effects that arise in superheavy elements, offering deeper insights into their complex structure [Ackermann 24].

To summarize, measuring nuclear masses in the $N = Z$, $N = 28$, and super heavy nuclei (SHN) regions is critical for advancing our understanding of nuclear structure, isospin symmetry, shell evolution, the limits of nuclear stability, proton-neutron correlations, shell closures, and exotic nuclear phenomena.

While the capability to measure masses with the double Penning trap PIPERADE, which I characterized during my thesis, is central to our research, the primary focus for PIPERADE was to select and purify exotic ions for the experiments conducted in the DESIR hall, giving access to observables other than the mass. The initial motivation for developing PIPERADE was high-purity beams, particularly for measuring half-lives and branching ratios (for instance, in the case of superallowed Fermi decays $0^+ \rightarrow 0^+$). In such high-precision measurements, any contamination in the ion beam can significantly impact the accuracy of the result. In addition, these high-purity beams will also be crucial for enhancing the precision of laser and decay spectroscopy experiments. We believe that this complementarity between mass measurement and purification for other experiments makes the characterization of PIPERADE a significant step towards the versatility of the DESIR hall.

1.4.2 Mass measurement experiment at Jyväskylä

The second part of this thesis focuses on mass measurements at the Jyväskylä accelerator laboratory, where the JYFLTRAP double Penning trap is located. This experiment targets neutron-rich isotopes in the region of $N = 40$, where significant structural changes are expected. Neutron-rich cobalt isotope mass measurements have been conducted to explore shell evolution between the $N = 28$ and $N = 50$ islands of inversion. It will provide crucial data for testing nuclear models in this region where nuclei experience competition

between single-particle and collective behavior. The improved precision and new mass values obtained at Jyväskylä will help to constrain the nuclear models and improve our understanding of the $N = 40$ gap and its impact on nuclear structure. A more detailed section of Chapter 5 is dedicated to thoroughly describing the motivations behind this experiment.

In conclusion, the common thread linking all these measurements is the Penning trap, a crucial tool for achieving high precision in our experiments. The trap's ability to effectively confine charged particles allows for the meticulous control and manipulation of exotic ions, enabling accurate and precise mass measurements and high purification of contaminated beams. In the following chapter, a description of the trap's principles and operational mechanisms will be given.

Chapter 2

Penning trap

Contents

A Penning trap is designed to confine charged particles, typically ions, by combining a homogeneous magnetic field with a harmonic electrostatic potential. Such a trap allows for precise manipulation of the charged particles within the trap. Through these manipulations, Penning traps find applications in various fields, including radioactive ion beam (RIB) facilities, where they purify a contaminated ion beam and accurately measure the masses of the atomic nuclei.

This chapter will first detail the equation of motion for an ion in an ideal Penning trap. It will then discuss the effect of the electric and magnetic field imperfections. Then, it will present how one can act on these motions through radio-frequency excitations or interactions with a buffer gas. Finally, it will show the different purification and mass measurement techniques.

2.1 Motion of a single particle in an ideal Penning trap

In the following, we will mathematically describe the principle of an ideal Penning trap. Confinement in all three dimensions is achieved through the combination of:

- A uniform axial magnetic field:

$$\vec{B} = B_0\hat{z}$$

- A quadrupolar electric field:

$$\vec{E} = E_0\alpha(\rho\hat{\rho} - 2z\hat{z})$$

where B_0 is the magnetic field strength along the z-axis, and $E_0\alpha$ represents the strength of the electric field, with ρ and z being the radial and axial coordinates, respectively.

In Figure 2.1, two popular realizations of the underlying Penning trap concept for mass spectrometry of exotic nuclides are shown: (a) a hyperbolic one and (b) a cylindrical one. In both cases, it comprises a central electrode named "ring" and two side electrodes named "endcaps". A potential difference V_0 is applied between the ring and the endcap electrodes, providing axial trapping. The magnetic field, represented by $\vec{B}$, provides the radial confinement of the ions. The constants z_0 and ρ_0 are the minimum axial and radial distances to the electrodes.

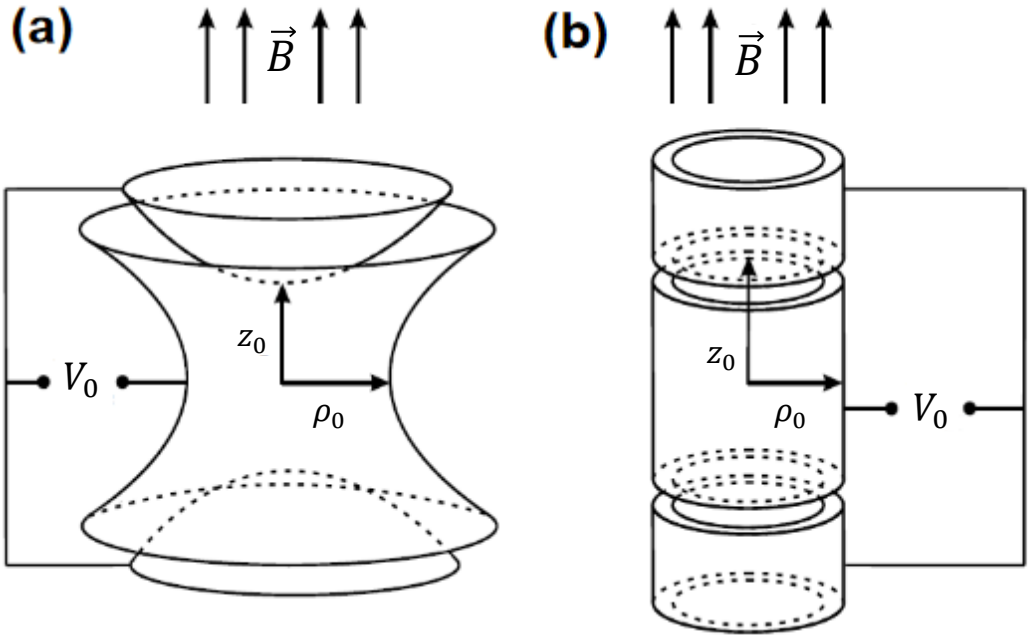

Figure 2.1: Two different representations of a Penning trap. (a) represents a hyperbolic Penning trap, and (b) represents a cylindrical Penning trap. In both cases, it is constituted by a central electrode named the ring electrode and two endcap electrodes. The magnetic field, represented by B, provides the radial confinement of the ions. A potential difference V_0 is applied between the ring electrode and the endcap electrodes, providing the axial trapping. Finally, z_0 and ρ_0 are the distances between the trap center and the endcaps and the ring electrode, respectively. Picture from [Naimi 10]

Even though the cylindrical shape is the one used in this thesis, the hyperbolic shape will be first discussed as it is a simpler case. In a hyperbolic ideal (entirely closed and

with electrodes extending to infinity) Penning trap, the ring obeys the geometry:

$$(\frac{\rho}{\rho_0})^2 - 2(\frac{z}{\rho_0})^2 = 1 \tag{2.1}$$

and the endcaps follow the form

$$\frac{1}{2}(\frac{\rho}{\rho_0})^2 - 2(\frac{z}{z_0})^2 = -1 \tag{2.2}$$

When a voltage $V_0 = V_e - V_r$ is applied between the ring and the endcaps, this creates an electrostatic potential of the form

$$V = \frac{V_0}{4d^2}(2z^2 - \rho^2) \tag{2.3}$$

in which d is the so-called "characteristic trap size" given by:

$$d^2 = \frac{1}{2}(z_0^2 + \rho_0^2/2) \tag{2.4}$$

The electric field will now be defined, as it plays a critical role in the dynamics of ion motion within the trap

$$\vec{E} = \frac{V_0}{2d^2}(\rho\vec{u_\rho} - 2z\vec{u_z}). \tag{2.5}$$

An ion of mass m with a charge q and a velocity $\vec{v}$ moving in the fields $\vec{E}$ and $\vec{B}$ experiences the Lorentz Force. Then, Newton's law gives:

$$m\frac{d\vec{v}}{dt} = q[\vec{E} + \vec{v} \wedge \vec{B}] \tag{2.6}$$

It is possible to project on each axis:

$$\begin{cases} \ddot{\rho} + \dfrac{qB_0}{m}\dot{\rho} - \dfrac{qV_0}{2md^2}\rho = 0 \\ \ddot{z} + \dfrac{qV_0}{md^2}z = 0 \end{cases} \tag{2.7}$$

Thus, the ion axial motion is a harmonic oscillator with a pulsation $\omega_z = \sqrt{\frac{qV_0}{md^2}}$. Additionally, we can identify in this equation $\omega_c = \frac{qB_0}{m}$ and rewrite it as:

$$\begin{cases} \ddot{\rho} - \omega_c\dot{\rho} - \dfrac{\omega_z^2}{2}\rho = 0 \\ \ddot{z} + \omega_z^2 z = 0 \end{cases} \tag{2.8}$$

A solution for the upper equation is $\rho(t) = exp(i\omega t)$ if ω is solution of the characteristic equation:

$$\omega^2 - \omega_c\omega - \frac{\omega_z^2}{2} = 0 \tag{2.9}$$

Thus, we obtain two solutions ω_+ and ω_-, the ion motion in a Penning trap is then defined

by three independent harmonics modes:

-the reduced cyclotron pulsation:

$$\omega_+ = \frac{\omega_c}{2} + \sqrt{\frac{\omega_c^2}{4} - \frac{\omega_z^2}{2}} \tag{2.10}$$

-the magnetron pulsation:

$$\omega_- = \frac{\omega_c}{2} - \sqrt{\frac{\omega_c^2}{4} - \frac{\omega_z^2}{2}} \tag{2.11}$$

-the axial pulsation:

$$\omega_z = \sqrt{\frac{qV_0}{md^2}} \tag{2.12}$$

To exist, these solutions need to respect the following conditions :

$$\begin{cases} \omega_c^2 - 2\omega_z^2 \geq 0 \\ qV_0 \geq 0 \end{cases} \tag{2.13}$$

This gives us:

$$\frac{|q|}{m} B_0^2 \geq \frac{2|V_0|}{d^2} \tag{2.14}$$

This defines the minimum magnetic field to apply in order to compensate for the quadripolar electric field and avoid allowing the ions to escape the trap in the radial direction.

One can replace ω_z and ω_c in the expressions of ω_+ and ω_-. For ω_- we get:

$$\omega_- = \frac{qB_0}{2m}(1 - \sqrt{1 - \frac{2mV_0}{qB_0^2 d^2}}) \tag{2.15}$$

Now, a Taylor series expansion is performed at first order:

$$\omega_- \approx \frac{qB_0}{2m}(1 - 1 + \frac{2mV_0}{2qB_0^2 d^2}) \tag{2.16}$$

leading to:

$$\omega_- \approx \frac{V_0}{2B_0 d^2} \tag{2.17}$$

This relation shows that the magnetron motion does not depend on the ion mass at first order. Also, if we add ω_+ and ω_- we get:

$$\omega_+ + \omega_- = \omega_c \tag{2.18}$$

and since we have:

$$\omega_c = |\frac{qB_0}{m}| \tag{2.19}$$

It means that we get:

$$\omega_+ = \frac{qB_0}{m} - \frac{V_0}{2B_0 d^2} \tag{2.20}$$

Looking at equation 2.20, we can understand that the reduced cyclotron motion is mass-dependent. For all these equations, one can find the frequency using $\nu = \frac{\omega}{2\pi}$; which we will consider in the following.

Figure 2.2 shows the compositions of the three harmonic modes that an ion follows in a Penning trap when the stability conditions are fulfilled.

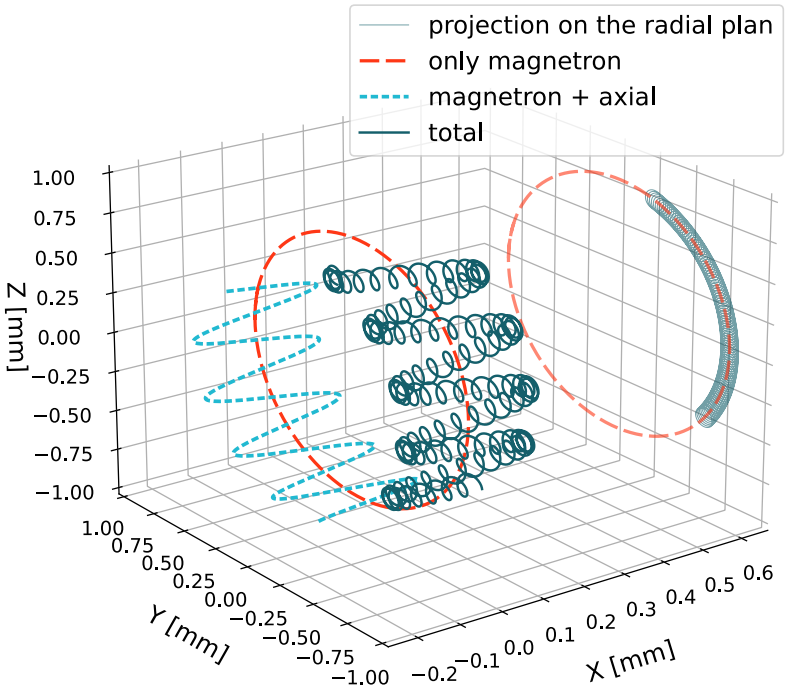

Figure 2.2: Schematic trajectory (three-dimensional and projection onto the x–z-plane) of the three independent eigenmotions of an ion in a Penning trap. The magnetron motion is shown in red. The light blue curves represent the superposition of the magnetron and axial motions. The real motion of the ions is plotted in dark blue. The projection highlights the two radial motions.

Once inside the Penning trap, an ion has three independent eigenmotions, each associated with an eigenfrequency. This allows their handling by applying radio-frequency fields to the corresponding frequencies. One can modify the amplitude of the oscillation with a dipolar excitation or couple the motions together and thus convert one to another with a quadripolar excitation at the sum of the corresponding motion frequencies. In this section, the ideal hyperbolic geometry inherently creates a quadrupolar potential, resulting in a harmonic electrical potential. However, it suffers from the drawback of

being infinite and entirely enclosed. A common remedy is to introduce holes or slits in the electrodes to inject ions. Both hyperbolic and cylindrical geometries are not ideal; however, the shape of hyperbolic trap electrodes makes manufacturing challenging, which is why cylindrical electrodes are often preferred. The following section will address the impact of the various imperfections of a real Penning trap.

2.2 Real Penning trap

Achieving reliable high-precision mass measurement experiments requires extreme accuracy in measuring the cyclotron frequency. Frequency shifts can be due to various factors. Imperfections of the electric and magnetic fields, machining imperfections, segmentation of electrodes, trap misalignments, ion-ion interactions, and collisions with residual gas perturb the ideal motions within the trap. The electric and magnetic field can be aligned with an electron gun (see in [Ascher 21]) to reduce the frequency shifts. Highly-optimized precision traps rely on minimizing all these factors, particularly electrostatic anharmonicities and magnetic inhomogeneities. In this part, these imperfections will be described more thoroughly.

Let us first focus on the electrical anharmonicities. Since the trap is an axisymmetric system, the electric potential V near the center can be expanded in Legendre polynomials:

$$V = \frac{V_0}{2}\sum_{\substack{k=0 \\ even}}^{\infty} C_k (\frac{r}{d})^k P_k(\frac{z}{r}) \tag{2.21}$$

Only the even k coefficients C_k, will be non-zero when assuming reflection symmetry across the $z = 0$ plane [Gabrielse 89].

The lowest order terms in Equation 2.21 are the most important for a particle trapped near the trap's center. C_0 is an overall constant and can be ignored. In a perfect quadrupole potential (approximated by a hyperbolic trap), $C_2 = 1$, and all other terms are zero. For cylindrical Penning traps, C_2 is typically about 0.5. Then, the dominant electric imperfection is characterized by the term C_4, the octupole component of the electrostatic potential.

$$\Delta V = V_0 \frac{C_4}{2d^2}(z^4 - 3z^2\rho^2 + \frac{3}{8}\rho^4) \tag{2.22}$$

One can see that this imperfection is driven by a term in ρ^4, implying that particles farther from the trap center will experience more significant imperfection. Thus, throughout this thesis, we will try to keep the ions as close to the trap center as possible. Additionally, correction electrodes between the ring and the endcap electrodes are usually added to minimize the octupolar and higher-order terms (not taken into account here). Chapter 4 will present the optimization of the potential application of these electrodes.

The following term C_6 (the dodecapole component) is suppressed with respect to the term in C_4 by a factor of $(\frac{r}{d})^2$, which is often of the order of 10^{-4} or smaller. Usually, terms above C_6 may be neglected for particles close to the trap center; their contribution is below the experimental resolution [Vogel 24].

Let us now focus on the magnetic field inhomogeneities and instabilities. Inhomogeneities in the trap region imply that ions traveling inside the trap will experience different magnetic field intensities. Since the cyclotron frequency is directly linked to the magnetic field, the frequency that will be measured depends on the position of the ions in the trap. This dependency would not be a problem if it were always the same. However, ions do not always have the same axial energy, so they will not experience the same trapping region, consequently shifting the frequency. Instabilities are problematic because any frequency shift between two or even within one measurement will compromise accuracy.

Four main contributions to these instabilities and inhomogeneities shall be briefly discussed. First, as the magnetic field is made by a coil that has a wire of finite size and the coiling is not perfectly asymmetric, this creates variation in the field regarding the ideal coil. Second, the materials used for the trap component or any magnetic materials around the magnet can cause perturbations in the field. Third, the current in the superconducting coils decreases with time. Fourth, temperatures and presssure fluctuate in the nitrogen and helium reservoirs of the superconducting magnet.

In most cases, the inhomogeneity due to the first or second contribution is compensated by additional superconducting coils. These other superconducting shim coils are optimized once the magnet is cooled down and loaded. These coils allow us to reach a homogeneity better than 1 ppm over $1\,\mathrm{cm}^3$. Details on the shimming for the PIPERADE magnet can be found in [Ascher 21].

Instabilities due to the third contribution can be mainly compensated for a limited period by a warm coil, in which one would inject the right increasing current to counter the drift of the superconducting magnet. Such a coil works for a limited time, as we can not inject infinite current. The current needs to be set back to zero from time to time. PIPERADE has such a coil; details can also be found in [Ascher 21]. One way to counteract the fluctuations due to temperature variation is to control the experimental hall temperature itself. Another way is to stabilize it locally like it is done at GSI [Droese 11]. However, this is not always easy, and the uncertainty emerging from these instabilities can become limiting. The minimization of the uncertainty coming from these contributions will also be discussed in chapter 4.

2.3 Ion manipulation

In this part, the tools used to manipulate ions inside a Penning trap will be described. First, the different radiofrequency excitations (RFE) will be presented and explained.

Then, the effect of using a buffer gas on the ions' motions inside a Penning trap will be detailed.

2.3.1 Radio-frequency excitations

To apply the excitations detailed further down, one needs a segmented electrode. In the case of radial motion excitations, the ring electrode is most commonly segmented. In most cases, 4-fold segmented (see figure 2.3) or 8-fold segmented ring electrodes (see figure 3.7) are used. Two types of excitation are commonly used to manipulate ions: the dipolar excitation and the quadrupolar excitation.

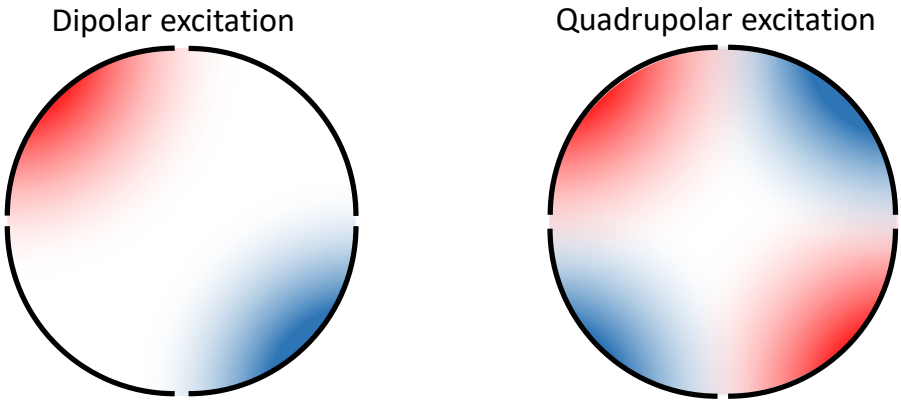

Figure 2.3: On the left, one can see a dipolar excitation applied using only two segments. The color represents the sign of the potential, while the saturation represents the amplitude. A quadrupolar excitation is represented on the right using the same convention.

- A dipolar excitation can be created by applying an RF field on two opposite segments in phase opposition (see left part of figure 2.3). Suppose the excitation is performed at the right eigenmotion frequency. In that case, one can amplify or diminish the oscillation amplitude of the corresponding eigenmotion, depending on whether the excitation is in phase or opposition phase with the motion, respectively. The duration of excitation defines how far the ions will be for a given amplitude of the RF signal.

- A quadrupolar excitation can be created by applying an RF signal with the same phase on two opposite segments and in phase opposition on another pair perpendicular to the first one (see right part of Figure 2.3). This type of field is applied only to sums of eigenfrequencies and allows to couple motions. For example, a quadrupolar RFE at $\nu_c = \nu_+ + \nu_-$ couples the modified cyclotron and magnetron motions. Thus, during the application of such excitation, a periodic conversion between the amplitudes of both motions occurs.

The dipolar excitation will not be explained in more detail. However, the conversion

of the motions using a quadrupolar RF field is less intuitive and thus requires more explanation. In a quadrupolar excitation, we apply an oscillating voltage to four segments. It means that the field applied to the ions is a beating quadrupolar field. And as a standing plane wave can be represented by the superposition of two counterpropagating traveling plane waves, we can describe the beating RF potential as two quadrupolar static fields rotating in opposite directions at $\frac{\omega_c}{2}$ (see figure 2.4). Looking at a frame of reference rotating at $\frac{\omega_c}{2}$ would then simplify the understanding of the situation. In such a frame of reference, the ions would only feel a quadrupolar static field, and the other field, rotating at $-\omega_c$, would not affect them. To fully understand the shape of the potential felt by the ions in this rotating frame, the force at stake in the inertial frame is needed.

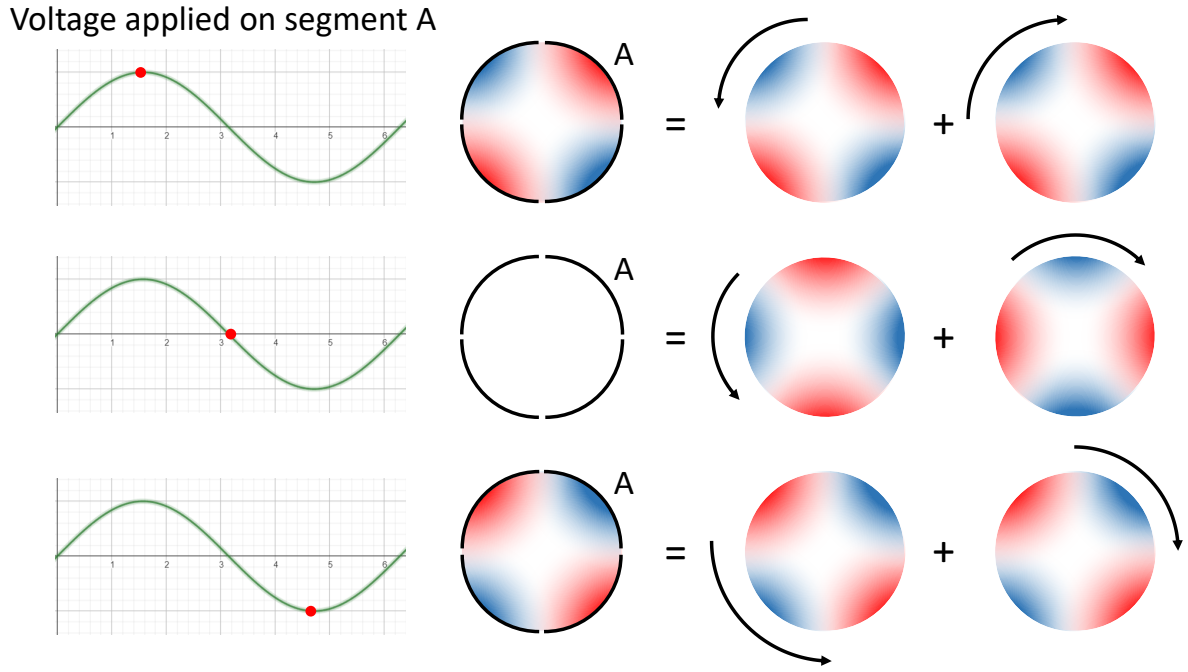

Figure 2.4: On the left, the signal sent to one of the four segments is pictured. Then, the map of the electrical field applied at the three different times highlighted on the sine wave. The color represents the sign of the potential, while the saturation represents the amplitude. The two right columns use the same convention to represent the two rotating quadrupolar fields, the sum of which is equivalent to the beating field pictured on the left.

The Newton's second law in the inertial frame is:

$$\sum \vec{F}_{ext} = m\frac{d\vec{v}}{dt} \tag{2.23}$$

with m the mass of the charged particle and $\vec{v}$ its velocity. The gravitational attraction is neglected. Thus, the sum of all the external forces can be reduced to only the Lorentz force, with its two components, magnetic and electric, defined as:

$$\vec{F}_L = \vec{F}_{Le} + \vec{F}_{Lm} = q\vec{E} + q\vec{v} \wedge \vec{B} \tag{2.24}$$

where q is the electric charge of the moving particle while experiencing the forces created by the $(\vec{E})$ electric and $(\vec{B})$ magnetic fields. The magnetic field is defined as $\vec{B} = B_0\vec{e_z}$ with $\vec{e_z}$ the unit vector parallel to its axis.

In the rotating frame, two pseudo-forces will appear: the Coriolis force and the centrifugal force. The Newton's second law will become:

$$\vec{F}_{Le} + \vec{F}_{Lm} + \vec{F}_C + \vec{F}_{cen} = m\frac{d\vec{v}}{dt} \tag{2.25}$$

Everything will work as if there were no magnetic field, as its impact on a charged particle is exactly compensated by the Coriolis force. Indeed, the Coriolis force can be defined as:

$$\vec{F}_C = -2m\vec{\omega} \wedge \vec{v} \tag{2.26}$$

with $\vec{\omega}$ the pseudo-vector representing the orbital angular velocity of the rotating frame in the inertial frame. The frame's rotation direction is the same as the ions', so it must depend on the charge (if the ions have a negative charge, they are spinning around $\vec{e_z}$. In contrast, positively charged ones rotate in the opposite direction due to the magnetic field).

A function δ can thus be defined as:

$$\delta = \begin{cases} -1 & if \quad q > 0 \\ +1 & if \quad q < 0 \end{cases} \tag{2.27}$$

and then $\vec{\omega} = \delta\frac{\omega_c}{2}\vec{e_z}$. In our case $q > 0$ and using 2.19 the following equation is obtained:

$$\begin{cases} \vec{F}_L = qB_0\vec{v} \wedge \vec{e_z} \\ \vec{F}_C = -|q|B_0\vec{v} \wedge \vec{e_z} \end{cases} \tag{2.28}$$

Now that the compensation of the magnetic field by the Coriolis force has been shown in this frame, only the centrifugal force and the electrical component of the Lorentz force remain. Here, the centrifugal force confines the ions radially, and the potential felt by the ions is shown on the left part of figure 2.5.

Now, if the quadrupolar excitation is applied at ω_c, a quadrupolar static field will be added to this paraboloid of revolution. This new field will have the shape of an elliptical paraboloid; see 2.5. The natural motions in this new potential are not circular anymore but more back and forth along the axes of the ellipse.

The magnetron and cyclotron motions in the rotating frame correspond to two circular motions with an angular velocity of $\omega' = \omega_+ - \omega_{c/2} = \omega_{c/2} - \omega_-$ spinning in opposite directions (in the frame direction for the cyclotron and the opposite direction for the magnetron).

Consider now the excitation is applied, these initial circular motions find themselves in a potential shaped as an elliptical paraboloid, and the natural tendency is for each of

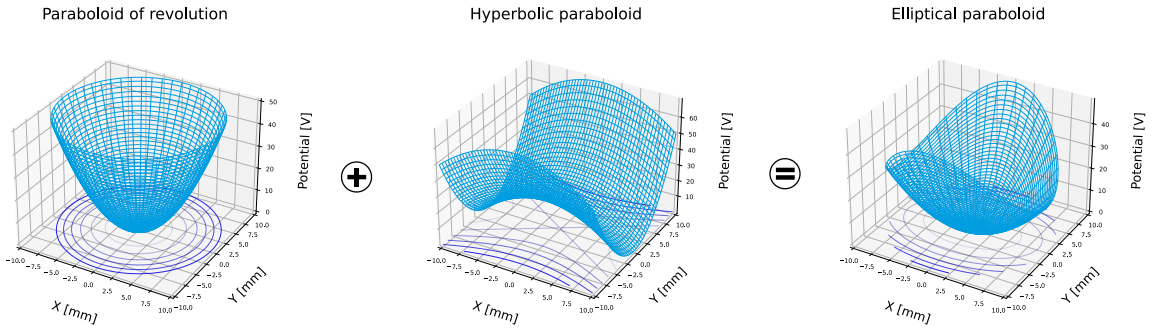

Figure 2.5: On the left, the potential seen by the ions without any excitation is plotted. In the center, the potential is applied by the quadrupolar excitation. On the right, the resulting field is felt by the ions. All of these potentials are plotted by placing ourselves in the rotating frame of reference.

them to evolve slowly towards an increasingly eccentric trajectory until it becomes linear (along the semi-major axis of the ellipse) before returning to an increasingly circular shape of the same amplitude as the initial motion but with the opposite direction of rotation, and so on, all this always at the frequency ω'.

As when you change the direction of rotation in the rotating frame of reference, the magnetron becomes a cyclotron, or vice versa, we have just shown that this excitation converts one movement into the other. In the frame of reference of the outside observer, this corresponds to the amplitude of one motion slowly decreasing while the amplitude of the other motion increases.

2.3.2 Buffer gas

Adding a buffer gas in a Penning trap is a double-edged sword. Later, it will be shown that it is a powerful tool for purifying contaminated ion bunches or even cooling bunches to prepare them for mass measurement. However, it will also be shown that it is a limiting factor in all measurement techniques.

If the trap is filled with a buffer gas, such as helium, collisions with the buffer gas will tend to equilibrate the energy of the ion with that of the gas. This will dampen the fast components of the ion motion and lead to a reduced axial amplitude and cyclotron radius. To understand the action of the gas on the magnetron motion, it is easier to look at the equations. The action of a buffer gas is very similar to a viscous drag and can be approximated as a damping force proportional to velocity. An analytic expression for the effect of buffer gas on ion motions can be obtained by solving the equations of motion, including the damping force $-\gamma\dot{r}$ with $\gamma = \frac{q}{2mk}$ and k the mobility of the ion in the buffer gas. For the radial motions with an initial amplitude of ρ_0^+ and ρ_0^-, we obtain:

$$\rho^{\pm}(t) = \rho_0^{\pm} e^{\mp \epsilon t} \tag{2.29}$$

with the coefficient:

$$\epsilon\pm = \gamma\frac{\omega_{\pm}}{\omega_{+} - \omega_{-}} \tag{2.30}$$

The energy loss of the two eigenmotions leads to a fast decrease in the high-frequency cyclotron motion and a slow widening of the magnetron motion [Savard 91]. Knowing these properties, one has all the tools needed to understand the purification and measurement techniques, which will be detailed below.

2.4 Techniques

In the previous sections, the reaction of the ions to RFE and collisions with gas was explained. In this section, the different methods using these properties will be detailed. Firstly, the two main purification techniques developed during this PhD, both using RFE, will be presented. Secondly, specifics about two mass measurement techniques will be given.

2.4.1 Purification

A commonly used technique for purification is the buffer gas cooling technique [Savard 91], which can reach a resolving power of 10^5. However, JYFLTRAP showed that it was possible to use another technique for purification called phase-dependent cleaning [Nesterenko 18]. With this method, a resolving power of 10^7 can be reached. Other techniques exist, but in this work, only these two were performed for the first time and characterized for the double Penning trap PIPERADE. In this section, a theoretical presentation of these techniques will be provided.

Buffer Gas Cooling

The buffer gas cooling (BGC) technique initially decenters all ions, then recenters only the ions of interest (IoI). A diaphragm is then used to select the IoI during their extraction from the trap [Savard 91]. This process involves applying a dipolar excitation followed by a quadrupolar excitation within a trap filled with buffer gas.

- After the capture of the ions in the trap (step 1 in Figure 2.7), their axial and cyclotron motions are cooled by collisions with the gas (see subsection 2.3.2 and step 2 in Figure 2.6 and 2.7).
- Then, the magnetron motion amplitude is increased using a dipolar excitation in phase with the magnetron motion of all the ions. Indeed, this excitation will affect all the ions because the corresponding frequency does not depend on the mass of the ions (see formula 2.17) (step 3 in Figure 2.6 and 2.7).

- Then, the quadrupolar excitation is applied at $\nu_{rf} = \nu_c = \nu_+ + \nu_-$. And since the cyclotron frequency is mass-dependent (see formula 2.19), only the IoI will be affected by the excitation, which will convert the magnetron motion into cyclotron motion. The gas continuously damps the amplitude of the reduced cyclotron motion while the quadrupolar excitation is applied. Therefore, by converting the magnetron motion, the ions of interest will be recentered while the contaminants will keep spinning at a larger radius (step 4 in Figure 2.6 and 2.7).

- The endcaps potentials will be lowered, releasing the ions from the trap toward the MCP. Therefore, the contaminants rotating in a large orbit will hit the diaphragm, whereas the IoI will go through it (step 5 in Figure 2.7).

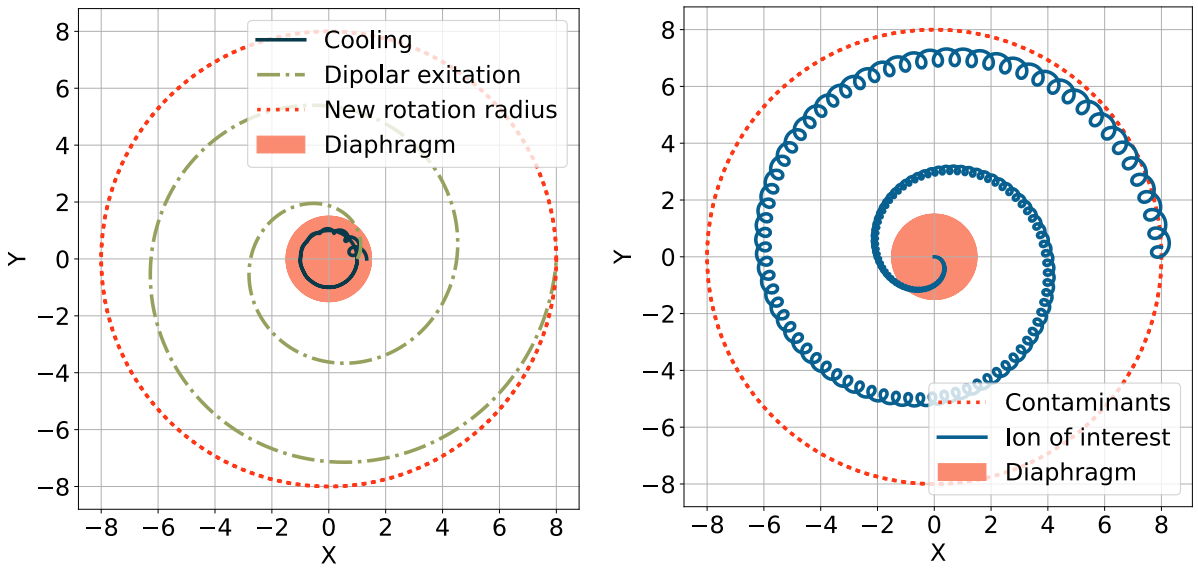

Figure 2.6: Scheme of the buffer gas cooling technique in the radial plane. The salmon pink circle represents the diaphragm. In the left part, steps two and three of the BGC are represented: Step 2: The small central dark blue curve represents the ions being cooled. Step 3: The green line represents the ions' trajectory under the influence of a dipolar excitation at the magnetron frequency. The dotted red line represents the ions' trajectory after the third step. On the right part, step four is represented. Step 4: The conversion is applied to the IoI, leaving the contaminants with a stable rotation radius on the red curve. The blue curve represents the IoI trajectory during the quadrupolar excitation at the cyclotron frequency of the IoI, during which the magnetron motion is converted to cyclotron motion, which is simultaneously cooled by the gas.

Using BGC, a resolving power $\frac{\nu_c}{\Delta\nu_c}$ of 10^5 is commonly reached, separating most of the isobars. However, this technique has some limitations. The main difficulties arise when a small number of IoI needs to be separated from a large number of contaminants. In such cases, the potential created by the charge of the contaminants adds frequency shifts and masks the excitation, decreasing recentering efficiency and resolution. Even though this technique is fast, it still needs tens or hundreds of milliseconds to purify, which can

become problematic for the most exotic cases. Additionally, it has the disadvantage of using gas, which can leak into the measurement trap, where any residual gas must be avoided. Optimizing this technique requires finding a good compromise between all of these constraints. However, despite all these difficulties, this technique remains one of the most commonly used purification techniques for Penning traps.

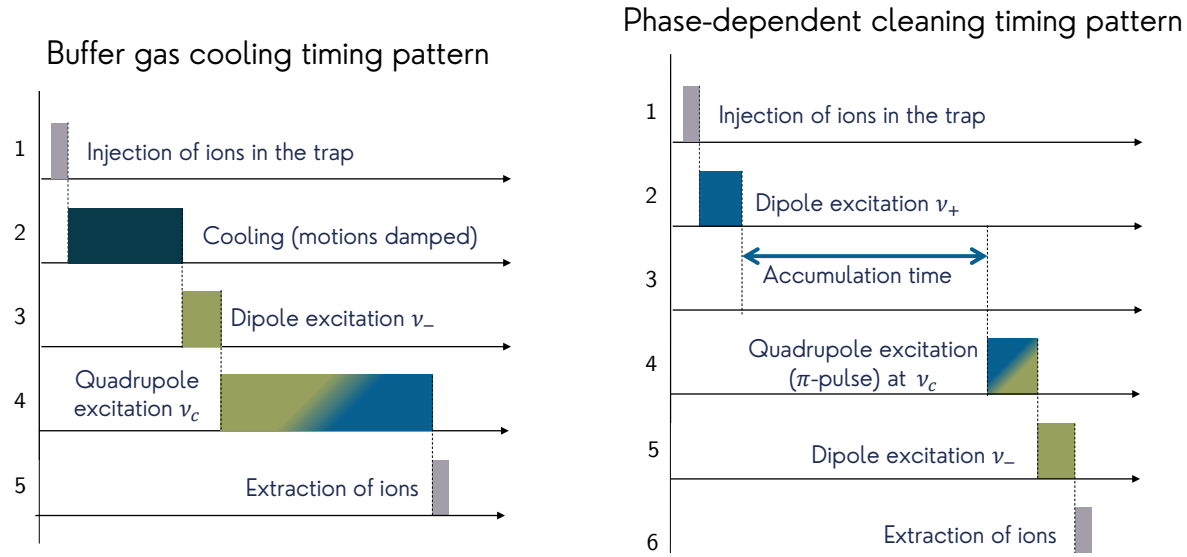

Figure 2.7: Timing patterns for the BGC on the left and the PDC on the right. Steps in gray represent steps where the ions are either injected or extracted from the trap. The only step in dark blue represents the cooling of the fast motions. In green are the steps where the magnetron motion is excited. In blue are the steps where the reduced cyclotron motion is excited. The steps from green to blue represent a conversion of magnetron motion into reduced cyclotron motion and vice versa.

Phase-dependent cleaning

The phase-dependent cleaning (PDC) technique is a truly innovative method [Nesterenko 18]. A resolving power of 10^7 can be reached, provided that the samples are not heavily contaminated from the beginning. Such a technique allows for the purification of isomeric states or neighboring contaminants.

The idea is to decenter all the ions, wait for a certain time while they spin at a mass-dependent frequency so that they separate in phase, and then recenter only the IoI, selecting them for example by using a diaphragm that would be placed after the traps. Although the general idea may seem quite similar to the BGC, as it is performed without any buffer gas, the excitations and the order in which they are applied are completely different.

At every step of this method, a position-sensitive detector can be used to monitor the ions' position in the trap after one or several excitations by extracting the ions from the trap. For simplicity, the ion bunch is considered at the trap center, with almost no initial

magnetron motion (it will be shown that even if there is magnetron motion, it can be damped).

- To decenter the ions, a dipolar excitation will be applied at the reduced cyclotron frequency. This frequency is mass-dependent, but this excitation is performed for a very short time to be broadband enough to decenter all the ions (step 2 in Figure 2.7). By doing so, the ions will be given maximum energy so that they separate as quickly as possible.

- Then, a waiting time called the accumulation time allows the ions, having different mass and thus different speeds, to separate in phase (step 3 in Figure 2.7).

- However, the ions cannot be spatially separated using the reduced cyclotron frequency because the reduced cyclotron period is of the same order as the ions' ToF dispersion. As a result, instead of forming a single spot, the ions will be uniformly distributed around the trap center at the rotation radius. Thus, one must apply a broadband quadrupolar excitation near the IoI cyclotron frequency to convert the reduced cyclotron motion into magnetron motion. After conversion, the ions move approximately a thousand times more slowly, allowing us to discriminate the different species. (see (a) in Figure 2.8 and step 4 in Figure 2.7)

- After this conversion, the ion species slowly spin around the trap center at different phases. By applying a dipolar excitation at the correct phase, i.e., in the opposite phase with the magnetron motion, one can recenter the IoI. The other species, being out of phase, will not be recentered as much as the IoI, allowing us to purify the sample by sending the ions toward the diaphragm (see (b) in Figure 2.8 and step 4 in Figure 2.7).

For such a technique, the resolving power is defined by the ability to resolve the phase difference of reduced cyclotron motions between two ion species after accumulating for a time T_{acc}

$$R = \frac{\nu_+}{\Delta\nu_+} \approx \frac{\pi T_{acc} r_+}{\Delta\varphi_+}\nu_+ \tag{2.31}$$

with $\Delta\varphi_+$ the radius of the spot and r_+ the rotation radius. Therefore, the optimization of the resolving lies in keeping the smallest spots as possible, further away from the trap center, for a longer time. Figure 2.8 demonstrates the separation and purification of a ground state and its isomeric state. The obtained resolution for the case presented in this figure is 1.7×10^6.

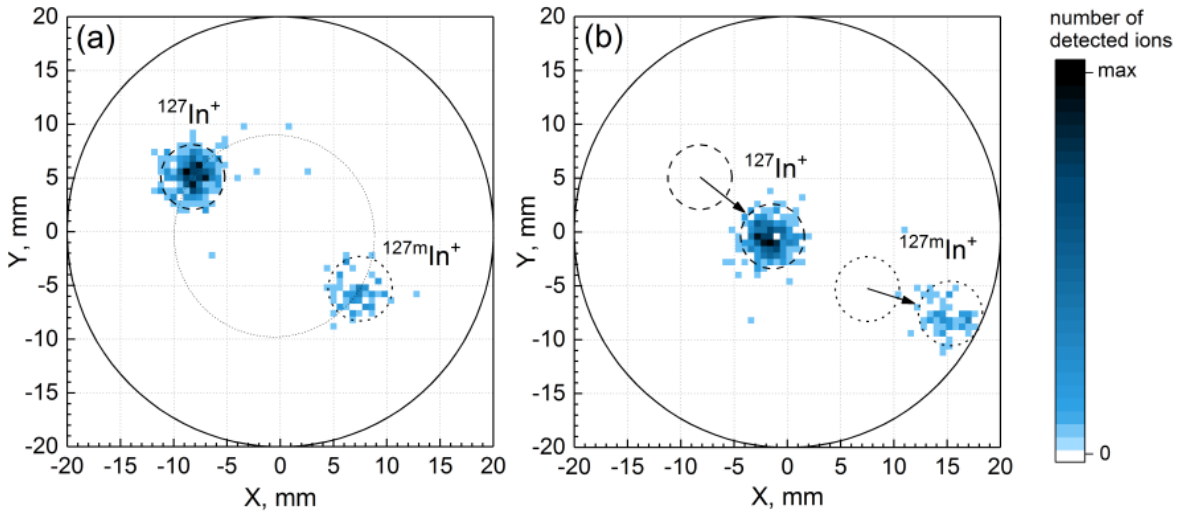

Figure 2.8: Image of ion distribution for the ground and first isomeric states of $^{127}In^+$ on a position-sensitive ion detector. (a): spots for g.s. and m. states are separated by 180 deg after an accumulation time of 160 ms (b): represent the step just after (a) with additional dipolar excitation pulse at the magnetron frequency. $^{127}In^+$ ions moves to the center while $^{127m}In^+$ ions moves further out. Since the two states do not exactly have 1π phase difference, the spots do not move exactly to the same direction. Plot from [Nesterenko 18]

.

2.4.2 Mass measurement techniques

The ion mass m can be determined via the direct measurement of the cyclotron frequency ν_c following the relation.

$$\nu_c = \frac{|q|B}{2\pi m} \tag{2.32}$$

where B is the strength of the magnetic field and q is the ion's electric charge. Mass measurements rely on a good knowledge of the magnetic field strength. Its calibration is done via the measurement of a so-called reference ion with a well-determined mass.

However, the magnetic field absolute value drifts over time (see section 2.2). Therefore, the magnetic field measurement via a reference mass is performed before and after the measurement of the IoI so that the field strength can be interpolated at the measurement time. The cyclotron frequency is the only parameter to measure for the reference and the IoI. Consequently, the two techniques described in this section involve cyclotron frequency measurements. The two techniques presented thereafter allow for the measurement of ν_c based on the relation:

$$\nu_c = \nu_- + \nu_+ \tag{2.33}$$

Time of flight ion cyclotron resonance (ToF-ICR)

The first technique presented hereafter is the so-called time of flight ion cyclotron resonance (ToF-ICR). The excitations and timing sequence for this technique are similar to those of the BGC, with the major difference being that there is no gas in the trap. Let us review the different steps of the BGC and explain them in the context of the ToF-ICR technique:

- The first step is a waiting time so that the ions get cooled by the gas. Here, there is no gas, so waiting is not necessary. However, to minimize initial movements, injection into the trap without gas is much more delicate, and this will be detailed in the section 4.3.
- Then, the magnetron motion amplitude is increased using a dipolar excitation at the magnetron frequency. This step is the same for BGC and ToF-ICR
- Finally, a quadrupolar excitation is applied to convert the magnetron motion into cyclotron motion. In the case of ToF-ICR, the purpose of this conversion is not to center the ions, as there is no gas in the trap, but to increase the ion's kinetic energy in the radial plane.

Ultimately, it simply involves a sequence where a dipolar excitation occurs at the magnetron frequency, followed by the scanning of a quadrupolar excitation around the cyclotron frequency.

Such a scan can be understood by considering the two principal configurations for the ions. In the first case, the RF excitation is on-resonance with the cyclotron frequency. Then, the magnetron motion is fully converted into a reduced cyclotron motion, making the ions rotate at a very high velocity. In the second case, the excitation applied is off-frequency; thus, the conversion does not occur, leaving them with a slower rotation velocity. This difference in speed means that ions rotating at the reduced cyclotron frequency will have more radial energy than the others. By extracting the ions from the trap through the magnetic field gradient towards a detector, this difference in energy will be transformed into a difference in time of flight. Indeed, the magnetic moment of an ion performing a cyclotron motion with kinetic energy ($E \approx Er(\omega_{rf})$) in a magnetic field $\vec{B(z)} = B(z)\vec{e_z}$ is:

$$\vec{\mu} = \frac{E_r(\omega_{rf})}{B(z)}\vec{e_z} \tag{2.34}$$

Its interaction with the gradient of the magnetic field causes the ion to experience an axial force:

$$\vec{F}(\omega_{rf}, z) = -\mu(\vec{\omega_{rf}}).\nabla\vec{B}(z) \tag{2.35}$$

which leads to an increase of the velocity and, therefore, a reduction of the time of flight from the trap to the detector. The total time of flight from the trap center to the location of the detector can be calculated using the following equation:

$$T(\omega_{rf}) = \int_{z_0}^{z_{max}} \sqrt{\frac{m}{2(E_0 - qV(z) - \mu(\omega_{rf})B(z))}} dz \tag{2.36}$$

where E_0 is the initial total energy of the ion, $V(z)$ and $B(z)$ are the electric potential and magnetic field along the ion path from the trap (z_0) to the detector (z_{max}). At $\omega_{rf} = \omega_c$, the magnetic moment $\mu(\omega_{rf})$ reaches its maximum, which leads to a minimum time of flight of the ions.

In Figure 2.9, the typical shape that can be fitted to obtain ν_c is shown. This will be detailed in section 4.3. This technique allows reaching precisions on the order of $\frac{\delta m}{m} \approx 10^{-7}$ to 10^{-9}. The resolution defined by the full width at half maximum (FWHM) is inversely proportional to the duration of the excitation. One can easily understand this dependency by considering the quadrupolar excitation as a sine function applied on a square pulse. The Fourier transform in frequency space is then a cardinal sine function, with the distance between the minima inversely proportional to the duration of the pulse (more details on this dependency will be given in Chapter 4)

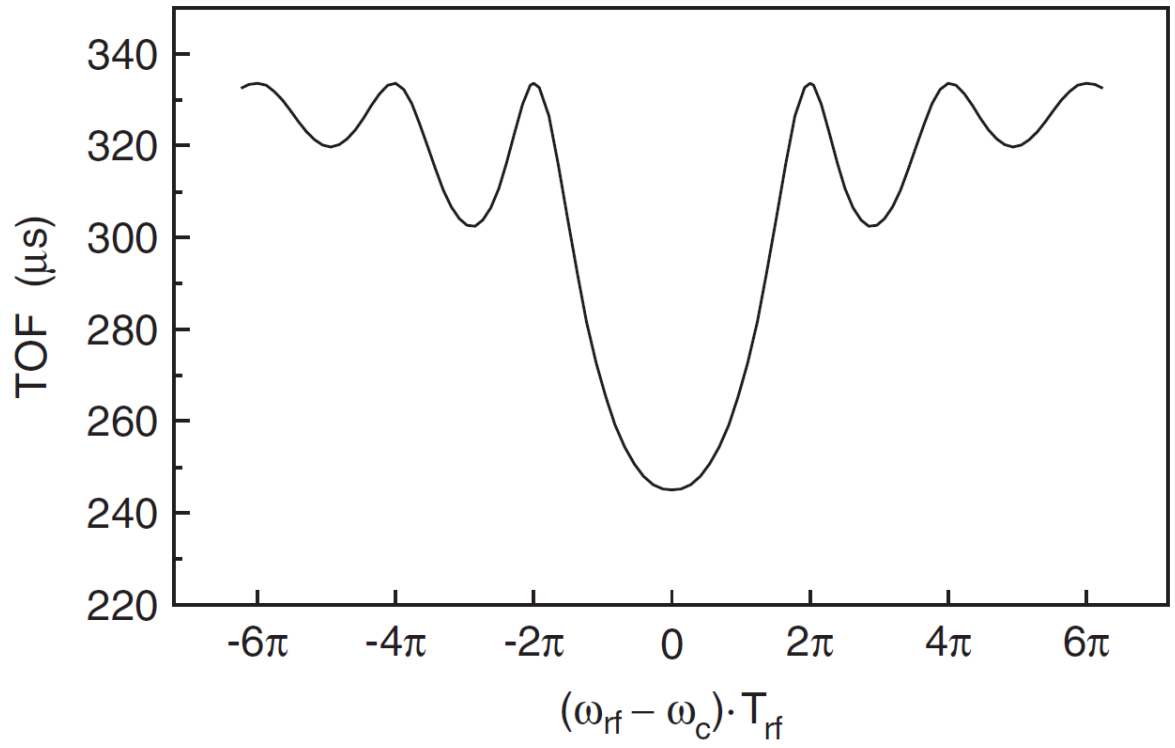

Figure 2.9: Theoretical shape of a time of flight ion-cyclotron-resonance. At $\omega_{rf} = \omega_c$, conversion takes place, increasing the IoI kinetic energy. Then, by passing through the magnetic field, this energy is transferred to the axial direction, making the ions arrive sooner on the detector. Plot from [Blaum 06]

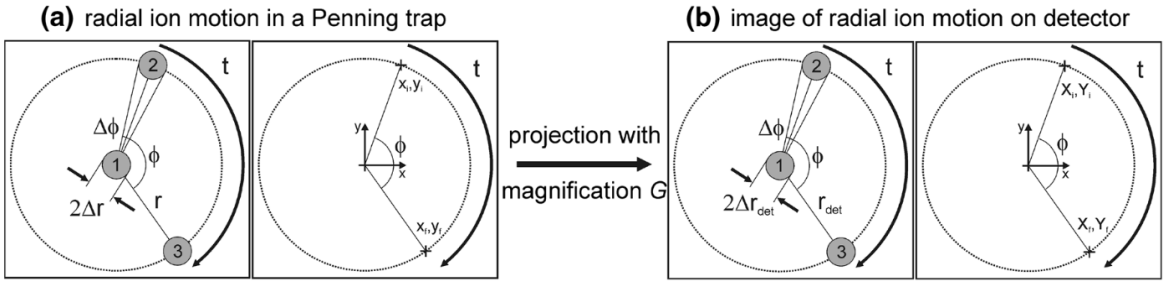

Figure 2.10: Principle of measuring the radial ion motions in a Penning trap. The radial ion motion within the trap (a) is projected onto the position-sensitive detector (b) with a specific magnification factor, denoted as G. Positions 1,2, and 3 in (a) and (b) correspond to the center of the motion, reference, and final phases, respectively. Plot from [Eliseev 13]

Phase-imaging ion-cyclotron-resonance

The phase-imaging ion-cyclotron-resonance (PI-ICR) technique is one of the most powerful techniques for mass measurement using Penning traps. It was developed at SHIPTRAP [Eliseev 13] almost ten years ago and has since been implemented in multiple Penning trap setups. Unlike previous methods, which were explained before, this one requires multiple timing patterns. The primary concept involves measuring frequencies by observing the ions' position projection on a position-sensitive detector. To measure the frequency of radial motion using position data, one must extract the ions at two different times and measure the phase difference between the two positions. For example, for the magnetron frequency, this would be defined as:

$$\nu_- = \frac{\phi_- + 2\pi n_-}{2\pi t_-} \tag{2.37}$$

with ϕ_- representing the angle difference between the reference and the final position, n_- denoting the number of full turns completed within t_-, where t_- is the duration during which the ions were spinning at the magnetron frequency. Three points are necessary to measure an angle; in that case, they are the trap's center position on the detector, the reference position, and the final position (see Figure 2.10).

It is important to remember that to determine the mass of an ion in a Penning trap, the cyclotron frequency is typically used (2.32). However, this motion is not one of the three eigenmotions in a Penning trap. Nonetheless, two motions rotating in opposite directions are linked to ν_c as $\nu_c = \nu_+ + \nu_-$. That is why the PI-ICR technique measures the two frequencies ν_+ and ν_-. In principle, six positions would be needed to measure two frequencies, three for each phase.

$$\nu_c = \nu_+ + \nu_- = \frac{\phi_+ + 2\pi n_+}{2\pi t_+} + \frac{\phi_- + 2\pi n_-}{2\pi t_-} \tag{2.38}$$

Nevertheless, that number of positions can be reduced to three if the accumulation time is the same for the two measurements and defined as :

$$\nu_c = \frac{(\phi_+ + \phi_-) + 2\pi(n_+ + n_-)}{2\pi t_{acc}} \tag{2.39}$$

There is no reason why the trap center would differ from one measurement to another, so it may be measured only once. Secondly, there is a method to use the same reference for the two frequencies. If the reference position is defined as R, the final as $F_\pm$, and the center as C, ϕ_- becomes $\widehat{RCF}_-$ and ϕ_+ becomes $\widehat{RCF}_+$. Then by defining n_c as equal to $n_+ + n_-$, one would have:

$$\nu_c = \frac{(\widehat{RCF}_+ + \widehat{RCF}_-) + 2\pi n_c}{2\pi t_{acc}} \tag{2.40}$$

By defining ϕ_c as $\widehat{F_+CF_-}$, one can rewrite this equation as:

$$\nu_c = \frac{\phi_c + 2\pi n_c}{2\pi t_{acc}} \tag{2.41}$$

This formula implies that only the angle between the two final spots of the magnetron and the reduced cyclotron frequency needs to be measured to perform the measurement.

Let us now examine the timing patterns P_C (pattern for the center spot), P_{mag} (pattern for the magnetron spot), and P_{cyc} (pattern for the cyclotron spot) required to measure these three positions. Concerning P_C, one might initially consider extracting the ions immediately after trapping to measure the center position. However, in most cases, the ion bunch does not arrive precisely at the trap center. Typically, this means that the ions will have initial magnetron motion. Therefore, the common practice is to apply a dipolar excitation at the magnetron frequency in phase opposition with the ions' motion. Extracting the ions after proper damping of the magnetron motion provides the trap center position on the detector.

With the ion bunch now centered in the trap, we can move on to explain the two remaining patterns, P_{mag} and P_{cyc}. These two patterns are visible in Figure 2.11 and will be detailed below:

- A dipolar excitation is applied at the reduced cyclotron frequency. Like phase-dependent cleaning, this frequency is mass-dependent, but the excitation is applied for a very short time, ensuring it is broadband enough to decenter all the ions. (see step 2 in Figure 2.11)

- The objective is to make the ions spin during the accumulation time: in one case at the magnetron frequency and in the other case at the reduced cyclotron frequency. (see steps 2 and 3 in Figure 2.11)

  - P_{mag}: a broadband quadrupolar excitation is performed to convert the reduced cyclotron motion of the ions into magnetron motion. After the accumulation time, the ions are extracted from the traps. (see the right side of Figure 2.11)

– P_{cyc}: no excitation is applied as the ions are already spinning at ν_+. However, as we already explained, one needs to convert to magnetron motion to obtain the ions' position projection after accumulation for phase-dependent cleaning. The only difference between these two patterns lies in whether the conversion is done before or after the accumulation time (see the left side of Figure 2.11)

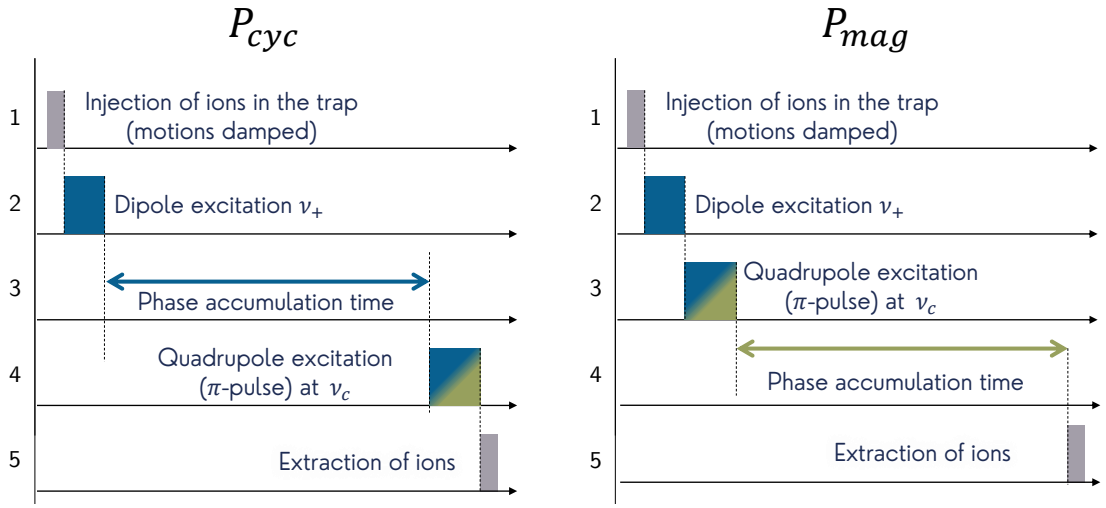

Figure 2.11: Two different timing patterns are used to measure the reduced cyclotron spot position (left) and the magnetron spot position (right). The blue indicates that ions are spinning at ν_+, and the olive green indicates that they are spinning at ν_-

This mass measurement technique allows for precision levels on the order of 10^{-8} to 10^{-10}, depending on the accumulation time used during the measurement process. It stands as one of the most powerful techniques for measuring masses today. In this thesis, its implementation on PIPERADE will be presented, as well as its utilization for actual mass measurements conducted at IGISOL on JYFLTRAP.

Chapter 3

The PIPERADE setup

Contents

This PhD work was conducted at the "Laboratoire de Physique des Deux Infinis de Bordeaux" (LP2iB). In Bordeaux, an experimental hall is dedicated to constructing and characterizing various preparation and purification devices for the future DESIR facility. This chapter will provide a general picture of the DESIR hall with a description of the devices developed at LP2iB and their use. Then, the beamline at LP2iB will be described, from the stable ion source upstream to PIPERADE downstream. Detailed explanations of the various beam transport tools and the GPIB will be included. Additionally, the chapter will present the different ion beam diagnostics used during this PhD work, focusing on installing the new micro-channel plate with three-layer delay lines at the end of the beamline. Finally, the control and command system and the software developed during this project will be discussed.

3.1 DESIR

As mentioned in Chapter 1, the DESIR facility at GANIL will receive neutron-deficient ion beams produced by fusion-evaporation at S3 (Super Separator Spectrometer) and exotic light nuclei produced by fragmentation at SPIRAL1. DESIR is an experimental hall designed for the study of nuclear structure, nuclear astrophysics, and weak interaction using β-decay spectroscopy, laser spectroscopy, and trap-based experiments at low energy (30 to 60 keV). These experiments require highly pure nuclei samples, contrasting with the non-selectivity of most production methods. In some cases, isomerically-pure ion beams may even be needed.

To provide large and very pure samples of exotic nuclei for various experiments, LP2iB is currently developing three new devices: a High-Resolution mass Separator (HRS) [Michaud 22], a Radiofrequency Quadrupole Cooler Buncher (GPIB – General Purpose Ion Buncher) [Gerbaux 23], and the double Penning-trap mass spectrometer, PIPERADE [Ascher 21]. These devices will be positioned at the entrance of the DESIR facility to ensure the delivery of cooled and purified ion beams to any experiments in the hall. Figure 3.1 illustrates the positions of the three devices at the entrance of DESIR.

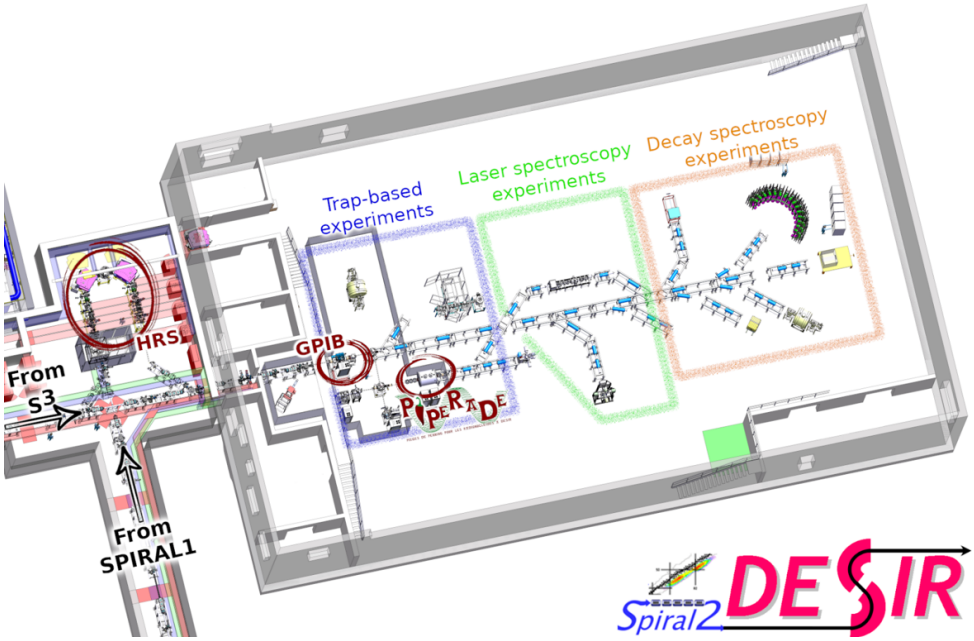

Figure 3.1: Scheme of the DESIR hall. Beams from S3 and SPIRAL1 arrive from the left and bottom, respectively. They are directed through the High-Resolution mass Separator (HRS), which feeds the General Purpose Ion Buncher (GPIB). The GPIB will either send a cooled and potentially bunched beam directly to experiments in the hall or route it to PIPERADE, which will measure masses, or purify the samples before sending them to other experiments.

The High-Resolution mass Separator (HRS) comprises two dipole magnets and a 48-pole electrostatic multipole for high-order aberration corrections. High-resolution magnetic mass separators have the advantage of being fast (with a flight time through the

instrument of a few microseconds) while providing sufficient mass resolving power to separate most isobars. After being fully commissioned in Bordeaux, it stands as one of the best HRS systems in the world ($\frac{M}{\Delta M} \approx 20\,000$). Nevertheless, the HRS is insufficient when masses are too close (some isobars or isomers) or when the counting ratio of contaminants versus ions of interest is too high. The HRS will be relocated to GANIL in the coming years and will deliver almost isobarically purified beams to the General Purpose Ion Buncher (GPIB) and PIPERADE.

The GPIB is a gas-filled radiofrequency quadrupole (RFQ) designed to cool the beam, reducing its emittance from $20\,\pi$ mm mrad at 30 keV, typical from accelerators, down to less than $10\,\pi$ mm mrad at 3 keV. It can also bunch the beams downstream in the hall while maintaining a high transmission. The mechanical design is an upgrade of the existing ISCOOL RFQ [Podadera Aliseda 04], [Podadera-Aliseda 06], [Frånberg 08] located on the HRS beamline at ISOLDE, CERN. However, the new radiofrequency system, based on a balun transformer, enables much stronger radial confinement of the ions inside the cooler, allowing it to handle the high production rates expected at DESIR: around 10^8 ions per second for most nuclides, but up to 10^{10} ions per second in some specific cases.

Finally, the PIPERADE double Penning trap is designed for two purposes: purifying contaminated beams for downstream experiments in the DESIR hall and performing high-precision mass measurements of exotic nuclei. The system uses two Penning traps to achieve these objectives. The first trap, one of the largest in the mass measurement community, is dedicated to the isobaric purification of a large number of ions (see 2.4.1). This initial purification step ensures that the beam is almost free of contaminants, which is crucial for the accuracy of downstream experiments. The second trap can be used in three distinct ways. First, it can provide an additional purification step, separating ions down to low-energy isomeric states, thus ensuring an even purer sample. Second, it can accumulate ions over several cleaning sequences in the first trap to deliver bigger bunches to downstream experiments. Alternatively, this trap can be employed to perform high-precision mass measurements. This last function will be detailed in this work.

3.2 Commissioning beam line at LP2iB

These three devices have been developed and commissioned in Bordeaux while the DESIR hall is under construction. They are installed in an experimental hall, as shown in Figure 3.2. The High-Resolution Separator (HRS) forms a U-shape on the left side, while the GPIB and PIPERADE are positioned along the same straight beamline on the right.

During this PhD, the focus was on this straight beamline. Before detailing its different components, a general overview of the beamline and its various high-voltage platforms are shown in Figure 3.3. The four gray-background regions in this figure represent different

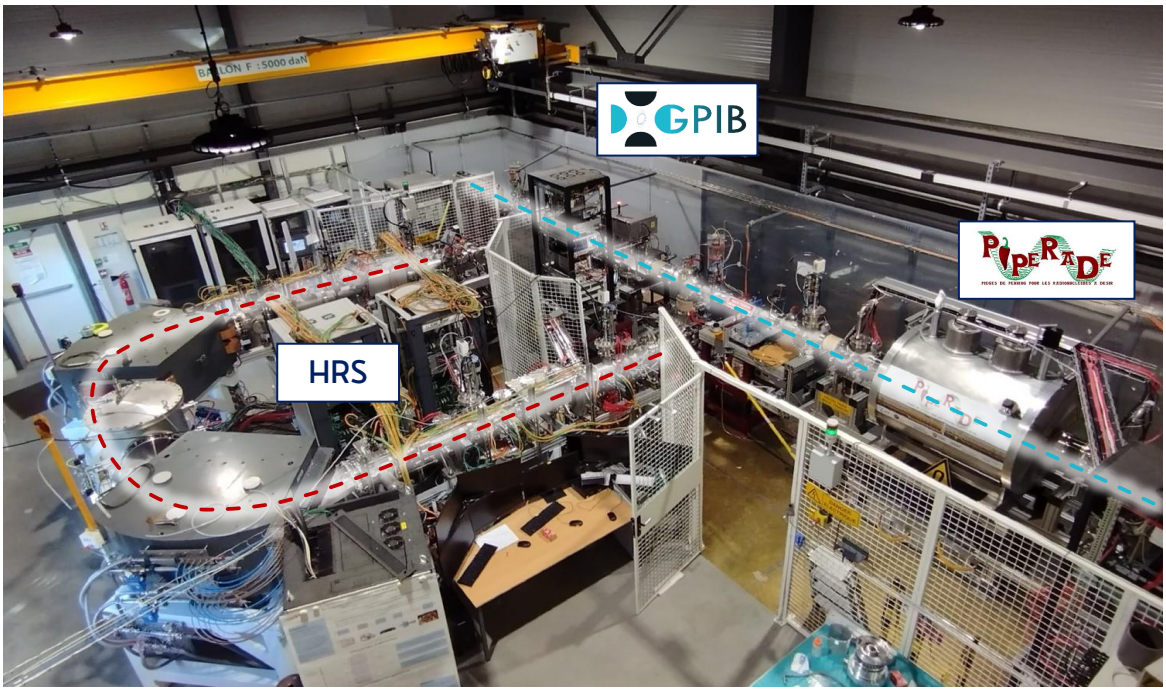

Figure 3.2: The layout of the experimental hall in Bordeaux is illustrated, highlighting key components and their positions. On the left, marked with a red dotted line, is the High-Resolution Separator (HRS) beamline. The commercial ion source is situated at the nearest end of the U-shape, while an emittancemeter is positioned at the far end. Close to this far end is the source position for the straight beamline, which is shown with a blue dotted line. Moving downstream along this straight beamline, the GPIB is followed by PIPERADE. The end of this beamline, which includes the position-sensitive MCP detector, extends further to the right and is not visible in the image.

HV platforms. The ion source, on the left side of the line, is biased at a high voltage of $V_{ref} = 30\,\text{kV}$. The three other platforms presented hereafter are all biased in reference to that one. By using a grounded electrode for extraction, the 1^+ ions are accelerated to 30 keV. They are then guided towards the GPIB, which stands on a high voltage platform set at $V_{ref}-100\,\text{V}$, slowing the ions down to 100 eV. The ions are subsequently cooled and trapped inside the GPIB before being extracted and re-accelerated as a bunch of ions toward PIPERADE at an energy of 2.9 keV by traversing the third HV-platform, which stands at $V_{ref}-3\,\text{kV}$. The last one is the Penning-trap platform which is set at $V_{ref}-75\,\text{V}$. Upon arrival at the entrance of the Penning trap's magnetic field, the ions need to be guided and slowed down again to a few tens of eV. This slowing down is done using dedicated DC electrodes. After purification or mass measurement in the traps, the ions are finally re-accelerated to 30 keV towards the final region, which is at ground. The final detector is in this region and is biased at a potential of $-2.4\,\text{kV}$ compared to the ground.

The technical description of all the upstream and downstream components will now be provided.

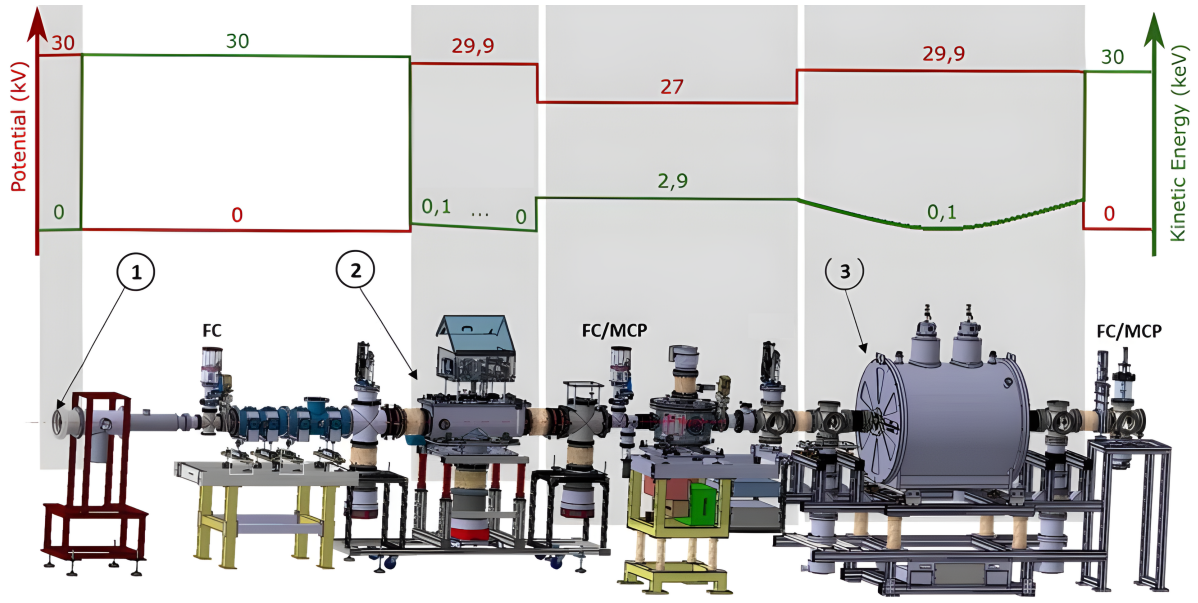

Figure 3.3: Experimental beam line at LP2iB. 1. Surface ionization source 2. General Purpose Ion buncher (GPIB) 3. 7-tesla magnet with its double Penning trap inside (PIPERADE). FC stands for Faraday cup, whereas MCP stands for microchannel plate. A deflector is visible between the GPIB and the traps, but it was removed to be commissioned on a dedicated setup and replaced by a drift tube. The different high-voltage platforms are highlighted with a gray background. The red curves show the different HV platform potentials; whereas the green curve shows the energy of the ions along the beamline (see text for more details).

Ion source

To test and commission the different devices, ions need to be produced. For this purpose, a custom-built ion source, initially developed for the MISTRAL installation at ISOLDE, is used. This FEBIAD-type ion source can operate in two modes: surface ionization or plasma. This work focuses on the surface-ionization mode, the only mode used during the commissioning.

In the surface-ionization mode, the source filament is heated to a point where it captures electrons from atoms present at the filament's surface. For this technique to be effective, the surface work function ($W(T)$) of the solid capturing the electron must be greater than the atom's ionization potential (E) from the surface deposit, which will then be converted into a positive ion. Figure 3.4 illustrates this principle. The produced ions are mainly alkalis due to their low ionization potential. In our case, primarily ^{39,41}K and ^{85,87}Rb are ionized.

Beam transport

Once the atoms are ionized, they are accelerated and conveyed using ion-beam transport optics. As the ions are transported at low kinetic energy (tens of keV), most of these optics are electrostatic ones with the advantage of being ion mass independent: beam

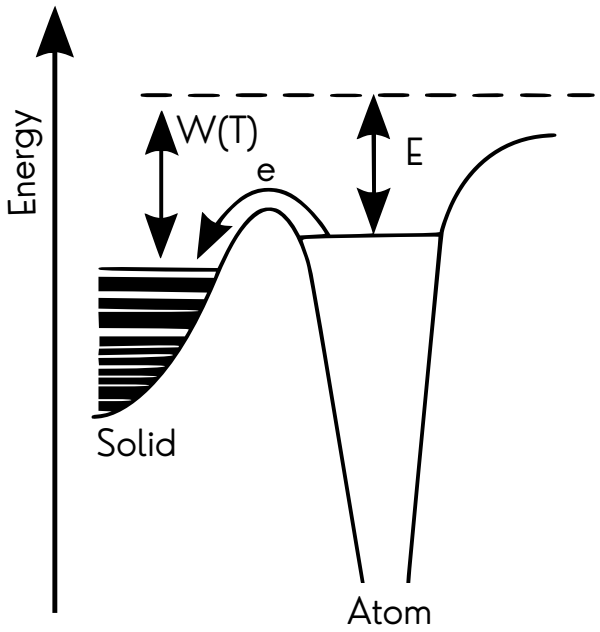

Figure 3.4: Principle of surface ionization - The atom yields an electron to the solid. On the left are represented the energy bands of the solid, the level of the last band being the Fermi level. On the right is the energy level of the atom's valence layer. Adapted from [Guerin 14]

tuning is the same for all ions with the same charge state. The devices used during this PhD are described below:

1. Pairs of steerers: Each electrostatic steerer comprises a pair of parallel metallic plates (electrodes) polarized to produce an electrostatic field orthogonal to the beam axis. One pair placed horizontally is used to steer the beam in the horizontal direction, and another pair is placed vertically to move the beam vertically. Two pairs are needed for each direction to compensate for the angle and the deviation of the ions. In the end, eight pairs of steerers are used in the entire beamline [Aouadi 17].

2. Electrostatic quadrupole triplet: An electrostatic quadrupole generates an electric field focusing on one plane, including the beam axis, while defocusing in the orthogonal plane (more details in [Hillert 21]). Another quadrupole rotated by 90 degrees around the beam axis is required to achieve focus in both transverse directions. However, this lens composed of two quadrupoles (quadrupole doublet) remains generally astigmatic compared to a symmetrical quadrupole triplet which is not. Thus, symmetrical triplets are used. Two triplets are positioned between the source and the GPIB to ensure optimal transport and injection into the RFQ. The first one, attached to the source, was designed to fit the MISTRAL ion source needs but does not allow an efficient injection into the GPIB. This is why a second one, being the prototype of the DESIR beam line triplets, was added before the GPIB.

3. Einzel lens: This device also controls the beam focusing. It comprises three cylin-

drical electrodes arranged in series, with the central electrode polarized and the two outer ones grounded (set to 0 V). One einzel lens is installed in the beamline between the GPIB and the Penning traps, where ions have energies around 3 keV.

General Purpose Ion Buncher

This device is a linear Paul trap filled with He buffer gas. Helium buffer gas is used to cool and trap the ions to produce small emittance bunched beams. However, if only buffer gas was present, the ions would deviate from their initial trajectory by inelastic collisions with the gas and eventually be lost. To confine ions along the beam axis, a Radiofrequency Quadrupole (RFQ) composed of two pairs of rods with opposite phase RF high voltages applied on each pair is used (see Figure 3.5). Additionally, DC segments are placed along the RFQ to guide the ions toward the exit of the GPIB. The voltage applied to the first extraction electrode, as well as to the last four segments, can be switched from a high voltage value (trapping to accumulate ions) to a lower voltage value to release ions out of this trap and then create ion bunches.

The transverse emittance (see definition in [Hillert 21]) of the continuous beam after being cooled in the GPIB was measured when the ions were extracted at 30 keV. At this energy, the measured emittance is $2.9(5)\,\pi$ mm mrad, corresponding to $9.2(16)\,\pi$ mm mrad at 3 keV, which complies with the needs of the setups downstream in the DESIR hall. In addition, the GPIB routinely delivers ion bunches to PIPERADE with a typical time-of-flight dispersion of about 1 μs (FWHM) and an energy dispersion lower than 10 eV. The characterization of the GPIB is still ongoing, and development is at the moment focused on the adaptation of a detection system that is able to measure low energy dispersion in the eV range.

Beam diagnostics

This part will describe the two main beam diagnostics used to measure continuous and/or bunched beam characteristics.

1. The Faraday cup (FC) is a device used to measure the beam intensity (continuous or bunched[1]) and also acts as a beam-stopper device. It is typically made of a refractory metal to withstand intense beams without melting. This is not a risk in our case; therefore, our FCs are in copper. When ions strike the metal surface, they capture electrons, causing a charge displacement (current). This electric current is measured to determine the beam intensity. However, ion impacts can also eject electrons from the FC surface (secondary electrons), significantly increasing the measured current. A guard ring biased negatively is placed in front of the cup to prevent this, repelling escaping electrons. DESIR-standard FCs were developed at GANIL. They cover an

[1] in this work only continuous

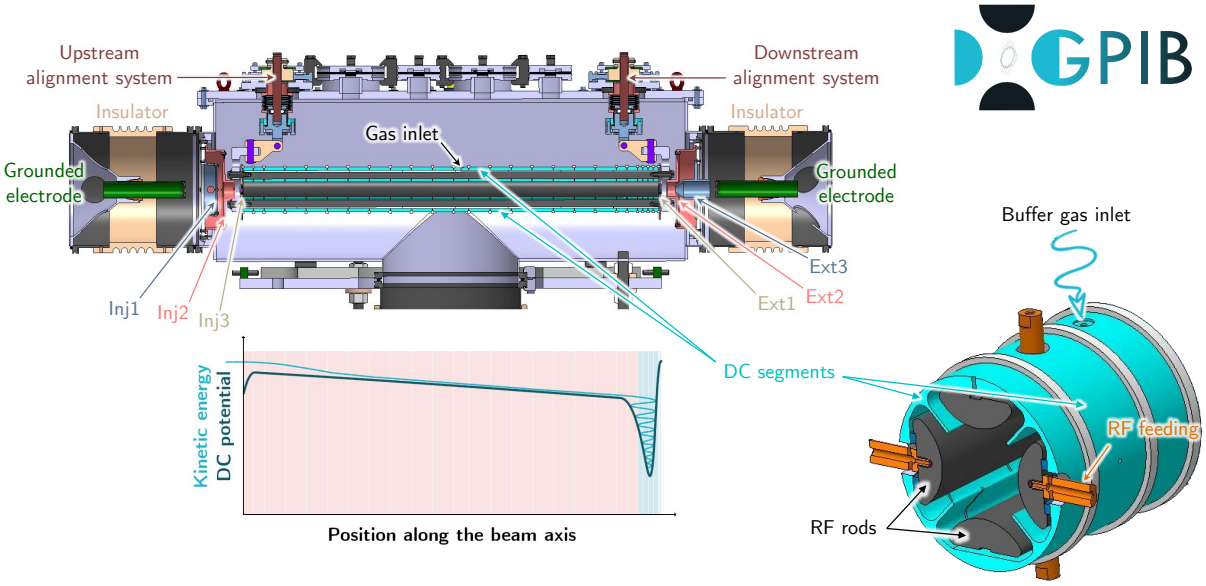

Figure 3.5: Top: Side view of the GPIB. The potential applied to the DC segments and the kinetic energy of the ions is shown at the bottom left. The four RF rods and the DC segments are shown on the right side of the picture.

extensive range of current intensities, from only 50 fA to 100 μA. To achieve such a high sensitivity, each FC is coupled to a low-bandwidth transimpedance linear amplifier called PicoLIN [Jamet 11]. Several Faraday cups are installed along the beamline, mounted on retractable arms (see Figure 3.2).

2. The Micro-Channel Plate (MCP) consists of a plate with numerous thin parallel channels, each approximately 10 µm in diameter, at an angle of typically 8(1)° to the surface. The front side is biased (up to several kilovolts) with respect to the rear side to create a strong electric field in the channels. The core material of the MCP is insulating (glass), but the inside of the channels is coated with a material having a high-secondary emission coefficient. Thus, when an ion strikes the channel surface, secondary electrons are released and accelerated toward the channel's rear face. These electrons will likely hit the channel surface again, initiating an avalanche effect where multiple secondary electrons are generated. This process results in an electron cascade reaching the anode placed just after the back side of the MCP. This anode is fixed at a higher potential than the outer MCP side to collect a measurable current pulse for most of the ions stopped on the MCP front side. The channel has a very high resistivity, so its neutralization after an avalanche takes time, resulting in a saturation effect when ions arrive in a short time window[2]. The MCPs provide excellent time resolution (10 ns FWHM or better) and are used to characterize low-intensity ion beams (for more details, see [Daudin 22]). Time measurements allow the determination of ions' time-of-flight distributions.

[2]Up to tens of ms for the most affected channels.

Two MCPs are installed along the beamline, one after the GPIB (model Topag MCPMA33/2) to characterize the ion bunches and the second one after the Penning traps to detect the ions accelerated out of the traps (see Figure 3.2). However, the MCP installed after the traps is a specific position-sensitive detector. In the following parts, a detailed explanation of PIPERADE will be provided, followed by a description of the position-sensitive MCP, and finally, a detailed view of the control system at Bordeaux.

3.3 PIPERADE

Once the ion bunches are extracted from the GPIB, they are sent to PIPERADE, which is a double Penning trap housed inside a 7 T superconducting magnet. A series of cylindrical electrodes keeps the ions closer to the beam axis along the magnetic field gradient. These electrodes are also used to slow down the ions so that they enter the traps with only a few tens of eV. The same principle is employed to extract ions from the traps; they are guided and accelerated by a series of extraction electrodes. Figure 3.6 shows the superconducting magnet and the electrodes.

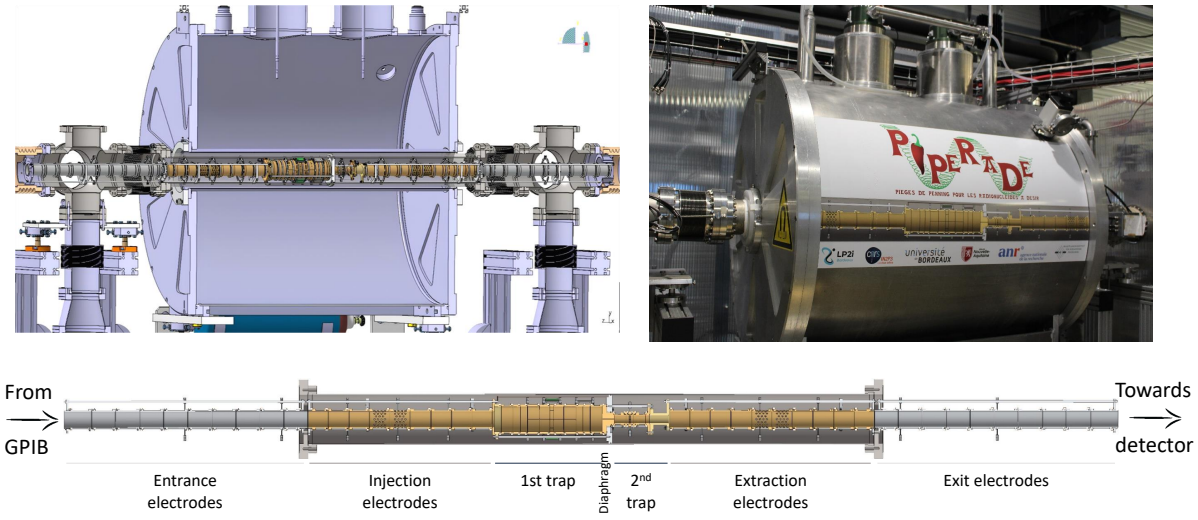

Figure 3.6: On the left a schematic of the 7 T superconducting magnet containing PIPERADE traps is presented. On the right is a photograph of the PIPERADE's magnet. At the bottom is a side view of the double Penning trap PIPERADE with its injection and extraction electrodes.

The traps

Let us now shift our focus to the two Penning traps. In Figure 3.7, a 3D view of the two traps is presented. The difference in size between them can be observed: the larger

one is called the purification trap (PT), while the smaller one is called the measurement trap (MT). Between them is a diaphragm used for differential pumping and purification purposes. The dimensions of the traps in Table 3.1 were chosen on two main criteria. The first one is that the electrical field at the traps' centers is more harmonic, and the second one is that the traps' centers would be in homogenous regions of the magnetic field. Since the distance between the two homogeneous regions of the magnetic field is limited, choosing a big first trap constrains the second to be a small one. The diaphragm radius used for the measurements shown in Chapter 4 is 1 mm, as listed in the table. However, different sizes of diaphragms exist; a diaphragm with a 2 mm radius was installed at the beginning of this work. However, it was found to be limiting (because too much gas was leaking into the MT, making it impossible to perform ToF-ICR for longer than 500 ms), so the decision to change it was made. Changing the diaphragm is a complex operation, as it requires removing the entire tower from the magnet. Figure 3.8 shows a picture of the traps outside the magnet taken by M. Gerbaux in February 2023 when the diaphragm was changed.

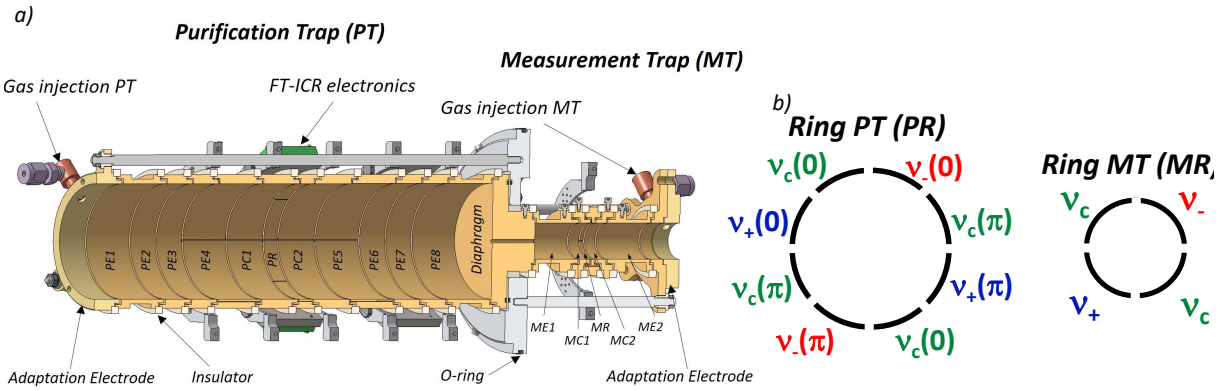

Figure 3.7: Figure from [Ascher 21]. (a) A diaphragm separates the two Penning traps of PIPERADE. The purification trap (PT) consists of eleven electrodes, including two endcap electrodes, which are four-fold axially segmented (PE1-PE4, PE5-PE8), two correction electrodes (PC1, PC2), and one central ring electrode (PR). The measurement trap (MT) consists of five electrodes, including two endcap electrodes (ME1, ME2), two correction electrodes (MC1, MC2), and one central ring electrode (MR). The electronics for broad-band FT-ICR detection can be seen atop the purification trap. Gas inlets for helium feedings are fixed on the adaptation electrodes on the far sides of the purification and measurement traps. (b) A schematic view of a central cut of the central ring electrodes of PT and MT. The segments used for dipolar excitation at ν_- are shown in red, those for dipolar excitation at ν_+ are shown in blue, and those used for quadrupolar excitation at ν_c are in green.

Adaptation electrodes are visible in Figure 3.7 at the first trap's beginning and the second's end. Gas inlets for helium feedings are fixed to these electrodes. In the PT, injection of helium gas is required for the buffer gas cooling technique. In the MT, helium gas injection may be necessary in cases where the trap is used to accumulate ions. This

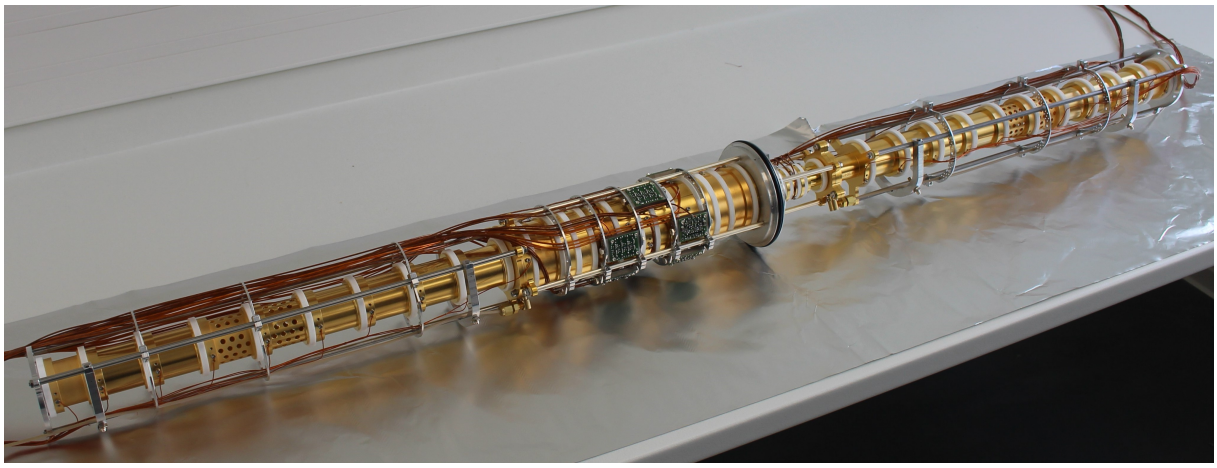

Figure 3.8: The Penning traps with their injection and extraction electrodes. The ion bunches typically arrive from the left and pass through the gold-plated electrodes to be guided into the first trap. The green PCB cards visible on its contour were originally placed for the FT-ICR technique but are not currently used. Moving to the right, we see a gray disc, indicating the location of the diaphragm. Behind it, the second trap is visible, followed by the extraction electrodes. Picture credits of M.Gerbaux

function was not used in this work. Both traps comprise five electrodes: two endcaps, which are axially segmented four times in the PT; two correction electrodes radially segmented in two parts; and one ring electrode, segmented eight times radially for the PT and four times for the MT.

The PT endcaps were initially segmented to facilitate injecting and extracting the ions with a smoother gradient, though the four segments are ultimately used as one single electrode.

The correction electrodes are used to address anharmonicities in the electric field. They were initially segmented for implementing a broad-band Fourier-Transform Ion-Cyclotron-Resonance (FT-ICR) detection [Ubieto-Díaz 09], allowing quick, broad identification of the most abundant trapped contaminants. This technique will not be discussed in this work.

Finally, the rings are segmented into 8 in the PT and 4 in the MT to apply RF excitations of various multipolarities (see right part of Figure 3.7). The excitations are applied to the different segments, requiring consistent DC potential across all segments coupled with the RF. A commercial coupling card was used for the first trap, while a custom-designed coupling card was developed before this PhD for the second trap. These cards allow us to couple the DC voltage required for the trapping and the RF signals needed for the excitations. These signals are sent via RF generators (Keysight 33500 B Series), which allows the control of amplitude and frequency and the excitation's starting phase, duration, or number of cycles.

Electrode	length (mm)
Purification trap (r = 32 mm)	
Endcap 1 (PE1)	30
Endcap 2 (PE2)	17.5
Endcap 3 (PE3)	17.5
Endcap 4 (PE4)	30
Correction 1 (PC1)	25.1
Ring (PR)	9.31
Correction 2 (PC2)	25.1
Endcap 5 (PE5)	30
Endcap 6 (PE6)	17.5
Endcap 7 (PE7)	17.5
Endcap 8 (PE8)	30
Diaphragm (r = 1 mm)	30
Measurement trap (r = 10 mm)	
Endcap 1 (ME1)	29.7
Correction 1 (MC1)	7.185
Ring (MR)	2.224
Correction 2 (MC2)	7.185
Endcap 2 (ME2)	29.7

Table 3.1: Table from [Ascher 21] showing the dimensions of the two trap electrodes. The electrodes are separated from each other by a gap of 1 mm. Generally, a tolerance of $\pm 30\,\mu$m has been achieved for the dimensions of all the electrodes.

Trap DC voltages

Trap DC voltages are supplied by power supplies (model: iseg EHS F205n), capable of delivering voltages between 0 to 500 V, with ripple and noise levels below 5 mV (typical values are provided in Table 4.1). Having the lowest noise possible in the second trap is critical, as the ions are very sensitive to electrical field variations; any perturbations will contribute to heat the cloud of ions. For the ring electrode, the DC voltage is routed through the coupling card. However, homemade switches are employed for the endcaps and diaphragm, which require switching to open and close the trapping potentials. These switches have a fall time (t_f) of approximately 20 ns and a rise time (t_r) of about 30 ns, defining the transition speed between voltage levels. Having the shortest rise and fall time is very important to give the least energy to the ions. However, the critical parameter is the settling time, which is the time before the switch reaches the range of the power-supply ripple and noise. This time is not easily measurable, but in our case, it was decided to put a 3 ms waiting time after the trapping so that the switches have the time to settle. The switches also add some electric noise; therefore, only the endcaps are switched, and the correction electrodes are directly connected to the power supply[3].

[3]It will be shown in section 4.1 that this does not prevent injection and extraction.

Pulse pattern generator

Precise timing control during and between the cycles is essential to coordinate the extraction of the ion bunches, the trapping, and the excitations. To achieve this, PIPERADE and GPIB require a configurable real-time "conductor". This sequencer, also known as the Pulse Pattern Generator (PPG), was initially developed for GSI-SHIPTRAP and CERN-ISOLTRAP on RIO FPGA [Ziegler 12], Real-Time PCI boards with LabVIEW software. A few years ago, a PPG for PIPERADE was developed by reusing the same LabVIEW FPGA state machine on a CompactRIO (NI-7410) to generate time sequences over 32 digital outputs with a 10 ns time resolution [Daudin 22].

3.4 Position-sensitive detection system

The Phase-Imaging Ion-Cyclotron-Resonance technique requires measuring the ions' position when arriving at the detector. Therefore, a position-sensitive Roentdek microchannel plate detector with a three-layer delay-line anode was purchased and installed during this PhD, and a significant part of its commissioning was also completed during this period. While similar detectors are used in other mass measurement experiments, they typically feature a smaller MCP and only two delay lines instead of three. The advantage of using three delay lines instead of two will be explained in section 3.4.3. The following provides a general description of the detector. Then, the data acquisition chain is presented, followed by a description of the association and reconstruction processes. Finally, the detector's characterization will be presented through time and position corrections.

3.4.1 General description

Let us now delve into the description of PIPERADE's detection device. It consists of a pair of MCPs in chevron configuration and a helical wire delay-line anode for two-dimensional position readout. Figure 3.9 shows a technical drawing with pictures of the actual detector.

The wire array consists of three helical wire propagation double (delay) lines rotated by 120° with respect to the neighboring ones. For each dimension, a differential wire pair is formed by a collection (signal) wire and a reference wire. A potential difference of 50 V between signal and reference wires (see Table 3.2) ensures that the electron cloud emerging from the MCPs is mainly collected on the signal wires and shared between the wire layers for different position encoding directions. The signal arrival time difference at both ends of each parallel-pair delay line for each layer independently encodes the position of the detected particle. While the signal speed along the delay line is close to the speed of light, one can define a perpendicular speed $v_\perp$ given by the pitch of one wire loop (typically 1 mm) and the time a signal needs to propagate through this loop. The

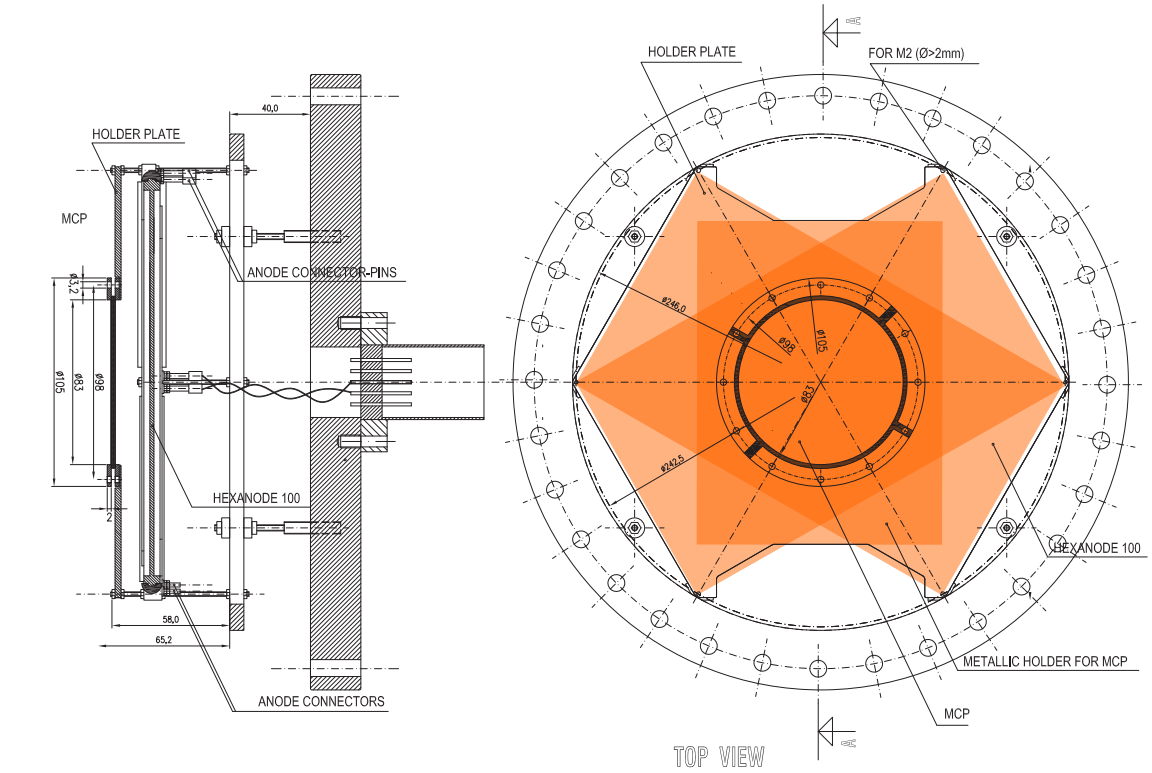

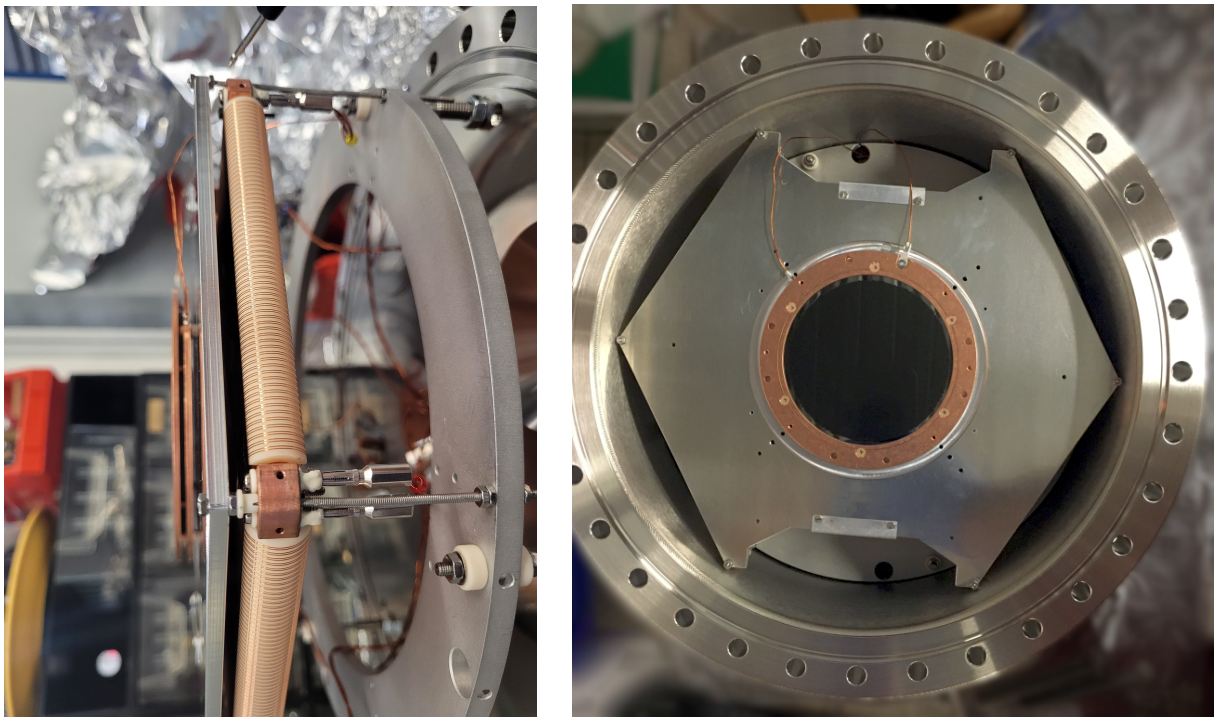

Figure 3.9: Top: side and top schematic of the hexagonal MCP detector. The three orange rectangles represent the positions of the three delay lines. Bottom: side and top picture of a delay line, showcasing its physical design and layout.

single pitch propagation time per 1 mm is $1/v_\perp$ (in units mm/ns).

Operation requires two DC voltages for an MCP stack on front and back contacts and three voltages for the anode's support plate ("Holder") and the anode wire array (detailed

MCP active diameter	80 mm
Position resolution	<100 μm
Temporal resolution	<0.2 ns
Maximum rate	1 MHz
Multi-hit dead time	10 to 20 ns
Dark count rate	0.132 count/s

Voltage settings	
MCP front	−2400 V
MCP back	0 V
Delay-line anode Holder	0 V
Reference wires	250 V
Collecting (signal) wires	300 V

Table 3.2: The left table gives the detector characteristics. The dark count rate is the only threshold-dependent parameter and was thus measured in this work (other parameters were given by the constructor). The value given for the rate is the highest value that can be reached with a good reconstruction program (more details can be found in [Jagutzki 02]). The right table lists the voltage settings applied to the different parts of the detector.

in the right part of Table 3.2). All voltages are supplied by a separate HV power supply coupled with a voltage divider.

The dimensions and characteristics of such a detector are detailed in Table 3.2. The dark count rate measurement was performed with only the MCP in an isolated chamber (valve closed and Penning gauge disconnected). The thresholds were optimized beforehand on real ions, and the veto was removed so that we could accumulate the statistics faster. The dark count rate is given per second, but we need to scale it accordingly for meaningful comparison to a typical time-of-flight gate. The usual gate of interest ranges from 2 µs for PI-ICR to 30 to 50 µs for ToF-ICR. Thus, the maximum dark count rate per cycle for the signal treatment is approximately 6.6×10^{-6} dark counts/cycle.

3.4.2 Data acquisition

Figure 3.10 shows the sequence of devices the signal must pass through to provide its information in a usable form. The system includes the decoupling box, the pre-amplifier, and the Constant-Fraction Discriminator (CFD), all of which were sourced from Roentdek as a package. However, for the Time-to-Digital Converter (TDC), a Swabian model was selected and paired with a custom-made software. This decision was influenced by the JYFLTRAP team's demonstration that the Swabian TDC offers better reconstruction efficiency than the Roentdek counterpart. The different steps of the data processing and acquisition are listed in the following (numbers below correspond to the numbers in Figure 3.10):

1. The corresponding ends of the delay lines for each dimension are located on the opposite corners of the wire array terminals on the rear side. The six terminal pairs are connected to vacuum feedthroughs by a twisted-pair cable configuration. Another signal, the so-called MCP signal inducted on the back of the MCP stack, is collected and sent to another vacuum feedthrough.

2. From the feedthroughs, the delay-lines signals are transmitted to the decoupling

box. This box allows the voltage difference between the reference and signal wires to be applied and the signals to be collected. The MCP signal is sent to the HF-signal-decoupler (HFSD/HFST) plug, which is used to apply the DC voltage to the MCP and recover the MCP signal.

3. These signals are then routed to a pre-amplifier, where they are amplified from 10–20 mV to 100–150 mV.

4. After amplification, the signals pass through a CFD to produce logic signals that can be used in the electronic chain to treat the timing information. This step requires a precise setting of the following parameters: threshold, delay, fraction, and walk level, in order to distinguish between noise and actual ion signals effectively. These settings are important to obtain the best time precision, which is essential for accurately reconstructing the positions. This step should be done only once and not be touched once optimized.

5. The seven digital signals are sent to a TDC, which measures the time difference between the start and stop logical signals

6. Finally, these timing values are sent to a server, making them accessible via EPICS (detailed in the next section).

3.4.3 Association and reconstruction

Once the timing signals are recovered, they must be associated with each other to reconstruct the position. As shown in Figure 3.11, an ion hitting the MCP is ideally followed by six corresponding delay line signals. The time difference between the MCP signal and each delay-line signal (in red in the bottom left of Figure 3.11) is labeled $t_{u_1,u_2,v_1,v_2,w_1,w_2}$. With t_{u_1,u_2}, the two signals associated with the u layer represent the time the signal took to traverse the wire to the end u_1 or u_2 of the wire. Since the wire has a fixed length and the signal speed is constant, the sum of t_{u_1} and t_{u_2} remains constant, referred to as T_{sum}. The position on the corresponding layer is determined by calculating the difference between the pairs of delay lines. From there, the intersection of the three layers provides the final position.

In some cases, one or more timestamps may be missing, but the position can still be reconstructed. Since T_{sum} remains a constant if only one signal from a layer is missing, the other can be calculated, allowing position reconstruction. Moreover, using three delay lines provides the advantage of tolerating the loss of two signals on one of the three layers, as only two are needed to determine the position. As a result, even if up to four signals are missing, the position can still successfully be reconstructed.

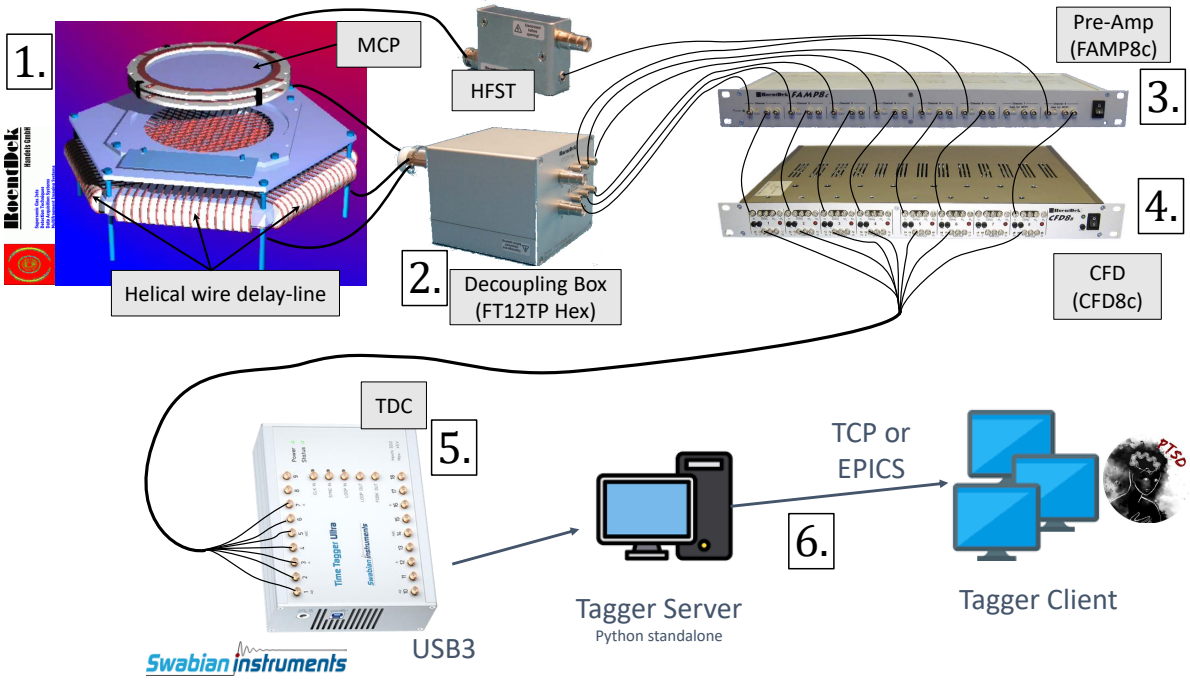

Figure 3.10: Chain of data processing for the delay-line MCP. Delay line signals go through a decoupling box. The so-called MCP signal inducted on the back face goes into an HF-signal-decoupler plug (HFSD/HFST). Then the delay lines and the MCP signals go to a pre-amplifier to send the signals into a constant fraction discriminator (CFD) so that logic signals are generated and sent to the time-to-digital converter and finally to a server that gives us access to the data via EPICS (Description of EPICS will be given in the next part 3.5.1). On the bottom is the PIPERADE Trap Scanner for DESIR (PTSD), which is nowadays the program to perform the final data acquisition (more details on this program will be given in section 3.5.2). The numbers correspond to the different step numbers listed above.

On the other hand, correctly associating events becomes quite challenging when there are more timestamps than expected. Such a scenario may happen if the threshold is too low for a delay line, triggering it twice or more instead of one. In this case, finding inconsistent time sums or reconstructed positions can help remove possible associations (for instance, if the reconstructed position is outside the MCP active area, the association is incorrect). Therefore, even if this is time-consuming, it is still possible to associate the good timestamps with the MCP hit. Another advantage of using three delay lines is that in such situations, two delay lines can help to associate with the right signals the last one (using the fact that they should cross at one point of the detector).

Finally, when two ions arrive almost simultaneously (within a maximum of 110 ns apart), it is complicated to distinguish which delay-line signal belongs to which MCP hit. Currently, these multi-hit events are not reconstructed, but the goal is to develop a program capable of doing so.

Additionally, the positions must be extracted from the data once the signals are associated. Thus, a Python program was developed during Yan Langlois' internship, supervised

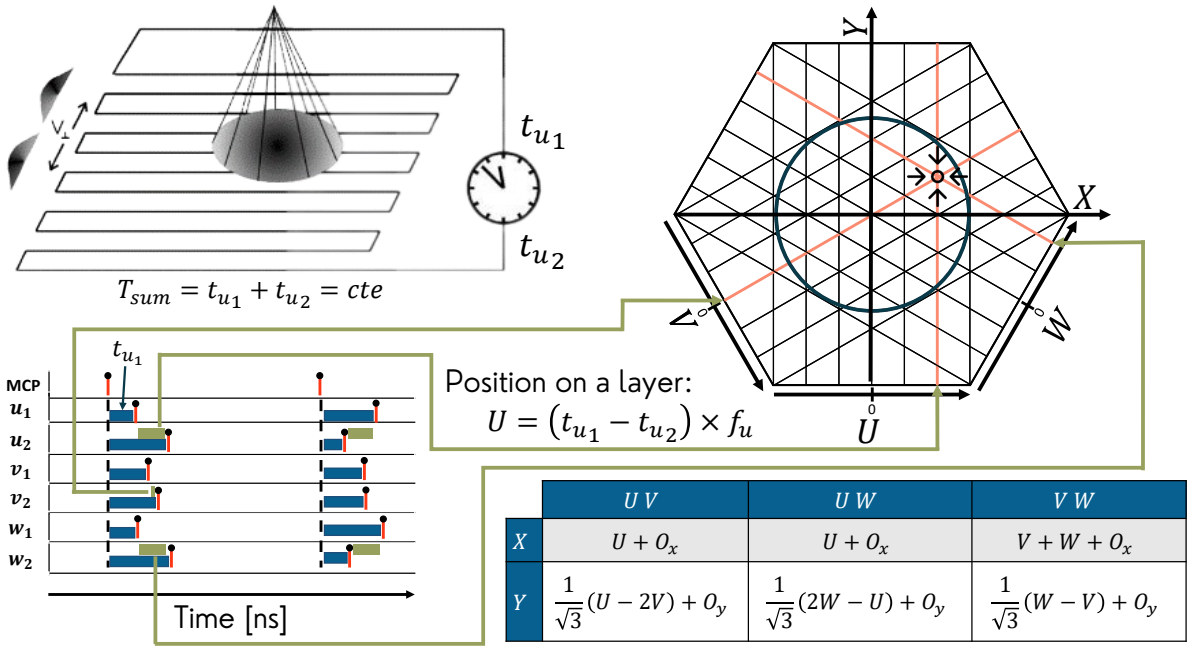

	$U\,V$	$U\,W$	$V\,W$
X	$U + O_x$	$U + O_x$	$V + W + O_x$
Y	$\frac{1}{\sqrt{3}}(U - 2V) + O_y$	$\frac{1}{\sqrt{3}}(2W - U) + O_y$	$\frac{1}{\sqrt{3}}(W - V) + O_y$

Figure 3.11: Principle of conversion from delay lines timing signals to positions. On the top left is a diagram (taken from [Jagutzki 02]) illustrating the electron shower from the MCP hitting a delay line. This diagram explains that for one delay line, two timing signals are measured, and their sum remains constant as the wire length is fixed. On the bottom left, it is shown that the position can be determined using the time differences (in green) between the two signals (in red) of the same layer (in blue) multiplied by a factor f_u (details on this factor are in the text). On the top right is a schematic view of the three layers. The salmon lines represent the position computed on each layer, and the crossing of these lines represents the reconstructed ion's position (note that this is not a realistic drawing of the delay lines as, in our case, one delay line is shorter than the other two). Finally, on the bottom right, a conversion table is provided to compute Cartesian coordinates using the three combinations of layers. See text for details.

by Dinko Atanasov and myself. This program enabled us to associate and reconstruct the ideal cases effectively. However, more complex cases still require further analysis to optimize the performance of this detector fully. By focusing on and plotting only the straightforward cases, we could carry out a more controlled characterization, minimizing the impact of any miss reconstructed events.

A detector calibration must be done every time the thresholds are modified or the MCP is moved to reconstruct and associate in the best way possible. The most helpful measurement for calibration was to perform a dark count measurement. Dark counts should be spread all over the detector, allowing this measurement to adjust the image size for each combination of layers. Figure 3.11 shows the formula for computing the ions' position on a layer.

$$U = (t_{u_1} - t_{u_2}) f_u \tag{3.1}$$

where t_{u_1} and t_{u_2} are the time between the MCP hit and the first and second wire of the u delay-line. U is the position on the layer, and the parameter f_u is a conversion factor specific to each layer that must be calibrated to obtain a correct shape for the reconstructed image. Then, the coordinates are changed to Cartesian ones using the three layers (detailed in the table in Figure 3.11). The offsets O_x and O_y must also be calibrated to properly center the image around the $[0, 0]$ position. These parameters were optimized through an iterative process to fit the dimensions of the MCP and confirmed by another program created by the detector manufacturer.

3.4.4 Time corrections

Another step of the calibration process is to consider that the total propagation time (T_{sum}) of the signals through the wires is not the same depending on the hit position. When plotting these T_{sums} for each layer as a function of the position on the layer, the dependence is visible (see Figure 3.12). This dependency is a significant issue because in cases where timestamps are missing, the time sums would be our best method to reconstruct the position. For instance, if t_{u_1} is missing, it can be computed using $T_{sums} - t_{u_2}$.

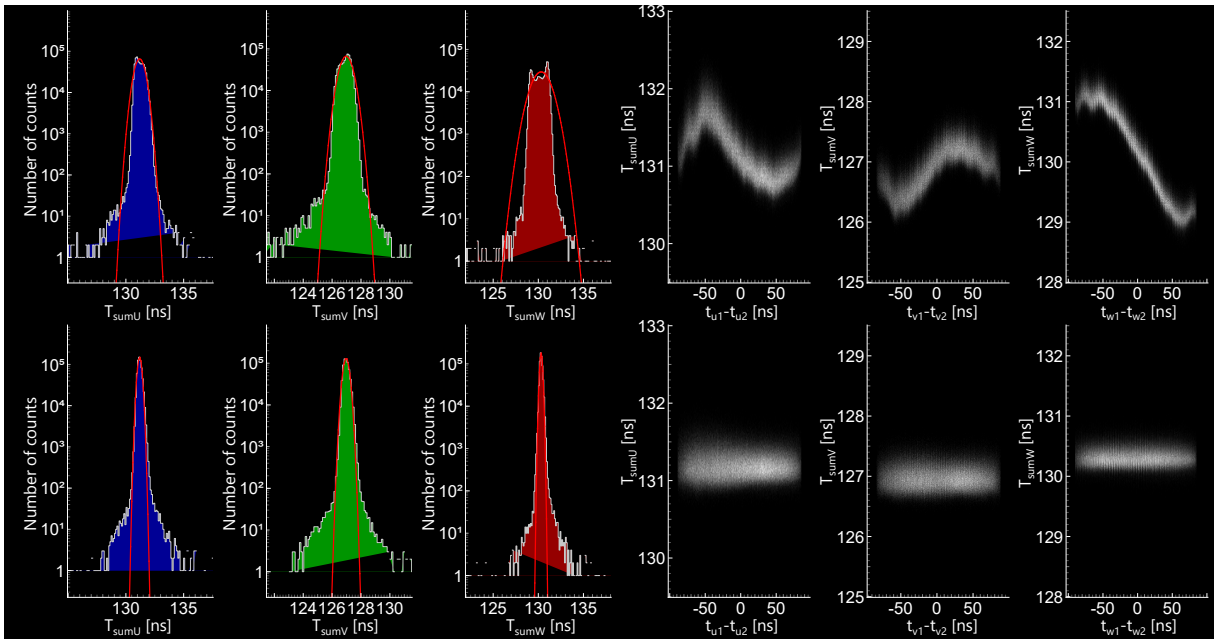

Figure 3.12: On the top left, the T_{sums} one-dimensional histogram is shown for each layer, with the red curve representing a Gaussian fit used for subsequent correction. On the top right, T_{sums} for each layer is plotted as a function of the time difference between the two delay line signals of the corresponding layer (e.g., $t_{u_1} - t_{u_2}$ for the U layer). The T_{sums} one-dimensional histograms, visible on the bottom left, are obtained by applying the corrections detailed in the text. The bottom right clearly shows that there is no longer any positional dependence.

To address this issue, a central value T_{central} is taken from a Gaussian fit made on all

non-corrected data. Then, slices are taken at multiple positions, resulting in numerous 1D histograms that display Gaussian-like curves. Gaussian fits are then performed on these histograms to generate a profile stored in a table. This data is subsequently used to correct all time sums on this layer, ensuring that the T_{sums} are truly constant. The correction is applied as follows:

$$\begin{cases} t'_{u_1} = t_{u_1} + (T_{central} - T_{table})/2 \\ t'_{u_2} = t_{u_2} + (T_{central} - T_{table})/2 \end{cases} \implies \begin{cases} t'_{u_1} - t'_{u_2} = t_{u_1} - t_{u_2} \\ t'_{u_1} + t'_{u_2} = T_{central} \end{cases} \tag{3.2}$$

These formulas ensure that the position is not affected, as the time difference between t_{u_1} and t_{u_2} is constant. Finally, the T_{sums} of all events are displayed in a histogram for each layer. The resulting distribution appears more Gaussian, with an FWHM below 0.5 ns, which meets the time dispersion specifications provided by the manufacturer for this detector. Once this correction is applied, it becomes possible to reconstruct reliably more complex cases where signals are missing.

3.4.5 Position corrections

The final step of the calibration involves ensuring that the reconstructed position does not depend on the combination of layers used for the reconstruction. The deviation, defined as follows, characterizes this difference:

$$D = \sqrt{(X_{uv} - X_{vw})^2 + (Y_{uv} - Y_{vw})^2} \tag{3.3}$$

with $X_{uv}, X_{vw}, Y_{uv}, Y_{vw}$ being the coordinates computed using the u and v layers or the v and w layers as defined in Figure 3.11's table. According to the constructor, optimizing the conversion factors (f_u, f_v, and f_w) mentioned earlier should reduce the mean deviation to below 0.6 mm. The linearity map on the left side of Figure 3.13 results from optimizing these conversion factors (f_u, f_v, and f_w). This map is a two-dimensional histogram that adds the deviations of all points in the same bin. Consequently, the color bar ranges from 0 to 2 mm, though most points do not exhibit a 2 mm deviation. At the bottom of each map, a histogram on a logarithmic scale displays the actual deviation values of all points. This correction allows reaching a deviation of 0.54 mm, which is within the constructor's specifications, as it remains below 0.6 mm. However, another correction must be done, as the deviation still depends on the position. According to the manufacturer, this second correction should bring the deviation below 0.1 mm. The process for this correction is detailed below.

The position measured by one layer for each event is compared against the positions measured by the other two layers to correct for these deviations. Three parameters are then defined:

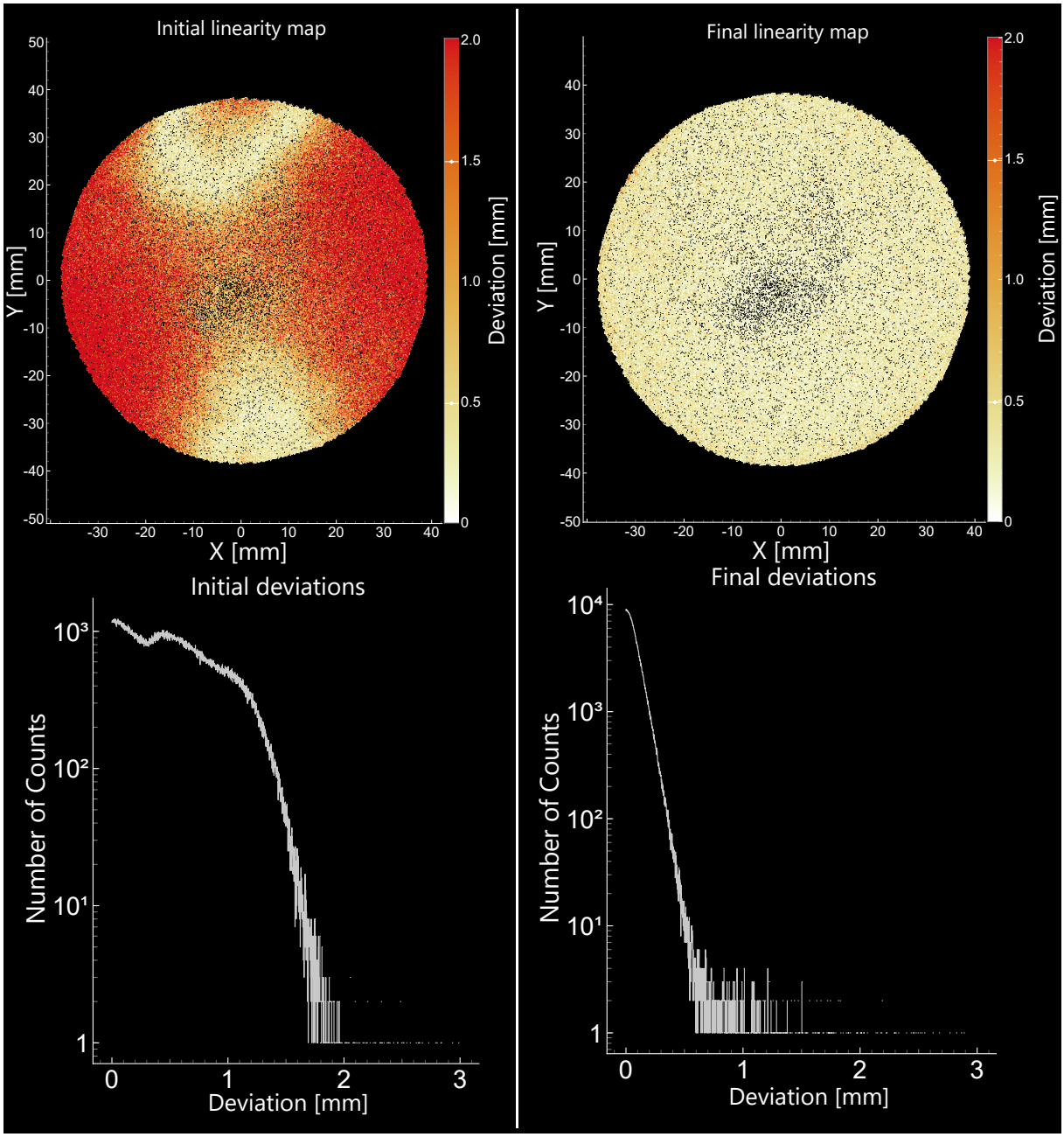

Figure 3.13: The linearity map, after adjusting the conversion factors, is shown on the upper left, and the final corrected map appears on the upper right. The associated histogram of the deviation for all the dark counts is at the bottom of each image.

$$\begin{cases} dU = V + W - U \\ dV = U + W - V \\ dW = U + V - W \end{cases} \tag{3.4}$$

In Figure 3.14, the three top two-dimensional histograms represent dU as a function of the U position, dV against V, and dW against W. Similar to the time corrections, slices of these plots are taken, and Gaussian fits are performed on each slice to generate a correction table, which allows us to plot the red curve visible on the top-left two-

dimensional histogram. This correction is then applied, and the process is repeated until it converges. The fit is done at each iteration, with the layer that appears to deviate the most. After four iterations, the mean deviation does not reduce any further. The deviation map obtained at the end is shown on the top right of Figure 3.13. The final mean deviation is lower than 0.1 mm, which is within the constructor's specifications. Calibrating this detector is challenging and must be redone whenever thresholds are modified, or the MCP is moved.

This work involved calibrating both position and time, enabling the precise reconstruction of common and more complex cases. However, to fully benefit from these calibrations and handle situations where timestamps are not exactly six after an MCP signal or where multiple hits occur, an advanced reconstruction program still needs to be developed.

3.5 Control system

3.5.1 General control of PIPERADE

As PIPERADE will be operated at the SPIRAL2-GANIL facility, all control system developments made at LP2iB for the HRS, GPIB, and PIPERADE have been performed under EPICS (Experimental Physics and Industrial Control System) with specific requirements to be fully compatible with the existing Control System. EPICS is a set of open-source software tools, libraries, and applications developed collaboratively and used worldwide for scientific instruments such as particle accelerators, telescopes, and other grand-scale scientific experiments [ANJ]. Based on a Client-Server architecture on an Ethernet network, the main force of EPICS is its communication protocol: Channel Access (CA) now enriched by the more recent pvAccess (pvA). These protocols make all parameters needed to control and command any beamline equipment accessible by any client (user interface, for example) connected on the network only by reading and/or writing on shared variables available on the network.

Figure 3.15 overviews the PIPERADE control system (CS) architecture. This diagram highlights the crucial role of EPICS within the CS architecture, as it is consistently used to establish the link between servers and clients. The main clients are three programs. The first is a control system software called CSS-Dev, which existed at the beginning of this work. It was used to manually modify and monitor the different parameters based on the SPIRAL 2 graphical user interface convention [Daudin 22]. However, it did not allow for any systematic scanning of these parameters. The two other main clients are described in the following dedicated section.

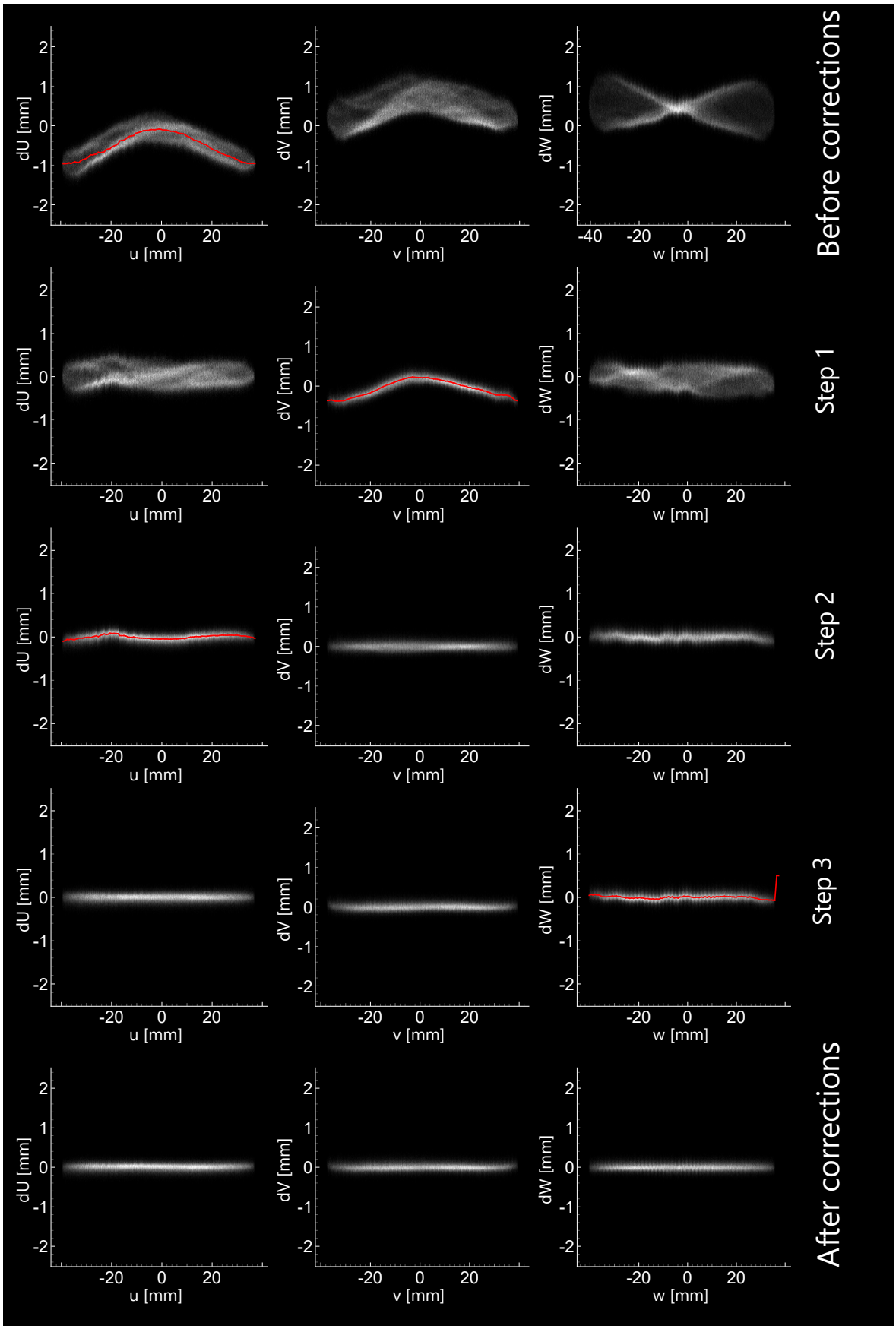

Figure 3.14: The three top two-dimensional histograms represent in the reading order dU as a function of the U position, dV against V, and dW against W. Then, by reading the image from top to bottom, every set of three plots represents a new iteration in the correction process. The red curves represent the results of the slice fits used for corrections.

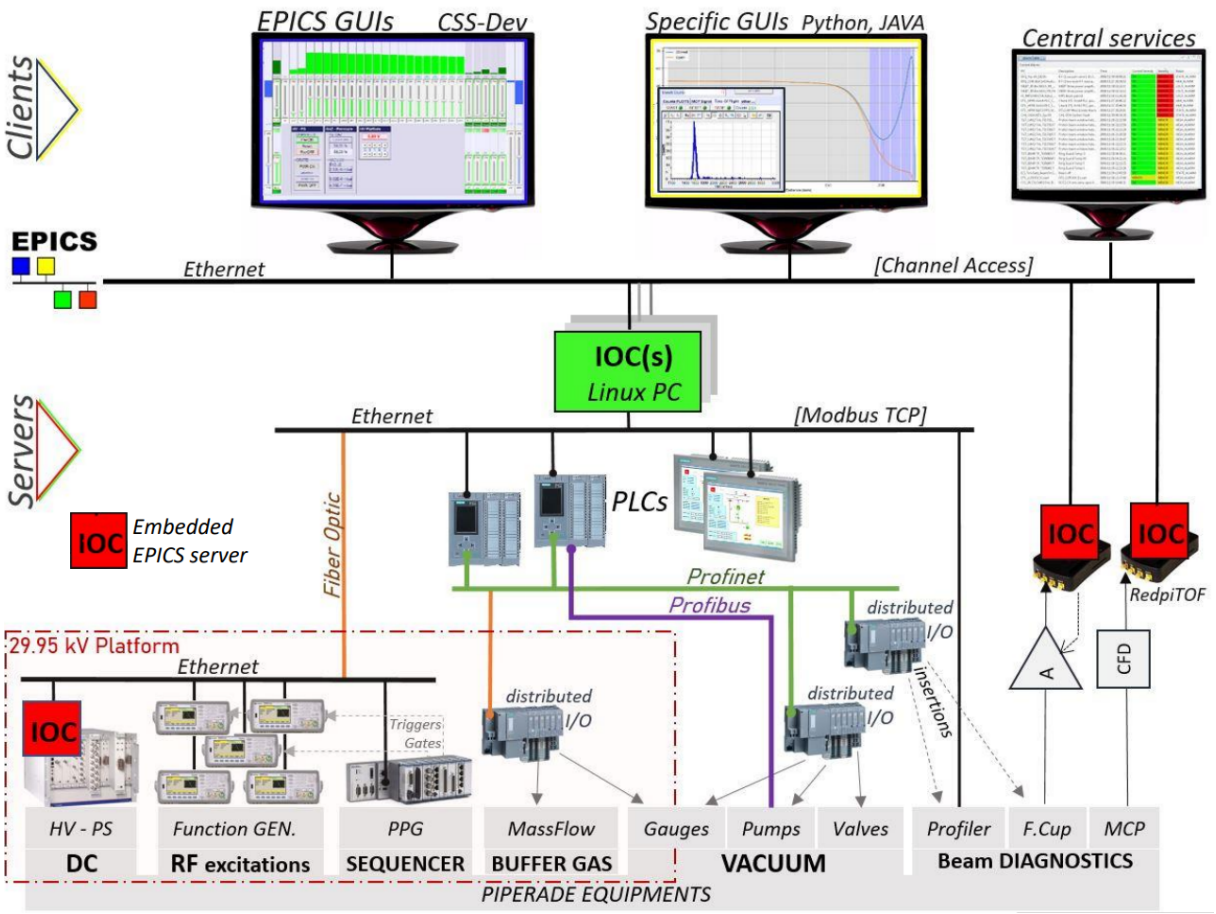

Figure 3.15: Plot from [Daudin 22]. Overview of the PIPERADE CS architecture. Equipment is illustrated in the lower part of this figure. These tools are controlled by PLCs (automation part) or directly by EPICS servers (IOC). Ethernet network is the main communication media, and field buses like Profibus and Profinet (Profibus on ethernet network) are used by PLCs. In the upper part of this figure, clients are the applications used to control the PIPERADE experiment.

3.5.2 PIPERADE Trap Scanner for DESIR (PTSD)

Many independent Python codes or LabVIEW programs were used to scan various parameters using Faraday Cups (FCs) or Microchannel Plates (MCPs). During this PhD, a significant effort was made to consolidate all these independent tools into two primary Python programs.

The first program, S3 (Start, Stop, and Save), is designed to switch the entire beamline on and off and save or load optimized parameter configurations.

The second program, named PTSD (PIPERADE Trap Scanner for DESIR), was developed by Dinko Atanasov and myself and is the primary program used today (see Figure 3.16). The graphical interface developed with PyQt5 has several parts.

The first part enables scanning all EPICS variables in one or two dimensions. That allows the parameters of the RF excitations (amplitude, frequency, delays) to vary, as well as the DC voltages applied to the electrodes of the traps or the optics or the times of the

sequence defined by the PPG. As it will be shown in Chapter 4, this scanning feature is crucial for the optimization of the spectrometer. This tab also includes the Experimental Mass Determination Replicator (EMDR), which automates the mass measurement process by alternately measuring the reference ion and the ion of interest in sequence, whether using the PI-ICR or ToF-ICR technique.

The second part enables the following:

1. Monitoring of the count rate (top left in Figure 3.16), time of flight (ToF) (bottom right in Figure 3.16), and position (Top right in Figure 3.16) on the MCP detector

2. Data gating by ToF, count rate, and position (defined by the blue regions in the two bottom plots of Figure 3.16). These gates can, for example, eliminate noise from the actual measurement in case of a spark or contamination in the traps.

3. Gaussian fitting function that can be very helpful to estimate the bunch ToF dispersion (an example is visible on the central plot of Figure 3.16 featuring a red curve) or to perform an online analysis of the PI-ICR spots. These parameters are particularly interesting for the optimization process, as the reduction of the bunch dispersion is crucial for the ToF-ICR technique, and the reduction of the spot size is crucial for the PI-ICR technique.

The third part is a calibration section linked to the AME to identify possible contaminants in future experiments. Quentin Delignac developed this part of the program during an M1 internship. This tab also allows for computations of frequencies and Injection/transfer time of an ion of interest with regard to calibration nuclei.

PTSD includes several safety features that can shut down the beamline if necessary. While it is currently configured to work with the various MCPs on the line, it can be easily adapted with other detectors. Its versatility means it can also be used for GPIB optimization. The program also supports offline operation and includes a Time-of-Flight Ion Cyclotron Resonance (ToF-ICR) fit function. This fit function, based on a similar Finnish program called Pymasscanner, uses the formula given in Equation 2.36 (more details in section 4.3.2).

With the established technical intricacies and methodologies, we now focus on the outcomes these tools have yielded.

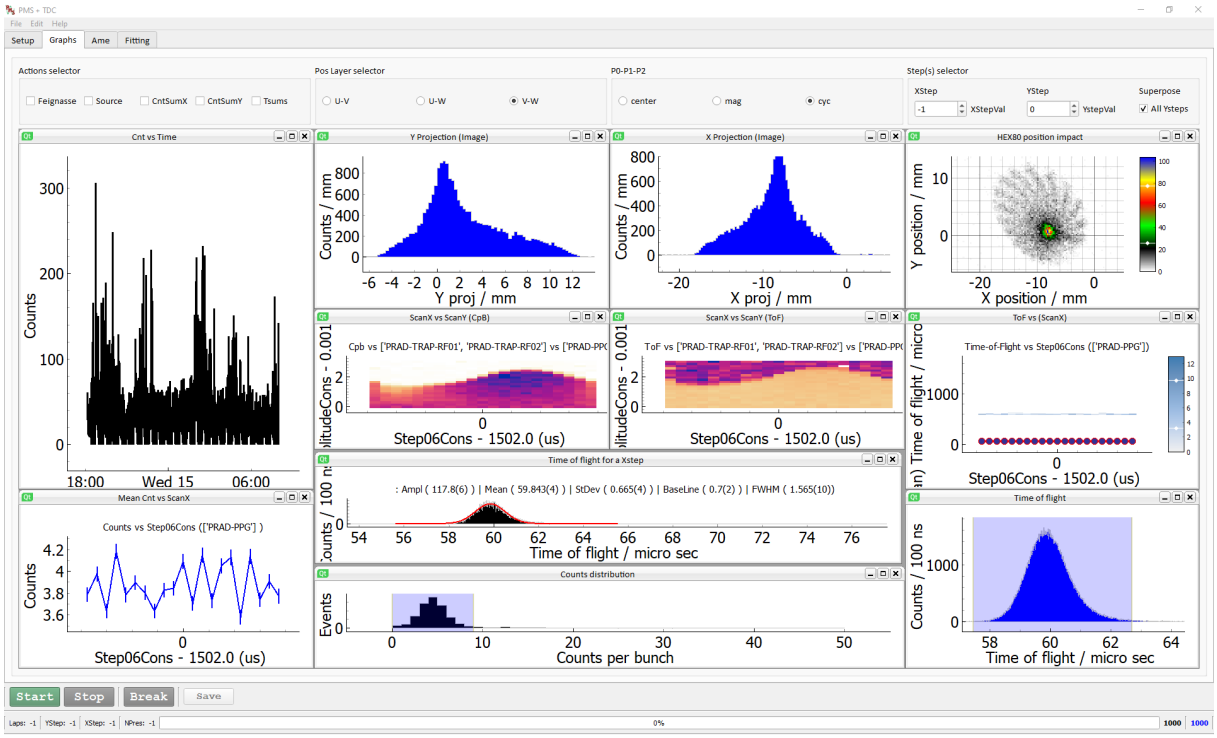

Figure 3.16: View of the scan tab of the PIPERADE Trap Scanner for DESIR program, showing the results of a two-dimensional scan using the position-sensitive detector. On the bottom, the number of counts per bunch can be gated so that a Z-class analysis can be performed in the future or to remove potential sparks. On the bottom right, the time-of-flight spectrum can also be gated. Gaussian fits of the ToF spectrum or position projections can also be performed, as visible in the central plot with the red curve.

Chapter 4

The PIPERADE characterisation

Contents

This chapter delves into the core work of this PhD project. It goes from implementing the techniques outlined in Chapter 2.4.1 to conducting an in-depth optimization of electrical and magnetic fields to reduce mass measurement systematics. Most of the results and plots in this chapter were directly generated by the PIPERADE Trap Scanner for DESIR (PTSD) program introduced in the previous chapter.

This chapter will begin with a brief overview of the trapping and measurement principles employed. The chapter then outlines the step-by-step implementation of the buffer gas cooling technique (BGCT) in the purification trap (PT). Then, it sheds light on the development of the transfer process from the PT to the measurement trap (MT). Yet, the focal point of this section lies in explaining the ToF-ICR mass measurement technique and culminates in the characterization of the PI-ICR mass measurement and purification technique.

4.1 Ion trapping

The trap's endcap electrodes are designed to switch between two states: Open (−85 V) and Closed (0 V). Table 4.1 provides the voltage settings for the trap electrodes in both states, while Figure 4.1 illustrates the corresponding electrostatic potential within the trap.

Purification trap potentials		
Electrode	Open(V)	Closed(V)
PE1-4	-85	0
PC1	-70	
PR	-80	
PC2	-70	
PE5-8	-85	0
Diaphragm	-85	0

Measurement trap potentials		
Electrode	Open(V)	Closed(V)
ME1	-85	0
MC1	-69.6	
MR	-80	
MC2	-69.6	
ME2	-85	0

Table 4.1: Electrode voltages for the open and closed states are displayed. These potentials are not all optimized, but this configuration was used for most scans. Electrodes where only one potential is displayed are not switched (they can be if needed). The particular value of the MC1/MC2 voltages was optimized, which will be shown afterward. These potentials are applied with respect to the trap HV platform potential (29.925 kV).

Each step of the optimization process detailed in this chapter involves capturing and releasing an ion bunch toward the MCP detector. The sequence required for trapping ions will be detailed below. Additionally, the traps can be kept fully open throughout the entire sequence in what is called the "shoot-through mode", primarily used for "aligning" the beam through the traps. The first step is to get the beam to pass through the traps and optimize transmission by adjusting the steering, injection optics, etc.

Assuming the proper alignment of the bunch trajectory, the key lies in timing. To capture an ion bunch, the trap must remain open while awaiting the bunch's arrival, closing exactly before ions rebound off the trap's exit. To determine precisely this timing, the closing time of the injection is scanned. To verify if ions were trapped at a given time, the electrodes at the trap's end switch to an open state, liberating the ions and directing them toward our MCP detector.

Figure 4.2 depicts a time scan illustrating the potential switch of the injection endcap electrodes from open to closed. The "zero" time (not shown in Figure 4.2) marks the release of the ion bunch from the GPIB (at this time, the Penning trap entrance is open). Therefore, the horizontal axis displays the time between the bunch release and the trap closure. The vertical axis represents the number of counts detected by the MCP. Zero count signals that ions are not trapped, indicating premature or delayed trap closure. A sudden increase or decrease in ion count implies partial capture, while a plateau denotes

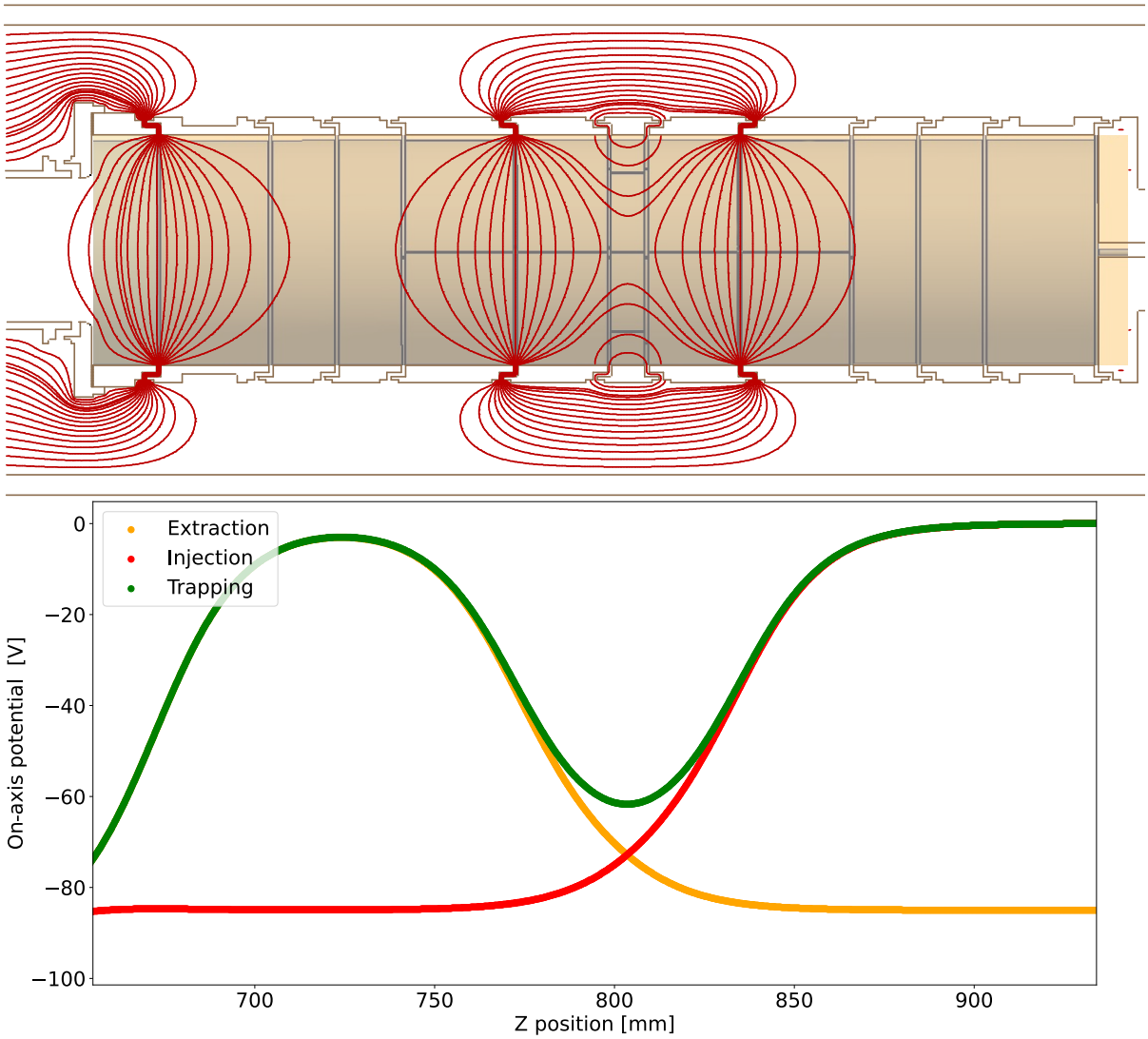

Figure 4.1: On top is a schematic view of the purification trap with the equipotentials plotted in red in the trapping configuration (extracted from SIMION simulations). The plot below displays the on-axis potential experienced by the ions in the simulations for different configurations as a function of their position. The green, red, and orange curves represent the on-axis potential when the trap is closed, open for the injection, and open for the extraction, respectively. These potentials are applied with respect to the trap HV platform potential (29.925 kV).

maximum bunch capture. On this particular plot, mainly two pics are visible: one for the ^{39,41}K ions and another for the ^{85,87}Rb ions, which are the main species ionized in the source.

4.2 Purification Trap

After capturing the ions, the process shifts to optimizing the buffer gas cooling technique (BGCT). The primary goal is to prepare the ions for RF field excitations optimally. A dipolar excitation at the magnetron frequency will then be applied to excite

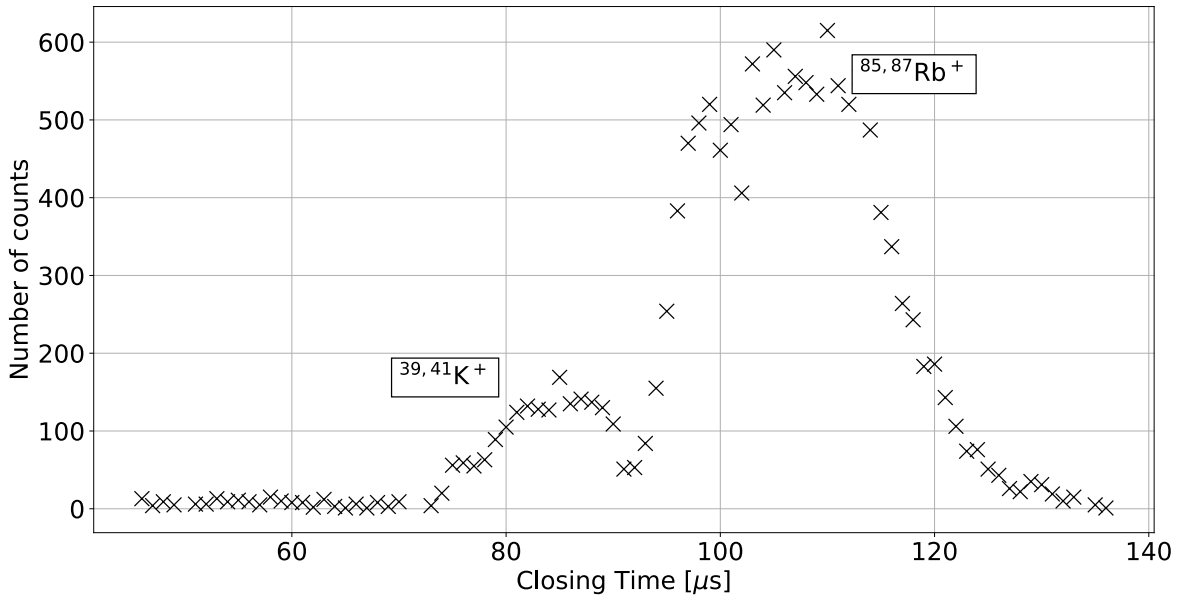

Figure 4.2: Number of counts on the MCP for 180 bunches against the closing time of the purification trap injection electrodes. On this scan, one can see the ^{39,41}K ions being optimally trapped at a time around 85 μs after the release from the GPIB and, similarly for the ^{85,87}Rb ones around 105 μs. Note that a large part of the ^{39}K ions are cut by the GPIB as the q parameter was optimized for ^{85,87}Rb.

the ions to an orbit around the trap center with a radius larger than the diaphragm's. In the final step, the main challenge will be to convert only the ions of interest's motion using a narrowband quadrupolar excitation at the cyclotron frequency until the reduced cyclotron motion gets cooled to recenter them (detailed in section 2.4.1). This part will explain the detailed optimization of these three steps.

In section 2.2, it was highlighted that ions positioned farther from the trap's center become increasingly susceptible to anharmonic perturbations and magnetic field inhomogeneities. Consequently, the aim will be to limit the region where the ions will be manipulated within the smallest volume possible, ensuring that the ions are as thoroughly cooled as possible. However, a key objective of this technique is to purify large samples of nuclei, which involves dealing with greater space charge effects and, consequently, larger ion bunches. As the number of ions increases, the bunches naturally expand (which is desirable so that the excitations are less screened), requiring a larger region for the purification process. In these situations, the ions are manipulated over larger regions of the trap, making them more susceptible to field imperfections.

The second challenge of this technique (like any Penning trap technique) is to handle the compromise between duration and resolution in the best way possible. Indeed, it was explained at the end of section 2.4.2 that the resolution and the duration of the quadrupolar excitation are inversely proportional. Both these parameters will be limiting

in online experiments for different reasons. On the one hand, most of the nuclei will be exotic, meaning that the total duration of the cleaning process should not be much greater compared to the Ion of Interest's (IoI's) half-life to limit decay losses. It is not limiting in offline measurements; however, avoiding overly long measurement cycles is still essential to ensure multiple repetitions within a reasonable time frame. On the other hand, the beams we will need to clean may be highly contaminated with nuclei close in mass, thus requiring a high resolution.

4.2.1 Cooling

The first objective is to prepare the ions for RF field excitations optimally. The quantity of gas within the trap directly influences the speed of ion cooling (more gas results in faster cooling). Various methods are available to investigate the energy dispersion of ions. Here, the focus is on examining the Time-of-Flight (ToF) dispersion. This approach considers that ions with distinct energies travel at different speeds from the trap to the MCP, resulting in their arrival at various times. Figure 4.3 displays the ToF dispersion of the ion bunch plotted against the cooling time, illustrating this relationship vividly. After some time, the ToF dispersion stabilizes, indicating the ions have reached a cooled state, signifying no need for further waiting. If this pre-cooling step were not perfectly done, this would reduce the resolution of the BGCT and force us to use a larger region of the trap, increasing the problems coming from anharmonicities and inhomogeneities. In this figure, at least two species are visible, the ^{39,41}K ions that are expected (arriving around 28 μs) and the ^{4}He ions that are probably being ionized either in the GPIB or along the way to the traps (arriving around 12 μs).

By adjusting the amount of gas in the trap, the cooling process can be either slowed down or accelerated. In Figure 4.4, each point represents the result of a Gaussian fit of the ion bunch time dispersion. For instance, fitting each scan slice displayed in Figure 4.3 gives the series of points red points in Figure 4.4. The evolution of this dispersion is shown for different percentages, which correspond to different openings of the gas injection valve. It was already explained before that this cooling time needed to be shortened to avoid decay losses when working with exotic nuclei. Still, experience with other Penning traps showed that this time step was of the order of 20 to 100 ms. The plot shows that 4% to 6% valve openings are better for a competitive cycle length [1].

However, it is important to note that the rate at which the helium-gas interaction dampens any ion motion is contingent upon the ion's mass. Therefore, if for light masses such as ^{39,41}K, the optimized valve opening is around 4%, a greater valve opening will be needed for ^{85,87}Rb. In the Figure 4.5, it is visible that the cooling time for the ^{85,87}Rb ions is double the time required for ^{39,41}K at similar pressure.

[1] the cycle length corresponds to the total time between the GPIB extraction and detection of the ions after the traps

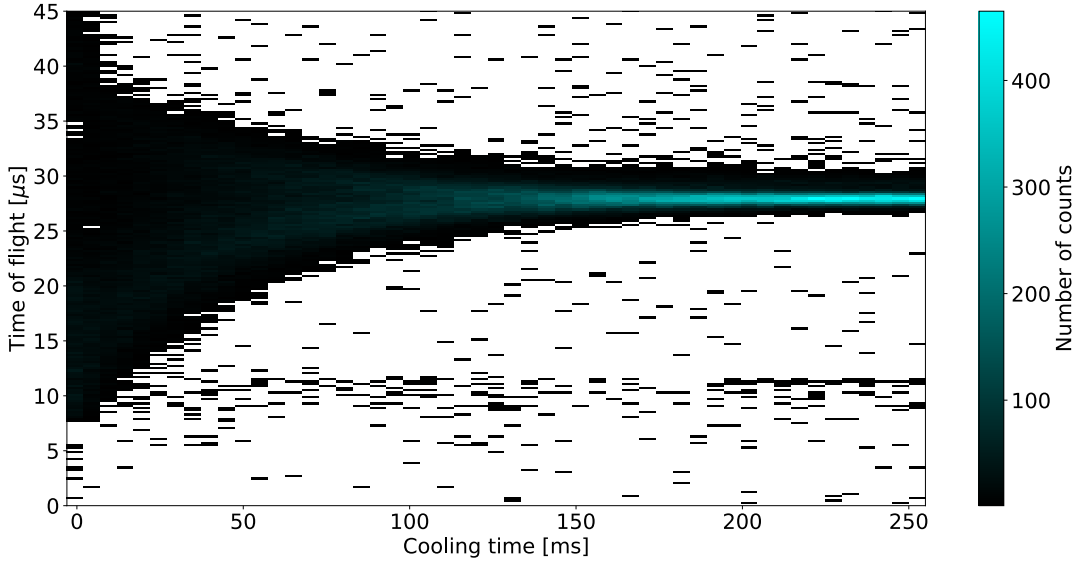

Figure 4.3: Evolution of the ion's ToF when scanning the cooling time in the first trap for ^{39,41}K at 2 % valve opening (it will be shown later that this corresponds roughly to a pressure of 2×10^{-5} mbar in the trap). The ions arriving at 12 μs are ^{4}He ions that were trapped with the ^{39,41}K ions. This scan was performed using 540 bunches for each cooling time.

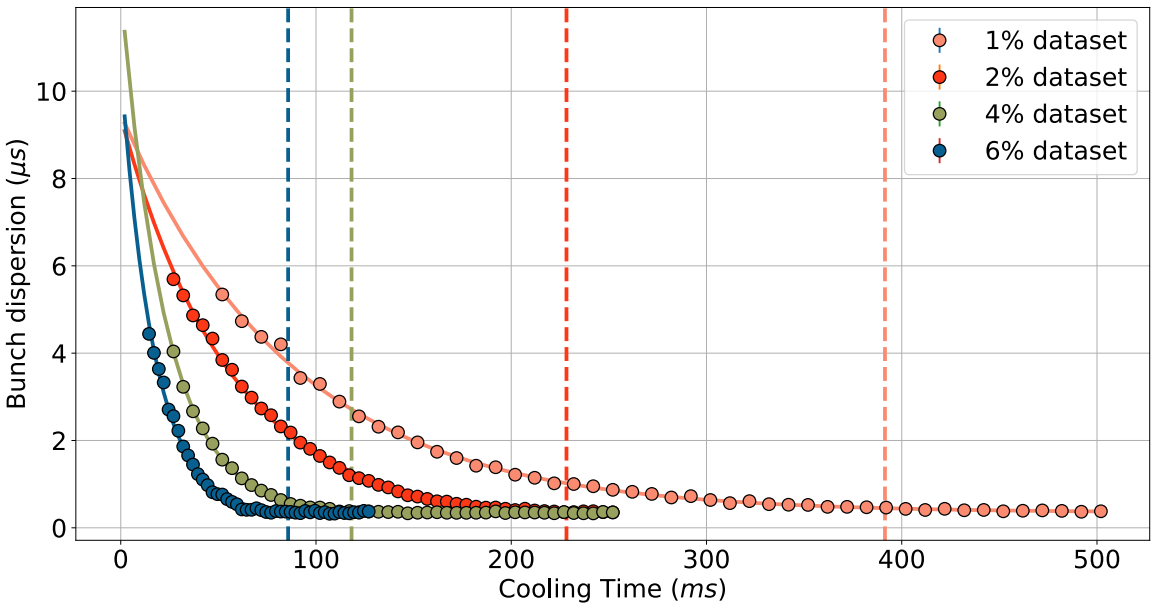

Figure 4.4: Bunch ToF dispersion as a function of the cooling time for different settings of the mass-flow controller. Each point is obtained by fitting the ion's ToF distribution with a Gaussian. The four curves are fitted with equation 4.2. The four vertical dotted lines are positioned to the point where the fitted curve reaches 120% of the final fitted dispersion value.

This valve opening does not correspond to any known pressure value. Thus, the pressure in the trap will be determined by looking at the evolution of the ToF dispersion as a function of the cooling time. One can define the damping constant δ as:

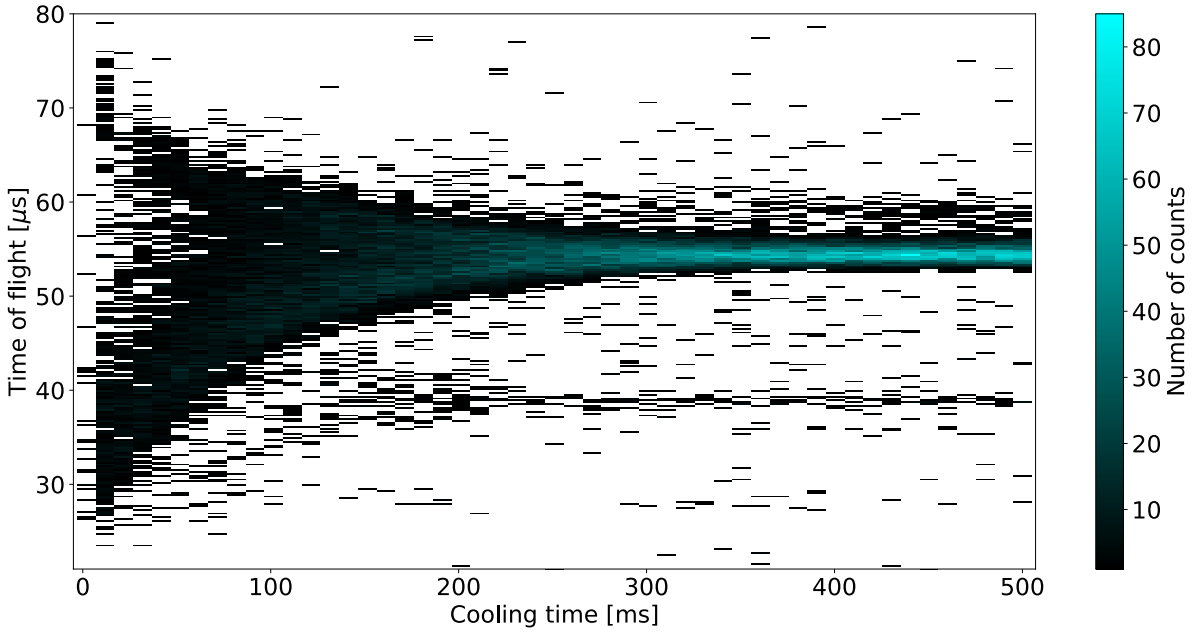

Figure 4.5: Bunch ToF dispersion as a function of the cooling time for ^{85,87}Rb at 2×10^{-5} mbar (reminder: cooling times for comparable pressure for ^{39,41}K twice shorter, see Figure 4.3). The ions arriving at 40 μs are ^{39,41}K ions that were trapped with the ^{85,87}Rb ions. The ToF absolute value changed for ^{39,41}K as the extraction used in this scan was different. This scan was performed using 70 bunches for each cooling time.

$$\delta = \frac{e}{m}\frac{1}{K}\frac{T_0}{T}\frac{p}{p_0} \tag{4.1}$$

Here, e is the ion's charge, T and p are the gas temperature and pressure, K is the ion reduced mobility ($K = 216(6) \times 10^{-5}\,\mathrm{m^2V^{-1}s^{-1}}$ for $^{39}K^+$ in He buffer gas), with $T_0 = 270\,\mathrm{K}$ and $p_0 = 1024\,\mathrm{mbar}$. Then, the axial motion amplitude variation is defined as:

$$\rho(t) = \rho_0 e^{-\delta t} \tag{4.2}$$

Since the amplitude of the axial motion, in our case, is directly linked to the bunch dispersion, the pressure inside the traps can be determined by fitting the evolution of this dispersion over time. Figure 4.6 shows the pressure values obtained using this method. It is worth noting that the valve manufacturer does not guarantee linearity below 5%, which is precisely the range we are currently using. However, the data appears relatively linear at first glance. As for reproducibility, it was not carefully tested. However, two measurements were performed at 4%, yielding pressures differing by 10^{-8} mbar.

As highlighted in section 2.4.1, it is crucial to note that only the axial and reduced cyclotron motions are affected by gas damping. A broadband quadrupolar excitation at the frequency of the ions of interest can be introduced to address any initial magnetron motion present in the ions. It is also important to note that the effect of the magnetron motion is not visible when looking at the ToF. This effect can be monitored only by

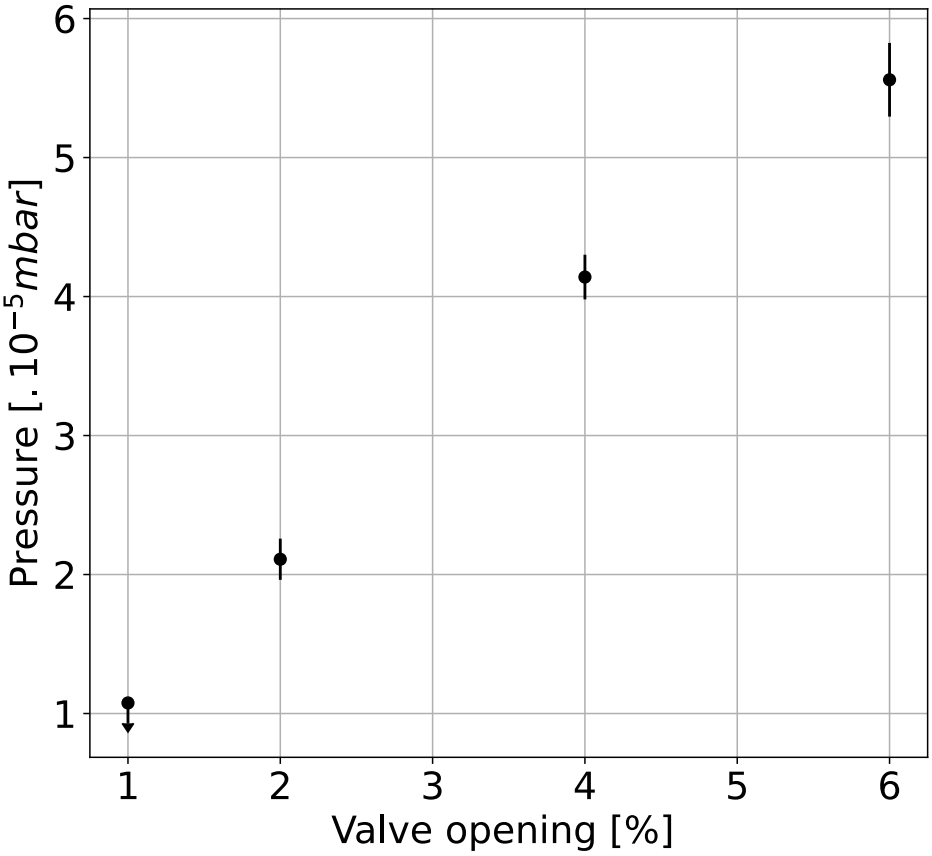

Figure 4.6: Pressure evolution as a function of the valve opening percentage. The points at 4% are averaged over two measurements. Unfortunately, only an upper limit could be established for the 1% valve opening as it was taken after a scan at 4%. The characteristic time for the pressure to stabilize in the trap after adjusting the flowmeter opening is around 8 hours.

looking at the image on the position-sensitive detector. In Figure 4.7, the evolution of the spot size is shown for different cooling with broadband cyclotron conversion. One can see the difference in spot size with or without this conversion after a few tens of milliseconds. In the following, a broad-band quadrupolar excitation is systematically applied in parallel with the cooling time.

4.2.2 Magnetron excitation optimization

Once the ions have reached a well-cooled and properly centered state, the first RF excitation can be optimized. As explained in section 2.4.1, the dipolar excitation, applied at the magnetron frequency, aims to expand the rotation radius of all ions beyond the radius of the diaphragm.

Applying this RF excitation implies handling three primary parameters:

- frequency;
- amplitude;

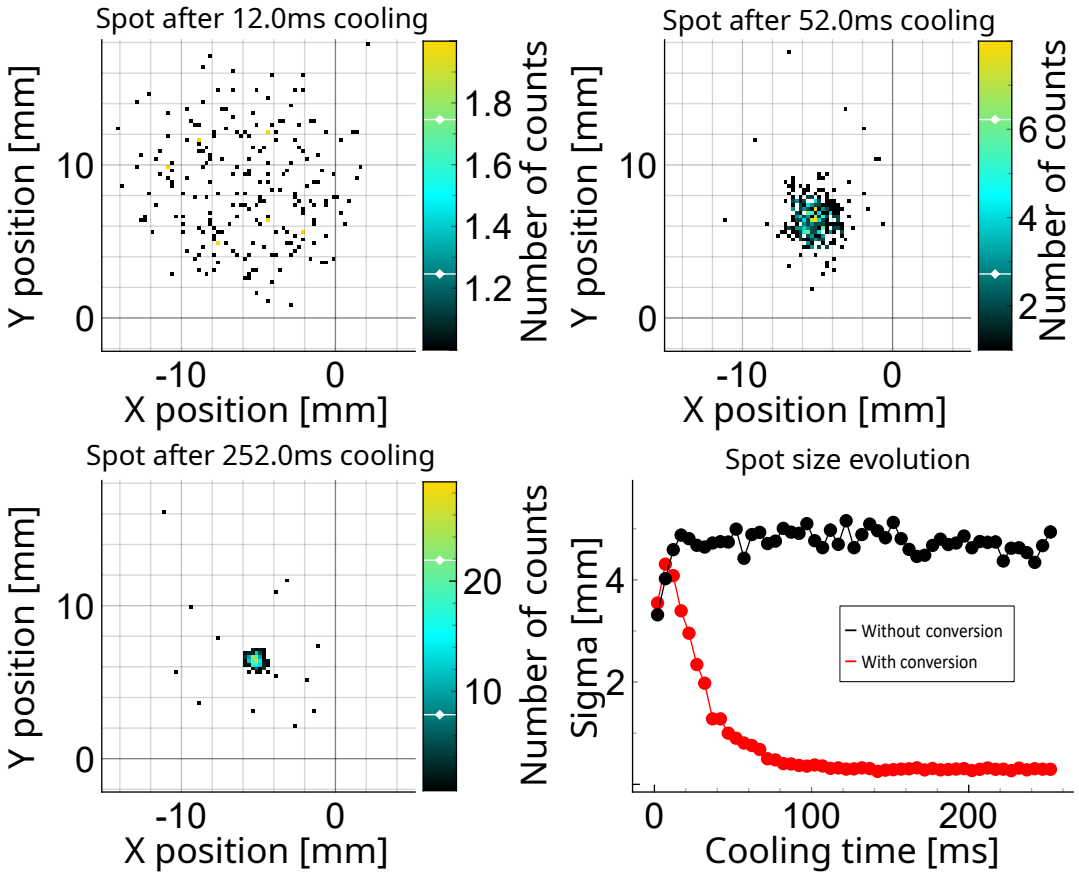

Figure 4.7: The top-left to bottom-left images show the ions' position projection for three different cooling times with conversion, and on the bottom right, the fitted size of the spot is shown as a function of cooling time with (red) and without (black) broadband cyclotron conversion. This scan was performed using 190 bunches for each cooling time.

- duration.

Contrary to what will be shown for the measurement trap, the phase is unimportant because the movements are well-damped beforehand. As detailed in section 2.1, it was shown that the frequency for this dipolar excitation can be considered independent of the ion mass and depends mainly on the trap potential, magnetic field strength, and trap dimensions. Since the trap dimensions are fixed, the trap potential rarely changes, and the effect of magnetic field drift on ν_- is minimal, this frequency can be considered constant as long as the trap potential remains unchanged.

The two other parameters to optimize, amplitude and duration, are linked and should be studied together. To reach a suitable radius (just beyond the diaphragm radius), a short excitation with a large amplitude will have the same effect as a longer excitation with a smaller amplitude. However, minimizing the total cycle time is still crucial. Therefore, the excitation time is set as short as possible, and the amplitude is optimized accordingly.

A scan will be performed around an estimated value to determine the frequency. When the frequency is incorrect, the ions pass through the diaphragm and reach the MCP. However, at the correct frequency, the ions will be decentered and unable to pass

through the diaphragm to the detector. Figure 4.8 shows the detector count rate as a function of frequency and amplitude. The graph indicates that at the resonance frequency (around 666 Hz), the count drops at lower amplitudes compared to the fringes. The fact that the number of cycles is the same for all the frequencies implies that the excitation duration for lower frequencies will be longer than the one for higher frequencies. Thus, the higher-frequency fringes appear broader, while the lower-frequency fringes are sharper. Another visible effect in this figure is that lower-frequency fringes are decentering the ions for higher amplitudes than the higher-frequency fringes. This is because the coupling card used for the excitations is a high-pass filter. Thus, lower frequencies are more attenuated than higher ones.

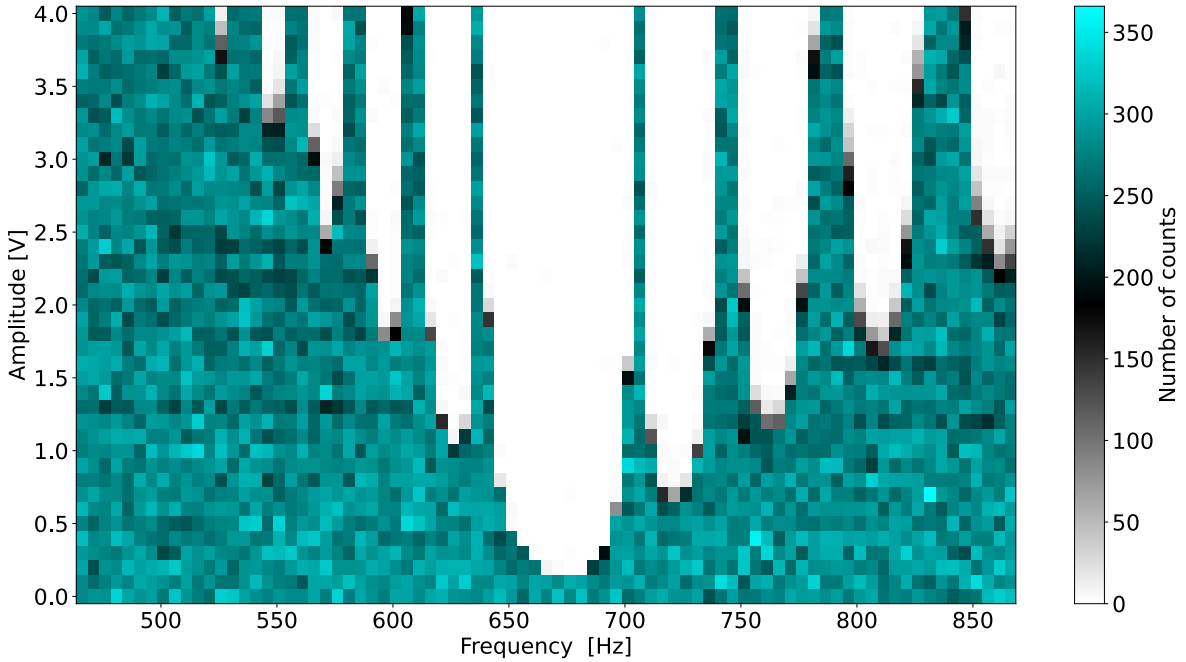

Figure 4.8: Number of counts over 110 bunches against excitation frequency and excitation amplitude. This scan was made by applying each excitation for 20 cycles (corresponding to 30 ms at the resonance frequency). The resonance is visible in the center, and the fringes are on the sides. The fact that fringes at higher frequencies are broader and more widely separated than the ones at lower frequencies is explained in the text.

Once the frequency is determined, the time will be chosen as short as possible while keeping in mind that the ions can still be excited at a larger radius than the diaphragm's. Our function generator is limited to 10 V excitation amplitude. To have a good range of amplitudes on the function generator while having a short cycle, the duration will be fixed at 3 ms ($\approx$ two whole periods), and the amplitude is the only parameter that will be left to optimize.

The scan shown in Figure 4.8 is usually not done to optimize the amplitude. Indeed, since the frequency does not significantly drift over time, we only need one vertical slice of this plot to select a suitable amplitude. These amplitude scans (usually done with

more steps) allow us to find the minimum amplitude required to move ions to a sufficient radius. This ensures they avoid passing through the diaphragm when the trap is opened. In most of the scans shown afterward, the excitation is applied at 6 V (this corresponds to 0.6 V amplitude in Figure 4.8) amplitude (for 3 ms at 666 Hz).

4.2.3 Cyclotron excitation optimization

Once the dipolar magnetron excitation has been applied, the ions would not pass through the diaphragm if released from the trap. Therefore, a quadrupolar excitation needs to be applied to selectively convert the ions of interest's (IoI's) motion (see pattern in Figure 2.6). The conversion of the magnetron motion into the cyclotron motion will be explained first.

The primary parameters for this excitation are frequency, amplitude, and duration. The frequency of the applied quadrupolar excitation is the cyclotron frequency. As established in section 2.1, this frequency depends on the mass of the ion of interest and the magnetic field. It was also shown in subsection 2.2 that the magnetic field strength is drifting over time. The cyclotron frequency, being very sensitive to the magnetic field, must be re-determined regularly. Additionally, as the cyclotron frequency is mass-dependent, the cyclotron frequency needs to be re-determined (or computed using the previously determined frequency) every time the IoI changes.

Figure 4.9 illustrates the ions' count as a function of the quadrupolar excitation frequency. This scan was performed for 500 ms excitation time and 1 V amplitude. It is clear that off-frequency, no recentering occurs, while on-frequency, the ions of interest pass through the diaphragm. The resolving power obtained for such a scan is $\frac{\nu_c}{\Delta\nu_c} \approx 2 \times 10^5$.

Once the frequency is roughly determined, optimization can begin. The excitation time is typically chosen based on the desired resolution, and the amplitude is adjusted to ensure that exactly one conversion occurs. Figure 4.10 shows amplitude scans conducted for different excitation times at the fixed frequency (in this case ν_c) and pressure (in this case 2×10^{-5} mbar). For each excitation time, the number of counts goes from zero (where the ions are not recentered) to a plateau (where the ions are recentered). A plateau is visible in our case because there is enough gas in the trap to completely cool all the IoI after the first conversion. Other shapes of amplitude scans are further detailed in [Rosenbusch 15]. The optimal amplitude is identified as the lowest amplitude within the plateau region. This amplitude ensures that only one conversion occurs, achieving optimal resolution (Additional details on these scans can be found in [Rosenbusch 15]). In stable ion sources during offline experiments, selectivity is not critical. Hence, excessively low amplitude is not imperative for our goals. Consequently, in most cases, large amplitudes with long excitation times are employed for subsequent studies to prioritize optimal ion cooling instead.

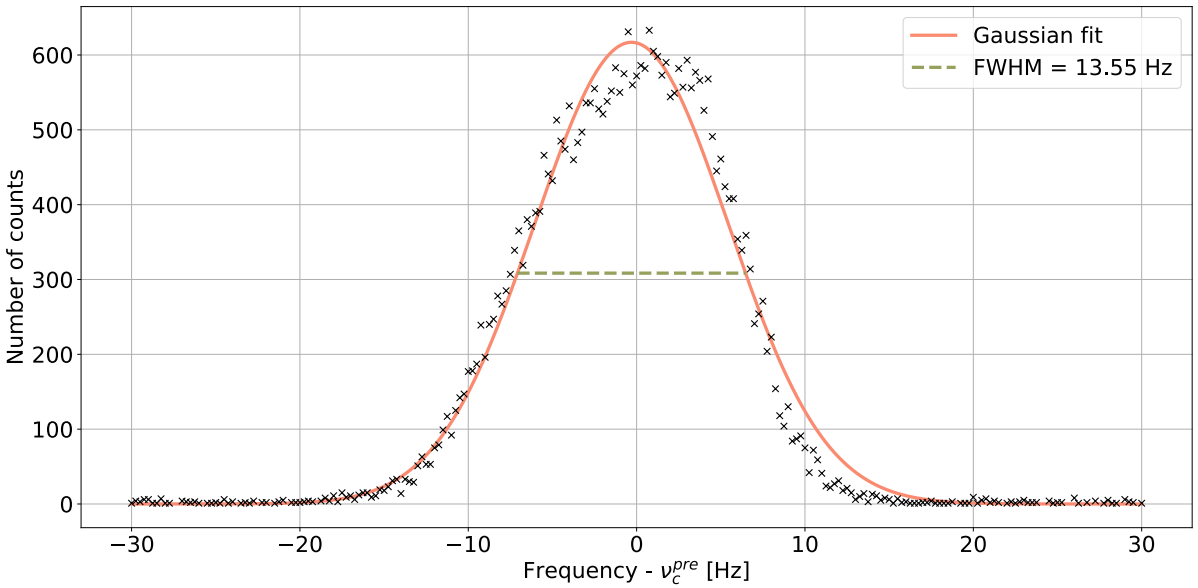

Figure 4.9: Number of counts on the MCP for 280 bunches against excitation frequencies around the ^{39}K cyclotron frequency. This scan, known as a cyclotron frequency scan, was performed with an excitation time of 500 ms and 1 V amplitude. It shows that, at frequencies far enough from ^{39}K cyclotron frequency, ions are not efficiently recentered and, hence, crash on the diaphragm when the extraction is performed. Conversely, at the correct frequency, ions pass through the diaphragm's hole. On the horizontal axis, "pre" in ν_c^{pre} stands for predicted. The salmon pink curve shows the result of the Gaussian fit performed. The resolving power obtained for such a scan is $\frac{\nu_c}{\Delta\nu_c} \approx 2 \times 10^5$.

Exciting at a slightly incorrect frequency requires a higher amplitude to recenter than exciting at the resonance frequency. Therefore, amplitude and frequency scans are typically performed iteratively for different excitation times until the expected resolution is reached. Once the frequency, amplitude, and excitation time are optimized, the buffer gas cooling technique is set up for a specific pressure. Reoptimizing excitation time and/or amplitude will be necessary each time the pressure is modified.

Adjusting the pressure will be a crucial step in future optimizations. Increasing the gas percentage can enhance cooling efficiency, reducing the cycle length. Since the half-life of the most exotic cases is typically comparable to the cycle duration, a shorter cycle allows more ions of interest to reach the measurement trap. However, reducing the gas percentage helps prevent excessive gas leakage into the measurement trap. Excessive leakage can dampen the cyclotron motion, which shortens the measurement time that can be used, thereby limiting the achievable precision for both the ToF-ICR and PI-ICR techniques (more details on the pressure effect on these techniques will be given in the following sections).

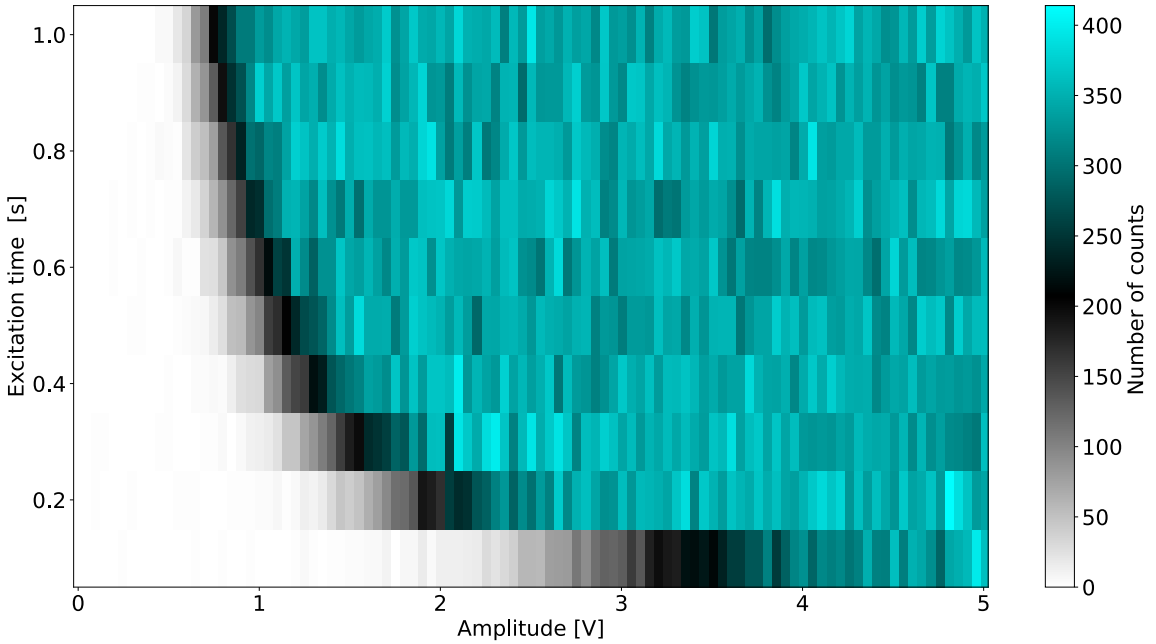

Figure 4.10: Number of counts on the MCP for 50 bunches against amplitudes and excitation times of the quadrupolar excitation applied at the ^{39}K cyclotron frequency with 2 % valve opening. The scan reveals three distinct regions for each excitation time: a low-amplitude region where ions are not recentered, a ramp-up region, and a plateau where ions are effectively recentered. Further details on these scans can be found in [Rosenbusch 15].

Summary

The ions were successfully trapped for the first time, allowing the study and optimization of ion cooling with buffer gas. The buffer gas cooling technique was implemented at PIPERADE for the first time, achieving a maximum resolving power of $\frac{\nu_c}{\Delta\nu_c} \approx 2 \times 10^5$ for 500 ms cycle length (at 2×10^{-5} mbar). Studies are still ongoing to further enhance the process to reduce the total cycle length and increase the number of ions purified per bunch. A smaller diaphragm opening will be crucial to work with higher pressure, thus reducing cooling times.

4.3 Measurement Trap

The following sections will detail the optimization of the ion transfer from the Purification Trap (PT) to the Measurement Trap (MT). The chapter will then focus on two main subjects: first, the optimization and characterization of the Time-of-Flight Ion Cyclotron Resonance (ToF-ICR) technique; and second, the set up and development of the Phase-Imaging Ion Cyclotron Resonance (PI-ICR) technique.

4.3.1 Transfer

Once the ions are cooled and the bunch purified in the first trap, transferring them to the second trap becomes a delicate and crucial step. Unlike in the purification trap, no gas is injected into the second trap, meaning there is no possibility of damping the ions' energy as effectively as before. This makes it imperative to transfer the ions in a way that minimizes any induced axial motion, as damping it afterward through excitations would take time. Therefore, careful control of the transfer process is essential to avoid adding unwanted energy to the system. Using the principles described earlier, the first trap's exit and the second trap's entrance are opened simultaneously for a specific duration and closed simultaneously at the optimal moment to impart minimal energy to the ions and preserve optimal initial conditions.

Figure 4.11 illustrates a scan of this transfer time, clearly showing that closing too early or too late gives different energy to the ions in the front or the back of the bunch, resulting in an increased Time-of-Flight (ToF) dispersion. This phenomenon observed in Figure 4.11 is expected and can be seen when simulating the transfer in SIMION as illustrated in Figure 4.12. These simulations model the two traps, the extraction, and the detector, including the gas pressure. In these simulations, ions are initially created in the center of the first trap, with the trap in a closed configuration, with a Gaussian distribution of 3 eV mean value and 1.5 eV full width at half maximum. They are then transferred to the second trap and, after several tens of microseconds of trapping time, directed toward the detector.

The left side of Figure 4.12 displays the mean position of the ion bunch at the time the second trap is closed, while the right side illustrates the ToF dispersion on the detector. Both sides use the same color code to visualize which position is associated with which dispersion. The simulations reveal an optimal transfer time when the ions are centered in the trap, providing insight into the ions' actual position at the second trap's closing time. In addition, associating a transfer time with a position allows one to understand the general trends of the plot. For instance, the fact that the dispersion increases for short and long transfer times is now clear as they correspond to positions where the ions will undergo very different potentials even if they are spatially close.

Although simulations provide an optimized transfer time, the actual time can differ slightly in practice, and the optimal value was not fully determined from the initial transfer scan. A more effective method to assess the ion energy in the trap is to examine the extraction time over one or two axial periods (typically around 5 μs to 6 μs in this setup). This approach helps evaluate the axial energy of the ions. To refine the transfer timing, both the transfer and extraction times of the second trap are scanned over one or two axial periods, allowing for the observation of ion bunch dispersion and axial energy.

Figure 4.13 presents a scan of the mean time of flight (ToF) for various transfer and extraction times. When the transfer time is not optimal, ions exhibit axial motion in the

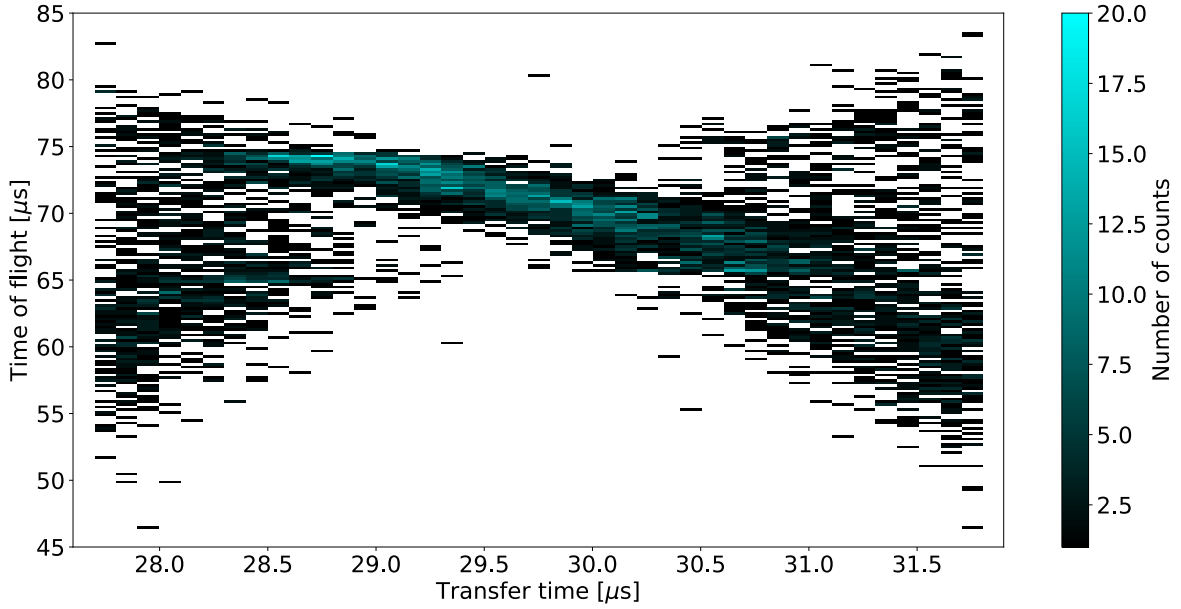

Figure 4.11: Time of flight of ions from the second trap to the detector as a function of the transfer time. The plot reveals three distinct regions. The bunch dispersion is increased in the first region, where the transfer time is too short. As the transfer time approaches the optimized value, the bunch dispersion reaches its minimum. In the final region, where the transfer time becomes excessively long, the ToF dispersion increases again. This scan was performed using 20 bunches for each transfer time.

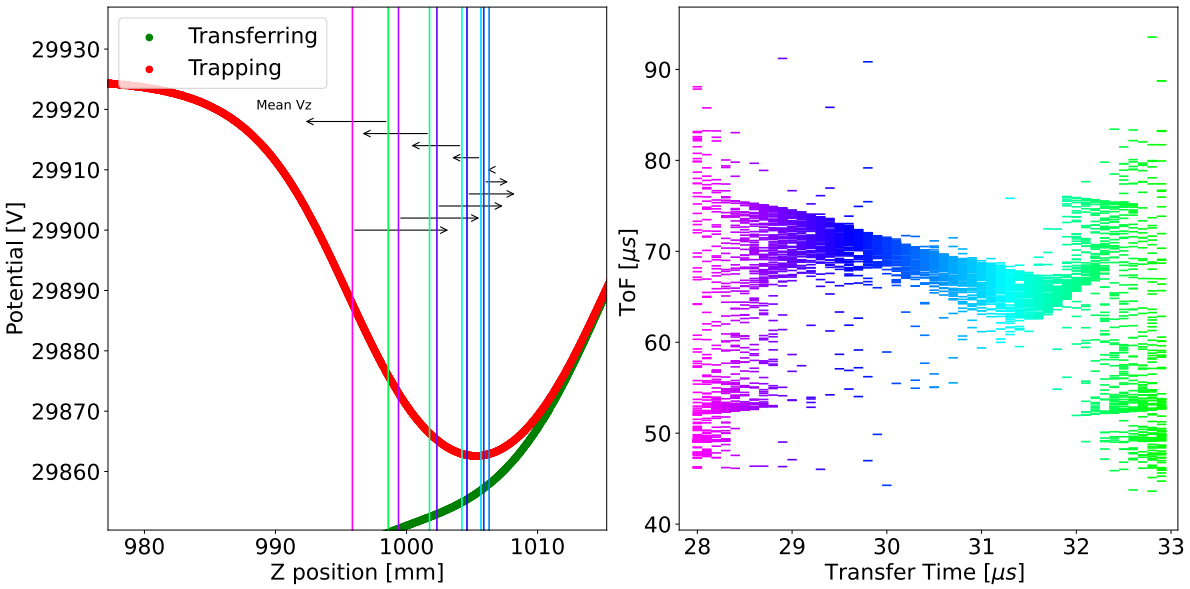

Figure 4.12: Left plot: Electric potential experienced by the ions as a function of their position along the beam axis. Vertical lines indicate the mean position of the ion bunch at the closing time, while arrows represent the mean velocity of the ions at this moment. Right plot: ToF of the ions as a function of the transfer time. The different colors in the left and right plots correspond to a given transfer time. This allows to have information on the position and velocity of the ions for each transfer time.

trap, leading to oscillations in the time of flight at the axial frequency, clearly visible in the plot. The variation in ToF reaches a minimum at 29.2 μs corresponding to the point where axial energy is minimized, indicating optimal transfer conditions.

Significant axial motion at the optimized transfer time may indicate insufficient cooling in the first trap or a suboptimal ring electrode potential. If the ring potential is set too high, the ions will never reach the trap's center, causing them to receive energy kicks regardless of the transfer timing. Conversely, if the ring potential is too low, the ions would still have axial energy after the trap is closed, regardless of the transfer time. In the scan shown in Figure 4.13, a residual axial motion was observed. Scanning the ring electrode potential revealed that −80.8 V provided a better result. However, further scans with shorter trapping times indicated that even with this new voltage, some axial motion persisted. This aspect remains under optimization, as reducing axial energy is crucial for improving the precision and accuracy of mass measurements.

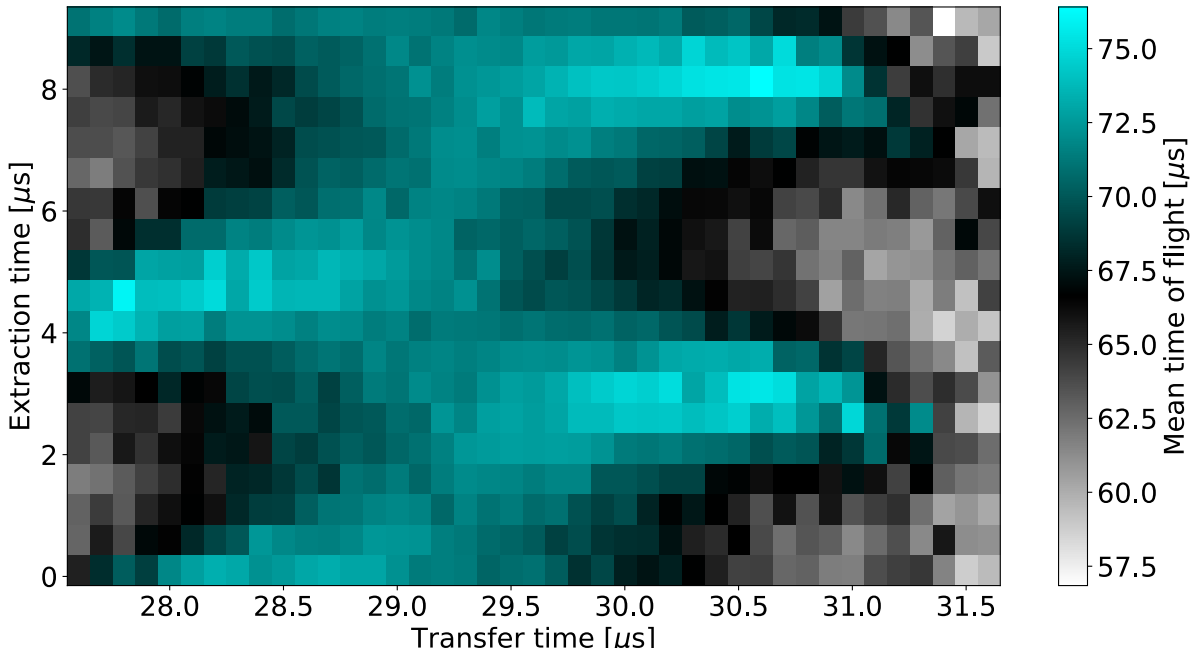

Figure 4.13: The mean ToF as a function of transfer and extraction times. The transfer time that minimizes fluctuations along the axial period is identified as the optimal value. In the plot, 29.2 μs appears to be the best choice for achieving this.

Measurement trap extraction

At the start of the PhD, a combination of extraction electrode potentials was empirically determined and allowed ions to reach the final detector. Later, during the optimization phase for the ToF-ICR method, the extraction process was fine-tuned to ensure that the kinetic energy of the ions is low when they arrive in the gradient zone so that the energy gain has a major effect on their ToF (see formula 2.35). The key principle was that the greater the time difference between ions with significant kinetic energy (on-

resonance) and those with minimal kinetic energy (off-resonance), the higher the precision of the ToF-ICR measurements. This time difference is referred to as the "ToF effect".

Table 4.2 lists the voltages applied to the extraction electrodes. Two configurations are presented: the first, as previously described, was optimized to maximize the ToF effect. The second configuration, intended for PI-ICR, is designed to preserve the relative positions of the ions both within the trap and on the final detector, ensuring their spatial arrangement remains unchanged. However, this configuration is not yet fully optimized for two main reasons: The first challenge is preventing the ions rotating at a large radius (potentially enhancing precision on mass determination) from approaching the extraction electrodes too closely. If this occurs, the ions nearer to the electrodes will experience greater deviation than the others. The second challenge lies in managing the focal point created by the 30kV-to-ground region, which can either overly disperse or focus the ions. This requires careful adjustment of the final extraction electrodes to ensure the image has the correct size.

Electrodes	ToF-ICR (V)	PI-ICR (V)	Electrodes	ToF-ICR (V)	PI-ICR (V)
Ext00	-90	-400	Out01	-145	-400
Ext01	-92	-400	Out02	-190	-1100
Ext02	-94	-400	Out03	-260	-1100
Ext03	-96	-400	Out04	-390	-2200
Ext04	-98	-400	Out05	-459	-1100
Ext05	-100	-400	Out06	-687	-700
Ext06	-104	-400	Out07	-1277	-2200
Ext07	-106	-400	Out08	-1390	-3830
Ext08	-108	-400	Out09	-2700	-3830
Ext09	-114	-400	Out10	-3500	-3000
Ext10	-120	-400			

Table 4.2: Extraction potentials for ToF-ICR and PI-ICR extractions. The potentials listed for ToF-ICR are optimized to ensure that the kinetic energy of the ions is low when they arrive in the gradient zone so that the energy gain has a major effect on their ToF, whereas those for PI-ICR are configured to enable a rapid extraction, allowing for a "snapshot" of the trap conditions.

Considerable effort has been invested during this PhD to identify effective parameter combinations for both ToF ICR and PI-ICR extractions. Nonetheless, it remains possible that alternative combinations could improve the ToF effect for ToF-ICR extraction and reduce image deformation for PI-ICR extraction. Note that new 3 kV power supplies will replace the actual 1 kV ones for these electrodes, allowing previously unreachable configurations.

Summary

The transfer of ions from the initial purification trap to the measurement trap was successfully accomplished for the first time. This process was investigated using Simion simulations and optimized through two-dimensional scans, aiming to minimize time-of-flight (ToF) dispersion and reduce the transmission of axial energy to the ions. These studies led to modifications to the ring potential and are still ongoing. Additionally, the extraction processes for both the TOF-ICR and PI-ICR techniques have been optimized.

4.3.2 ToF-ICR

Section 2.4.2 details the basic principles of the ToF-ICR technique. This section will now address the technical tests performed on PIPERADE. Figure 4.14 displays the time of flight (ToF) of the ions as a function of the frequency of a 100 ms quadrupolar excitation, illustrating a typical ToF-ICR measurement. The precision of the cyclotron frequency determination relies on fitting the ToF-ICR resonance curve.

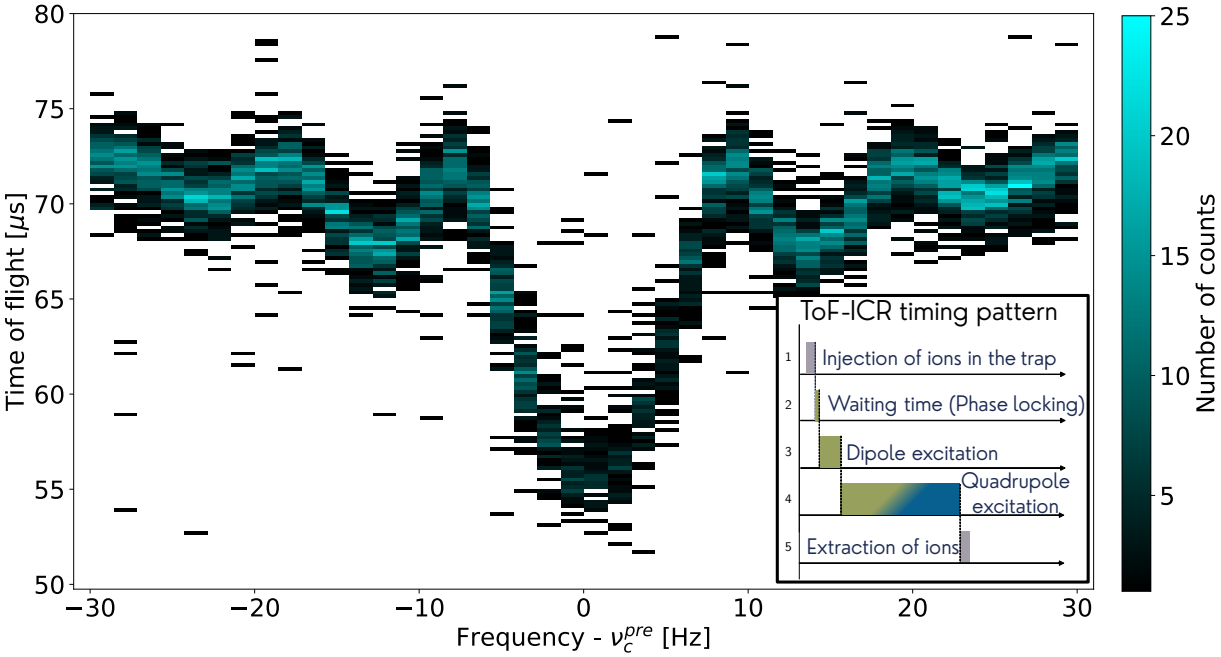

Figure 4.14: Time of flight of ions as a function of the excitation frequency around the predicted cyclotron frequency (ν_c^{pre}), known as a ToF-ICR scan. This measurement was conducted with an excitation time of 100 ms. The frequency associated with the shortest ToF is the cyclotron frequency. This scan was performed using 20 bunches for each frequency.

General setup of the technique

As illustrated in the timing pattern of Figure 4.14, two excitations are required for this technique. It was explained earlier that the duration and amplitude of RF excitations are interrelated. For a given amplitude optimized at a specific time, if the excitation time changes by a factor C_{excit}, the amplitude needs to be adjusted by a factor $C_{amp} = 1/C_{excit}$. Therefore, the key to effective optimization is generally to fix the duration and optimize the amplitude accordingly.

- For the magnetron motion, a very short time is chosen, and the amplitude is adjusted based on the number of ions and the trap size.
- For the conversion, the time is selected according to the desired precision of the measurement, and the amplitude is then adapted to the defined parameters.

Before calibrating the excitations, the first step is to accurately determine the magnetron frequency ν_- in the second trap; the ions can be sent back to the first trap before extracting them directly. Using the diaphragm, this method enables a straightforward frequency scan, similar to the example in Figure 4.8.

However, another type of scan that requires a simpler timing pattern can be carried out. Nevertheless, such a scan requires knowing ν_c in advance. A dipolar excitation, during which the excitation frequency is scanned across the expected range of ν_-, will be followed by a broadband conversion. When the excitation frequency matches ν_-, the ions acquire maximum radial energy after conversion, resulting in a shorter ToF towards the detector as they pass through the magnetic field gradient. The results of such a scan, with a 100 ms excitation time, are presented in Figure 4.15. The magnetron frequency found in the second trap is 6715 Hz.

After determining the frequency, optimization of amplitude can start. Figure 4.16 shows the result of a dipolar amplitude scan. Ions were excited at ν_- for 10 ms and then converted with a broadband excitation at ν_c. At first glance, increasing the magnetron excitation amplitude may seem to improve ion acceleration continuously (and consequently, ToF-effect). However, an excessively high excitation amplitude results in fewer ions reaching the detector (which could be attributed to a non-optimized extraction optics). Therefore, a compromise must be found. In addition, as will be discussed later, higher radial energies can also reduce the accuracy of the measurements, making it crucial to balance the excitation amplitude carefully. In most of the results displayed below, an excitation time of 10 ms with an amplitude of 4 V was used.

One crucial aspect must be addressed before delving further into the details of the ToF-ICR technique. A common issue in many Penning traps is that the traps may not be perfectly aligned with the magnetic field axis. Even a slight misalignment can induce an initial magnetron motion to the ions within the second trap. Consequently, the dipolar

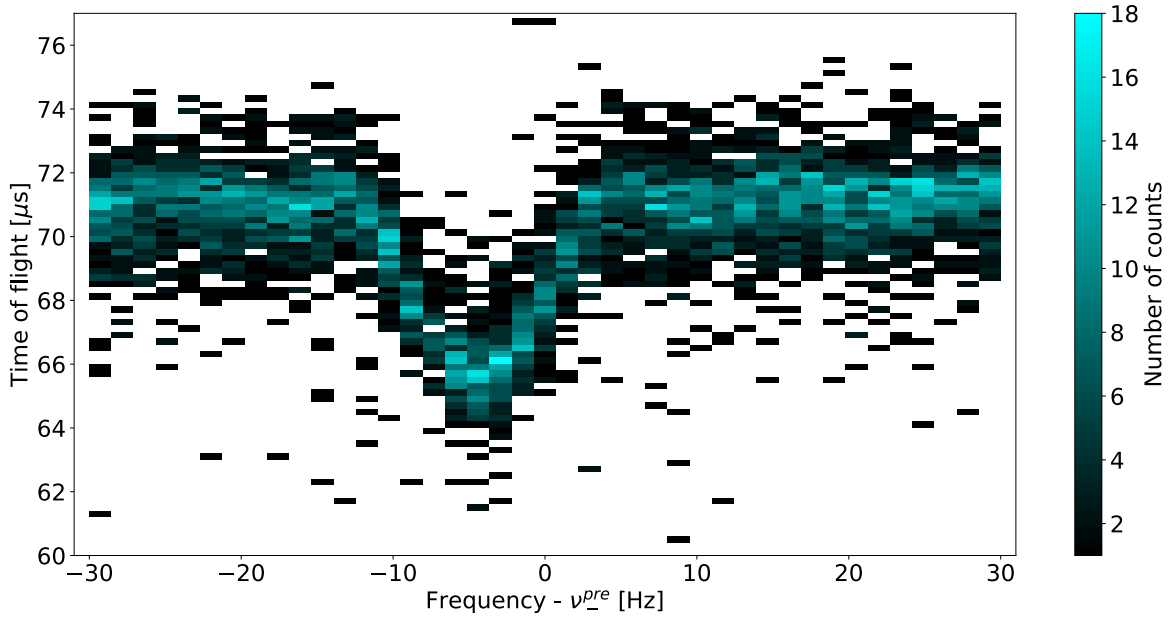

Figure 4.15: Time of flight (ToF) of ions as a function of the excitation frequency around the predicted magnetron frequency (ν_-^{pre}). A distinct resonance is observed when the ions' magnetron rotation radius is amplified, leading to a corresponding increase in radial energy conversion. The frequency associated with the shortest ToF is the correct magnetron frequency. This scan was performed using 20 bunches for each frequency.

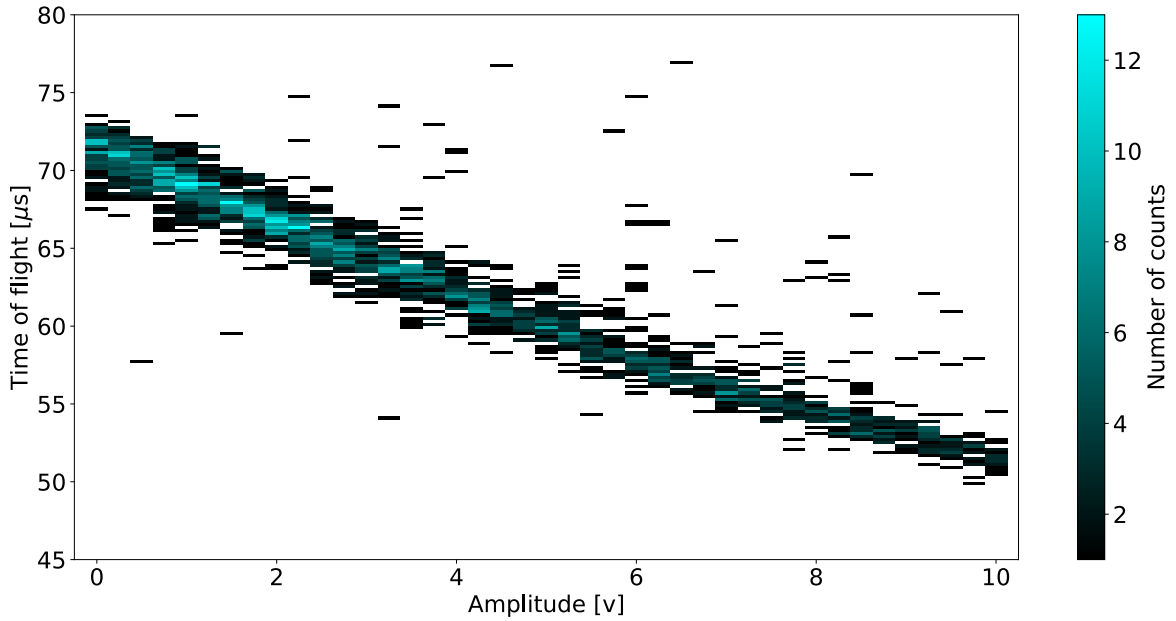

Figure 4.16: Time of flight as a function of the dipolar excitation amplitude at the magnetron frequency. As the dipolar excitation amplitude increases, the ions are accelerated due to the subsequent conversion at ν_c. This scan was performed using 10 bunches for each amplitude.

magnetron excitation must be synchronized with this initial motion. The duration of the waiting time before the excitation (phase locking step in the pattern of Figure 4.14) was

scanned over two magnetron periods (each period being 150 μs). Scanning this duration means scanning the phase in which the ions will be at the beginning of the excitation. The result of this scan is shown in Figure 4.17[2]. An increase in the mean ToF, indicative of a reduction in the ToF effect, is observed when the magnetron excitation is initiated out of phase with the initial motion, compared to when both are in phase. When the excitation is out of phase, the resulting rotation radius of the ions is smaller, whereas in-phase excitation results in a larger orbit. This variation in orbit size leads to differences in ToF because the conversion from magnetron motion to cyclotron motion imparts radial energy to the ions. As the ions travel through the magnetic field, this radial energy is transformed into axial energy, ultimately affecting the mean ToF observed. Although this misalignment is not a significant problem, adjustments to the excitation's phase and amplitude are required to amplify or dampen the motion accordingly.

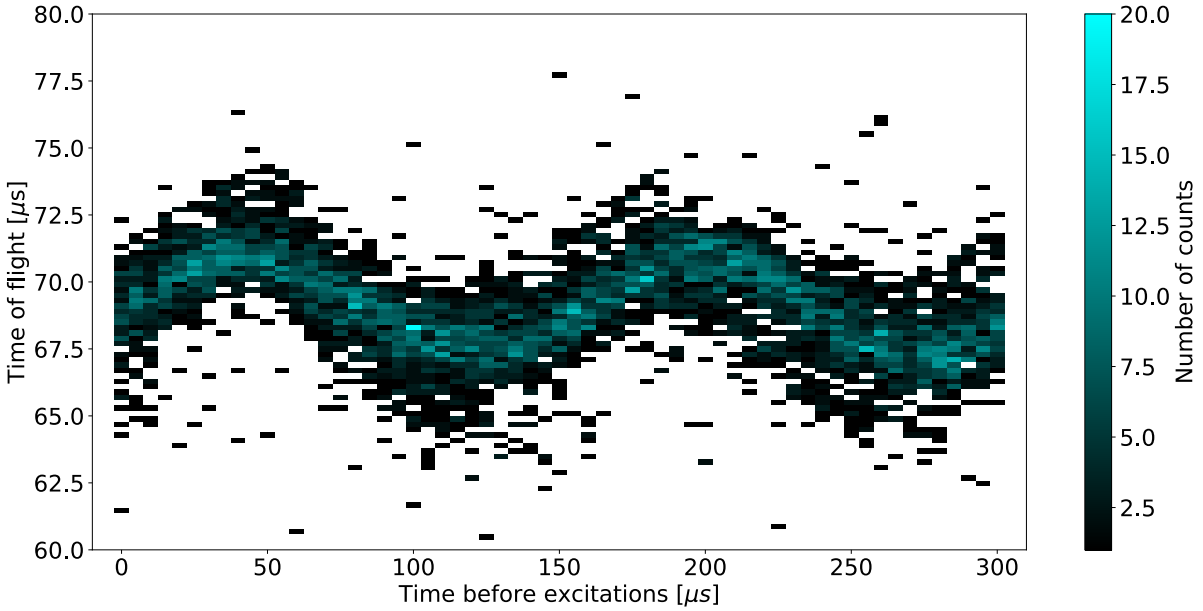

Figure 4.17: Ions' time of flight as a function of the beginning of the magnetron excitation over two magnetron periods (each period being 150 μs). A quadrupolar excitation at ν_c is applied after the dipolar excitation, which will translate any difference in radius by a difference in ToF. This scan was performed using 60 bunches for each time before excitations.

After the phase is locked and the dipolar excitation is optimized, the amplitude optimization for the quadrupolar excitation can be performed. Figure 4.18 shows a scan of the ToF as a function of this amplitude. The time of flight of the ions shows the periodic conversion between the two radial motions. The ToF is long at lower amplitudes because the ions are spinning at ν_- when extracted from the trap. As the conversion efficiency increases, the ToF decreases until it reaches a minimum (ions spin at ν_+). If the amplitude is increased further, the conversion efficiency decreases as the fixed duration of the

[2]This excitation is once again followed by a broad-band conversion at ν_c

excitation now represents more than half the conversion period, resulting in an increasing magnetron motion at the end of the conversion. This cycle repeats, and it will be shown later that achieving only one complete conversion is optimal.

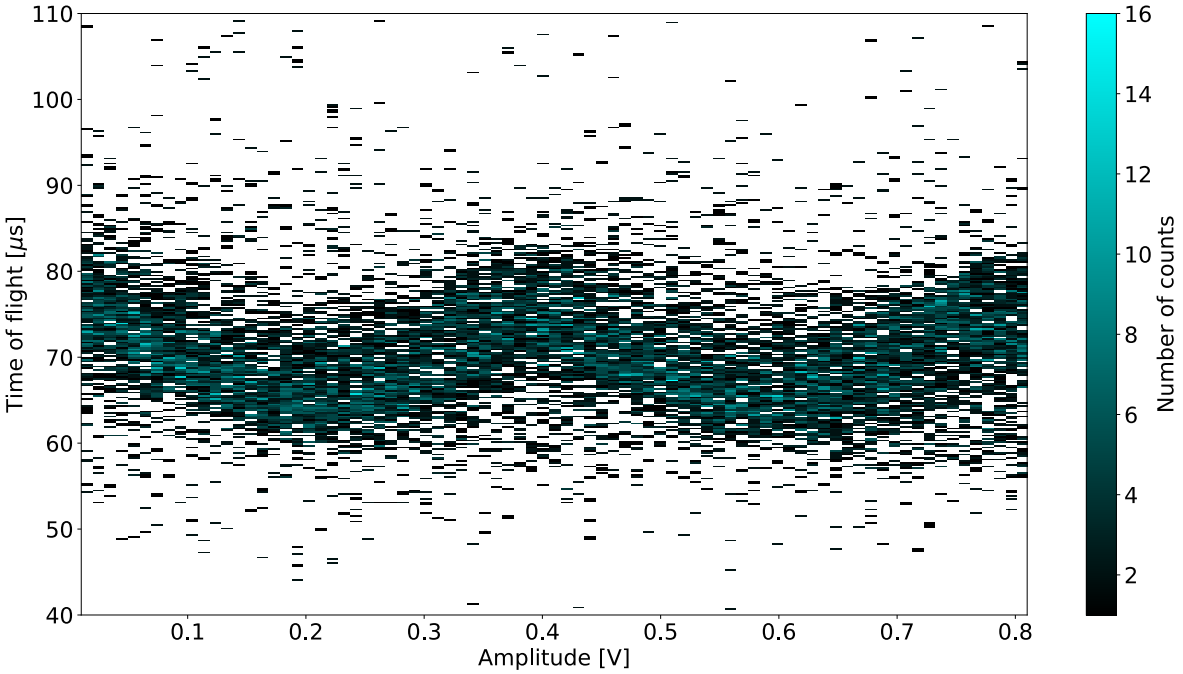

Figure 4.18: Time of flight as a function of the quadrupolar excitation amplitude at the cyclotron frequency. The ions are accelerated due to the dipolar excitation at ν_- applied before the quadrupolar excitation. The optimized value seems to be 0.2 V. This scan was performed using 20 bunches for each amplitude.

ToF-ICR fit

The general explanation of the ToF-ICR technique focused primarily on maximizing the ToF effect to help the fit process converge successfully. However, the goal is to obtain a precise and reliable frequency, which is not always guaranteed by a stronger ToF effect.

A program was developed (and implemented in PTSD afterward) based on an existing program from Jyväskylä called PyMasScanner to perform these fits and extract the frequency. Performing the fit, with equation 2.36 that is reminded below, requires a map of the magnetic and electrical fields along the axis.

$$T(\omega_{rf}) = \int_{z_0}^{z_{max}} \sqrt{\frac{m}{2(E_0 - qV(z) - \mu(\omega_{rf})B(z))}} dz \tag{4.3}$$

Fast calculation while maintaining good precision is achieved by splitting the extraction into 10 to 20 regions, approximating the electrical field as constant in each of them, and fitting the magnetic field with a second-degree polynomial.

To benchmark the program, ISOLTRAP data for ^{39}K, ^{85}Rb, and ^{133}Cs were fitted with their program (EVA using minuit as a fitting routine) and compared to the results

obtained from PTSD (using LMFIT: Non-Linear Least-Squares Minimization and Curve-Fitting for Python). Figure 4.19 shows the fit with PTSD on ISOLTRAP data for ^{133}Cs on the left and the frequency differences fitted by the two programs on the right. A clear agreement is visible for all three masses, indicating that PTSD is reliable for ToF-ICR resonance fits.

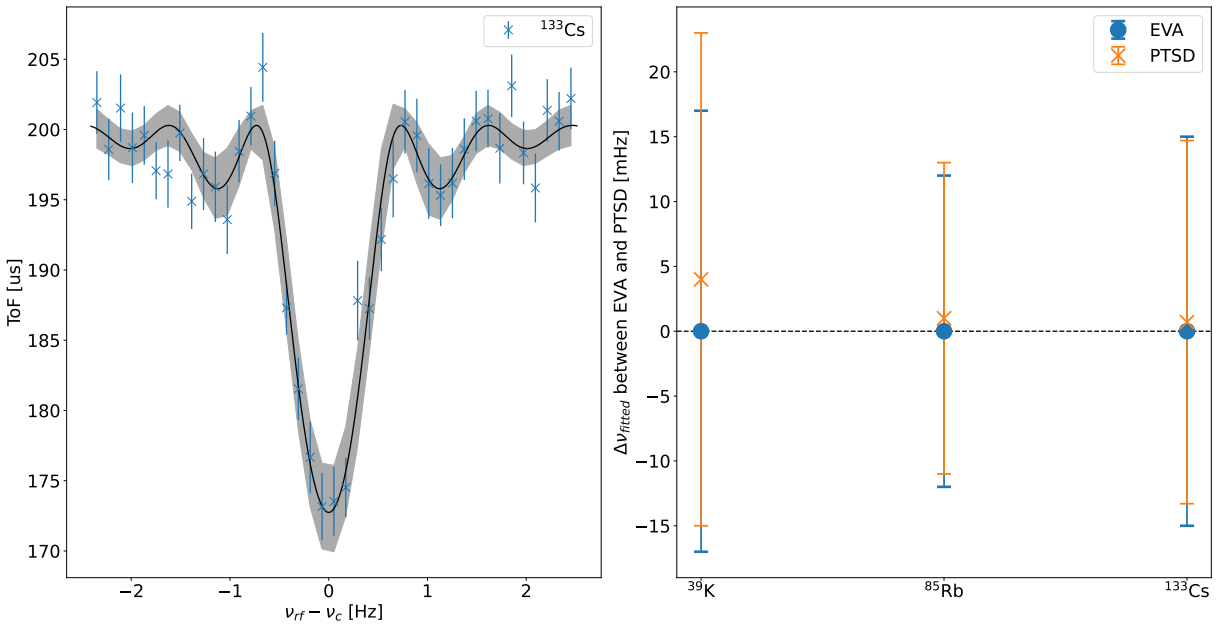

Figure 4.19: The left part displays the fit with PTSD on ISOLTRAP data for ^{133}Cs. The right part shows the difference in the fitted frequencies from the two different programs for ^{39}K, ^{85}Rb, and ^{133}Cs.

The effects of different parameters are then examined in more detail. Figure 4.20 illustrates the impact of four key parameters: initial magnetron radius, pressure, number of conversions, all of those three affecting the $\mu(\omega_{rf})$ function, and axial energy E_0 in the formula 4.3.

- A larger initial magnetron radius results in a deeper resonance curve but increases sensitivity to pressure, field imperfections, and extraction efficiency. This is illustrated in Figure 4.16, where both the ToF-effect and the number of counts are shown. Additionally, it is further examined in Figure 4.22 in terms of accuracy and precision.

- Lower pressure leads to a significantly deeper resonance that will reduce uncertainty. Future optimizations of this parameter are discussed below.

- Axial energy primarily influences the ToF-ICR offset, but if the volume enclosing the ion trajectory in the trap becomes excessively large, it can lead to frequency shifts due to the presence of magnetic field inhomogeneities and electrical field anharmonicities. Axial energy can be minimized by optimizing the transfer (see Section 4.3.2).

- The number of conversions determines the overall shape of the fringes and the central peak, with one conversion being optimal for achieving high precision. The number of conversions is fixed to one by selecting the first dip in the quadrupolar excitation amplitude scan.

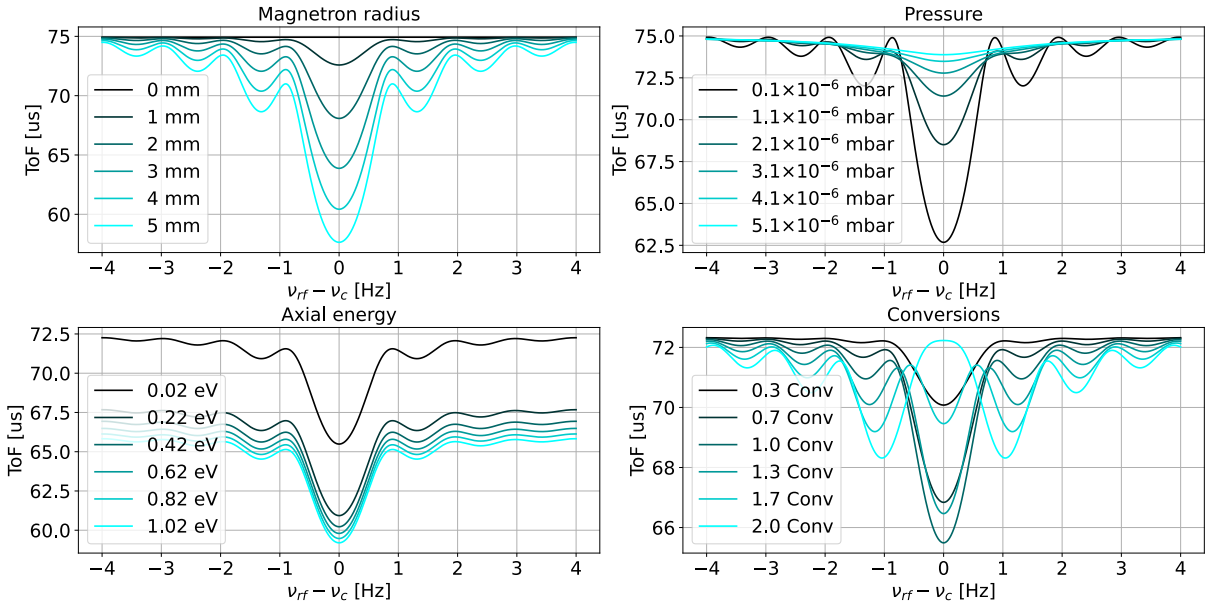

Figure 4.20: Impact of 1 s ToF-ICR fit parameter values on the resonances. The black curves indicate low values, while the cyan ones represent high values. The top-left panel shows the effect of the initial magnetron radius. The top-right panel illustrates the impact of pressure. The bottom-left panel depicts the effect of the ions' axial energy. Finally, the bottom-right panel represents the number of conversions from magnetron to cyclotron.

These fits offer a practical way to determine the pressure inside the trap. By analyzing the results of the fit, the pressure can be accurately estimated, providing insight into the cooling conditions and optimizing the experimental setup. Figure 4.21 shows pressure coming from ToF-ICR fits with 1 s excitation time at 2 %, 4 %, and 6 %. The plot shows that the pressure variation in MT is significantly smaller than in PT, which is expected given the differences in gas flow dynamics between the two traps. As mentioned earlier, reducing the diaphragm opening is essential to improve cooling efficiency, particularly in PT, where higher gas pressure is required to shorten the cycle time. Currently, the diaphragm has a diameter of 2 mm, but it will be replaced with a smaller diaphragm of 1 mm, which would allow us to increase the valve opening percentage for PT while allowing to reach lower pressure in MT. Since the gas flow scales with the cube of the radius, this reduction would result in a pressure around 1.2×10^{-7} mbar at 6 % valve opening, improving the overall cycle duration. The expected benefits of this change can be seen in Figure 4.20.

The last parameter to optimize is the magnetron radius in terms of accuracy and precision instead of the ToF effect. To achieve this, multiple scans with 100 ms excitation time

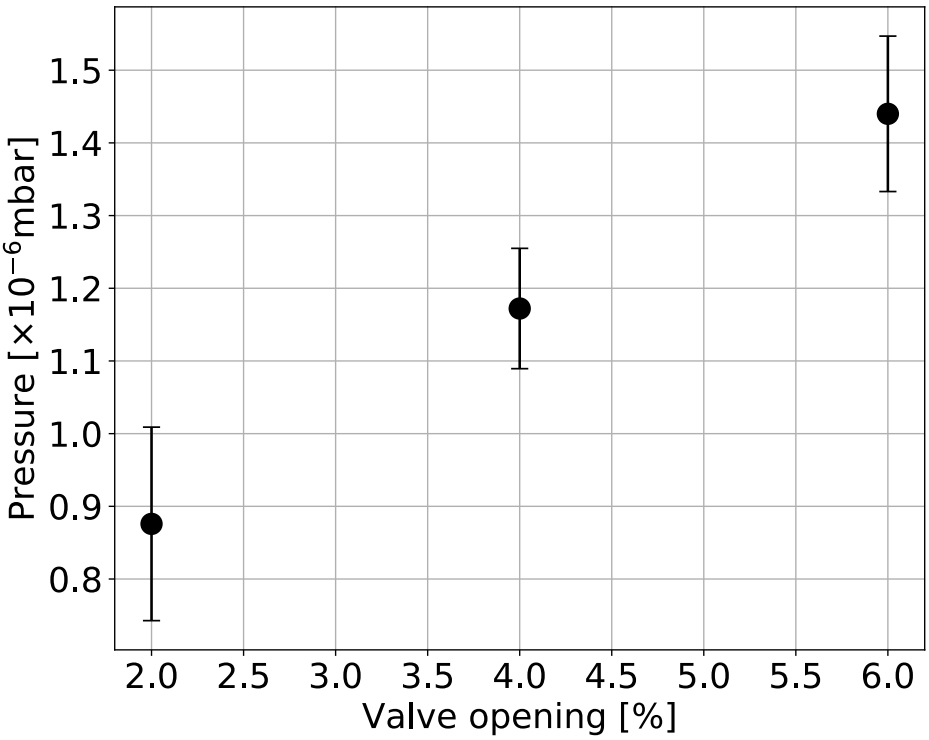

Figure 4.21: Pressure determined from the ToF-ICR resonance fit as a function of the valve opening in the first trap. These pressures were extracted for 1 s ToF-ICR fits.

were performed for different magnetron amplitudes to study the effect on the measured frequency, which is shown in Figure 4.22. A significant uncertainty is observed at a low radius due to a small ToF effect. Note that this uncertainty goes lower as we go between 2 V and 6 V. Beyond this range, the fitted frequency starts to deviate from the stable value, and the uncertainty grows again because the ions are now reaching regions where the homogeneity of the magnetic field gets poor and/or the electrical field diverges from an ideal quadrupole's.

Mass measurements

As explained previously, the ion mass m can be determined via the direct measurement of the cyclotron frequency ν_c following the relation:

$$\nu_c = \frac{|q|B}{2\pi m} \tag{4.4}$$

For singly-charged ions, it is clear that the determination of the mass will depend on the precise determination of the frequency and the magnetic field strength. To achieve this, the cyclotron frequency ν_c of a well-known reference ion is measured both before and after the measurement of the ion of interest. This allows us to determine the magnetic field B at two distinct times. The magnetic field at the moment of the ion of interest's

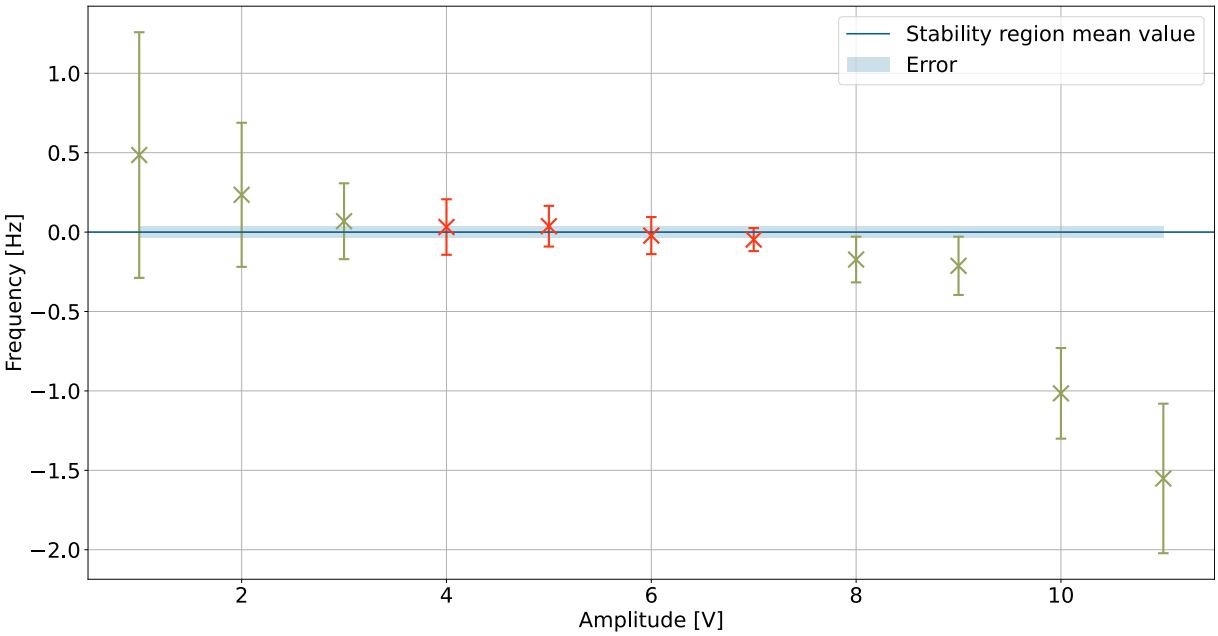

Figure 4.22: Cyclotron frequency determined from ToF-ICR fits from 100 ms ToF-ICR scans with different dipolar excitation amplitudes (which is directly linked to the initial magnetron radius). A mean frequency value was computed using the four red points.

measurement is then determined by interpolating between these two reference points. The interpolation ensures that any drift in the magnetic field is accounted for, allowing for an accurate determination of the mass. The linear interpolation of the magnetic field B at the moment of the measurement of the ion of interest is performed using the equation:

$$B(t_{IoI}) = B(t_{ref_1}) + \frac{B(t_{ref_2}) - B(t_{ref_1})}{t_{ref_2} - t_{ref_1}} \cdot (t_{IoI} - t_{ref_1}) \tag{4.5}$$

where $B(t_{IoI})$ is the magnetic field at the time t_{IoI} of the measurement of the ion of interest, and $B(t_{ref_1})$ and $B(t_{ref_2})$ are the magnetic fields determined at times t_{ref_1} and t_{ref_2} from the cyclotron frequencies of reference ions measured before and after the ion of interest. This linear interpolation is an approximation that only accounts for linear drift, while non-linear fluctuations, such as the ambient pressure and temperature effect, are also present. The impact of this approximation on the measurement precision will be assessed in future studies. Finally, the standard way to access the mass is by using frequency ratios. The mass value is easily derived from those when the mass of the reference is well-known. If the reference ion has a mass m_{ref}, the atomic mass of the species of interest m_{meas}, neglecting the binding energy of the electron removed from the atom to form the IoI, is:

$$m_{\text{meas}} = r \times (m_{\text{ref}} - m_e) + m_e \tag{4.6}$$

where m_e is the mass of an electron and r is the measured cyclotron frequency ratio $\frac{\nu_{c,\text{ref}}}{\nu_{c,\text{meas}}}$. The uncertainty on the mass is defined as (neglecting the uncertainty in m_e):

$$\Delta(m_{\text{meas}}) = \sqrt{(\Delta r)^2(m_{\text{ref}} - m_e)^2 + (\Delta m_{\text{ref}})^2 r^2} \tag{4.7}$$

Figure 4.23 presents two separate mass measurements of ^{41}K using ^{39}K as a reference. The first measurement uses a 100 ms excitation time, while the second uses 1 s. The improvement in precision from the first to the second measurement is evident, consistent with the fact that precision should be inversely proportional to conversion time (as explained in Section 2.4.2). Note that the uncertainty displayed is only statistical (computed as in equation 4.7); a precise study of systematic errors was initiated during this PhD and will be presented shortly, although a complete systematic study is still ongoing.

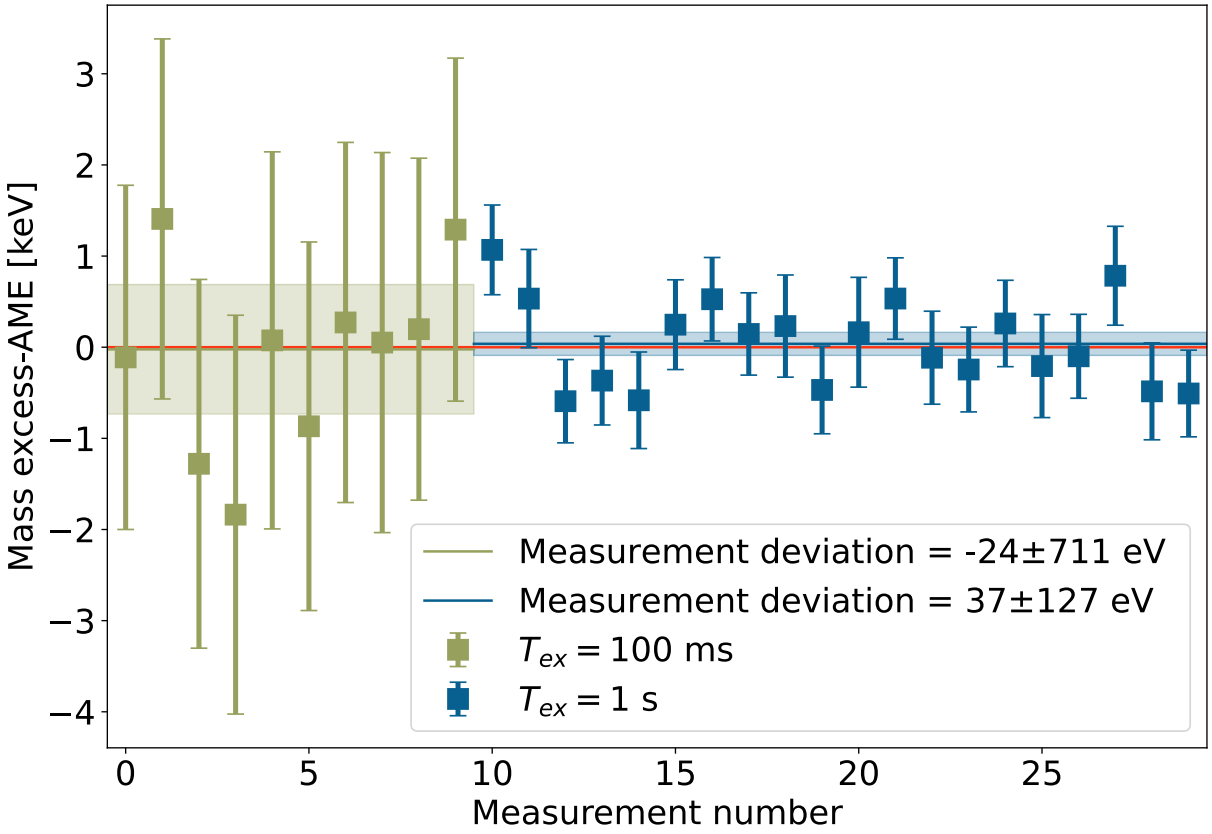

Figure 4.23: Difference in mass excess between the experiment and the AME 2020 [Huang 21]. Comparison of mass measurements for 100 ms and 1 s durations using ^{39}K as a reference for ^{41}K. The figure shows the mass measurement accuracy and precision differences between the two excitation times.

Magnetic field studies

As explained in the previous section, the mass was measured using the cyclotron frequency and the magnetic field strength. In addition, it was shown in section 2.2 that magnetic field inhomogeneities would induce shifts in the measured frequency. Therefore, the precise determination of the magnetic field value is critical for measurement accuracy and precision. In the following, the impact of magnetic field inhomogeneities and temporal

fluctuations on the precision of cyclotron frequency measurements will be examined.

For the homogeneity, as discussed in Section 2.2, shimming was performed early in PIPERADE's operation and has not been updated since. As explained, ions with different axial energies will experience different trapping regions. Additionally, if the magnetic field was homogeneous in the trapping region, the measured cyclotron frequency would not depend on the axial energy of the ions. Therefore, to probe the effectiveness of the shimming, ToF-ICR scans performed with ions of different axial energy can be used to detect inhomogeneities. The transfer time is scanned over a small region to have ions with different energies, and for each transfer time, a ToF-ICR fit is performed. The result of such a scan is displayed in Figure 4.24. A 500 ms excitation was chosen as it provided a good balance between achieving precise frequency measurements and minimizing the effect of pressure. Indeed, if the reduced cyclotron motion is damped, and thus the ToF effect is reduced, the resonance will be too difficult to fit, even with a small amount of axial energy. At the level of precision we could reach, the magnetic field seems relatively homogeneous. Nevertheless, further systematic studies with different excitation times and finer transfer time steps are required for optimization.

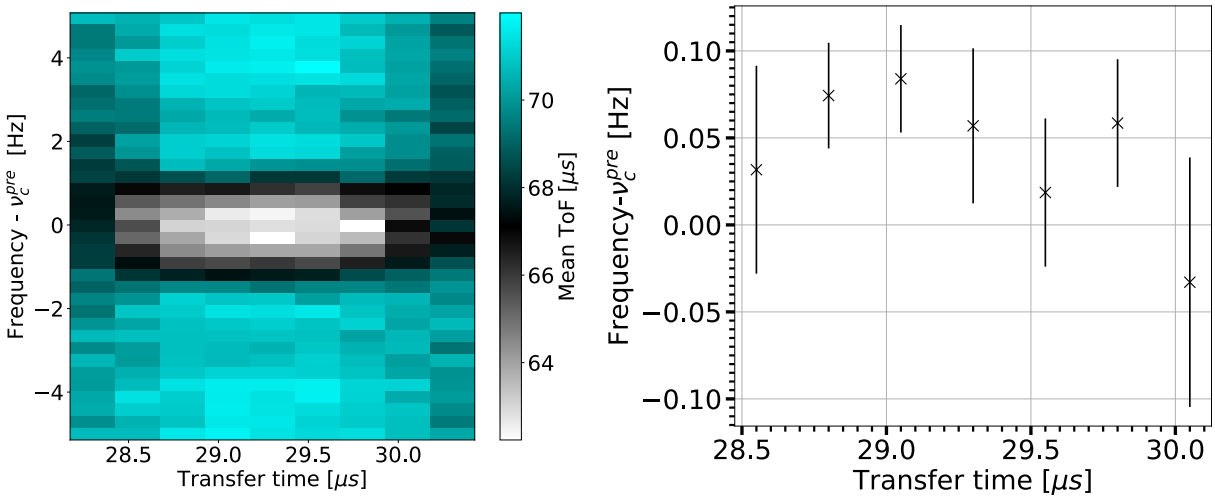

Figure 4.24: The left plot represents the mean ToF as a function of the transfer time and excitation frequency. The right one displays fitted ν_c values for each transfer time of the left plot. These ToF-ICRs were measured with 500 ms excitation time. The left plot has two more points than the right one, as the first and last transfer times ToF effect was too small, and the fit could not converge to a consistent value.

In order to probe long-term fluctuations of the magnetic field, multiple 100 ms ToF-ICR of ^{39}K scans were conducted over six days, which are shown in Figure 4.25. The plot also shows a tentative fit with a linear drift component and a sinusoidal oscillation. The parameter c reflects the general drift of the magnet, with a drift rate of 0.006(2) Hz/day which is equivalent to 2.18(73) ppb/day (performed with the compensating coil mentioned in section 2.2). The sinusoidal component roughly approximates daily temperature and pressure variations. This scan underscores the need for precise temperature control in

the future DESIR experimental hall and pressure regulation in the magnet helium vessel. In future studies, a precise measurement of temperature and pressure along such a measurement could allow for a better estimation of the drift.

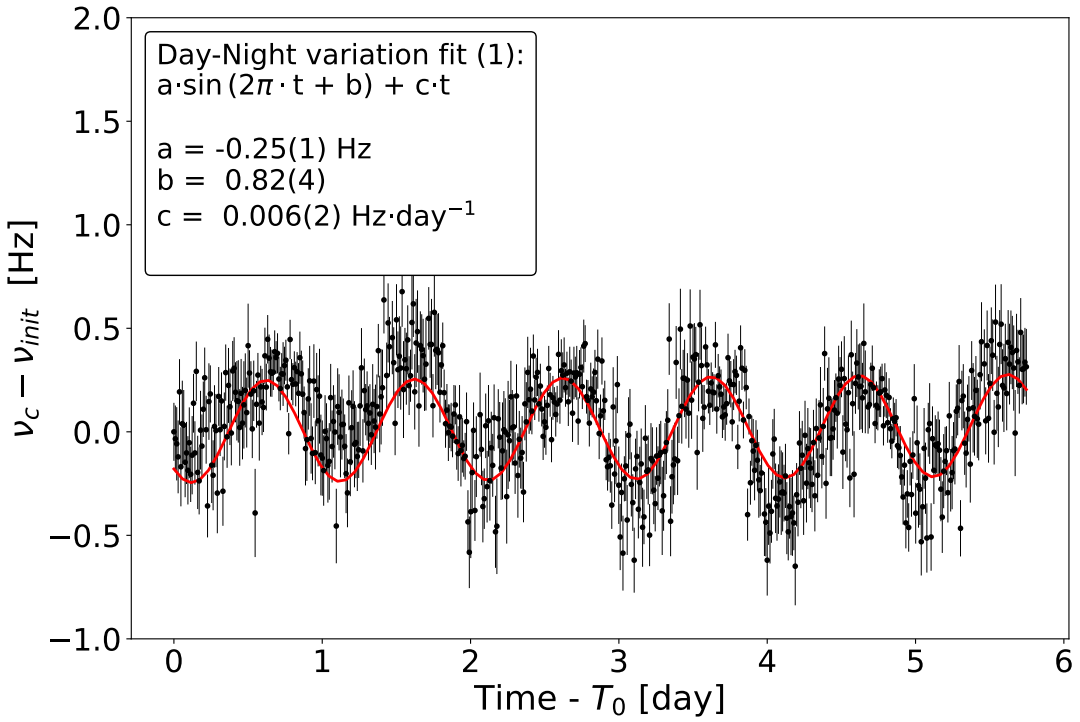

Figure 4.25: Fitted ν_c values from ToF-ICR scans conducted over six days. Although measurements over such an extended period are typically unnecessary for estimating the magnetic field error, this data was collected to monitor the frequency's behavior over time. This approach allowed us to observe the sensitivity of the frequency to temperature and pressure variations. The red curve represents a fitting attempt to model day/night temperature fluctuations with a sinusoidal function.

In the usual case of a mass measurement, the magnetic field value is interpolated using two ToF-ICRs performed before and after the one of the reference nuclei. Two reference measurements must be performed for each mass measurement, and the time interval between these two references directly impacts the precision of the actual mass determination (see equation 4.5). To estimate the additional error induced by the linear interpolation on the frequency determination precision, a systematic study was performed using the data collected over these six days.

A real measurement process is simulated by taking three measurement files, the first and the third for reference and the intermediate one for the ion of interest. A frequency value is interpolated from the references and compared to the measured value in order to obtain the difference ΔB. The whole 6 days of data are treated like this, and a distribution of $\Delta B/B$ for different $\Delta T (= t_{ref_2} - t_{ref_1}$ see equation 4.5) is obtained (see insert of Figure 4.26).

Finally, the standard deviations of the different distributions as a function of time interval are obtained as shown in Figure 4.26. It shows that the standard deviation increases as a function of the time difference. However, after 9 h, it seems that the standard deviation increases with a steeper trend. This is probably due to the day/night effect that is visible in Figure 4.25, making the linear interpolation less valid for larger time differences. Therefore, the only points used for the linear fit in red are the ones before the black dotted line. This linear fit allows for the determination of standard deviation of $\Delta B/B$ ($\sigma(\Delta B/B)$ over time. In our case, the standard deviation will evolve at a rate of 3.1×10^{-11} per minute of difference between reference measurements. For online experiments, measurement times can range from hours to days, while reference measurements take minutes. Therefore, performing a reference measurement every 2 to 3 hours (or even more often) is not excessively time-consuming. Consequently, the uncertainty due to magnetic field value linear interpolation will be not more than 5.6×10^{-9} after 3 hours difference between reference measurements. Nevertheless, this value should be reduced with the stabilization of temperature and pressure mentioned in section 2.2.

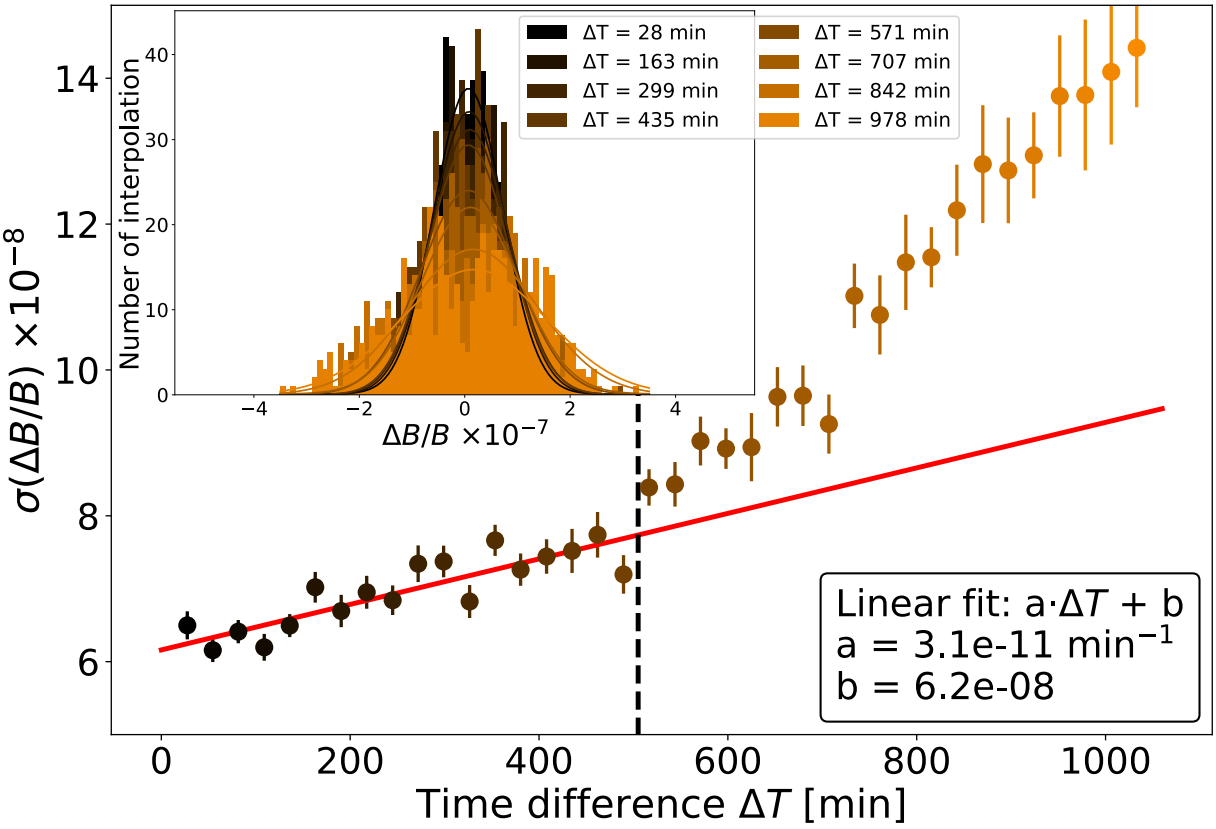

Figure 4.26: Standard deviation of the histograms in the insert as a function of the time difference. In the insert are plotted distributions of $\Delta B/B$ for different ΔT. A linear fit is displayed in red. This fit uses only the points before the black dotted line.

Electrical field studies

Section 2.2 emphasized the importance of generating as harmonic an electric field as possible (see equation 2.21). The voltages applied to the correction electrodes can be adjusted to improve the harmonicity. A useful way to probe anharmonicities is by increasing the ions' axial energy, allowing them to explore a larger trap region. The magnetic field optimization was performed first to ensure that B and thus ν_c are constant along the axial direction of the trap. Consequently, the variation of ν_+ is directly related to the electric field via V_0 with the approximation $\nu_+ = \nu_c - \frac{V_0}{4\pi B d^2}$ [Beck 09]. Therefore, by adjusting the ion transfer time, ν_+ can be measured at different axial energy levels to detect frequency shifts due to these anharmonicities.

To measure the modified cyclotron frequency ν_+, a frequency scan using a dipolar excitation can be performed. Exciting the ions at this frequency imparts sufficient energy to induce a measurable change in their ToF. The results of this scan are shown in Figure 4.27. Then, by fitting with an inverted Gaussian curve the mean ToF evolution over frequency, the modified cyclotron frequency ν_+ is determined.

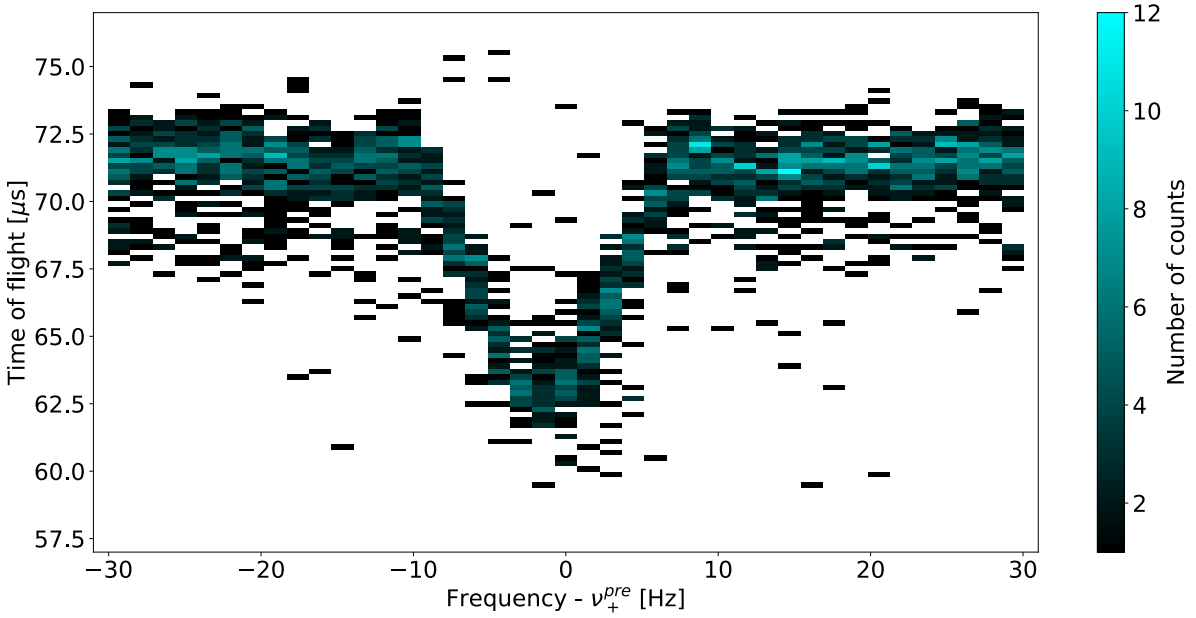

Figure 4.27: ToF of ions as a function of excitation frequency around the predicted reduced cyclotron frequency (ν_+^{pre}). A clear resonance is observed when the reduced cyclotron rotation radius is amplified. The frequency associated with the shortest ToF is the correct reduced cyclotron frequency. This scan was performed using 10 bunches for each frequency.

This process is then repeated for various transfer times and three correction electrode voltages to assess the influence of axial energy and electric field anharmonicities. The objective is to find the correction electrode potential that minimizes any dependency of ν_+ on the transfer time, ensuring the most harmonic electric field possible. Figure 4.28 illustrates this, with the top plot showing three curves corresponding to different correction

electrode voltages, where each point represents the central value from a ν_+ frequency scan performed at a given transfer time. A polynomial fit is then performed for each correction electrode voltage, allowing a more precise determination of frequency differences between optimized and non-optimized transfer times. The plot below shows the difference between the resonance ν_+ frequencies obtained for optimized transfer time (30.097 µs) and 29.2 µs for the three curves. A linear fit provides the extrapolated optimized correction electrode value. Anharmonicity-related uncertainties in mass measurements could be minimized by using this correction electrode value. Several other curves of this kind were generated; however, they are not shown here because measurements over too wide an interval result in frequency shifts, making the graph difficult to interpret. Nonetheless, the differences observed are consistent with the plot presented below.

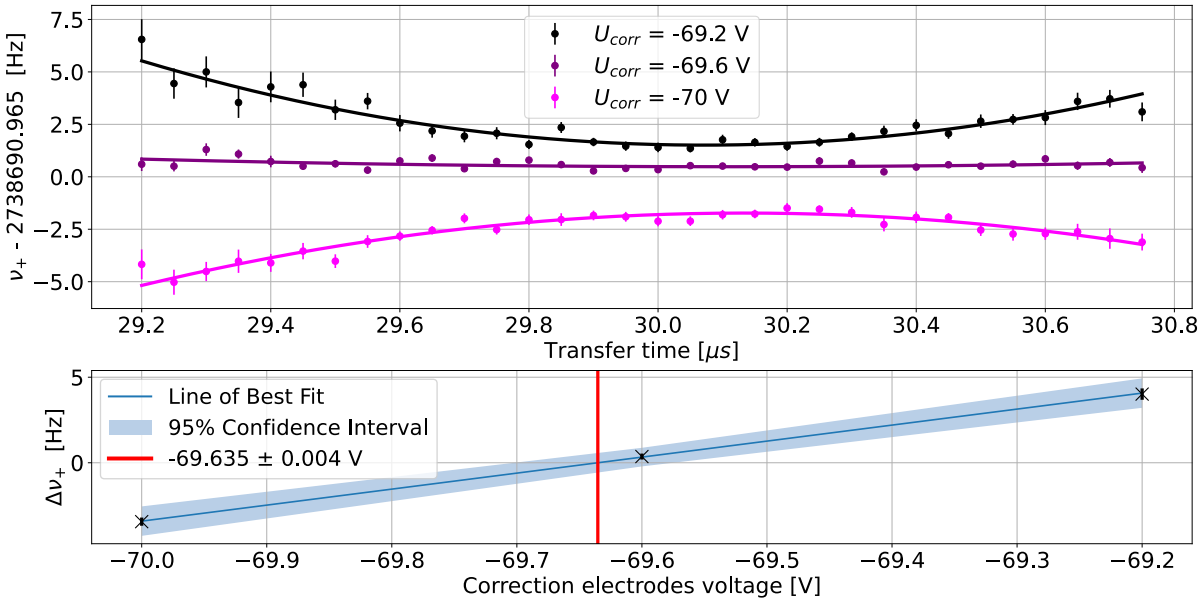

Figure 4.28: The top panel shows the results of three series of ν_+ frequency scans conducted at various transfer times, with adjustments made to the correction electrode voltage for each series. The bottom panel displays the difference between the resonance ν_+ frequencies obtained for the optimized transfer time of 30.097 µs and 29.2 µs. The red line represents the intersection point of the linear fit with the $\Delta\nu_+ = 0$ line.

Summary

The ToF-ICR technique was successfully implemented on PIPERADE for the first time. A dedicated program was developed to scan frequencies and fit the ToF-ICRs. First mass measurements were conducted using excitation times of 100 ms and 1 s. It was shown that the future reduction of the diaphragm size will greatly improve the ToF effect. Additionally, a magnetic field study was initiated, and the correction electrodes were optimized to improve the harmonicity of the electric field. Determining systematic errors for PIPERADE is ongoing and must be revisited when the trap is moved to GANIL. A study on the mass-dependent errors, as well as the count rate-dependent errors, still needs to be conducted.

4.3.3 PI-ICR

As for the ToF-ICR technique, the PI-ICR technique was not implemented on PIPERADE at the beginning of this PhD. The successful implementation of the PI-ICR technique required several essential modifications to the experimental setup to obtain exploitable images. One of the most significant changes was installing and characterizing a new position-sensitive detector (detailed in Chapter 3), which was crucial for accurately tracking the ions' positions. Additionally, the voltages applied to the extraction electrodes had to be carefully adjusted to ensure optimal extraction conditions (values are visible in Table 4.2). In this section, we present the results of the scans needed to implement the PI-ICR technique.

As explained in chapter 2, the frequency measurement in this technique is made using this formula:

$$\nu_c = \frac{\phi_c + 2\pi n_c}{2\pi t_{acc}} \tag{4.8}$$

with ϕ_c the angle between the center, the magnetron spot, and the cyclotron spot, t_{acc} the accumulation time, and n_c represent the addition of the number of turns made by ions rotating at ν_+ during the accumulation time, with the turns made by ions rotating at ν_- during the same period. Thus, the uncertainty is defined as:

$$\Delta\nu_c = \frac{\Delta\phi_c}{2\pi t_{acc}} = \frac{\Delta r}{\pi r t_{acc}\sqrt{N}} \tag{4.9}$$

with Δr being the size of the spot, r being the distance of the spot from the center, and N being the number of ions in the spot. This formula underscores the necessity of positioning the ions at a greater distance from the center while minimizing the spot size. At the same time ions cannot be excited too far from the center to avoid effects due to field imperfections. During the implementation of this technique, efforts have been made to optimize this arrangement to reduce the final uncertainty.

General setup of PI-ICR

It was shown before, when the ions enter the second trap, they are not perfectly at the trap center (see Figure 4.17). With the imaging of the ion bunch in the trap, we can now visualize this. The left panel of Figure 4.29 shows the ions' locations on the position-sensitive detector for five different extraction times evenly spaced over one magnetron period. This plot illustrates that the ions are orbiting around the trap's center due to initial magnetron motion, which poses a problem for accurate mass measurements and must be damped. A dipolar excitation at the magnetron frequency is applied in phase opposition to the motion in order to dampen it.

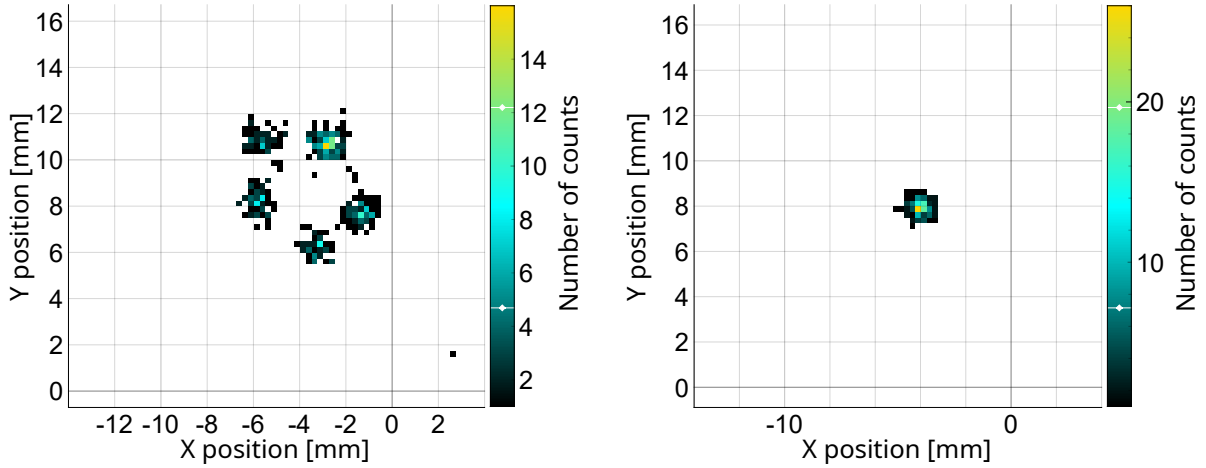

Figure 4.29: Ions' positions for various extraction times over a magnetron period. On the left, the 5 phases are displayed before the magnetron damping and on the right, after the damping. Both scans were performed using 20 bunches for each phase.

The five extraction phases are overlapped on the right part of Figure 4.29, showing that the initial magnetron motion is well-damped. The position of this spot will be used as the projection of the trap center onto the detector plane. Note that the position is not centered at (0,0) on our detector, likely due to misalignments. The latter could be between the trap and the magnetic field, the extraction tower and the beam axis, or even the MCP relative to the beam axis. However, it is not a real issue for the first tests of the PI-ICR technique, but it will need to be re-aligned so that the entire detector surface can be used. Additionally, such misalignments can generate deformation in the image of the ion position in the trap, as aberrations are typically stronger near the edge of the detector.

Once the ions are correctly centered, optimizing the steps presented in Figure 2.11 can start. The ν_+ dipolar excitation will be performed to increase the rotation radius of the ions. However, unlike magnetron motion, the phase of the ions cannot be visualized for the reduced cyclotron frequency because the reduced cyclotron period is smaller than the ToF dispersion (typically by an order of magnitude). As a result, instead of forming a single spot, the ions will be uniformly distributed around the trap center at the rotation

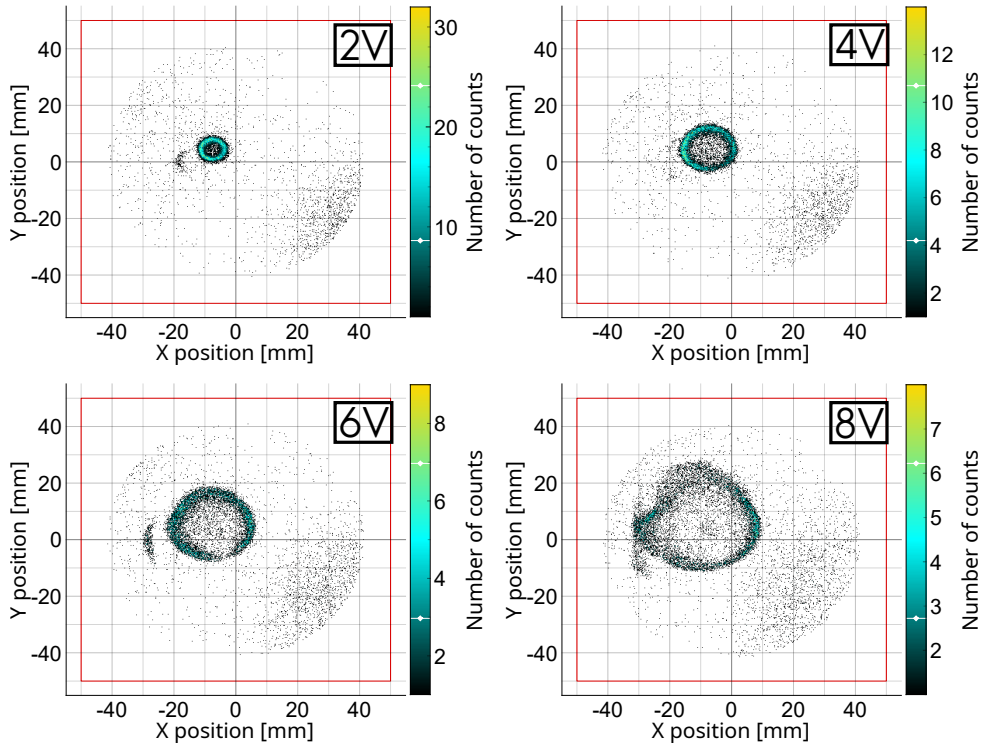

Figure 4.30: Projection of the cyclotron motion for four different excitation amplitudes, ranging from 2 V in the top left to 8 V in the bottom right, for a dipolar excitation applied at ν_+. During this measurement, the MCP image reconstruction was suboptimal, leading to significant ion misplacement, particularly in the bottom right of the image, with a noticeable vertical line of counts in the middle left part. Despite these issues, it is evident that lower amplitudes produce a nice circular ring, while higher amplitudes cause deformation. This scan was performed using 8000 bunches for each amplitude.

radius, creating a visible ring. In Figure 4.30, different excitation amplitudes were used. The "rings" are visible, with some strange artifacts on the image. Firstly, the efficiency drops in the 3^{rd} quadrant around (-5,-5), and it is more visible on the bottom left image (already explained in section 3.4). Secondly, the smaller radius rings seem circular, whereas the higher ones seem deformed. As mentioned earlier, this can be due to an imperfect alignment in the extraction tower, causing aberrations. Strong deviations of the ions' trajectory have indeed been observed in SIMION simulations when they are too close to the electrodes.

After that, the motion radius is excited with a broad-band cyclotron excitation; converting the reduced cyclotron motion to a magnetron one with a quadrupolar excitation at ν_c. The projection on the detector plane, following the application of quadrupolar excitations at various amplitudes, is illustrated in Figure 4.31. This illustrates the conversion of reduced cyclotron motion identified by the ring projection into the magnetron motion identified by the spot. This spot must be as small and far from the center as possible. The spot size and distance optimization are directly linked to the optimizations presented in section 4.3.2. As the ions rotate at the ν_+ frequency, their increasing orbit radius

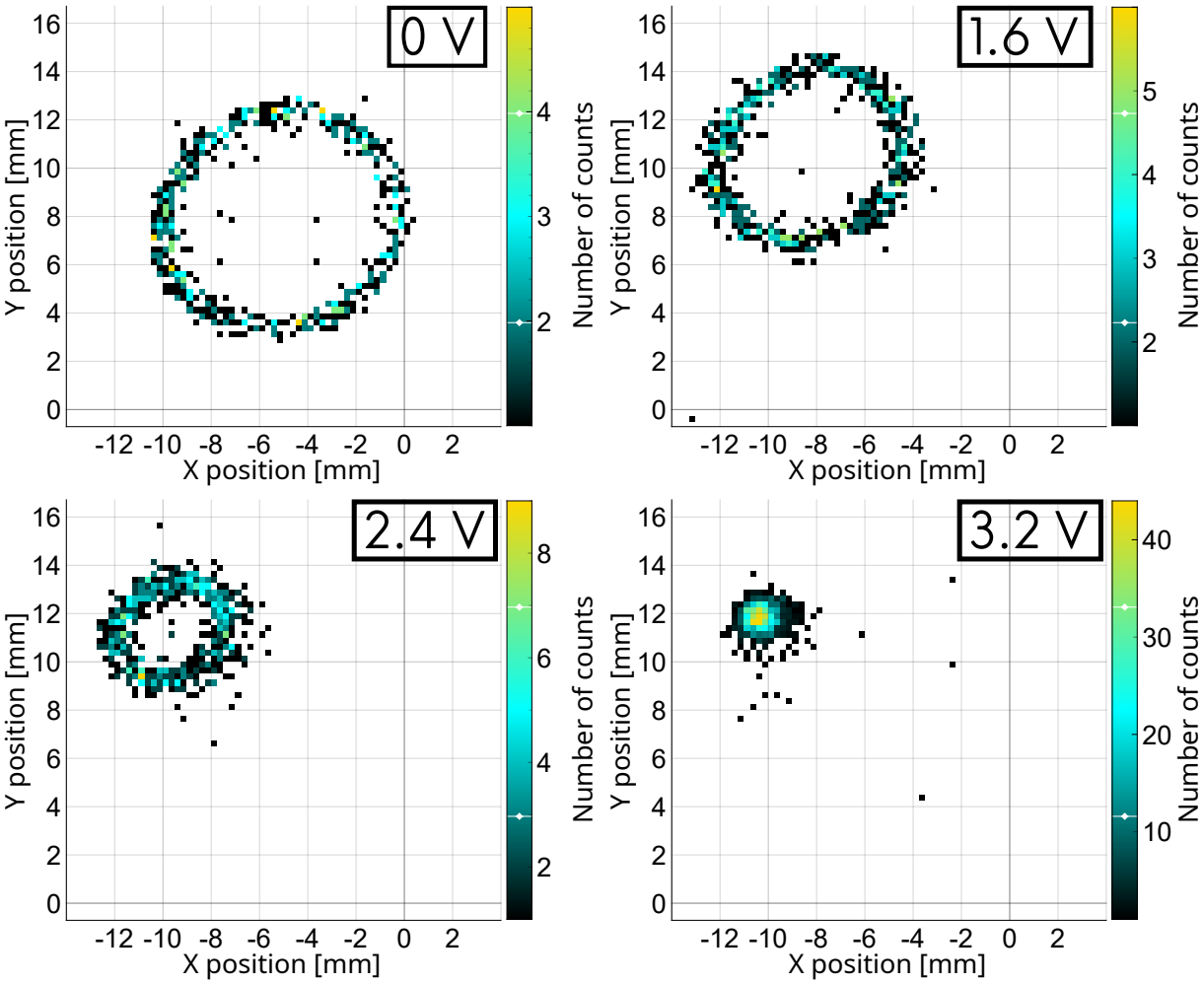

Figure 4.31: Projection of the ions for four different conversion amplitudes, ranging from 0 V in the top left to 3.2 V in the bottom right, for a quadrupolar excitation applied at ν_c. This scan was performed using 300 bunches for each time before excitations.

makes them progressively more sensitive to pressure and electrical field anharmonicities. This heightened sensitivity manifests as a larger spot size after conversion, potentially accompanied by a decrease in the count rate.

After numerous optimizations, the first PI-ICR measurement with a 100 ms accumulation time was successfully performed on PIPERADE. Figure 4.32 shows two images displaying the three spots required for phase shift measurement. On the left is the 100 ms PI-ICR, and shortly after, a 1 s accumulation time measurement was performed, as shown on the right. For the 1 s PI-ICR, the center, and magnetron spots are well-defined, but the third spot, corresponding to the cyclotron spot, is significantly larger. This larger size is likely due to either electric field anharmonicities or excessively high pressure, the respective impact of those being still under investigation.

After these optimizations, the first PI-ICR mass measurement could be performed on PIPERADE. A 100 ms accumulation time was chosen as a compromise between the achievable precision and the ease of getting a well-defined spot image. This measurement

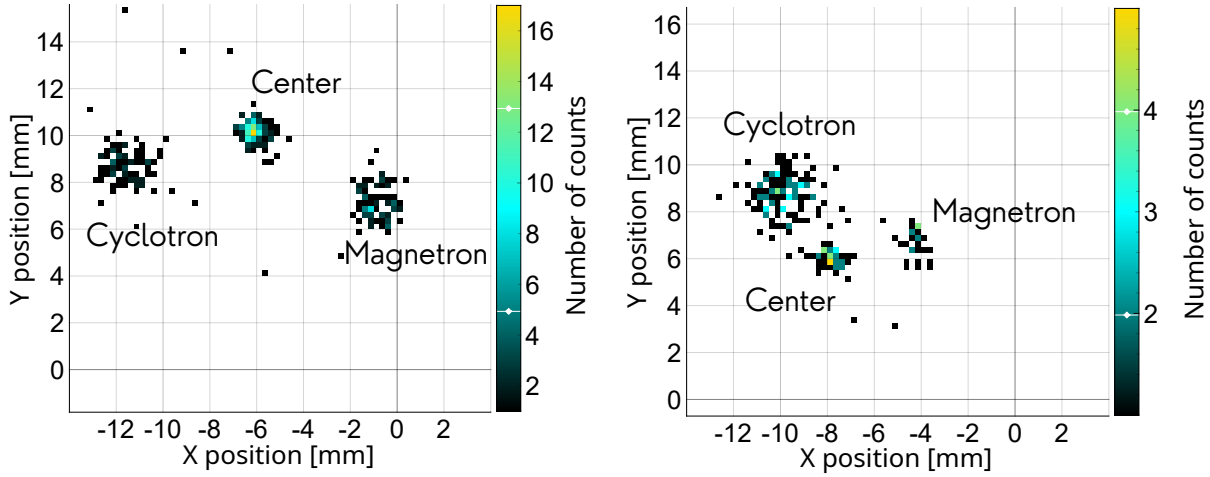

Figure 4.32: First 100 ms PI-ICR with $^{39}K^{+}$ ions on the left and 1 s PI-ICR with $^{85}Rb^{+}$ on the right. Note that the central spot shifted between the two measurements, an issue that will be discussed at the end of this chapter. The left scan was performed using 70 bunches for each spot, whereas the right one was performed using 60 bunches for each spot.

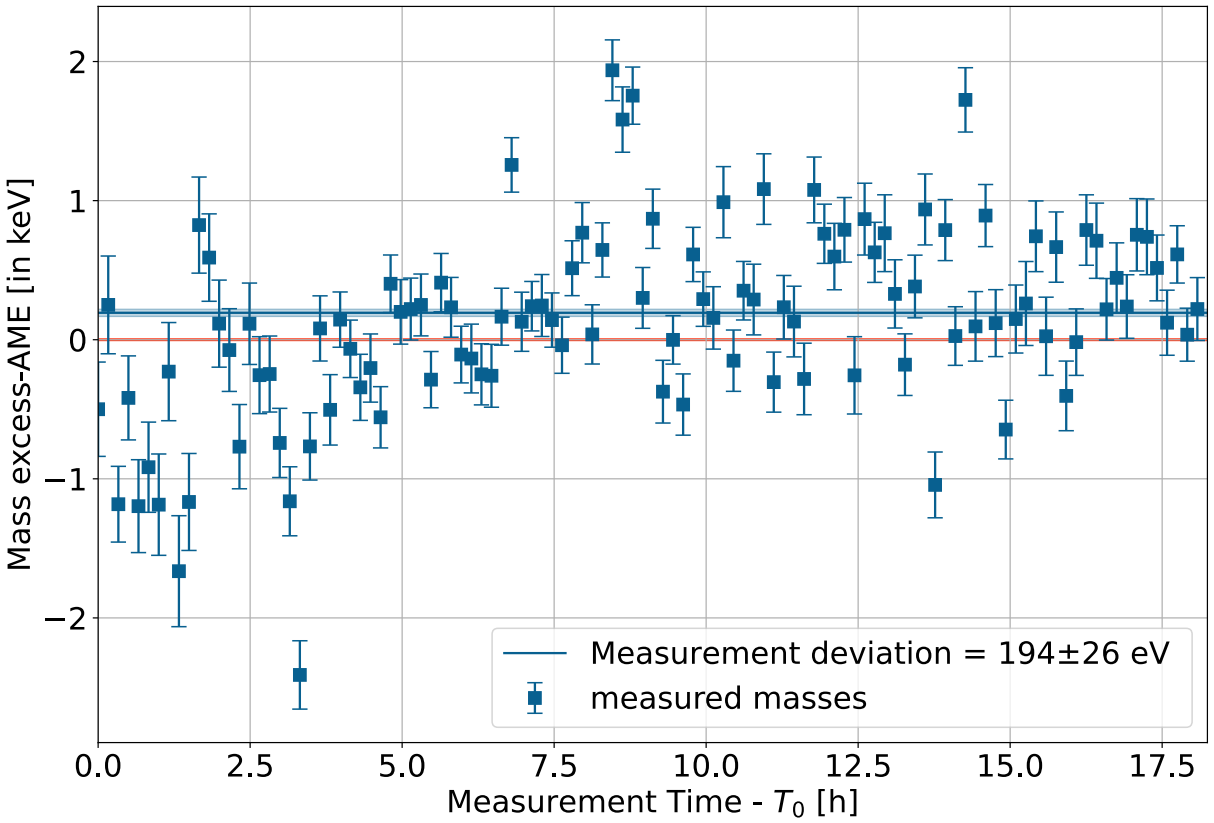

Figure 4.33: Difference in mass excess between the experiment and the AME as a function of the measurement time taking T_0, the time of the first measurement, as a reference. This is the first PI-ICR mass measurement of ^{41}K using ^{39}K as a reference on PIPERADE. The accumulation time was 100 ms, and the measurement was performed over 20 h.

was conducted using ^{39}K as a reference to measure the mass of ^{41}K. The result of this mass measurement is presented in Figure 4.33. A precision of 26 eV was obtained, but this low statistical uncertainty allows us to highlight a clear systematic deviation from the

AME. The reduced $\chi^2(\approx 8)$ allows us to say that the uncertainties of the measurements are underestimated, showing that the systematic uncertainties are not properly handled. The interpretation of this result is ongoing, as is the investigation into the known issues discussed hereafter.

One notable problem is that the positions of the central and other spots were observed to shift over time. This shift is of the order of 1 mm to 3 mm, and sometimes it can shift that much in less than one hour. Such rapid changes should not happen and are currently regarded as one of the potential explanations for the deviations observed in mass measurements using the PI-ICR technique. Diagnostics have indicated that this drift is not originating from the traps themselves but rather from the extraction process. To address this issue, modifications will be made to the extraction setup to improve the electrical potential difference of the 30 kV platform to ground and in particular to ensure that the insulator remains out of the ions' line of sight.

Summary

The PI-ICR technique was successfully implemented on PIPERADE for the first time, with the installation and commissioning of a dedicated detector. The first PI-ICR mass measurements were performed using 100 ms accumulation times.
Future modifications include changing the diaphragm to achieve clearer cyclotron spots with extended accumulation times. Additionally, mechanical adjustments to the extraction setup will be made to address the issue of spot drift. Control over temperature and pressure will also be enhanced. Subsequent systematic studies will focus on the imperfections in the electric and magnetic fields, as well as those specific to the PI-ICR technique, such as angle determination-related errors.

Chapter 5

Mass Measurements at JYFLTRAP

Contents

In this chapter, we present the results of a mass measurement experiment conducted at the Ion Guide Isotope Separation On-Line (IGISOL) facility [Moore 13] in Jyväskylä, Finland, using the double Penning trap system, JYFLTRAP [Eronen 12]. This experiment measured the masses of ^{68,69,70}Co isotopes and several other neutron-rich nuclei. The aim was also to measure the mass of ^{71}Co, but the contamination rate was too high. These nuclei are situated in a region of the nuclear chart that is particularly intriguing due to its proximity to the semi-doubly magic ^{68}Ni nucleus, which has a closed $Z = 28$ proton shell and a closed $N = 40$ neutron sub-shell.

The first section of this chapter will delve into the scientific context of this region, outlining the motivations behind our experimental investigation. Special emphasis will be placed on the significance of precise mass measurements for enhancing our understanding of nuclear structure, particularly with shell model calculations and the structural effects near the $N = 40$ region and the island of inversion (details on the discovery of the island of inversion can be found in [Nowacki 21a]).

Then, the experimental setup at Jyväskylä will be described, highlighting the IGISOL facility's unique capabilities and the JYFLTRAP system's operational principles.

Following this, we will discuss the data analysis methodology and present the results obtained from the mass measurements.

The next section will present the data evaluation using the Atomic Mass Evaluation (AME) and the impact of the present results on the AME database.

Finally, we will provide a theoretical interpretation of our results in a shell model framework and discuss their implications for nuclear structure.

5.1 Status of the region

The region around neutron number $N = 40$ and proton number $Z = 28$ has been the subject of intense investigations due to the particular structure effects arising from the interplay between the spin-orbit $Z = 28$ and the harmonic oscillator $N = 40$ shell closures. This region exhibits a rich variety of phenomena, such as shell structure evolution, deformation, and shape coexistence, which are influenced by the complex interplay between single-particle behavior and collective properties that favor deformation.

5.1.1 The harmonic oscillator magic number 40

A schematic representation of the shell structure of ^{68}Ni is visible in Figure 5.1 to visualize the different orbitals at play in this region. In spherical nuclei, the $1g_{9/2}$ orbital is distinctly separated from other higher single-particle levels, which contributes to the well-established magicity at neutron and proton numbers $N, Z = 50$. This separation is due to the spin-orbit interaction that lowers the $g_{9/2}$ orbital, and that consequently also reduces the harmonic oscillator shell gap at 40 (already detailed in 1.2). Nevertheless, the $Z = 40$ subshell closure is demonstrated by the well-studied level structure of the ^{90}Zr nucleus [Broda 95], where the lowest excited level is a 0^+ state at 1.76 MeV, and the first 2^+ state appears at 2.19 MeV [Ekström 92].

The neutron number $N = 40$ has been particularly interesting in the context of nickel isotopes, especially ^{68}Ni. Experimental signatures in ^{68}Ni, such as a high first-excited 2^+ state energy and a small $B(E2; 0^+ \rightarrow 2^+)$ transition strength compared to neighboring isotopes [Broda 95], [Sorlin 02], support the notion of a subshell closure at $N = 40$. However, compared with what could be expected with a strong shell closure, the energy

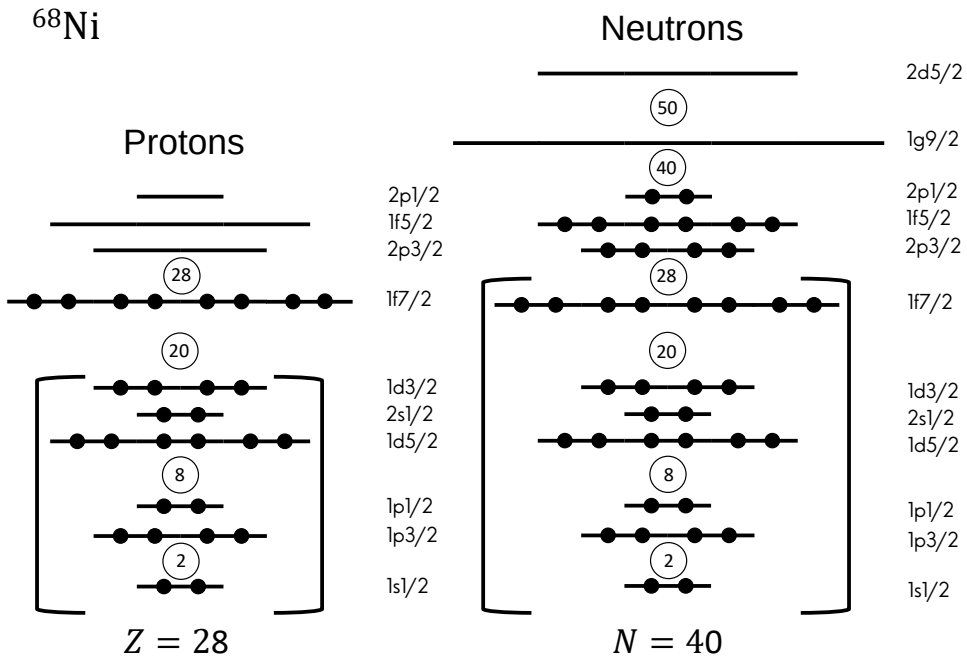

Figure 5.1: Schematic representation of the energy levels for the protons (left) and neutrons (right) in ^{68}Ni. In the shell-model calculations detailed later in 5.5.1, the core part of the nuclei corresponds to the orbitals in between the brackets, whereas the rest of the orbitals are the ones defined in the valence space

of the first 2^+ state in ^{68}Ni is not excessively high. In addition, the $B(E2)$ value, which measures the probability of the 0^+ to 2^+ transition, is not that low, suggesting an erosion of the subshell. Additionally, the presence of a low-lying deformed excited state in ^{68}Ni also highlights the complexity of this region at the edge of the so-called "island of inversion".

5.1.2 Island of inversion

As nucleons are added to or removed from ^{68}Ni, the nucleus experiences significant changes in its shape and structure, leading to deviations from spherical symmetry. It has been shown that this nucleus exhibits shape co-existence [Tsunoda 14], also[Suchyta 14]. The left part of Figure 5.2 illustrates the evolution of neutron orbitals as a function of the proton number at $N = 40$. This figure reveals that removing protons from ^{68}Ni weakens the neutron's pf-gd gap, which in turn facilitates additional neutron excitations across the $N = 40$ gap. This behavior is due to the monopole component of the Hamiltonian, which can be decomposed into a central force, spin-orbit interaction, and tensor force.

Nuclei such as ^{66}Fe and ^{64}Cr, which have 2 and 4 fewer protons than ^{68}Ni, exhibit prolate shapes due to the protons-neutrons interactions in the $sd - pf$ shells and the $pf - gds$ shells respectively [Caurier 02]. This has been demonstrated in various experiments [Rother 11], [Lunardi 07], [Hannawald 99], [Aoi 09], [Ljungvall 10].

Shape coexistence, which refers to a situation in which configurations with different shapes coexist at similar energies, is observed in ^{65,67}Co isotopes. These nuclei, located

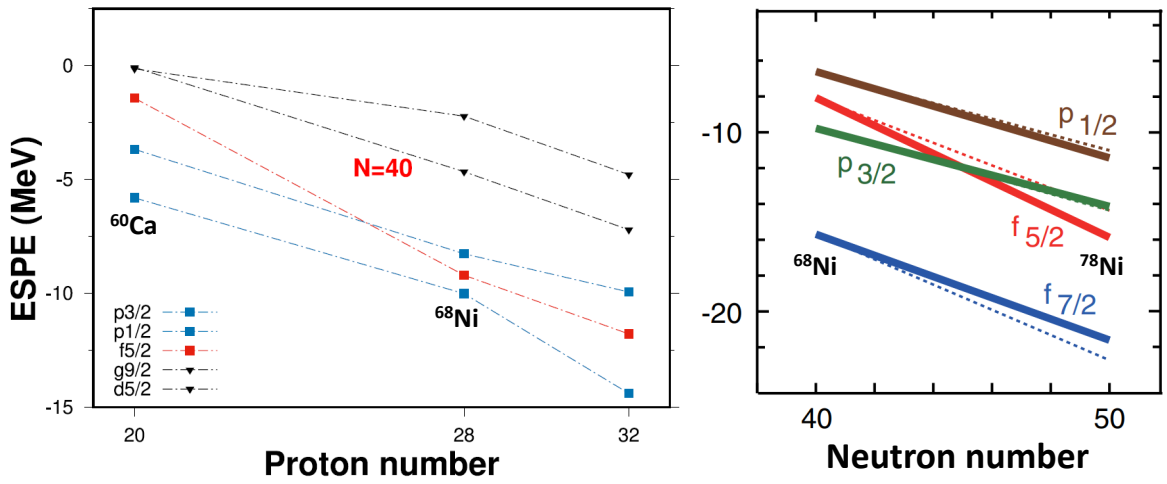

Figure 5.2: The left part of the plot represents the effective neutron single-particle energies (ESPE) at $N = 40$ calculated with the LNPS-U effective interaction [Nowacki 21b]. On the right part are the effective proton single-particle energies at $Z = 28$ calculated with the GXPF1A interaction [Otsuka 10]. The dashed lines are obtained only by the central force, while the solid lines include the central and tensor forces.

between the spherical ^{68}Ni and the deformed ^{66}Fe/^{64}Cr, exhibit evidence of both spherical and deformed configurations in their level structures. The presence of low-lying intruder states in ^{67}Co, with only one proton less than ^{68}Ni, confirms a weakening of the $N = 40$ shell gap, reflecting the complex interplay between shell closures and nuclear deformation [Recchia 12].

The "island of inversion" concept emerges when the standard ordering of nuclear energy levels associated with spherical configurations is disrupted due to strong mixing between nucleon configurations. This island of inversion manifests when the ground states of specific nuclei exhibit intruder configurations from higher energy shells. In the context of neutron-rich nuclei around ^{68,69,70}Co, as the $g_{9/2}$ orbital is filled by neutrons, the energy level of the $f_{5/2}$ is lowered with respect to the $f_{7/2}$ proton orbital (see right part of Figure 5.2). The figure illustrates this with solid and dashed curves, representing the evolution of single-particle energies as a function of neutron number from $N = 40$ to $N = 50$ with and without tensor force. As the neutron number increases, the $f_{5/2}$ and $f_{7/2}$ levels draw closer due to the effect of the tensor force. This proximity favors proton excitations across the $Z = 28$ shell gap. In this scenario, states with neutrons and protons in higher orbitals may become energetically more bound due to additional correlations than in the "normal" configuration.

For instance, in ^{68}Ni, despite the expectation of a closed neutron shell at $N = 40$, the presence of states at low excitation energies with configurations including the $g_{9/2}$ orbital suggests significant mixing of states from different shells. This mixing is driven by the energy proximity between the pf-shell and the $g_{9/2}$ orbital due to the spin-orbit interaction, supporting the idea that neutron-rich cobalt isotopes might belong to the island of inversion [Recchia 12; Caurier 02].

5.1.3 Masses of cobalt isotopes

Recent experiments, first at LEBIT in 2018 and then at JYFLTRAP in 2020, have precisely measured nuclear properties in the ^{68,69,70}Co isotopes. These measurements of binding energies for both ground and isomeric states have significantly contributed to our understanding of the island of inversion phenomenon, offering insights into the interplay between shell closures and intruder configurations. However, these measurements alone are not sufficient to definitively resolve the ambiguities that will be discussed below.

In Figure 5.3, the trends in two-neutron separation energies (S_{2n}) are illustrated. The green data points represent measurements by LEBIT, where they claimed to have measured the ground states of ^{68}Co and ^{69}Co [Izzo 18]. In contrast, the red data points correspond to measurements by JYFLTRAP, which reported both the ground state (g.s.) and isomeric state (m.) of ^{69}Co, as well as the ground state of ^{70}Co [Canete 20]. The plot presents two distinct scenarios: one showing a smooth trend, suggesting minimal structure changes, and another displaying a noticeable kink, indicating a potential change in collectivity. The discrepancy arises because JYFLTRAP's measurements, which include both the ground and isomeric states of ^{69}Co, suggest that LEBIT may have mistakenly measured the isomeric state rather than the ground state of ^{69}Co, this error resulting in an underestimation of the S_{2n} value for $N = 42$.

JYFLTRAP's interpretation proposes that LEBIT's measurement of the ground state for ^{68}Co might also be erroneous, considering that an isomeric state is known through beta decay experiment [Mueller 99] in this nucleus. If true, this would elevate the S_{2n} at $N = 41$ and lower the S_{2n} at $N = 43$; thus remove the kink in the S_{2n} trend. Therefore, independent measurements of both the ground and isomeric states are necessary. Similarly, for ^{70}Co, where only one state has been measured, there is a pressing need to measure both states individually to confirm that JYFLTRAP measured the ground state mass excess instead of the isomeric one.

5.1.4 Long-lived states

For the odd-odd cobalt isotopes ^{68}Co and ^{70}Co, the status before the experiment is depicted in Table 5.1. In both cases, two long-lived states were identified in beta-decay experiments, one being associated with the ground state and the second one with a long-lived isomeric state [Mueller 99], [Mueller 00]. Although half-lives of these states could be measured and spin/parity could be tentatively assigned based on subsequent beta decay studies [Kondev 21], [Flavigny 15], [Morales 17], it was not possible to establish the ordering of the states. Additionally, the excitation energies had never been experimentally measured (the values followed by a # sign are extrapolated). This lack of experimental data made it impossible to compare theoretical spectroscopy calculations for these nuclei with actual experimental results, thereby hindering our understanding of the different

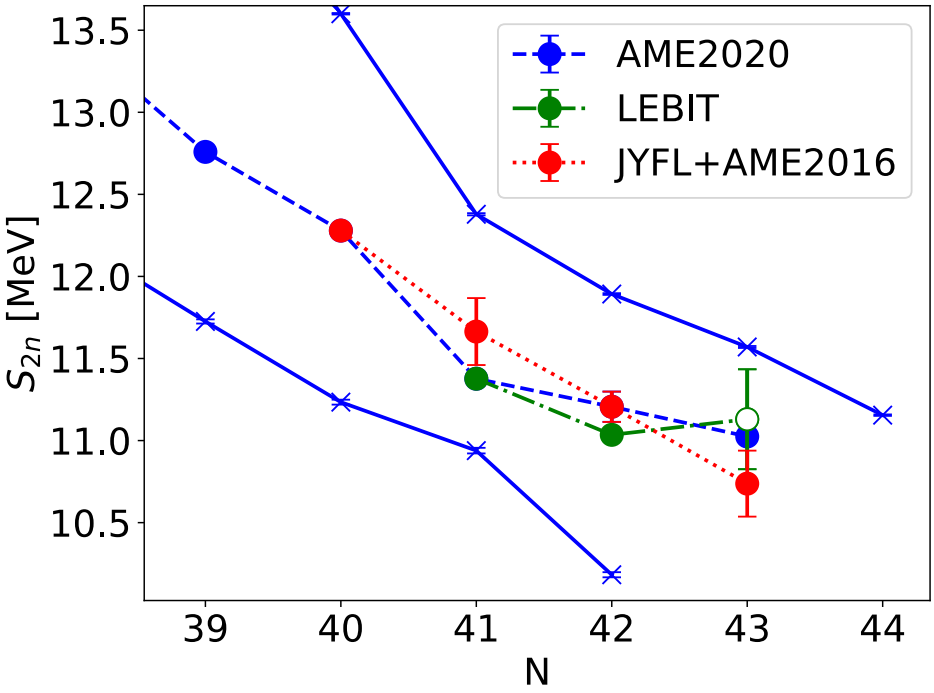

Figure 5.3: Two-neutron separation energies based on experimental values from AME20 [Huang 21] in blue (for the Fe isotopes new values from [Porter 22] are used), the results from JYFLTRAP [Canete 20] with a value from AME16 [Huang 17] for the ^{68}Co (in red). and the ^{68,69}Co measurements at LEBIT [Izzo 18] (in green). For ^{70}Co, the open symbol indicates that the value is based on extrapolations. The discrepancies between JYFL and LEBIT trends are explained in the text. Adapted from [Canete 20]

possible configurations for the two states.

In odd-even Cobalt isotopes, an $1/2^-$ excited state has been observed and interpreted in both ^{65}Co [Pauwels 09] and ^{67}Co [Pauwels 08] as an intruder state, based on proton excitations above the $Z = 28$ shell gap. In contrast, the ground state is believed to be in the "normal" configuration corresponding to a $7/2^-$, which can be understood as a proton hole in the $f_{7/2}$ orbital. In Figure 5.4, the evolution of the excitation energy of the $1/2^-$ intruder state is plotted for odd-even Cobalt isotopes. The figure shows that the excitation energy of this intruder state decreases as one moves towards and beyond $N = 40$. This drop indicates that the intruder configuration increasingly competes with the ground state as the neutron number increases. Since the excitation energies of ^{65}Co and ^{67}Co were already well known, this experiment focused on Cobalt isotopes with $N > 40$. In ^{69}Co the $1/2^-$ isomeric state, is measured at 182(100) keV[Canete 20] and in ^{71}Co, it is predicted at 60 keV [Lokotko 20]. In the case of the ^{69}Co, the assignment of spin, parity, and half-lives with ground and isomeric state was done. However, for ^{71}Co, a potential $1/2^-$ isomer has never been observed, laying a shadow upon the frontier of the island of inversion. Therefore, the goal of this experiment was to improve the precision of the excitation energy measurement for ^{69}Co and measure for the first time the excitation

	$T_{1/2}$ [ms]|J^π	State	Mass excess [keV]
^{68}Co	200(20) | (7^-)	g.s. or m	-51643(4) or −51796#(150#)
	1600(300) | (2^-)	g.s. or m	-51643(4) or −51490#(150#)
^{69}Co	180(20) | $(7/2^-)$	g.s.	-50390(90)
	750(250) | $(1/2^-\#)$	m	117(91)
^{70}Co	112(7) | $(6^-, 7^-)$	g.s. or m	-46525(11) or −46720#(200#)
	508(7) | $(1^+, 2^+)$	g.s. or m	-46525(11) or −46330#(200#)
^{71}Co	80(3) | $(7/2^-)$	g.s. ?	-44370(470) ?
	Unknown	m ?	Unknown

Table 5.1: Status of knowledge prior to this experiment for ground and isomeric states in $^{68-71}$Co. The values followed by a # sign are extrapolated. Data from [Kondev 21].

energy of ^{71}Co, allowing to constrain nuclear models and determine if an inversion of the intruder and "normal" state was occurring in this nucleus.

It is also worth noting that the previously mentioned mass measurements were all conducted using the ToF-ICR technique, which is limited in separating states close in energy. In the case of ^{69}Co, they could measure the two states by taking advantage of the large difference in half-life between them. They performed two ToF-ICRs, one with a short cycle ensuring that both states would not decay before the end of the measurement and the second where they added a waiting time of 500 ms so that the short-lived state ($t_{1/2}$ = 180(20)) would fully decay. This way, they had two different fitted frequencies and could identify which state belonged to which mass (more details can be found in [Canete 20]).

For ^{70}Co, JYFLTRAP also used the PI-ICR technique during that experiment. However, it was their first time using this method, and it had not been fully commissioned. As a result, the PI-ICR technique was not used to measure the masses but only to ensure that only one state was being measured.

If the two states are well separated, the PI-ICR technique has the potential to independently measure the mass of each state by measuring the position of the associated spots. Additionally, it allows monitoring of the number of ions in each state independently by counting the number of ions in the associated spot. It is then possible to change the time the ions spend in the traps to measure the evolution over time of the number of counts

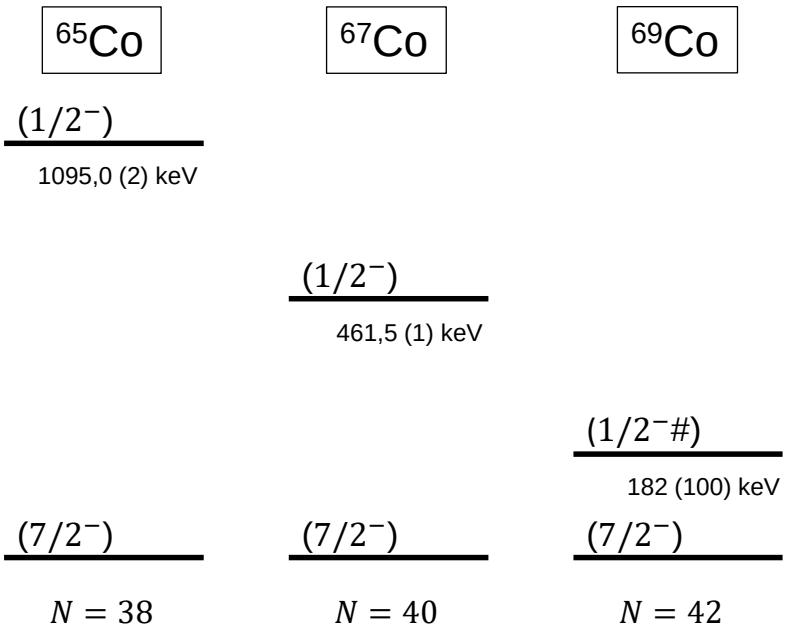

Figure 5.4: Excitation energy of the $1/2^-$ intruder state in the odd-even Cobalt around N=40. The ^{71}Co does not appear on the plot, but an excited state $1/2^-$ was computed at 60 keV using the Lenzi-Nowacki-Poves-Sieja (LPNS) interaction [Lokotko 20]. Section 5.5.2 will give more details on this interaction.

for each state. Therefore, it allows for assigning a specific half-life to an individual state. With the commissioning of the PI-ICR technique at JYFLTRAP [Nesterenko 18], it is now possible to perform such measurements.

Motivated by the need to constrain nuclear models and determine which cobalt isotopes are part of the island of inversion, an experiment was conducted to gather new experimental data on these four nuclei. The technical details of the experiment will be provided in the following section.

5.2 Setup Presentation

The measurements were performed at the Ion Guide Isotope Separator On-Line facility (IGISOL) [Moore 13] with the JYFLTRAP double Penning trap mass spectrometer [Eronen 12] at the University of Jyväskylä, Finland. A schematic view of the experimental setup is shown in Figure 5.5.

The experimental procedure involved the production of various nuclei through fission in a uranium target foil, induced by a 30 MeV proton beam from the K-130 cyclotron. Then, the produced ions were stopped and thermalized in a helium-filled gas cell and extracted with the gas flow and electric fields via a sextupole ion guide [Karvonen 08].

The extracted ions were accelerated to 30 keV and transported through a 55° dipole magnet with a mass resolving power of $M/\Delta M \approx 500$. This step allowed for mass

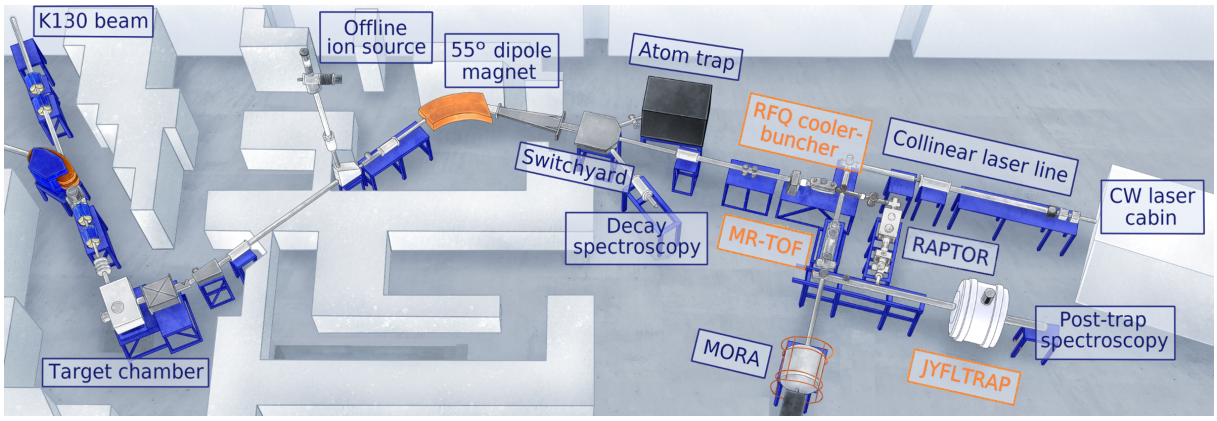

Figure 5.5: Illustration of the current IGISOL facility. Primary beams from the K130 heavy-ion cyclotron are guided to the target chamber, where secondary beams are produced in various nuclear reactions. Offline beams are produced using a discharge ion source mounted inside the target chamber or an offline ion source on the second floor. A dipole magnet is used to mass-separate the ion beam, after which it arrives at the Switchyard, where the beamline separates into three possible ways. In the experiment presented in this work, the ions only go through the devices highlighted in orange. The ions are guided to an RFQ cooler-buncher. The bunched and cooled beam is then shot through the MR-TOF to reach the double Penning trap JYFLTRAP. Adapted from [Kujanpää 23]

separation, ensuring that only ions with the same mass-to-charge ratio (A/q) as the ion of interest (IoI) were selected. Then, the ions were directed to a radiofrequency quadrupole (RFQ) cooler-buncher [Nieminen 01], where they were accumulated, cooled, and bunched before being sent to the JYFLTRAP double Penning trap mass spectrometer for further purification and final mass measurements.

JYFLTRAP consists of two cylindrical Penning traps of the same size operating in a 7 T magnetic field. This mass spectrometer is very similar to the previously discussed PIPERADE system. The first trap, filled with helium buffer gas, performs isobaric[1] purification using the buffer gas cooling technique (explained in section 2.4.1). The second trap is used for precise mass measurements using both ToF-ICR and PI-ICR techniques, presented in section 2.4.2.

In addition to the Penning traps, a Multi-Reflection Time-of-Flight Mass Spectrometer (MR-ToF MS) is being commissioned between the RFQ and JYFLTRAP setups. This instrument is particularly advantageous for scenarios where contamination levels are high relative to the ion of interest and for measuring masses of species with short half-lives that cannot be measured in Penning traps. The experiment aimed to demonstrate the combined use of MR-ToF MS and Penning traps; however, due to ongoing commissioning, the MR-ToF MS was not operational during the measurements presented below.

The mass measurement data analysis will be presented and discussed in the upcoming section.

[1] it is also an (A/q) separation; however, the resolving power is usually 200 to 600 times greater than the dipole magnet resolving power

5.3 Analysis and results

During the experiment, the masses of ^{68,69,70}Co isotopes ground states (g.s.) and isomeric states, along with ^{79}Ge and ^{73}Ni ground states, were measured using the Phase Imaging Ion Cyclotron Resonance (PI-ICR) technique. Unfortunately, the ^{71}Co stayed out of reach in this experiment due to high contamination of $^{142}Ce^{2+}$. The data acquisition software, PymassScanner, developed by T. Eronen and D.A. Nesterenko at IGISOL, allows the creation of files for subsequent analysis.

An image illustrating the mass measurement of ^{69}Co using this software is displayed in Figure 5.6, with examples of the Gaussian fits used for position determination of the isomeric state shown on the right. As shown in this figure, spatial gates need to be defined, and it is also important to note that a first selection through a gate in time of flight (see bottom left of Figure 5.6) is also applied. Indeed, the ions should have a relatively similar time of flight (all the ions exit the trap with only magnetron motion, resulting in minimal differences in kinetic energy).

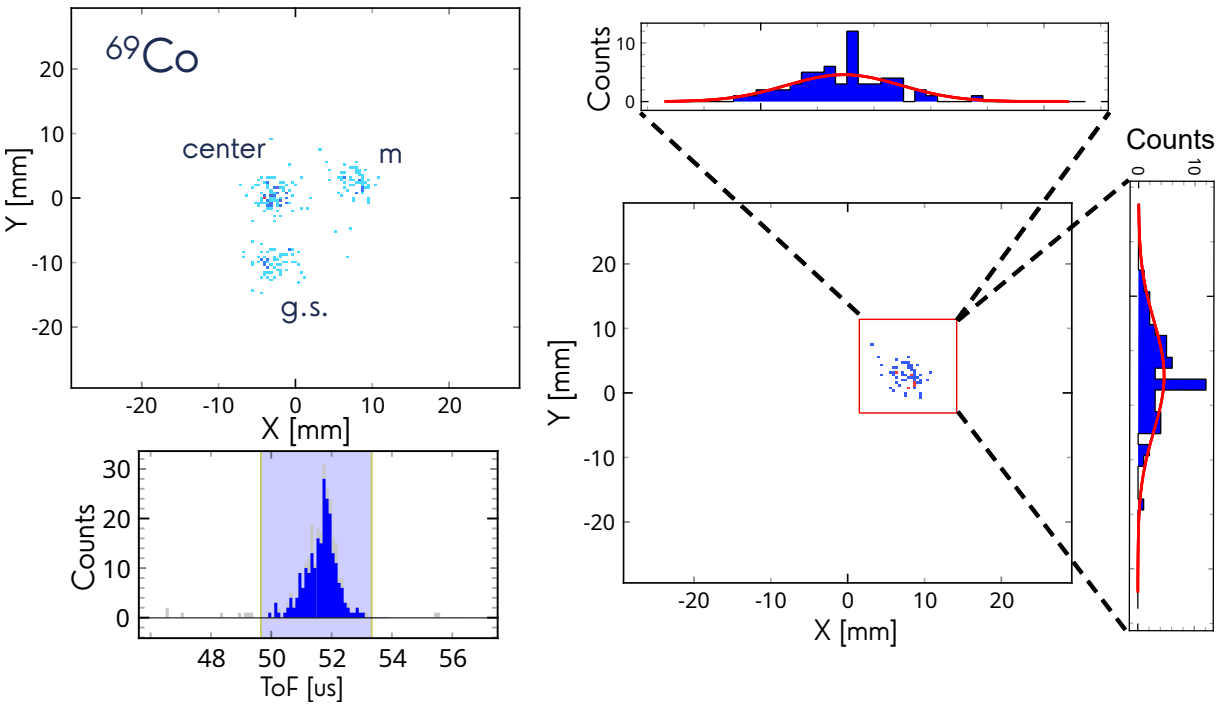

Figure 5.6: On the top left is the image of ^{69}Co ground state and isomeric state on the position-sensitive detector. The center contains both g.s. and m. and was obtained by extracting the ions after step 2 in Figure 2.11. The separation of ground and isomeric states is obtained using the pattern on the left of the Figure 2.11. On the bottom left, the blue region represents the gate in ToF; all the ions outside this region are not plotted on the other graphs. On the right, the red square represents the gate in position made to fit the isomeric state's position correctly. The Gaussian fits are made on the X and Y projections, which are also visible on the right.

After the data acquisition, another program called Cloudberry, developed by D.A. Nesterenko, allowed for further analysis. The formulas to determine the frequency ratios

and mass excesses and their associated uncertainties used within Cloudberry are the same as those detailed in Section 4.3.3 and Section 2.4.2, with additional corrections specific to JYFLTRAP for addressing distortions on the positions on the MCP. Comprehensive details on the systematic aspects of the PI-ICR technique at JYFLTRAP can be found in [Nesterenko 18]. No further information will be provided in this work since statistical uncertainty is highly dominant in the measurements presented below.

In Table 5.2, the results of the analysis can be found, including the mass excess of all the nuclides studied in our experiment, along with the spin parity and half-life assignments for ^{68}Co (ground state and isomeric state) and ^{70}Co (ground state and isomeric state). The discussion will start with the mass excesses, followed by an overview of the assignments.

			Mass Excess [keV]					
	$T_{1/2}$ [ms]	I^π	Δ_{exp}	Δ_{AME}	Δ_{exp}-Δ_{AME} [keV]	E^*_{exp} [keV]	Ratios($=\nu_{ref}/\nu$)	Ref
^{68}Co	**200(20)**	**(7$^-$)**	-51652.5(7)	-51643(4)	9(4)		1.000290095(8)	^{68}Zn
^{68m}Co	**1600(300)**	**(2$^-$)**	-51573.0(21)	#-51490(#150)	-83(150)	79.5(22)	1.000291352(32)	^{68}Zn
^{69}Co	180(20)	(7/2$^-$)	-50320.2(63)	-50390(90)	70(90)		0,999997612(72)	^{69m}Co
^{69m}Co	750(250)	(1/2$^-$#)	-50171.9(43)	-50213(13)	41(14)	148.3(76)	1.000298364(65)	^{69}Ga
^{70}Co	**508(7)**	**(1$^+$,2$^+$)**	-46508.1(17)	-46525(11)	17(11)		1.000353979(18)	^{70}Zn
^{70m}Co	**112(7)**	**(6$^-$,7$^-$)**	-46239.7(47)	#-46330(#200)	90(200)	268.4(50)	1.000358107(68)	^{70}Zn
^{79}Ge	18980(30)	(1/2$^-$)	-69472.3(7)	-69530(40)	58(40)		0.929498483(9)	^{85}Rb
^{73}Ni	840(30)	(9/2$^+$)	-50106.8(13)	-50108(2)	1(2)		1.000130704(7)	^{73}Cu

Table 5.2: Half-lives, spins, and parities based on the NUBASE2020 [Kondev 21], mass-excess values from this work (Δ_{exp}), from AME 2020 (Δ_{AME}) [Huang 21], the comparison between the two, and the previous (E^*_{AME}) and new (E^*_{exp}) excitation energies for the isomeric states. In bold are the values that were newly assigned with the analysis discussed below. "#" denotes a value based on extrapolations. Singly-charged ions in the last column were used as a reference for the studied cases.

5.3.1 Mass Excesses

In Figure 5.7, the values from Table 5.2 are compared to previous measurements reported in [Izzo 18], [Canete 20], or the 2020 Atomic Mass Evaluation (AME2020).

For ^{68}Co, the isomeric state was measured for the first time, and the precision of the ground state was improved. The comparison shown in Figure 5.7 indicates that [Izzo 18] most likely measured the ground state or a mixture of the ground state and a small proportion of the isomeric state, which contradicts the suggestion by [Canete 20] that only the isomeric state was measured.

For ^{69}Co, our results are consistent with [Canete 20], confirming that [Izzo 18] likely measured the isomeric state or a mixture of the ground state and a high proportion of the isomeric state. The precision has been improved by more than a factor of 10.

For ^{70}Co, the isomeric state was measured for the first time, and the precision of the ground state measurement was also improved. This study further confirms that [Canete 20] likely measured the ground state.

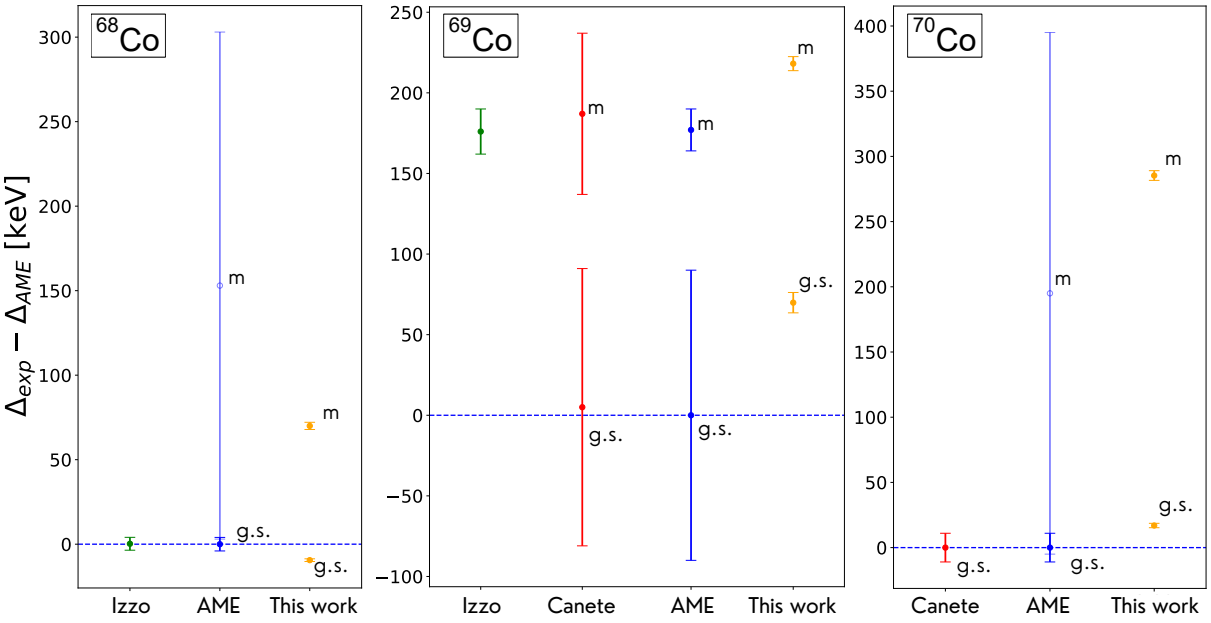

Figure 5.7: Difference between AME 2020 [Huang 21] mass excess values (blue), and the measured mass excess by [Izzo 18] (green), [Canete 20] (red), and in this work (orange) for ^{68,69,70}Co. Extrapolated values from the AME are represented with open symbols. For ^{70}Co, the AME value for the ground state is also [Canete 20]'s previous value.

After presenting the mass excess values, we now turn to the S_{2n} trends. As previously mentioned, discrepancies in the region of interest make it crucial to analyze their final trend in order to understand the structure evolution better. In Figure 5.8, the results of this work are compared to previous measurements. The S_{2n} values determined in this work allow us to distinguish between the two distinct scenarios presented in section 5.1.3, confirming the presence of a kink around $N = 43$ in the cobalt isotopic chain. These results will be further discussed later in this section and compared to shell model calculations.

Two additional mass excesses were measured during this experiment. The uncertainties in the mass excesses of the region were reviewed, and it was noted that the uncertainty for ^{79}Ge was around 40 keV. Consequently, it was decided to measure its mass with a greater precision down to 0.7 keV.

In addition, the mass excess of ^{73}Ni required further investigation because a previous measurement at RIKEN [Rosenbusch 24] showed a deviation of 30 keV from the value measured at Jyväskylä [Rahaman 07]. This raised two possibilities: either one of the measurements was incorrect, or the observed deviation could be explained by the presence of an isomeric state. Three different accumulation times (200 , 400 , and 600 ms) were used to favor our chances of finding this hypothetical isomeric state. However, no isomeric state could be observed at these accumulation times. In addition, our measurement corroborates the value obtained in the previous experiment performed at Jyväskylä [Rahaman 07] for the ground state.

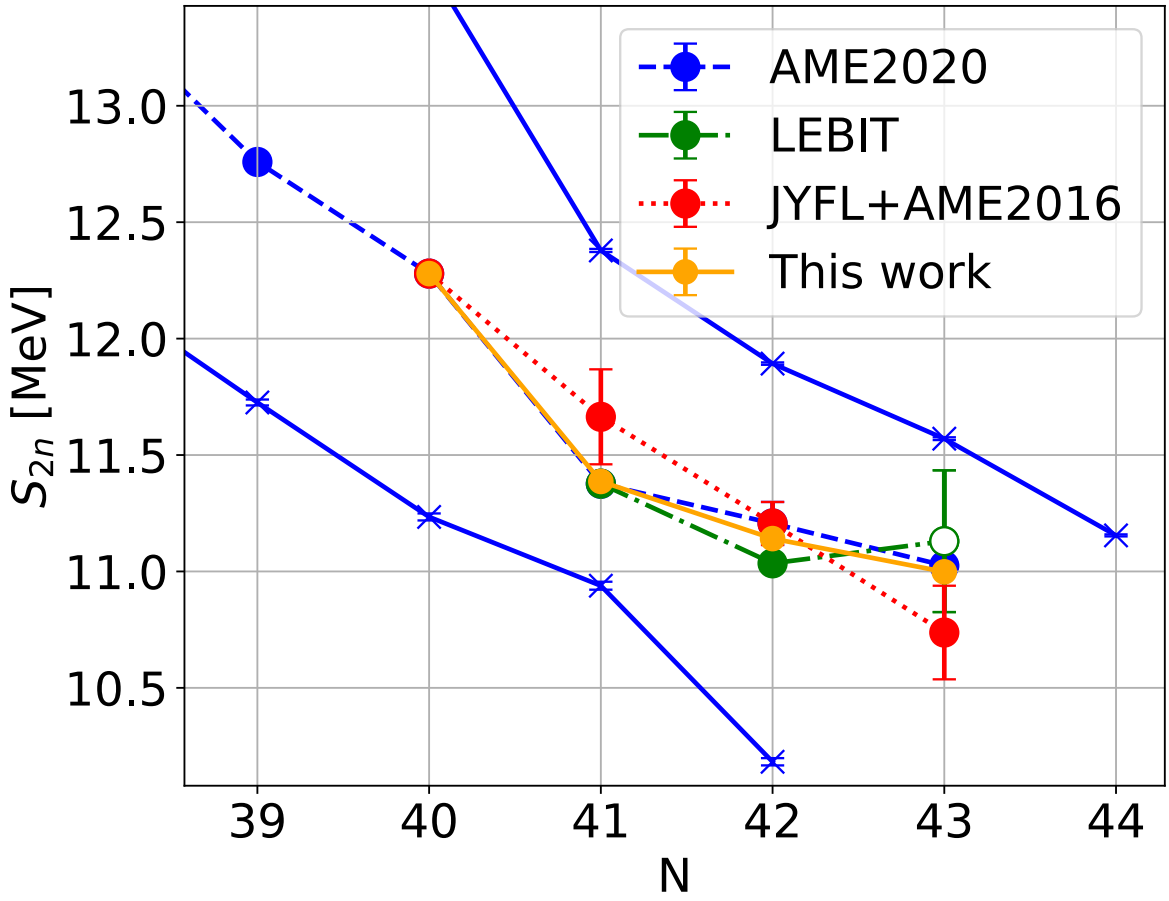

Figure 5.8: S_{2n} values computed with the masses measured in this work (in orange) compared to the two-neutron separation energies based on experimental values from AME2020 in blue (for the Fe isotopes new values from [Porter 22] are used), the results from JYFLTRAP [Canete 20] with the AME2016 [Huang 17] value for the ^{68}Co (in red) and the measurements at LEBIT [Izzo 18] (in green).

5.3.2 Half lives and spin-parity assignments

Before this work, two states were known (in ^{68}Co and ^{70}Co) with measured half-lives and spin-parity assignments but without knowing which one is the ground or isomeric state [Flavigny 15], [Morales 17]. It was shown in the previous section that the masses of both states were measured in this work. In the following, the assignment of these states to the known spin-parity/half-lives states will be presented. It was already explained in section 5.1.4 that once the states are separated with the PI-ICR technique, it is possible to count the number of ions for each state independently. Therefore, by varying the trapping time in the measurement trap, the evolution of each state's quantity over time and, thus, their decay curve can be determined. To ensure that the numbers of counts for different trapping times are well-comparable and to avoid any bias from any beam fluctuations, the count rates need to be measured relative to the rate of a reference ion.

- As the origin of the contaminants and the ion of interest may be different, it is

crucial to keep the path of the ion beam constant (no tuning of the beamline).

- The detection efficiency must be well known, especially since it can vary depending on the position of the ion spot on the MCP. This means either ensuring the ion spot remains at the same position across measurements for consistency or knowing the efficiency at different spot positions. In our case, the exact efficiency of the position-sensitive detector was unknown because the thresholds were adjusted prior to the experiment. As a result, the only way to maintain consistent efficiency was to ensure that the ion spots remained at the same position for all measurements.

In our case, the references used were the same as the ones for the mass measurements, i.e., ^{68}Zn and ^{70}Zn, for ^{68}Co and ^{70}Co, respectively. Between multiple measurements, beamline tunings were done, and the position of the zinc and cobalt isotope spots on the position-sensitive detector was changed, resulting in a modification of the ion of interest and reference ion ratio. After eliminating these biased data, only two measurements were exploitable for the ^{68}Co and four for the ^{70}Co. In addition, only the ground-state count rates were used for this study as the count rate of the two isomeric states was too low, making the uncertainties too big to discriminate between any possible half-lives. All the comparable points are plotted in Figures 5.9 and 5.10 for ^{68}Co and ^{70}Co, respectively. The formula that was used to fit the half-life is the following:

$$N(t) = N_0 e^{\frac{-ln(2)t}{t_{1/2}}} \tag{5.1}$$

with N_0 being the initial number of the ions that will decay and $t_{1/2}$ the half-life. The blue curves in Figures 5.9 and 5.10 represent the results of the non-linear least squares regression used to determine N_0 and $t_{1/2}$. For the case of ^{68}Co, it was said that only two different cycle lengths were comparable, explaining why the fit has no uncertainty.

The red and yellow curves illustrate the results of the non-linear least squares regression used to determine only N_0, with $t_{1/2}$ fixed to the values of the short-lived and long-lived states. By analyzing the reduced chi-squares of the fit performed for the ^{68}Co, it appears that the half-life of 200 ms better describes the data than the 1.6 s half-life. Similarly, by looking at the reduced chi-squared of the fit performed for the ^{70}Co, the one with the half-life fixed at 508 ms seems more accurate. This analysis allowed us to claim that the ground state of ^{68}Co corresponds to the short-lived, high-spin state, while the ground state of ^{70}Co is identified as the long-lived, low-spin state. These assignments will be discussed later in this section and will be compared with shell model calculations.

5.4 Mass evaluation

All masses are measured relative to a reference one, and any changes to this reference will affect the masses of all other nuclei measured relative to it. By linking the newly

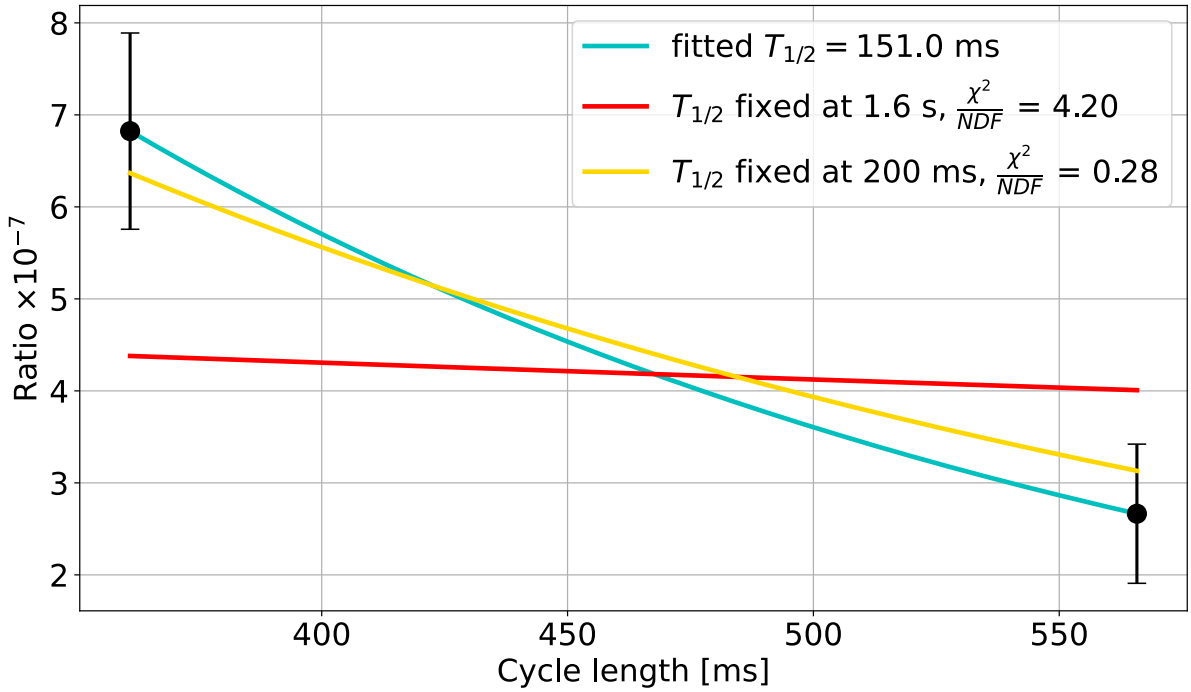

Figure 5.9: Ratio of ^{68}Co ground state rate divided by the rate of ^{68}Zn as a function of the cycle length. The red and yellow curves illustrate the results of the non-linear least squares regression used to fit only N_0, with $t_{1/2}$ fixed to the values of the short-lived and long-lived states. The blue curve shows the half-life value that goes through the two points for a given N_0.

measured masses with their respective reference, one can create a network connecting the nuclei of interest. The network constructed by the Atomic Mass Evaluation (AME) uses ^{12}C as the main reference. Multiple schemes of this network can be found in [Huang 21]. This section will discuss how our measurements have impacted the masses of related nuclei.

The frequency ratios presented in Table 5.2 were sent to one of the AME evaluators. She compared our data with the existing experimental results. Figure 5.11 illustrates the case of ^{68}Co. On the left, the diagram shows the connections in the AME 2020, where the measurements with ^{18}O and ^{34}S were obtained through Time-of-Flight Ion Cyclotron Resonance (ToF-ICR) measurements[2] performed by [Izzo 18]. On the right, the updated diagram for AME 2024 is presented. Since in our measurement, by using the PI-ICR method, we improved the precision of the mass excess of ^{68}Co using ^{68}Zn as a reference, the new AME value for ^{68}Co mass excess will be based on our measurement for 94.55% (see Figure 5.11. Reversely, our measurement will contribute 3.85% to the ^{68}Zn mass evaluation, resulting in a modification of 0.4 keV. In total, this experiment contributed for more than 90% for 7 mass excesses and one for 59.51% (in ^{73}Ni the mass excess was already well known).

[2]The link between ^{34}S and ^{18}O (in molecule with ^{16}O) comes from the fact that they were used as monocharged reference for the measurement of ^{68}Co in a doubly charged state.

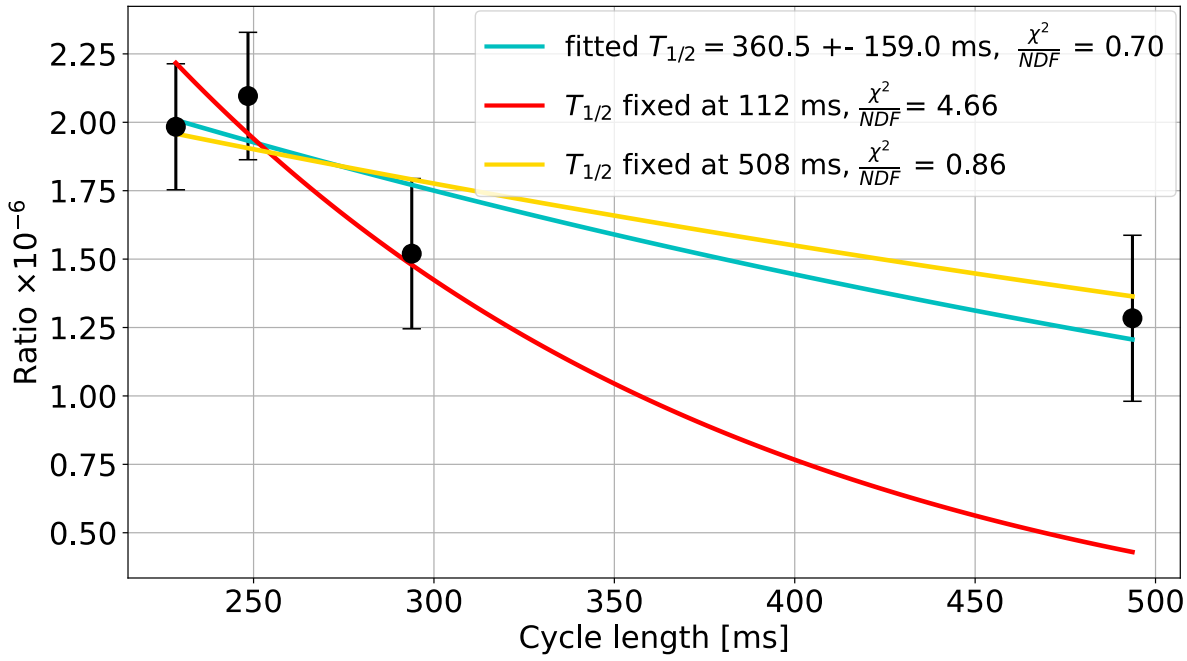

Figure 5.10: Ratio of ^{70}Co ground state rate divided by the rate of ^{70}Zn as a function of the cycle length. The red and yellow curves illustrate the results of the non-linear least squares regression used to determine only N_0, with $t_{1/2}$ fixed to the experimentally known values of the short-lived and long-lived states. The blue curve shows the fitted half-life value with both N_0 and $t_{1/2}$ as free parameters.

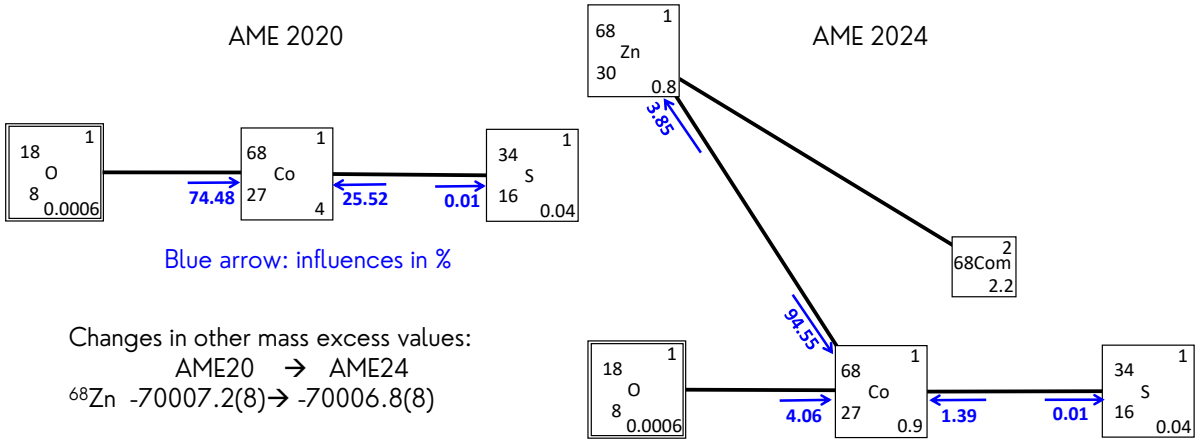

Figure 5.11: Comparison of the diagram of connections for ^{68}Co in AME 2020 (left) and AME 2024 (right) updated with this work. For ^{18}O, the box has a double contour, meaning that it is known using ^{12}C as a reference. Then, the number on the top right is one if the nucleus was measured with at least two different experiments; otherwise, it is two. The number on the bottom right is the uncertainty on the mass excess value in keV. The most important value is marked in blue with an arrow representing the percentage of each value used to compute the final mass excess.

Table 5.3 summarizes all the modified values after the complete evaluation. While the changes may seem modest, it is crucial and insightful to follow the entire process of integrating new mass measurement values into the AME.

	Mass excess (keV)	
	AME 2020	AME 2024
^{68}Co	-51643(4)	-51652.0(9)
^{68m}Co	#-51490(#150)	-51572.6(22)
^{69}Co	-50390(90)	-50330(6)
^{69m}Co	-50213(13)	-50176(4)
^{70}Co	-46525(11)	-46509.4(22)

	Mass excess (keV)	
	AME 2020	AME 2024
^{70m}Co	#-46330(#200)	-46240(5)
^{79}Ge	-69530(40)	-69472.3(7)
^{73}Ni	-50108(2)	-50107.8(15)
^{68}Zn	-70007.2(8)	-70006.8(8)
^{69}Ga	-69327.8(12)	-69328.2(12)

	Mass excess (keV)	
	AME 2020	AME 2024
^{70}Zn	-69564.7(19)	-69565.4(19)
^{79}Ga	-62548.4(12)	-62548.3(12)
^{73}Cu	-58987.4(19)	-58987.7(15)

Table 5.3: Mass excesses of nuclei that were updated following our experiment. Note that this table does not only include the nuclei we directly measured (see Table 5.2).

5.5 Interpretation

This section is organized into four parts. First, the principles of shell-model calculations will be introduced. Next, the results of such calculations performed in collaboration with F. Nowacki and D. D. Dao in the context of this work will be presented, focusing on the spectroscopy of the measured nuclei. Following this, the computed binding energies and S_{2n} will be compared to the new experimental data input. Finally, the structure of neighboring cobalt and nickel isotopes will be discussed regarding shape and configuration mixing using the Large-Scale Shell Model (LSSM) and the Discrete NonOrthogonal Shell Model (DNO-SM).

5.5.1 Discrete nonorthogonal shell-model and shell-model calculations

In chapter 1, it was shown that the Hamiltonian was often assumed to have a one-body kinetic energy term $T(k)$ and a two-body interaction term $V(k,l)$ that describe the forces acting between the nucleons. For a system of A interacting nucleons, it is expressed as :

$$H = \sum_{k=1}^{A} T(k) + \sum_{1 \leq k < l}^{A} V(k,l) \tag{5.2}$$

Generally, solving the Schrödinger equation for a system as complex as the nucleus is not a trivial task, and we usually have to resort to approximate methods such as the Density Functional Theory using density-dependent forces [Ring 80] or the Shell Model framework [Caurier 05].

In this work, we adopt the latter to interpret our data. In the shell model framework (see Figure 5.12), the orbitals are defined by a mean-field chosen to represent, at best, the nuclear properties in the region of interest. An inert core where orbitals are always full is defined, whereas the orbitals that contain the physical degrees of freedom relevant to a given mass region of interest are termed the valence space. In this region, nucleons can freely move between orbital as long as they possess the necessary energy to occupy them. All remaining orbitals, which are always empty, are considered part of the external space.

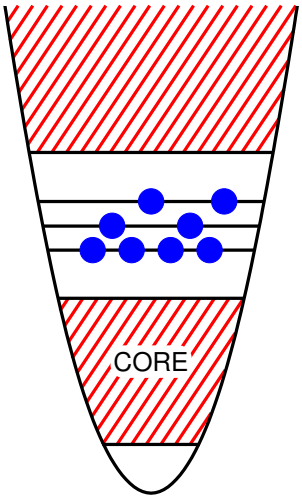

Figure 5.12: Defined valence space for shell model. At the bottom is the core part; then, going upwards, there is the valence and external space.

Instead of solving the Schrödinger equation in the (infinite) Hilbert space, the shell model seeks solutions within the valence space using an "effective" interaction that takes into account the interactions that are not considered in the starting mean field and the fact that we do not solve the complete A-body problem. This effective interaction can be diagonalized in a spherical Slater determinant basis:

$$H\Psi = E\Psi \longrightarrow H_{eff}\Psi_{eff} = E_{eff}\Psi_{eff} \tag{5.3}$$

It was demonstrated by [Zuker 95] and [Dufour 96] that any effective interaction can be split into two parts:

$$H_{eff} = H_m + H_M \tag{5.4}$$

where H_m represents the monopole part responsible for global saturation properties and the evolution of spherical single-particle levels. H_M is the multipole part, accounting for correlations and detailed spectroscopy, including pairing, quadrupole, and octupole deformations. On one side, H_m can be expressed as:

$$H_m = E_0 + \sum_i n_i\epsilon_i + \sum_{i\leq j} \frac{n_i(n_j - \delta_{ij})}{1+\delta_{ij}} V_{ij} \tag{5.5}$$

where E_0 represents the binding energy of the inert core, n_i or n_j represents the number of nucleons in the i-th or j-th orbitals, ϵ_i is the effective single-particle energy of the i-th orbital defined by the starting mean field, and V_{ij} is the nucleon-nucleon interaction for nucleons in the i-th and j-th orbitals. Finally, δ_{ij}, the Kronecker delta, is a function equal to 1 if i and j are identical and 0 otherwise.

On the other side, H_M can be represented in two forms, particle-particle and particle-hole, both of which can be diagonalized. This diagonalization reveals that only a few

terms are coherent, making the computation of the multipole part well-understood and manageable.

5.5.2 Spectroscopy

In this study, the core used is ^{48}Ca, and the valence space is illustrated in Figure 5.1. The Lenzi-Nowacki-Poves-Sieja (LNPS) interaction is used because it is known to provide a good description of the island of inversion at $N = 40$. This effective interaction is derived from a G-matrix based on a realistic nucleon-nucleon potential. The monopole part of this interaction is empirically corrected to produce effective single-particle energies (ϵ_i in formula 5.5.1) that align with experimental data (for more details on this interaction, see [Lenzi 10]). This interaction is diagonalized in the following with two methods: the standard Large Scale Shell Model (LSSM) and the newly developed Discrete NonOrthogonal Shell Model (DNO-SM), an alternative of LSSM to describe the deformed states by diagonalizing in a deformed Slater determinant basis. In principle, both approaches converge towards the same solutions.

Figure 5.13 presents the theoretical and experimental energy spectra for $^{65,67-71}$Co, separately for odd-even and odd-odd cases. Concerning the odd-even cases, the decrease in energy of the $1/2^-$ intruder states was well reproduced, although their energies were found to be too low. Therefore, fine adjustments were made to the $N = 40$ gap by ensuring that the properties of other nuclei in the region remain well reproduced. The spectrum computed with LSSM is now in rather good agreement with the experiment.

The case of the odd-odd nuclei is much more complicated as multiple states are computed, and one can see that the description from LSSM calculations is less satisfactory. As a starting point, we can see that the inversion of the intruder and "normal" state is clearly reproduced in the ^{70}Co. On the contrary, for the particular case of the ^{68}Co, the excitation energy is very low and the model struggles to accurately reproduce the correct ordering of the states as their relative position is highly sensitive to subtle details of the interactions.

Even if the ordering of the states is different in the experiment and the calculations, it is still interesting to look at the composition of the different states. For this purpose, the occupancies of the ground and excited states in $^{67-70}$Co have been computed with LSSM and are displayed in Figure 5.14, illustrating the occupancy differences between excited states in $^{67-70}$Co and their respective ground states. It was already mentioned that the theoretical ordering for the particular case of ^{68}Co was not reproducing the measurements. Consequently, the ordering in Figure 5.14 for this nucleus is the experimental one.

For the proton side (left part of Figure 5.14) of ^{67,68,69}Co, the excited state corresponds to the promotions of protons from the lower $f_{7/2}$ orbital towards the higher $p_{3/2}$, $f_{5/2}$ and $p_{1/2}$ orbitals. In contrast, the situation is inverted in ^{70}Co, for which the ground state contains more protons in the highest orbitals. For the neutron side (right part of

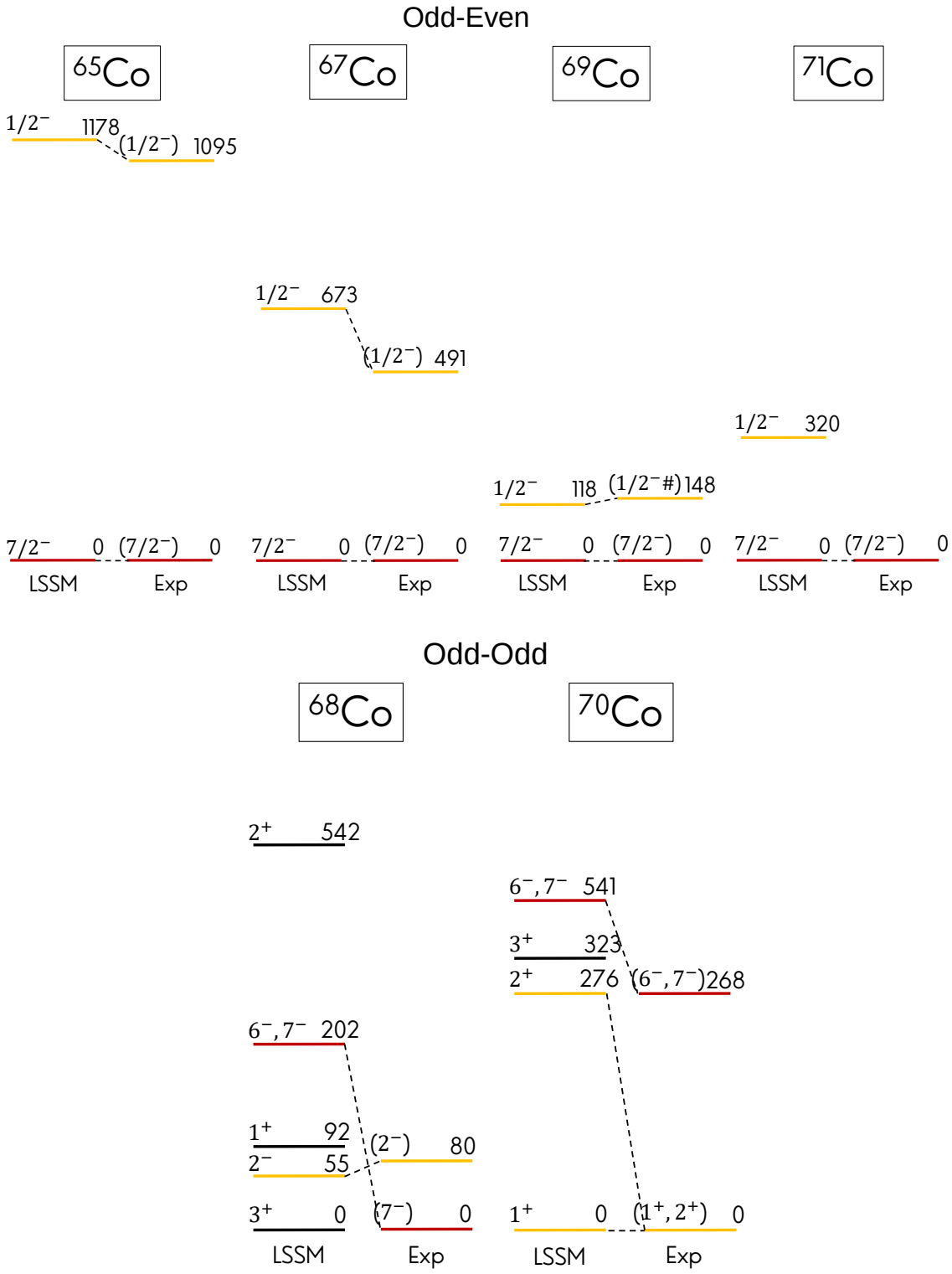

Figure 5.13: Energy spectrum for $^{65,67-71}$Co with LSSM calculation compared to experiments for odd-even nucleus on the top and odd-odd on the bottom. The orange states are interpreted as intruder-deformed states, and the red ones are the spherical "normal" states.

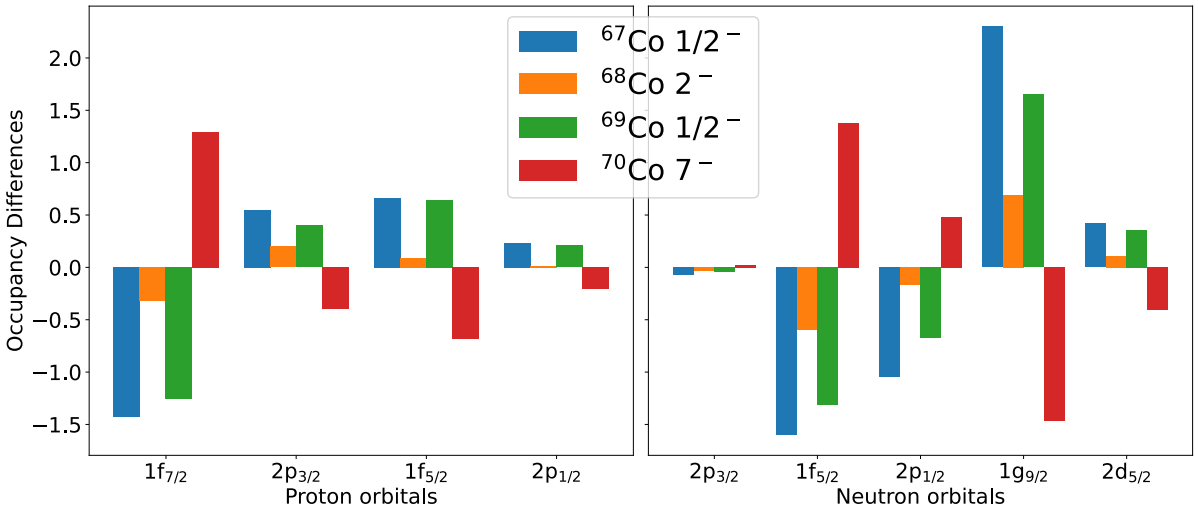

Figure 5.14: Occupancy differences between excited states in $^{67-70}$Co with their respective ground states. Proton orbitals are displayed on the left part, and neutron orbitals on the right.

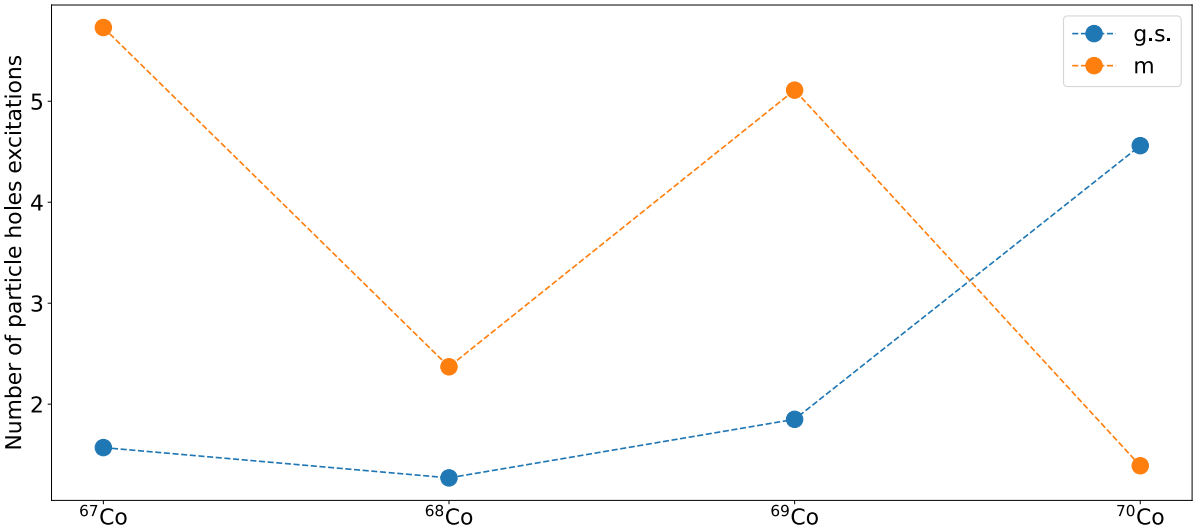

Figure 5.15: Number of proton and neutron excitations for the $^{67-70}$Co ground state and isomeric state.

Figure 5.14) of ^{67,68,69}Co, the excited state corresponds to the promotions of neutrons from the lower $p_{3/2}$, $f_{5/2}$ and $p_{1/2}$ orbitals towards the higher $g_{9/2}$ and $d_{5/2}$ orbitals. In contrast, the situation is inverted in ^{70}Co, for which the ground state contains more neutrons in the highest orbitals. Therefore, we observe an inversion in ordering between the intruder (deformed) and "normal"(spherical) state of ^{69}Co and ^{70}Co. Figure 5.15 plots the number of excited protons and neutrons in $^{67-70}$Co ground and isomeric state. Once again, this plot shows the clear inversion in ordering between "normal" and intruder state.

5.5.3 Binding energies

The previous section explained that the effective Hamiltonian can be divided into two parts (see equation 5.4). While the multipolar part is well understood, the monopolar part requires a phenomenological correction.

The Hamiltonian H_m can be rewritten to separate a global term H_0, which depends only on the total number of particles above the core nuclei $n = \sum_i n_i$, from two other terms H_1 and H_2 [Zuker 94]. The phenomenological correction made on the monopolar part will be done using this H_0 term, which is defined as:

$$H_0^{2N,\boldsymbol{3N}} = n\epsilon_0 + \frac{n(n-1)}{2}W_0 + \frac{\boldsymbol{n(n-1)(n-2)}}{\boldsymbol{6}}\boldsymbol{W_d} \tag{5.6}$$

Here, ϵ_0, W_0, and W_d are parameters that can be adjusted. The W_0 term accounts for 2-body interactions and W_d for 3-body interactions. Typically, the three-body term is not required, but its necessity will be evaluated in our particular case. The overall spectroscopy will remain unchanged by applying this phenomenological correction that depends only on the number of nucleons. This correction will, therefore, only modify the binding energies.

The left side of Figure 5.16 shows the difference in binding energies between experimental data and theoretical predictions for the chain of Cobalt isotopes. The binding energies are computed compared to ^{55}Co as it is at the edge of the operating region of the LNPS interaction (above $N = 28$). The first fit shown in blue is done without the 3-body term, labeled H_0^{2N} in the plot, and we see that the calculated binding energies cannot fully reproduce the trend of the experimental data. For a better agreement between calculations and experimental data, the red curve on the left represents the resulting fit performed with the 3-body term. The 3-body correction provides a final root-mean-square (RMS) of 170 keV, whereas the 2-body fit provides an RMS of 513 keV. This confirms that adding the 3-body term is needed in this region. The right side of the same figure shows the difference between experiment and theory with the correction. Figure 5.17 shows how well the fit with the 3-body is improving the LSSM binding energies. Before correction, the difference is clearly visible, whereas after corrections, the two curves completely overlap.

The necessity of the 3-body term was also studied in the nickel isotopic chain. The masses of isotopes between ^{56}Ni and ^{75}Ni were computed with LSSM and compared to the AME, coupled with the two newly measured ^{74}Ni and ^{75}Ni mass excesses [Giraud 22]. Figure 5.18 shows the difference between the theoretical results and these experimental data. Once again, the improvement of using 3-body instead of only 2-body is evident as the RMS for 3-body is 207 keV compared to 893 keV with only 2-body interactions.

Now that the correction on the binding energy has been applied, it is interesting to look at the S_{2n}. Figure 5.19 shows the S_{2n} derived from experimental mass values, as well as the ones from uncorrected LSSM calculations and corrected with H_0^{2N} and H_0^{3N}.

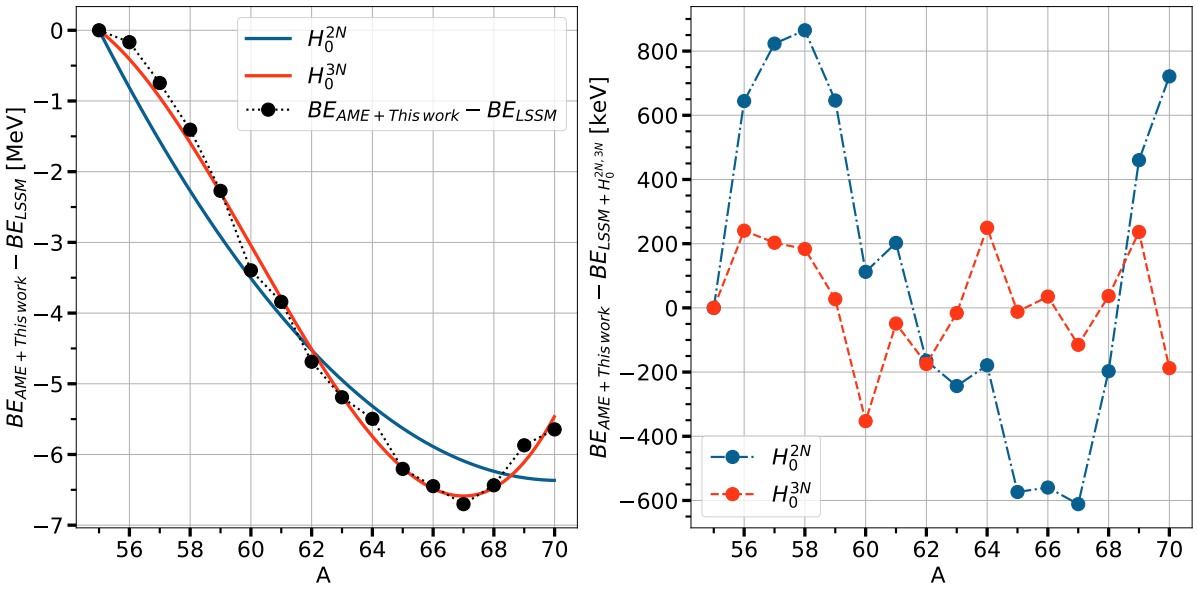

Figure 5.16: Difference of binding energies between experiment and theory as a function of A for cobalt isotopes before on the left and after correction on the right. The red curve is the fit result of the H_0^{3N} function. The blue curve is the fit result of the H_0^{2N} function. Uncertainty from AME is not visible at this scale, and the uncertainty from the theory is not determined.

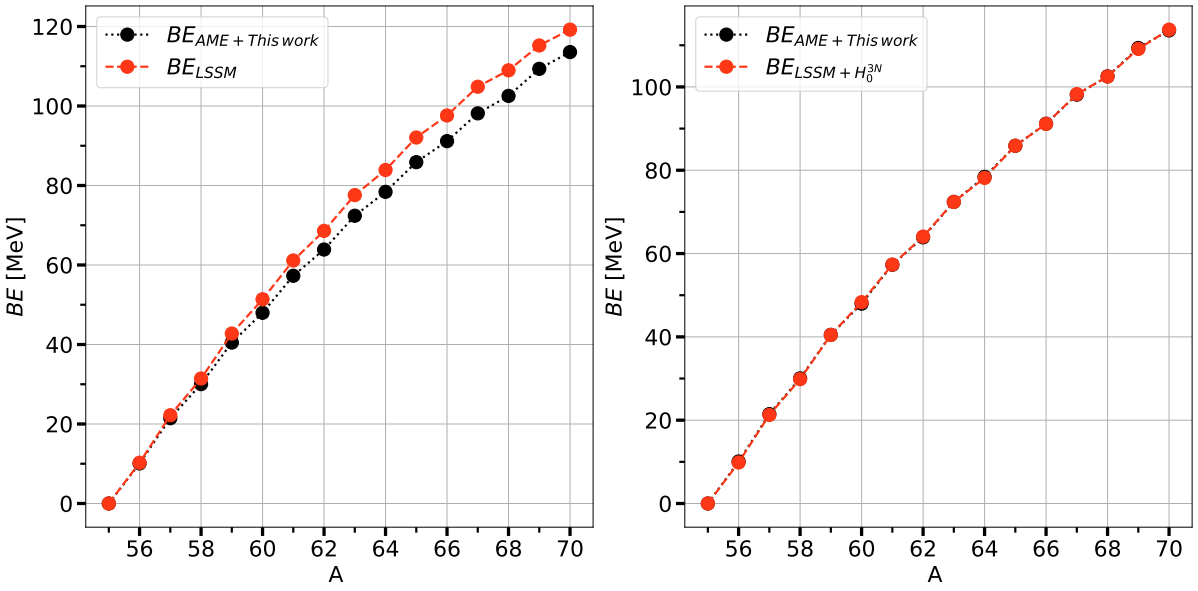

Figure 5.17: Binding energies of experiment and theory as a function of A before on the left and after correction on the right. This is shown for the cobalt isotopic chain.

Once again, it is clear that the H_0^{3N} correction is needed so that the theory agrees with the general trend of experimental values. In addition, the change visible in the general trend of experimental S_{2n} at $N = 68$ is also observed in the computations. This highlights the need for further mass measurement toward neutron-rich cobalt isotopes to study the evolution of the S_{2n} beyond $A = 70$.

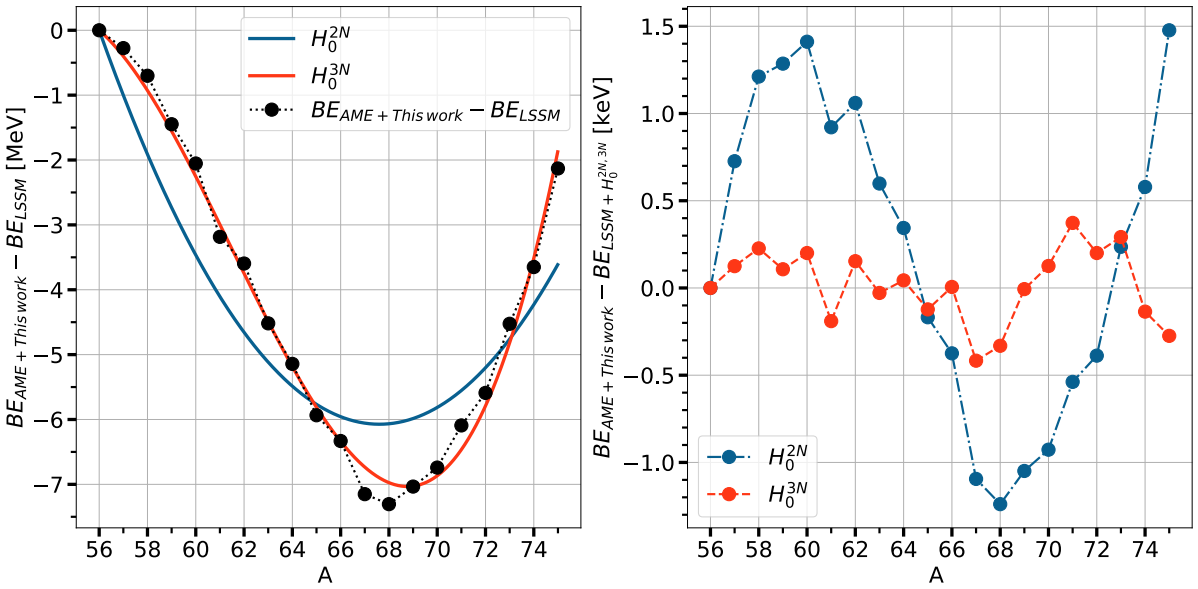

Figure 5.18: Difference of binding energies between experiment and theory as a function of A for nickel isotopes before on the left and after correction on the right. The red curve is the fit result of the H_0^{3N} function. The blue curve is the fit result of the H_0^{2N} function.

5.5.4 Potential energy surface (PES)

In this section, the ground and isomeric states of cobalt and nickel isotopes will be studied with regard to shape and deformation with DNO-SM. The results in this section come from the work conducted by D.D. Dao.

It was mentioned at the end of section 5.1.2 that in ^{68}Ni, shape coexistence between spherical and deformed states occurs. The same shape coexistence was shown for the Cobalt isotopes in the present work, and a useful method to visualize these deformed states is to examine the content of the wave function using the potential energy surface.

The potential energy surface is computed through the constrained Hartree-Fock method using the same LNPS interaction within the same valence space used for the spectroscopy. The constraints are defined by the quadrupole moments (q_{20}, q_{22}) and the total quadrupole moment ($Q = \sqrt{q_{20}^2 + q_{22}^2}$) as follows:

$$\begin{cases} \beta = \frac{b^2 Q \sqrt{5\pi}}{3 r_0^2 A^{5/3}} \\ \gamma = \arctan(\frac{q_{22}}{q_{20}}) \end{cases} \tag{5.7}$$

where b^2 (in fm^2) is the harmonic oscillator parameter [Brussaard 78], [Suhonen 07],

$$b^2 = \frac{41.4}{45A^{-1/3} - 25A^{-2/3}} \tag{5.8}$$

and A and $r_0 = 1.2\ fm$ are the nuclear mass number and radius parameters. Each point (β, γ) of Figure 5.20 represents a Hartree-Fock deformed Slater determinant with which we construct the deformed Hartree-Fock basis. Instead of performing an exact diagonalization

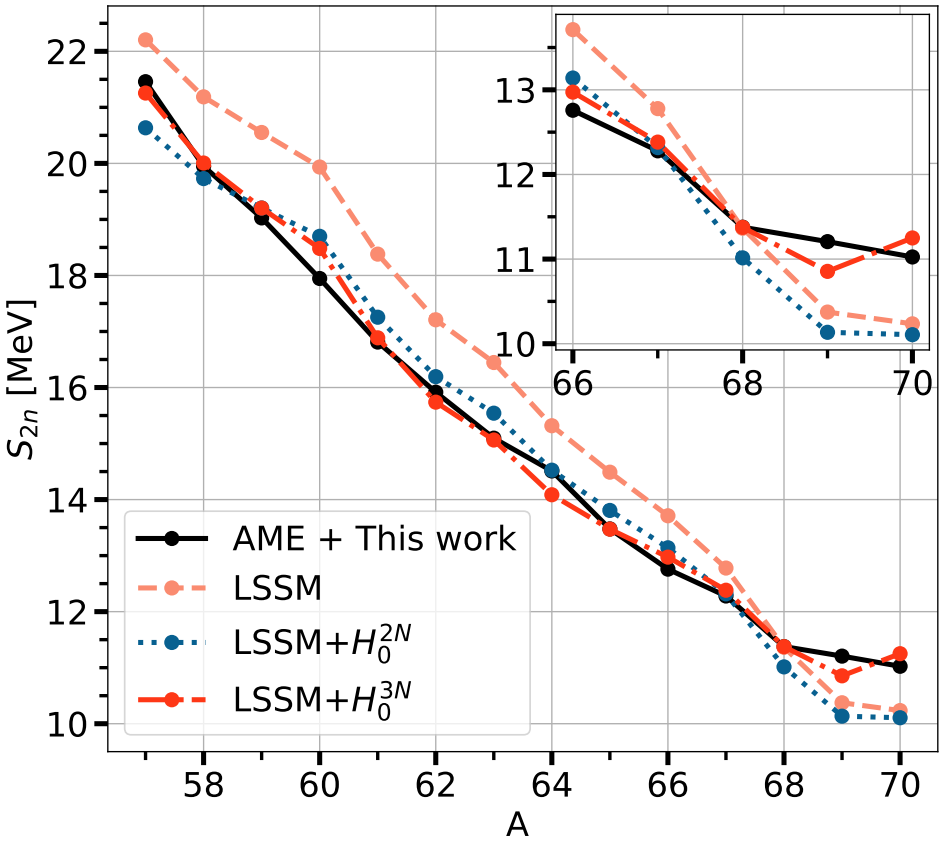

Figure 5.19: Two neutrons separation energies taken from experimental mass values in black, as well as the ones from uncorrected LSSM calculations in salmon and corrected with H_0^{2N} in blue and H_0^{3N} in red. Uncertainty from AME is not visible at this scale, and the uncertainty from the theory is not determined.

as the LSSM calculation, we perform the diagonalization of the LNPS Hamiltonian in this deformed Hartree-Fock basis by minimizing specific nuclear states of interest, taking into account the restoration of the rotation symmetry by angular momentum projection technique. In the following, the so-called single states are defined by a single (β, γ) combination corresponding to the minima of the PES region of the studied state. The minimization of the mix of state is then carried out within the Discrete NonOrthogonal Shell Model (DNO-SM) where only relevant (β, γ) points contributing the most in energy are selected (for details, see [Dao 22]). By using this deformed basis, the DNO-SM can compute more complex cases (e.g. heavy nuclei) than LSSM.

It was demonstrated in a recent paper [Nies 23] that the PES can be an appropriate theoretical tool to interpret shape-coexistence and to provide a direct link between neighboring even- and odd-nuclei with regard to nuclear shape mixing. A similar study will be conducted in this work.

Figure 5.20 displays the PES for the ground state and deformed excited states in ^{67}Co and ^{68}Ni. The surface of the circles represents the normalized probability of finding a deformation point (β, γ) in the corresponding state. An apparent similarity is observed

between the spherical ground states of ^{67}Co $(7/2^-)$ and ^{68}Ni (0_1^+), and the deformed excited states of ^{67}Co $(1/2^-)$ and ^{68}Ni (0_3^+). Additionally, it can be noted that the removal of one proton lowers the excitation level.

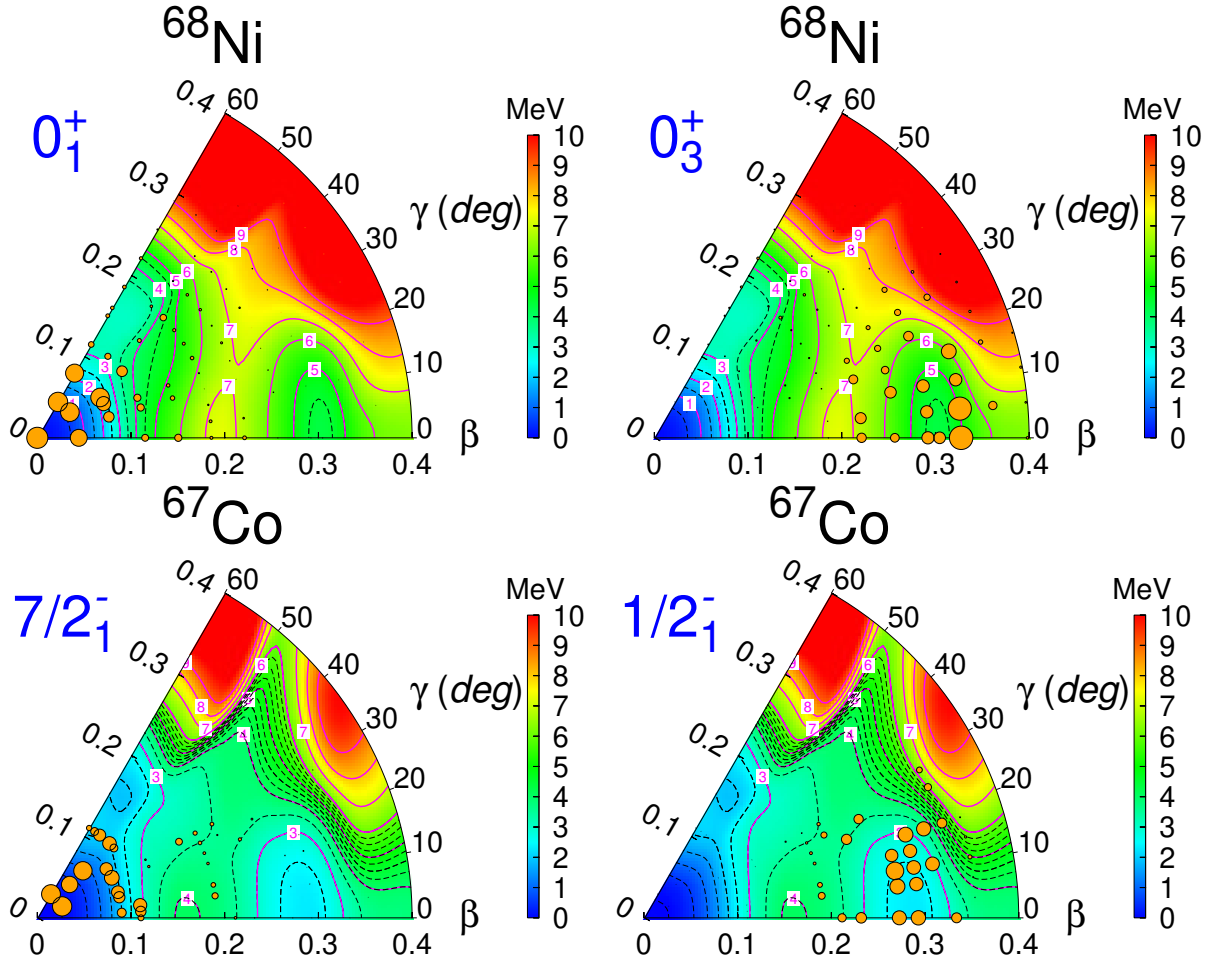

Figure 5.20: PES for ground state (left) and deformed excited states (right) in ^{67}Co (top) and ^{68}Ni (bottom). The surface of the circles represents the normalized probability of finding a deformation point (β, γ) in the corresponding state.

As for the LSSM, the DNO-SM technique provides access to the occupations of the different states. It is also important to note that using either a single state or a mix of states will result in nearly identical occupancies. This is demonstrated in Figure 5.21. In this figure, the similarities between ^{67}Co and ^{68}Ni are once again clearly evident.

Figure 5.22 shows the computed spectrum for ^{67}Co using various methods. The left-most spectrum is obtained by considering only one state in a potential energy surface (PES), while the DNO-SM spectrum is obtained by mixing multiple states. Despite the compression of the spectrum (compared to LSSM), which is primarily due to pairing [Borrajo 15], it does not impact the particle-hole structure (see Figure 5.21).

Such calculations are particularly complex for odd-odd nuclei. Therefore, examining neighboring isotopes' PES can give an idea of what their PES might look like for odd-odd cases. In this context, the PES for ^{69}Co and ^{70}Ni was also computed and is displayed in

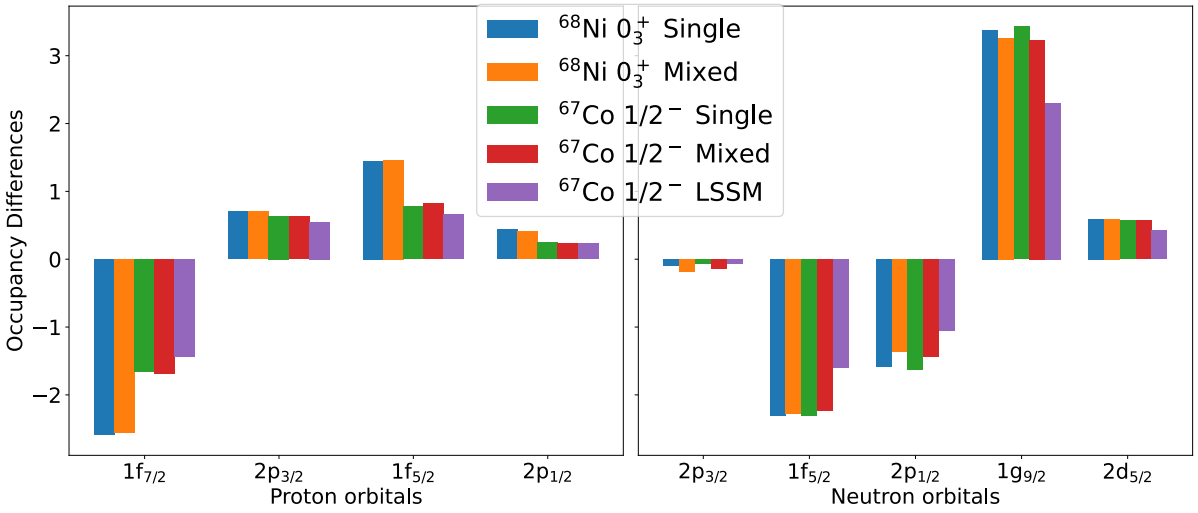

Figure 5.21: Occupancy differences between excited states in ^{67}Co, and ^{68}Ni with their respective ground states. These occupancy differences come from the DNO-SM calculation method and are computed for the mixed and single states. The ^{67}Co, the occupancies difference is also shown when computed with LSSM.

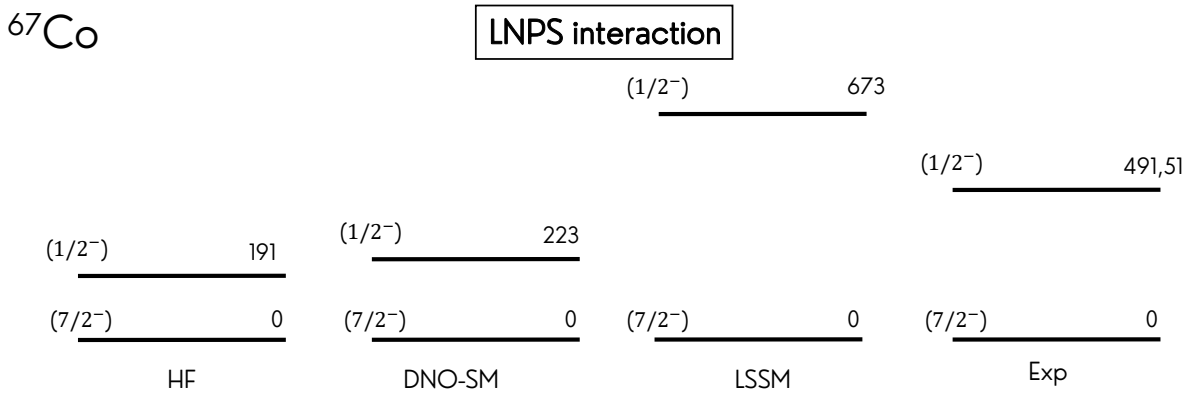

Figure 5.22: Comparison of the $1/2^-$ state of ^{67}Co between the previously shown LSSM, experimental spectrum, and the other calculation methods. HF represents the spectrum obtained by taking only one state in a PES, and then by computing the spectra with a mix of states, it gives the DNO-SM spectrum.

Figure 5.23. This intruder state decreases in energy from ^{68}Ni to ^{70}Ni making it closer to the ground state energy. This is even more pronounced for ^{69}Co, where the intruder state is nearly at the same level as the ground state, which is in complete agreement with the results of this experiment. The different parentalities between even-even nickel and odd-even give a good insight into the odd-odd cobalt isotope configurations. This makes the DNO-SM a very efficient and powerful model to approximate and visualize the different states in the region N=40.

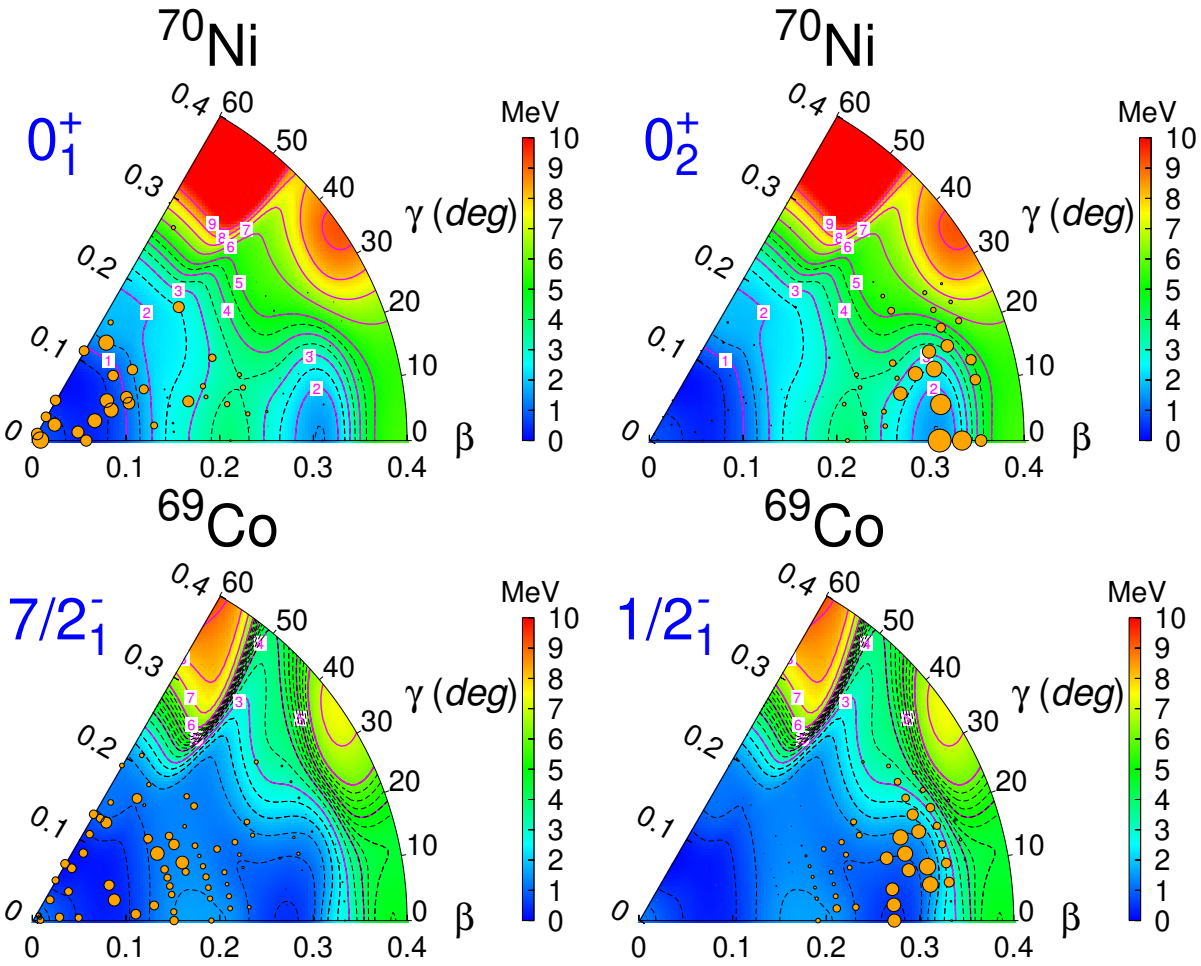

Figure 5.23: PES for ground state (left) and deformed excited states (right) in ^{69}Co and ^{70}Ni. The surface of the circles represents the normalized probability of finding a deformation point (β, γ) in the corresponding state.

Conclusions and perspectives

This work presented the trapping of ions in PIPERADE, allowing their cooling to be optimized. This was followed by successfully applying the buffer gas cooling technique with a resolving power of $\frac{\nu_c}{\Delta\nu_c} \approx 2\times10^5$, preparing the ions for precise mass measurements. In addition, the studies on ion transfer between traps and the optimization of ion bunches using 2D scans were crucial for minimizing time-of-flight dispersion and limiting the energy transmission to the ions.

The ToF-ICR technique was used to perform the first high-precision mass measurements on PIPERADE with accumulation times up to 1 s. Despite initial limitations due to gas pressure effects, which led to the modification of the diaphragm size, the data collected showed promising results. Furthermore, a thorough study of the magnetic field's influence was conducted, and optimization of the correction electrodes was achieved, significantly improving the harmonicity of the electrical field.

Parallel to this, the new MCP detector with three delay-line anodes was installed and commissioned, allowing the implementation of the PI-ICR technique. This technique was also successfully implemented on PIPERADE, further expanding the system's capabilities and allowing for the first PI-ICR mass measurements performed at 100 ms. Further, improvements like a new reduction of the diaphragm's opening size or better control of temperature and pressure will greatly help improve both techniques and demonstrate the versatility and potential of PIPERADE in nuclear mass measurements. Overall, this work has demonstrated significant advancements in ion cooling, trapping, and mass measurement techniques, positioning PIPERADE as a valuable tool in nuclear physics.

Several steps remain to be undertaken in order to further optimize and enhance the performance of PIPERADE. These can be divided into near-term improvements and long-term developments.

In the near future, efforts will focus on fine-tuning the transfer and extraction potentials to improve ion handling, overall efficiency, and reliable and non-distorted image projection. Another point of interest will be the exploration of lower voltage differences during the trapping process, reducing the current value from -80 V to -10 V, with the aim of achieving improved confinement conditions and reducing uncertainty in both PI-ICR

and ToF-ICR mass measurement techniques. The characterization of the MCP, as well as the development of its associated reconstruction program, will be a crucial step . Additionally, the installation of an attenuation grid in front of the MCP detector will enable systematic studies of cooling and trapping with larger ion bunches. An important step will also involve aligning the traps, magnet, and extraction electrodes system using the precision technique of PI-ICR, ensuring that PIPERADE's setup is optimally configured for future experiments. Moreover, the maximum resolving power achievable with phase-dependent cleaning (PDC) in the second trap will be studied, as this will help assess the full capacity of the system for ion separation. Finally, a detailed investigation of the systematic effects related to the magnetic (B) and electric (E) fields will be necessary to reduce sources of error and refine the overall measurement precision.

Looking further ahead, there are several ambitious long-term developments planned. One such advancement involves testing the operation of the Penning trap without buffer gas, which will subsequently allow for the implementation of laser cooling, followed by the combined use of PDC and PI-ICR techniques. This combination would significantly enhance the precision of measurements and ion purification. Additionally, an important long-term goal is to achieve full integration of PIPERADE with other DESIR devices, including the High-Resolution Separator (HRS) and the Multi-Reflection Time-Of-Flight (MRTOF) mass spectrometer. The coupling of these systems will allow for the production of highly purified ion beams, facilitating more accurate measurements across a broader range of isotopes and significantly contributing to the scientific program at DESIR.

Finally, mass measurements were carried out during an experiment with the JYFLTRAP system at the IGISOL facility, providing essential data for nuclei around the neutron-rich $N = 40$ region. The masses of the $^{68-70}$Co isotopes, both in their ground and isomeric states, have been measured, with the isomeric states of ^{68}Co and ^{70}Co being measured for the first time. Additionally, the masses of ^{73}Ni and ^{79}Ge have been determined. These results represent a significant achievement, with substantial reductions in experimental uncertainties for these nuclides. These results offered valuable insights into nuclear structure and contributed significantly to the overall objectives of this thesis. The experiment in Jyväskylä also enabled collaboration with leading experts and working with advanced detectors, reinforcing the broader scientific context of this research. Moreover, the isomer's excitation energies were computed with LSSM calculations and compared with the experimental results. In addition, a phenomenological correction was applied to the binding energies to reproduce and study the S_{2n} trends in the cobalt and nickel isotopes. Furthermore, the potential energy surfaces (PES) were examined to better comprehend the deformation effects and shape coexistence in certain nuclei. This work has presented promising preliminary discussions regarding nuclear structure, which will be pursued after this thesis.

Two articles are currently being prepared based on the data collected. Additionally, a

broader study on the binding energies in the region of the island of inversion is planned, which will provide deeper insights into the nuclear structure in this critical area. In the long term, a future operational MR-ToF system will allow for the investigation of more exotic nuclei.

Bibliography

[Ackermann 24] Ackermann, D. and Antalic, S. and Heßberger, F. P. *Isomers in superheavy nuclei*. The European Physical Journal Special Topics, vol. 233, no. 5, pages 1017–1036, 2024. doi:10.1140/epjs/s11734-024-01150-1. (Back to page 20)

[ANJ] ANJ. *EPICS Home at Argonne*. https://epics.anl.gov/index.php. (Back to page 64)

[Aoi 09] N. Aoi *et al.* *Development of Large Deformation in* ^{62}Cr. Phys. Rev. Lett., vol. 102, page 012502, Jan 2009. doi:10.1103/PhysRevLett.102.012502. (Back to page 109)

[Aouadi 17] Aouadi, Mehdi. *Détermination du rapport d'embranchement de la transition super-permise du carbone 10 et développement et intégration de la ligne de faisceau PIPERADE au CENBG*. Theses, Université de Bordeaux, December 2017. (Back to page 48)

[Ascher 21] P. Ascher *et al.* *PIPERADE: A double Penning trap for mass separation and mass spectrometry at DESIR/SPIRAL2*. Nuclear Instruments and Methods in Physics Research Section A: Accelerators, Spectrometers, Detectors and Associated Equipment, vol. 1019, page 165857, 2021. doi:https://doi.org/10.1016/j.nima.2021.165857. (Back to page 27, 28, 44, 52, 54)

[Beck 09] D. Beck *et al.* *Electric and magnetic field optimization procedure for Penning trap mass spectrometers*. Nuclear Instruments and Methods in Physics Research Section A: Accelerators, Spectrometers, Detectors and Associated Equipment, vol. 598, no. 2, pages 635–641, 2009. doi:https://doi.org/10.1016/j.nima.2008.09.019. (Back to page 99)

[Bethe 36] Bethe, H. A. and Bacher, R. F. *Nuclear Physics A. Stationary States of Nuclei.* Rev. Mod. Phys., vol. 8, pages 82–229, Apr 1936. doi:10.1103/RevModPhys.8.82. (Back to page 11)

[Blaum 06] Klaus Blaum. *High-accuracy mass spectrometry with stored ions.* Physics Reports, vol. 425, no. 1, pages 1–78, 2006. doi:https://doi.org/10.1016/j.physrep.2005.10.011. (Back to page 39)

[Borrajo 15] Marta Borrajo and Tomás R. Rodríguez and J. Luis Egido. *Symmetry conserving configuration mixing method with cranked states.* Physics Letters B, vol. 746, pages 341–346, 2015. doi:https://doi.org/10.1016/j.physletb.2015.05.030. (Back to page 132)

[Broda 95] R. Broda *et al.* $N = 40$ *Neutron Subshell Closure in the* ^{68}Ni *Nucleus.* Phys. Rev. Lett., vol. 74, pages 868–871, Feb 1995. doi:10.1103/PhysRevLett.74.868. (Back to page 108)

[Brussaard 78] Brussaard, P. J. and Glaudemans, P. W. M. and Klein, Abraham. *Shell-Model Applications in Nuclear Spectroscopy.* Physics Today, vol. 31, no. 11, pages 68–70, 11 1978. doi:10.1063/1.2994818. (Back to page 130)

[Canete 20] L. Canete *et al. Precision mass measurements of* ^{67}Fe *and* ^{69,70}Co*: Nuclear structure toward* $N = 40$ *and impact on r-process reaction rates.* Phys. Rev. C, vol. 101, page 041304, Apr 2020. doi:10.1103/PhysRevC.101.041304. (Back to page 111, 112, 113, 117, 118, 119)

[Caurier 02] Caurier, E. and Nowacki, F. and Poves, A. *Large-scale shell model calculations for exotic nuclei.* The European Physical Journal A, vol. 15, pages 145–150, 2002. doi:https://doi.org/10.1140/epja/i2001-10243-7. (Back to page 109, 110)

[Caurier 05] E. Caurier *et al. The shell model as a unified view of nuclear structure.* Rev. Mod. Phys., vol. 77, pages 427–488, Jun 2005. doi:10.1103/RevModPhys.77.427. (Back to page 123)

[Clement 03] R.R.C. Clement *et al. Sensitivities of rp-process calculations to nuclear mass uncertainties.* Nuclear Physics A, vol. 718, pages 617–619, 2003. doi:https://doi.org/10.1016/S0375-9474(03)00903-5. (Back to page 19)

[Dao 22] Dao, D. D. and Nowacki, F. *Nuclear structure within a discrete nonorthogonal shell model approach: New frontiers.* Phys. Rev. C, vol. 105, page 054314, May 2022. doi:10.1103/PhysRevC.105.054314. (Back to page 131)

[Daudin 22] L. Daudin *et al.* *CENBG Control System and Specific Instrumentation Developments for SPIRAL2-DESIR Setups.* In Proc. ICALEPCS'21, numéro 18 in International Conference on Accelerator and Large Experimental Physics Control Systems, pages 98–103. JACoW Publishing, Geneva, Switzerland, 03 2022. doi:10.18429/JACoW-ICALEPCS2021-MOPV002. (Back to page 50, 55, 64, 66)

[Droese 11] Ch. Droese *et al.* *Investigation of the magnetic field fluctuation and implementation of a temperature and pressure stabilization at SHIPTRAP.* Nuclear Instruments & Methods in Physics Research Section A-accelerators Spectrometers Detectors and Associated Equipment, vol. 632, pages 157–163, 2011. (Back to page 28)

[Dufour 96] Dufour, Marianne and Zuker, Andres. *The realistic collective nuclear Hamiltonian.* Phys. Rev. C, vol. 54, pages 1641–1660, 1996. doi:10.1103/PhysRevC.54.1641. (Back to page 124)

[Ekström 92] L.P. Ekström and J. Lyttkens-Linden. *Nuclear data sheets for A = 90.* Nuclear Data Sheets, vol. 67, no. 4, pages 579–691, 1992. doi:https://doi.org/10.1016/0090-3752(92)80027-H. (Back to page 108)

[Eliseev 13] S. Eliseev *et al.* *A phase-imaging technique for cyclotron-frequency measurements.* Applied Physics B: Lasers and Optics, vol. 114, pages 396–, 09 2013. doi:10.1007/s00340-013-5621-0. (Back to page 40)

[Eronen 12] T. Eronen *et al.* *JYFLTRAP: a Penning trap for precision mass spectroscopy and isobaric purification.* The European Physical Journal A, vol. 48, no. 4, page 46, 2012. doi:10.1140/epja/i2012-12046-1. (Back to page 107, 114)

[Flavigny 15] F. Flavigny *et al.* *Characterization of the low-lying* 0^+ *and* 2^+ *states in* ^{68}Ni *via* β *decay of the low-spin* ^{68}Co *isomer.* Phys. Rev. C, vol. 91, page 034310, Mar 2015. doi:10.1103/PhysRevC.91.034310. (Back to page 111, 119)

[Frånberg 08] H. Frånberg *et al.* *Off-line commissioning of the ISOLDE cooler.* Nuclear Instruments and Methods in Physics Research Section B: Beam Interactions with Materials and Atoms, vol. 266, no. 19, pages 4502–4504, 2008. Proceedings of the XVth International Conference on Electromagnetic Isotope Separators and Techniques Related to their Applications, doi:https://doi.org/10.1016/j.nimb.2008.05.097. (Back to page 45)

[Gabrielse 89] G. Gabrielse and L. Haarsma and S.L. Rolston. *Open-endcap Penning traps for high precision experiments.* International Journal of Mass Spectrometry and Ion Processes, vol. 88, no. 2, pages 319–332, 1989. doi:https://doi.org/10.1016/0168-1176(89)85027-X. (Back to page 27)

[Gade 19] A. Gade *et al.* *Is the Structure of* ^{42}Si *Understood?* Phys. Rev. Lett., vol. 122, page 222501, Jun 2019. doi:10.1103/PhysRevLett.122.222501. (Back to page 19)

[Gamow 30] G. Gamow. *Mass defect curve and nuclear constitution.* Proceedings of the Royal Society A: Mathematical, Physical and Engineering Sciences, vol. 126, no. 801, pages 632–649, 1930. doi:10.1098/rspa.1930.0032. (Back to page 11)

[Gerbaux 23] Mathias Gerbaux *et al.* *The General Purpose Ion Buncher: a radiofrequency quadrupole cooler-buncher for DESIR at SPIRAL2.* Nuclear Instruments and Methods in Physics Research Section A: Accelerators, Spectrometers, Detectors and Associated Equipment, vol. 1046, page 167631, 2023. doi:10.1016/j.nima.2022.167631. (Back to page 44)

[Giraud 22] S. Giraud *et al.* *Mass measurements towards doubly magic 78Ni: Hydrodynamics versus nuclear mass contribution in core-collapse supernovae.* Physics Letters B, vol. 833, page 137309, 2022. doi:https://doi.org/10.1016/j.physletb.2022.137309. (Back to page 128)

[Guerin 14] Guerin, Hugo. *Développement d'un refroidisseur-regroupeur quadripolaire radiofréquence pour PIPERADE et mesure de la demi-vie de 17F.* Theses, Université de Bordeaux, December 2014. (Back to page 48)

[Hannawald 99] M. Hannawald *et al.* *Decay of Neutron-Rich Mn Nuclides and Deformation of Heavy Fe Isotopes.* Phys. Rev. Lett., vol. 82, pages

1391–1394, Feb 1999. doi:10.1103/PhysRevLett.82.1391. (Back to page 109)

[Hao 23] Y.W. Hao and Y.F. Niu and Z.M. Niu. *Sensitivity of the r-process rare-earth peak abundances to nuclear masses.* Physics Letters B, vol. 844, page 138092, 2023. doi:https://doi.org/10.1016/j.physletb.2023.138092. (Back to page 19)

[Hardy 20] Hardy, J. C. and Towner, I. S. *Superallowed $0^+ \rightarrow 0^+$ nuclear β decays: 2020 critical survey, with implications for V_{ud} and CKM unitarity.* Phys. Rev. C, vol. 102, page 045501, Oct 2020. doi:10.1103/PhysRevC.102.045501. (Back to page 19)

[Haxel 49] Haxel, Otto and Jensen, J. Hans D. and Suess, Hans E. *On the "Magic Numbers" in Nuclear Structure.* Phys. Rev., vol. 75, pages 1766–1766, Jun 1949. doi:10.1103/PhysRev.75.1766.2. (Back to page 14)

[Hillert 21] Hillert, Wolfgang. *Transverse Linear Beam Dynamics.* arXiv e-prints, page arXiv:2107.02614, July 2021. doi:10.48550/arXiv.2107.02614. (Back to page 48, 49)

[Huang 17] W.J. Huang *et al.* *The AME2016 atomic mass evaluation (I). Evaluation of input data; and adjustment procedures.* Chin.Phys.C, vol. 41, no. 3, page 030002, 2017. doi:10.1088/1674-1137/41/3/030002. (Back to page 112, 119)

[Huang 21] W.J. Huang *et al.* *The AME 2020 atomic mass evaluation (I). Evaluation of input data, and adjustment procedures*.* Chinese Physics C, vol. 45, no. 3, page 030002, mar 2021. doi:10.1088/1674-1137/abddb0. (Back to page 17, 95, 112, 117, 118, 121)

[Izzo 18] C. Izzo *et al.* *Precision mass measurements of neutron-rich Co isotopes beyond $N = 40$.* Phys. Rev. C, vol. 97, page 014309, Jan 2018. doi:10.1103/PhysRevC.97.014309. (Back to page 111, 112, 117, 118, 119, 121)

[Jagutzki 02] O. Jagutzki *et al.* *Multiple hit readout of a microchannel plate detector with a three-layer delay-line anode.* IEEE Transactions on Nuclear Science, vol. 49, no. 5, pages 2477–2483, 2002. doi:10.1109/TNS.2002.803889. (Back to page 57, 60)

[Jamet 11] C. Jamet *et al.* *Beam diagnostic overview of the SPIRAL2 RNB section.* 10th European Workshop on Beam Diagnostics and Instrumentation for Particle Accelerators (DIPAC 2011), May 2011. Poster, https://in2p3.hal.science/in2p3-00625423. (Back to page 50)

[Kamil 21] M. Kamil *et al.* *Isospin mixing and the cubic isobaric multiplet mass equation in the lowest $T = 2$, $A = 32$ quintet.* Phys. Rev. C, vol. 104, page L061303, Dec 2021. doi:10.1103/PhysRevC.104.L061303. (Back to page 20)

[Karvonen 08] P. Karvonen *et al.* *A sextupole ion beam guide to improve the efficiency and beam quality at IGISOL.* Nuclear Instruments and Methods in Physics Research Section B: Beam Interactions with Materials and Atoms, vol. 266, no. 21, pages 4794–4807, 2008. doi:https://doi.org/10.1016/j.nimb.2008.07.022. (Back to page 114)

[Kondev 21] F.G. Kondev *et al.* *The NUBASE2020 evaluation of nuclear physics properties *.* Chinese Physics C, vol. 45, no. 3, page 030001, mar 2021. doi:10.1088/1674-1137/abddae. (Back to page 111, 113, 117)

[Kujanpää 23] S. Kujanpää *et al.* *RAPTOR: A new collinear laser ionization spectroscopy and laser-radiofrequency double-resonance experiment at the IGISOL facility.* Nuclear Instruments and Methods in Physics Research Section B: Beam Interactions with Materials and Atoms, vol. 541, pages 388–391, 2023. doi:https://doi.org/10.1016/j.nimb.2023.05.014. (Back to page 115)

[Lam 13] Yi Hua Lam *et al.* *The isobaric multiplet mass equation for A71 revisited.* Atomic Data and Nuclear Data Tables, vol. 99, no. 6, pages 680–703, 2013. doi:https://doi.org/10.1016/j.adt.2012.11.002. (Back to page 20)

[Lenzi 10] S. M. Lenzi *et al.* *Island of inversion around* ^{64}Cr. Phys. Rev. C, vol. 82, page 054301, Nov 2010. doi:10.1103/PhysRevC.82.054301. (Back to page 125)

[Lilley 01] J. S. Lilley. Nuclear physics: Principles and applications. Wiley, Chichester, UK, 2001. (Back to page 12)

[Ljungvall 10] J. Ljungvall *et al. Onset of collectivity in neutron-rich Fe isotopes: Toward a new island of inversion?* Phys. Rev. C, vol. 81, page 061301, Jun 2010. doi:10.1103/PhysRevC.81.061301. (Back to page 109)

[Lokotko 20] T. Lokotko *et al. Shell structure of the neutron-rich isotopes* ^{69,71,73}Co. Phys. Rev. C, vol. 101, page 034314, Mar 2020. doi:10.1103/PhysRevC.101.034314. (Back to page 112, 114)

[Lunardi 07] S. Lunardi *et al. Spectroscopy of neutron-rich Fe isotopes populated in the* ^{64}Ni+^{238}U *reaction.* Phys. Rev. C, vol. 76, page 034303, Sep 2007. doi:10.1103/PhysRevC.76.034303. (Back to page 109)

[Mayer 49] Mayer, Maria Goeppert. *On Closed Shells in Nuclei. II.* Phys. Rev., vol. 75, pages 1969–1970, Jun 1949. doi:10.1103/PhysRev.75.1969. (Back to page 14)

[Michaud 22] J. Michaud *et al. Status on the DESIR High Resolution Separator Commissioning*, 2022. (Back to page 44)

[Moore 13] I.D. Moore *et al. Towards commissioning the new IGISOL-4 facility.* Nuclear Instruments and Methods in Physics Research Section B: Beam Interactions with Materials and Atoms, vol. 317, pages 208–213, 2013. XVIth International Conference on ElectroMagnetic Isotope Separators and Techniques Related to their Applications, December 2–7, 2012 at Matsue, Japan, doi:https://doi.org/10.1016/j.nimb.2013.06.036. (Back to page 107, 114)

[Morales 17] A.I. Morales *et al. Type II shell evolution in A=70 isobars from the N40 island of inversion.* Physics Letters B, vol. 765, pages 328–333, 2017. doi:https://doi.org/10.1016/j.physletb.2016.12.025. (Back to page 111, 119)

[Mueller 99] W. F. Mueller *et al. Beta decay of neutron-rich Co: Probing single-particle states at and above the N=40 subshell closure.* AIP Conference Proceedings, vol. 481, no. 1, pages 264–267, 09 1999. doi:10.1063/1.59515. (Back to page 111)

[Mueller 00] W. F. Mueller *et al.* β *decay of* ^{66}Co, ^{68}Co, *and* ^{70}Co. Phys. Rev. C, vol. 61, page 054308, Apr 2000. doi:10.1103/PhysRevC.61.054308. (Back to page 111)

[Naimi 10] Naimi, Sarah. *Onsets of nuclear deformation from measurements with the isoltrap mass spectrometer*. PhD thesis, 2010. Thèse de doctorat dirigée par Lunney, David Champs, particules, matière Paris 7 2010. (Back to page 23)

[Nesterenko 18] Nesterenko, D. A. *Phase-Imaging Ion-Cyclotron-Resonance technique at the JYFLTRAP double Penning trap mass spectrometer*. The European Physical Journal A, vol. 54, 09 2018. doi:https://doi.org/10.1140/epja/i2018-12589-y. (Back to page 33, 35, 37, 114, 117)

[Nieminen 01] A. Nieminen *et al.* *Beam cooler for low-energy radioactive ions*. Nuclear Instruments and Methods in Physics Research Section A: Accelerators, Spectrometers, Detectors and Associated Equipment, vol. 469, no. 2, pages 244–253, 2001. doi:https://doi.org/10.1016/S0168-9002(00)00750-6. (Back to page 115)

[Nies 23] L. Nies *et al.* *Further Evidence for Shape Coexistence in* ^{79}Zn^{m} *near Doubly Magic* ^{78}Ni. Phys. Rev. Lett., vol. 131, page 222503, Nov 2023. doi:10.1103/PhysRevLett.131.222503. (Back to page 131)

[Nolen 69] Nolen, J A and Schiffer, J P. *Coulomb Energies*. Annual Review of Nuclear and Particle Science, vol. 19, no. Volume 19, 1969, pages 471–526, 1969. doi:https://doi.org/10.1146/annurev.ns.19.120169.002351. (Back to page 18)

[Nowacki 21a] F. Nowacki and Alexandre Obertelli and A. Poves. *The neutron-rich edge of the nuclear landscape. Experiment and theory*. Progress in Particle and Nuclear Physics, page 103866, 2021. (Back to page 108)

[Nowacki 21b] Frédéric Nowacki and Alexandre Obertelli and Alfredo Poves. *The neutron-rich edge of the nuclear landscape: Experiment and theory*. Progress in Particle and Nuclear Physics, vol. 120, page 103866, 2021. doi:https://doi.org/10.1016/j.ppnp.2021.103866. (Back to page 110)

[Okamoto 64] K. Okamoto. *Coulomb energy of He3 and possible charge asymmetry of nuclear forces*. Physics Letters, vol. 11, no. 2, pages 150–153,

1964. doi:https://doi.org/10.1016/0031-9163(64)90650-X. (Back to page 18)

[Otsuka 10] Takaharu Otsuka *et al. Novel Features of Nuclear Forces and Shell Evolution in Exotic Nuclei.* Phys. Rev. Lett., vol. 104, page 012501, Jan 2010. doi:10.1103/PhysRevLett.104.012501. (Back to page 110)

[Pauli 25] W. Pauli. *Über den Zusammenhang des Abschlusses der Elektronengruppen im Atom mit der Komplexstruktur der Spektren.* Zeitschrift für Physik, vol. 31, no. 1, pages 765–783, February 1925. doi:10.1007/BF02980631. (Back to page 12)

[Pauwels 08] D. Pauwels *et al. Shape isomerism at* $N = 40$*: Discovery of a proton intruder state in* ^{67}Co. Phys. Rev. C, vol. 78, page 041307, Oct 2008. doi:10.1103/PhysRevC.78.041307. (Back to page 112)

[Pauwels 09] D. Pauwels *et al. Structure of* ^{65,67}Co *studied through the* β *decay of* ^{65,67}Fe *and a deep-inelastic reaction.* Phys. Rev. C, vol. 79, page 044309, Apr 2009. doi:10.1103/PhysRevC.79.044309. (Back to page 112)

[Podadera Aliseda 04] I. Podadera Aliseda *et al. Design of a second generation RFQ Ion Cooler and Buncher (RFQCB) for ISOLDE.* Nuclear Physics A, vol. 746, pages 647–650, 2004. Proceedings of the Sixth International Conference on Radioactive Nuclear Beams (RNB6), doi:https://doi.org/10.1016/j.nuclphysa.2004.09.043. (Back to page 45)

[Podadera-Aliseda 06] Podadera-Aliseda, I. *New developments on preparation of cooled and bunched Radioactive Ion beams at ISOL facilities: the ISCOOL project and the rotating wall cooling*, 2006. Presented on 07 Jul 2006, doi:10.17181/CERN.A80J.OPTX, https://cds.cern.ch/record/975263. (Back to page 45)

[Porter 22] W. S. Porter *et al. Mapping the* $N = 40$ *island of inversion: Precision mass measurements of neutron-rich Fe isotopes.* Phys. Rev. C, vol. 105, page L041301, Apr 2022. doi:10.1103/PhysRevC.105.L041301. (Back to page 112, 119)

[Rahaman 07] S. Rahaman *et al. Masses of neutron-rich Ni and Cu isotopes and the shell closure at* $Z = 28$*,* $N = 40$*.* The European Physical Journal A, vol. 34, no. 1, pages 5–9, oct 2007. doi:10.1140/epja/i2007-10489-y. (Back to page 118)

[Ramirez 12] E. Minaya Ramirez *et al.* *Direct Mapping of Nuclear Shell Effects in the Heaviest Elements.* Science, vol. 337, no. 6099, pages 1207–1210, 2012. doi:10.1126/science.1225636. (Back to page 20)

[Recchia 12] F. Recchia *et al.* *Spectroscopy of odd-mass cobalt isotopes toward the $N = 40$ subshell closure and shell-model description of spherical and deformed states.* Phys. Rev. C, vol. 85, page 064305, Jun 2012. doi:10.1103/PhysRevC.85.064305. (Back to page 110)

[Ring 80] Ring, Peter and Schuck, Peter. The nuclear many-body problem. Springer-Verlag, New York, 1980. (Back to page 123)

[Rosenbusch 15] Rosenbusch, Marco. *Development of new ion-separation techniques for short-lived nuclides and the first mass measurements of 52,53K*, 2015. Presented 2015, https://cds.cern.ch/record/2244768. (Back to page 79, 81)

[Rosenbusch 24] Marco Rosenbusch. *Private communication*, 2024. Private communication. (Back to page 118)

[Rother 11] W. Rother *et al.* *Enhanced Quadrupole Collectivity at $N = 40$: The Case of Neutron-Rich Fe Isotopes.* Phys. Rev. Lett., vol. 106, page 022502, Jan 2011. doi:10.1103/PhysRevLett.106.022502. (Back to page 109)

[Savard 91] Guy Savard. *A new cooling technique for heavy ions in a Penning trap.* Physics Letters A, vol. 158, no. 5, pages 247–252, 1991. doi:https://doi.org/10.1016/0375-9601(91)91008-2. (Back to page 33)

[Severijns 23] N. Severijns *et al.* *$\mathcal{F}t$ values of the mirror β transitions and the weak-magnetism-induced current in allowed nuclear β decay.* Phys. Rev. C, vol. 107, page 015502, Jan 2023. doi:10.1103/PhysRevC.107.015502. (Back to page 19)

[Sorlin 02] O. Sorlin *et al.* *$^{68}_{28}Ni_{40}$: Magicity versus Superfluidity.* Phys. Rev. Lett., vol. 88, page 092501, Feb 2002. doi:10.1103/PhysRevLett.88.092501. (Back to page 108)

[Suchyta 14] S. Suchyta *et al.* *Shape coexistence in* ^{68}Ni. Phys. Rev. C, vol. 89, page 021301, Feb 2014. doi:10.1103/PhysRevC.89.021301. (Back to page 109)

[Suhonen 07] Jouni Suhonen. *From Nucleons to Nucleus: Concepts of Microscopic Nuclear Theory*. 2007. (Back to page 130)

[Talmi 62] Talmi, Igal. *Effective Interactions and Coupling Schemes in Nuclei*. Rev. Mod. Phys., vol. 34, pages 704–722, Oct 1962. doi:10.1103/RevModPhys.34.704. (Back to page 16)

[Tsunoda 14] Yusuke Tsunoda *et al. Novel shape evolution in exotic Ni isotopes and configuration-dependent shell structure*. Phys. Rev. C, vol. 89, page 031301, Mar 2014. doi:10.1103/PhysRevC.89.031301. (Back to page 109)

[Ubieto-Díaz 09] M. Ubieto-Díaz *et al. A broad-band FT-ICR Penning trap system for KATRIN*. International Journal of Mass Spectrometry, vol. 288, no. 1, pages 1–5, 2009. doi:https://doi.org/10.1016/j.ijms.2009.07.003. (Back to page 53)

[Van Isacker 95] Van Isacker, P. and Warner, D. D. and Brenner, D. S. *Test of Wigner's Spin-Isospin Symmetry from Double Binding Energy Differences*. Phys. Rev. Lett., vol. 74, pages 4607–4610, Jun 1995. doi:10.1103/PhysRevLett.74.4607. (Back to page 19)

[Vogel 24] Vogel, Manuel. Hyperbolic and cylindrical penning traps, pages 37–46. Springer International Publishing, Cham, 2024. doi:10.1007/978-3-031-55420-9_4. (Back to page 28)

[Weizsacker 35] Weizsacker, Carl Friedrich von. *Zur Theorie der Kernmassen*. Z. Phys., vol. 96, pages 431–458, 1935. doi:10.1007/BF01337700. (Back to page 11)

[Xayavong 24] Xayavong, L. and Smirnova, N. A. *Higher-order isospin-symmetry-breaking corrections to nuclear matrix elements of Fermi β decays*. Phys. Rev. C, vol. 109, page 014317, Jan 2024. doi:10.1103/PhysRevC.109.014317. (Back to page 18)

[Ziegler 12] F. Ziegler *et al. A new Pulse-Pattern Generator based on LabVIEW FPGA*. Nuclear Instruments and Methods in Physics Research Section A: Accelerators, Spectrometers, Detectors and Associated Equipment, vol. 679, pages 1–6, 2012. doi:https://doi.org/10.1016/j.nima.2012.03.010. (Back to page 55)

[Zuker 94] Andrés P. Zuker. *On the microscopic derivation of a mass formula*. Nuclear Physics, vol. 576, pages 65–108, 1994. (Back to page 128)

[Zuker 95] Zuker, Andres P. and Dufour, Marianne. *Separation of the monopole contribution to the nuclear Hamiltonian*. 5 1995. (Back to page 124)

Résumé/Abstract

Development and characterisation of the double Penning trap PIPERADE and mass measurements of neutron-rich isotopes near N=40

Abstract: The objective of this thesis focuses on the development and characterization of the PIPERADE double Penning trap (PIèges de PEnning pour les RAdionucléides à DESIR) at LP2i Bordeaux, as well as on mass measurements in the N=40 region conducted at the University of Jyväskylä, Finland. Mass spectrometry with Penning traps allows for the precise measurement of atomic nuclei masses. Nuclear binding energies, derived from atomic masses, are crucial for studying the structure of exotic nuclei and constraining nuclear physics models.

PIPERADE is dedicated to precision mass measurements and the selection of exotic ions of interest within the DESIR (Désintégration, Excitation et Stockage d'Ions Radioactifs) research facility at GANIL (Grand Accélérateur National d'Ions Lourds). This work presents the implementation of various purification and mass measurement techniques as well as the implementation of a new position-sensitive detector using microchannel plates and with three-layer delay-lines. The first technique explored is purification by Buffer Gas Cooling (BGC), followed by the "Time-of-Flight Ion Cyclotron Resonance" (ToF-ICR), applied for the first time with PIPERADE in November 2021. The optimization of these two techniques was subsequently pursued in parallel with the implementation of a new method, the "Phase-Imaging Ion Cyclotron Resonance" (PI-ICR). This method was successfully applied for the first time on PIPERADE in September 2023. This work also presents the first mass measurements using the ToF-ICR and PI-ICR techniques on PIPERADE.

In the second part of the thesis, mass measurements of neutron-rich nuclei were performed using the JYFLTRAP Penning trap, at the IGISOL facility. The masses of both ground and isomeric states of the isotopes of cobalt ^{68}Co to ^{70}Co, were measured, either for the first time for the isomeric states of ^{68}Co and ^{70}Co or with greatly improved precision for the others. The masses of the ground states of ^{79}Ge and ^{73}Ni were also measured. The analysis of the results allowed for comparison with theoretical models such as the Large Scale Shell Model (LSSM) and the Discrete Nonorthogonal Shell Model (DNO-SM). The results have a direct impact on understanding the N=40 gap and the region of the island of inversion.

Keywords: mass measurements, exotic nuclei, Ion traps

Développement et caractérisation du double piège de Penning PIPERADE et mesures de masses d'isotopes riches en neutrons proches de N=40

Abstract: L'objectif de cette thèse est le développement et la caractérisation du double piège de Penning PIPERADE (PIèges de PEnning pour les RAdionucléides à DESIR) au LP2i Bordeaux, ainsi que la réalisation de mesures de masses dans la région de N=40 à l'Université de Jyväskylä, en Finlande. La spectrométrie de masse à l'aide de pièges de Penning permet de mesurer les masses des noyaux atomiques avec une très grande précision. Les énergies de liaison nucléaire, déduites de ces masses atomiques, sont essentielles pour étudier la structure des noyaux exotiques et pour contraindre les modèles de physique nucléaire.

PIPERADE est dédié aux mesures de masse de précision et à la sélection d'ions exotiques d'intérêt pour l'installation de recherche DESIR (Désintégration, Excitation et Stockage d'Ions Radioactifs) du laboratoire GANIL (Grand Accélérateur National d'Ions Lourds). Ce travail présente la mise en œuvre des différentes techniques de purification et de mesure de masse ainsi que l'installation d'un nouveau détecteur sensible en position basé sur des galettes à microcanaux et avec trois couches de lignes à retard. La première technique étudiée est la purification par refroidissement avec gaz tampon ("Buffer Gas Cooling", BGC), suivie de la méthode "Time-Of-Flight Ion Cyclotron Resonance" (ToF-ICR), appliquée pour la première fois avec PIPERADE en novembre 2021. L'optimisation de ces deux techniques a ensuite été poursuivie parallèlement à la mise en place d'une nouvelle méthode, la "Phase-Imaging Ion Cyclotron Resonance" (PI-ICR). Cette méthode a été appliquée avec succès pour la première fois sur PIPERADE en septembre 2023, suivie d'une optimisation continue des trois techniques. Ce travail présente également les premières mesures de masse utilisant les techniques ToF-ICR et PI-ICR sur PIPERADE.

Dans la seconde partie de cette thèse, des mesures de masses de noyaux riches en neutrons ont été effectuées avec le piège de Penning JYFLTRAP, sur l'installation IGISOL. Les masses des états fondamentaux et isomériques des isotopes du cobalt ^{68}Co à ^{70}Co, ont été mesurées, soit pour la première fois pour les états isomériques des ^{68}Co et ^{70}Co, soit avec une précision grandement améliorée pour les autres. La masse de l'état fondamental du ^{79}Ge ainsi que celle du ^{73}Ni ont également été mesurées. L'analyse des résultats a permis de comparer les nouvelles valeurs de masses aux prédictions des modèles théoriques tels que le Large Scale Shell Model (LSSM) et le Discrete Nonorthogonal Shell Model (DNO-SM). Ces résultats ont un impact direct sur la compréhension du gap N=40 et de la région de l'îlot d'inversion.

Keywords: noyaux exotiques, pièges à ions, mesures de masse

Unité de recherche

LP2iB UMR 5797, 33170 Gradignan, France.